SAPIENZA
UNIVERSITÀ DI ROMA

Department of Chemical Materials and Environmental Engineering

Doctoral program in Electrical, Materials, Raw Materials and Nanotechnology Engineering

XXXVII cycle

New routes for carbon nanostructures growth with applications in structural composite materials and environmental remediation

PhD Candidate

Ginevra Lalle

Supervisor

Prof. Jacopo Tirillò

Academic year 2023-2024

Table of Contents

PART III – RESULTS AND DISCUSSION

Introduction

Nowadays, fibre-reinforced polymer composites (FRPs) find extensive application in a wide range of industrial sectors, including aerospace, automotive, and energy. Their ever-increasing widespread use is driven by the demand for materials with ultra-light weight and high mechanical performances [1] which are accomplished in FRPs through the synergistic interaction of at least two distinct phases, i.e., the polymer matrix and the reinforcing fibres, across their interface [2]. However, contrarily to the excellent longitudinal (to fibres) tensile properties, debonding at the fibre/matrix interface under transverse loading remains the dominating failure mode in FRPs [3], leading the scientific community to devote numerous resources to exploring new strategies for interface optimization.

In this context, the incorporation of an additional nanoscale reinforcement within FRPs, either dispersed in the polymer matrix or attached to the fibre surface, has emerged as a promising solution inspired by the multiscale hierarchical architectures often found in nature, e.g., bone and nacre, where the interaction of each constituent across multiple length scales often results in superior and sometimes contradictory properties, such as combined high strength and toughness [4], [5]. Specially, anchoring nanomaterials to the fibre surface creates nanostructured interfacial regions with enhanced strength transfer and interfacial adhesion thanks to increased fibre surface area, mechanical interlocking and local stiffening at the fibre/matrix interface [6]. Carbon nanostructures (CNSs), particularly carbon nanotubes (CNTs), are regarded as ideal candidate nano-reinforcements which, thanks to their extraordinary lightweight, mechanical, electrical and thermal properties, can enhance the structural performance of FRPs while providing, in addition, inherent multifunctionalities [7]. Therefore, a new generation of hierarchical FRPs may be developed which combines high structural performances with embedded multifunctionalities, such as the ability to sense damage [8], remediate the environment [9], or store electrical energy [10], fulfilling the requirements of a wider range of industrial applications.

CNT deposition onto the surface of fibres has been achieved by dip coating [11], spray coating [12], electrophoretic deposition (EPD) [13], chemical grafting [14] and direct growth through chemical vapour deposition (CVD) [15]. Among these techniques, the CVD method is often the preferred option, allowing to produce higher CNT loadings with a potential radial orientation [16], [17] which provide superior improvements in the interfacial shear strength (IFSS) as well as transverse reinforcement. Conventional thermal CVD growth of CNTs involves the decomposition of carbonaceous gases in the presence of nanoparticles of a transition metal catalyst (e.g., Fe, Ni, Co) acting as nucleation sites for CNT growth. By modifying catalyst features (i.e., type, size, uniformity over the underlying substrate) and CVD parameters, such as process gas mixture and flow rates, growth temperature, and reaction time, the CVD method enables to tailor the morphology and quality of synthesized carbon nanostructures. Furthermore, the potential scalability of the process has already been addressed, with some works proposing a continuous production line integrating all the steps required for a CVD growth process [16], [18], [19].

Despite being promising, direct CVD growth features a major drawback related to the high-temperature environment (600 – 1000 °C) and reactive conditions typically required in the CVD chamber, which can seriously compromise the mechanical properties of the fibre substrate. Significant loss of tensile strength was reported for carbon fibres at temperatures as low as 550 °C in both hydrocarbon-containing and inert atmospheres [20] while, at higher temperatures (~700 °C), these fibres are usually damaged by the interaction with the iron catalyst. More severe strength loss, starting at temperatures as low as 250 °C [21], has been reported for general-purpose glass fibres, which are thus typically considered not suitable substrates for direct CNT growth.

Quartz fibres, also known as ultrapure silica glass fibres, are designed for in-use temperatures much higher than E- or S-glass fibres, with an operating temperature limit of ~1200 °C and softening temperatures around 1710 °C for quartz fibres compared to ~460 °C and 600 °C, respectively, for E-glass fibres [19], [22]. These fibres, therefore, emerge as interesting candidates for direct CNT growth. Analogously, basalt fibres, with an operating temperature limit of ~650 °C and softening temperatures around 1050 °C,

are expected to be more suitable CVD substrates than glass fibres [23], [24]. Moreover, thanks to their volcanic rock-based origin, specific mechanical properties comparable to those of E-glass fibres and a lower environmental impact during manufacturing [25]–[27], basalt fibres are considered a viable eco-friendlier alternative to glass fibres. Direct CNT growth onto the surface of basalt fibres is, therefore, a promising strategy for interface optimization in basalt fibre composites, usually suffering from weak interfacial properties [28], and for the implementation of additional functionalities that would allow the use of basalt fibre-reinforced composites in a wider range of industrial fields. Nevertheless, even in the case of quartz and basalt fibres, exposure to typical CVD temperatures is expected to have a non-negligible impact on the original fibre mechanical properties [29], [30].

In sight of this, the main objective of this research is achieving the direct growth of carbon nanotubes on the surface of quartz and basalt fibres via low temperature CVD (≤550 °C), thus mitigating the degradation of the mechanical properties of the fibre substrates following high temperature exposure. To this aim, two strategies are proposed and investigated both separately and in combination with each other: (i) a plasma enhanced (PE)-CVD technology, and (ii) innovative catalysts, requiring lower temperatures to be activated. In PE-CVD, a high energetic plasma supplies some of the energy required for the CVD chemical reactions (i.e., hydrocarbon decomposition, carbon diffusion through the catalyst nanoparticles, carbon precipitation and crystallization in a cylindrical network) enabling lower operating temperatures [31] than conventional thermal CVD, which exploits only thermal energy for the growth. Moreover, PE-CVD technology permits to control not only the location, dimensions, and structure of carbon nanotubes (CNTs) during the synthesis, as in the case of thermal CVD, but also the alignment of the tubes due to interaction with the electric field [32]. Low temperature formation and activation of the catalyst nanoparticles is also a crucial factor to achieve the low temperature synthesis of carbon nanostructures. To date, the use of bi- or tri-metallic combinations of traditional CVD growth catalyst, such as Fe, Ni and Co, have been found to decrease process temperatures below 500 °C [33]. However, innovative catalyst materials might be capable of growing CNTs at even lower temperatures, as in the case of sodium being recently demonstrated to be active towards the growth of CNTs onto a

variety of substrates, including carbon and alumina fibres, at temperatures around 400 °C [34].

In the present work, a PE-CVD technique is first investigated and compared to thermal CVD in the presence of a traditional Fe-based catalyst. Afterwards, the use of a copper-based catalyst is proposed, being previously reported to catalyse the growth of carbon nanofibres at temperatures as low as 250 °C [35]. Additionally, a novel *in-situ* catalyst generation approach is explored for CNT synthesis on basalt fibres, allowing to exploit the native iron content of basalt without any external catalyst deposition. This strategy, reported for the first time by Foster et al. [15] and optimized by Sarasini et al. [36] through high temperature CVD (>700 °C), is here combined with a PE-CVD technique to investigate its potential at low synthesis temperatures (below 550 °C). The research focusses on the optimization of the CVD growth parameters and provides a detailed characterization of the morphology of CNT-decorated fibres through scanning electron microscopy (SEM), transmission electron microscopy (TEM), and Raman spectroscopy, to assess the effects of novel catalysts and plasma assistance on the spatial arrangement, structure, and growth modes of CNTs synthesized onto the selected fibre substrates.

As a baseline for this investigation, a systematic study of the effects of typical CVD temperatures (600 – 800 °C) on the mechanical properties of quartz fibres is conducted to clarify possible thermally-induced damage mechanisms which, unlike those occurring in general-purpose glass and basalt fibres [37], were rarely investigated in the literature. Various experimental characterizations, including single fibre tensile testing, SEM investigation of lateral and fracture surfaces, TEM investigation of fibre cross-sections, X-ray diffraction analysis (XRD), thermogravimetric analysis (TGA), density measurements, and nanoindentation-based techniques, are carried out to highlight possible variations in the fibre mechanical properties, surface morphology and microstructure following thermal exposure and suggest the related controlling mechanisms.

In conclusion, the properties of CNT-modified fibres are addressed with a focus on their potential structural and multifunctional applications. As regards the use within structural composite materials, the effect of the optimized CVD protocols on the tensile strength of

single fibres is evaluated, while the wetting properties of CNT-modified fibres towards a structural epoxy matrix are assessed and compared to those of commercially sized fibres. Finally, the electrochemical properties of CNT-decorated fibres are investigated to showcase potential environmental remediation and energy harvesting opportunities of these materials, opening possibilities for the development of high-performance structural composites with integrated multifunctionalities.

PART I – STATE OF THE ART

PART I – STATE OF THE ART

Chapter 1.

Fibre-reinforced composite materials

Over the past century, composite materials have gained ever-growing attention and usage in the most diverse application fields. Especially the use of fibre-reinforced polymer composites (FRPs) has seen a rapid spread in a wide range of industrial sectors, including aerospace, automotive, construction, energy, sports, and many others, due to their remarkable structural and mechanical properties, with a global fibre-reinforced composites market size valued at USD 93,254.56 million in 2023 and expected to grow at a compound annual growth rate (CAGR) of 5.9% during the period 2024–2032, reaching USD 133,053.11 million by 2032 [1].

Composite materials consist of two or more distinct phases that, while retaining their intrinsic chemical and physical identities, synergistically interact across the interface to provide the final product with unique and enhanced properties [2]. An outstanding combination of high strength, stiffness, lightweight, and corrosion resistance arises from the synergistic interaction between the individual constituents of these materials, making them excellent replacements for traditional materials, such as steel and aluminium, especially for lightweight components in the automotive and aerospace industries.

At least three different elements can be identified in a composite material: the reinforcement, the matrix, and the reinforcement/matrix interface. The matrix material can be a metal, a ceramic or, more often, a polymer, such as epoxy resin, vinyl ester or polyester, whereas the reinforcement can be in the form of particles, fibres, or whiskers of various synthetic or natural materials. Composites composed of a fibrous reinforcement, either short (discontinuous) or long (continuous) fibres, dispersed in a polymeric matrix are often referred to as fibre-reinforced polymers (FRPs). The fibres are the principal load-carrying element, while the functions of the matrix include holding the

reinforcement together, shaping the final product, transferring the load to the reinforcement, and preventing direct contact of the reinforcement with the external environment.

1.1.Reinforcing fibres

Reinforcing fibres are the principal load-carrying element in a composite material. They can be classified into synthetic and natural fibres according to their origin. Synthetic fibres do not occur in nature and require chemical synthesis processes to be produced from chemical resources, most generally petrochemicals [38]. On the other hand, natural fibres derive from materials readily available in nature. Therefore, despite the superior mechanical performance of synthetic FRP composites, their cost, poor recycling and non-biodegradability have triggered growing attention for the development of environmentally friendly composite materials using natural fibres [39], [40]. Particularly, thanks to the low density and satisfactorily high specific properties of natural FRPs, these materials have found extensive applications in the automotive and transportation industry, as well as in construction and in packaging industries [41].

1.1.1. Synthetic fibres

Synthetic fibres can be distinguished into polymer base, such as fibres produced from polyamides and polyesters, or mineral base, such as glass and carbon fibres. Glass, carbon, and aramid fibres are the most widely used.

The production of synthetic fibres usually requires different stages depending on the type of fibres. Generally, the spinning stage is the process in which the raw materials are formed into continuous fibre from solution or molten state. The raw materials are rapidly drawn through a spinneret, which contains a high number of orifices, into fine diameter fibres [42]. The manufacturing of carbon fibres typically starts with the solution or suspension polymerization process of polyacrylonitrile (PAN), which is the most used precursor for carbon fibres (~96% of the carbon fibre market) [43]. Afterwards, the polymeric fluid is spun into fibres which are washed and stretched to the desired diameter, stabilized, and then carbonized at 1000-3000 °C in inert atmosphere to lose most of non-

carbon atoms and achieve well-ordered carbon crystals aligned mainly parallel to the fibre axis [44]. Finally, surface treatments, including oxidation and sizing application, are performed to increase the fibre compatibility with the polymer matrix. Glass fibres are produced from the co-melting of silica with various oxides to a desired composition in order to facilitate melting, homogenizing, removal of gaseous inclusions, and fibre formation at optimum temperatures [22]. The molten glass is then extruded through a platinum-rhodium alloy bushing with several thousand orifices. As the fibres exit the bushing, they are cooled rapidly to avoid devitrification and then a sizing is applied before they are gathered into strands to prevent abrasion between the filaments and impart resin compatibility [45], [46].

The application of a sizing agent on the surface of glass fibres after the spinning step is fundamental to obtain composite materials with good mechanical properties. The sizing formulation usually includes suitable lubricants and emulsifiers, aiming at reducing the abrasion between filaments and facilitate handling, as well as a film former and a coupling agent, usually an organofunctional silane, to promote the adhesion with the polymeric matrix in the final composite. In addition, the silane coupling agent and/or the film former have been proved to have a great influence on the tensile strength and Weibull parameters of single fibres, with the ability of reducing the population of inherent flaws on the fibre surface [47], [48].

Based on the complexity, high cost and high energy consumption involved in the production of these fibres, glass and carbon fibre composites remain more expensive than conventional materials such as wood, steel, and aluminium. Despite their cost, carbon fibres occupy a leading role among synthetic fibres for applications in which excellent strength and weight reduction are required. Carbon fibres are extensively used in aviation and automotive industries to produce lightweight structural components due to the higher strength-to-weight ratio than steel which allow a significant reduction in the CO_2 emissions during the product life cycle. In addition to the low density, high strength and stiffness, these fibres exhibit excellent resistance to chemical agents, corrosion, vibration, and abrasion, as well as high conductivity, all of them arising from the chemical structure

of carbon, characterized by the high stability of the hexagonal rings surrounded by delocalized electrons [49], [50].

Compared to carbon fibres, glass fibres have lower specific strength and modulus but are less expensive. Consequently, nearly three-quarters of FRPs produced are reinforced with glass fibres and their market share is expected to growth at a CAGR of 5.8 % in the next years (2024–2032). Glass-fibre reinforced polymers find applications in various fields, including wind energy, transportation, pipes and tanks, construction, electrical and electronics, aerospace and defence [51]. Glass fibres are classified in several categories based on their composition and key properties for specific applications. In general, all types of glass fibres fall in two categories, namely general-purpose glass fibres and special-purpose glass fibres.

General-purpose glass fibres are known with the designation E-glass and are defined according to ASTM D578 specifications. They are primarily composed of CaO, Al_2O_3, and SiO_2, with B_2O_3 content varying from 0 to 10 wt.%. Due to environmental and legislative regulations, requiring the introduction of expensive abatement systems to eliminate boron from the off-gases of the melts, boron-free E-glass were developed. Boron-free E-glass fibres usually possess a tensile strength at room temperature equal to that of boron-containing E-glass fibres and a slightly higher (around 5%) elastic modulus.

Special-purpose glass fibres include fibres with high strength (S-, R-, and Te-glass), with low dielectric constants (D-glass), with high corrosion resistance (ECR-glass), with high silica content (high silica, pure and ultrapure silica fibres). High silica fibres (95% SiO_2) and pure silica fibres are designed for applications requiring high in-use temperatures. Particularly, ultrapure silica glass fibres or quartz fibres (99.99% SiO_2) combine superior properties at high temperatures, including low coefficient of thermal expansion, low thermal conductivity, high thermal shock resistance, and ablation resistance, with lightweight properties, low dielectric constant and dielectric loss, good chemical stability and excellent transparency to ultraviolet and longer wavelength radiation. Consequently, quartz fibres are extensively used in wave-transparent composite radomes and antenna windows in aviation, aerospace, and 5G communication services. Although the name

“quartz” fibres would imply the presence of a crystalline structure, quartz fibres are amorphous glass fibres.

1.1.2. Natural fibres

Natural fibres can be obtained from vegetable, animal or mineral resources [52], [53]. Animal fibres include silk, wool, cashmere, while examples of natural fibres of mineral origin are basalt, wollastonite, and attapulgite. According to the different sections of plant and trees from which the fibres are produced, vegetable fibres can be further categorized into seed fibres (cotton, kapok), leaf fibres (sisal, agave), skin fibres (flax, jute, hemp), fruit fibres (coir), stalk fibres (bamboo, wood). Due to their vegetable origin, plant fibres are completely biodegradable, abundantly available, renewable, often relatively inexpensive, and possess low density and good specific strength and elastic modulus.

In the last decades, the commitment of most countries towards environmental issues has led to more restrictive policies in the field of environmental pollutions and directives encouraging the use of materials from renewable sources. In particular, the European Parliament promulgated two important directives limiting the end-of-life disposal of composite materials reinforced with synthetic fibres in landfills: “Directive on Landfill of Waste (Directive 99/31/EC)” and the “End-of-life Vehicle Directive (Directive 2000/53/EC)” [54]. In 2008, the directive 2008/1/EC in the field of Integrated Pollution Prevention and Control (IPPC) issued many regulations addressing waste management and industrial emissions [55]. Consequently, an increasing demand for sustainable and eco-friendly alternatives to synthetic fibres is driving a significant growth of the global natural fibre composite market, which was valued at USD 356.29 million in 2023 and is estimated to attain around USD 743.94 million by 2033, growing at a CAGR of 7.64% from 2024 to 2033 [56]. Thanks to their lightweight properties and good strength-to-weight ratio, plant fibres-reinforced composite materials find extensive applications in the automotive industry, allowing for a reduction in fuel consumption and CO_2 emissions [57]. However, the widespread use of plant fibres as alternative to synthetic fibres is limited by several factors, including reduced durability, low thermal stability, poor resistance to chemical agents, and high variability in mechanical properties [58]. In

particular, they exhibit a high tendency to absorb moisture, which causes the fibre to swell, leading to dimensional instability and degraded mechanical response of the composite [59]. The chemical-physical response of vegetable fibres depends on their chemical composition, which includes cellulose, hemicellulose, lignin, pectin and wax in different percentages [60]. Large amounts of hemicellulose increase the moisture absorption tendency and reduce the durability of the fibre [61]. Additionally, the presence of hydrophilic cellulose as main constituent of plant fibres is responsible for a poor interfacial adhesion with the hydrophobic polymer matrices, resulting in inefficient stress transfer at the interface in the final composite [62], [63]. To address this issue, physical and chemical treatments are carried out to improve the wettability and increase the surface roughness of the fibres, including alkaline, silane, benzyl, acrylate, maleated coupling treatments [64], [65]. Another strategy to overcome the limitations of vegetable fibres is their use in combination with synthetic fibres in hybrid composites [40], [41].

Basalt fibres are mineral fibres of volcanic-rock based origin. Compared to plant fibres, they offer several advantages, including excellent chemical stability, minimal moisture absorption, good resistance to weather, acid and alkali environments, significant heat and acoustic insulation, and a good range of thermal performance, with operating temperature limits ranging from -200 °C to 600-800 °C [27], [66], [67]. These properties, along with a mechanical performance superior to that of E-glass fibres [68], make them an effective alternative to glass fibres for various applications, such as shipbuilding, automotive, pipelines, fire protection, sport equipment, etc.

Basalt, a volcanic rock originated from frozen lava, is mainly composed of two minerals: plagiocene and pyroxene. Basalt fibres' composition, therefore, includes different oxides, with SiO_2 as the main constituent and Al_2O_3 as the second one [69], [70]. A typical composition of basalt fibres is reported in Table 1.1. The presence of iron oxides has been reported to exert a key role for the higher mechanical performance of basalt fibres compared to glass fibres, at the expense of a higher density [68]. Despite the similar chemical composition to asbestos, the different morphology and surface properties of basalt fibres avoid carcinogenic or toxicity effects to human beings [66].

Table 1.1 Typical composition of basalt fibres according to two different authors [69], [70].

Constituent	**Content [wt%]**	
	[69]	[70]
SiO_2	43.3–47	42.43–55.69
Al_2O_3	11–13	14.21–17-97
Fe_2O_3	<5	10.80–11.68
CaO	10–12	7.43–8.88
MgO	8–11	4.06–9.45
Na_2O	<5	2.38–3.79
TiO_2	<5	1.10–2.55
K_2O	<5	1.06–2.33

The manufacturing process of basalt fibres, consisting in drawing molten basalt rocks at temperatures around 1450-1500 °C through a platinum/rhodium bushing [66], is similar to that of glass fibres. This favours the spreading of basalt fibres thanks to the good adaptability of the industrial plants already available. In 2024, the global basalt fibre market has reached a value of USD 121.8 million and is expected to grow at 12.4% CAGR, up to a value of USD 392.1 million by 2034 [71]. Compared to glass and carbon fibres, basalt fibres are considered more environmentally sustainable as their manufacturing process has a lower energy consumption and does not require chemical additives, solvents, pigments or other hazardous substances [26], [27]. The lower environmental impact of basalt fibres compared to glass fibres has been recently demonstrated by Ghali et al. [25]. The life cycle assessment (LCA) performed on each fibre showed a lower global warming potential of basalt fibres (2.19 kg of CO_2-eq emissions against the 3.43 kg of glass fibres) and a lower acidification of soil and water, calculated as 0.01 kg of SO_2-eq emissions for basalt fibres against the 0.02 kg of glass fibres.

All this makes basalt fibres a valid green alternative to synthetic fibres, particularly glass fibres. Moreover, thanks to the lower amount of hydroxyl groups on their surface, basalt

fibres exhibit a higher compatibility with the polymer matrices than fibres of vegetable origin. However, compared to the more common synthetic fibres, the interfacial adhesion of basalt fibres is relatively weak. As a consequence, there is a great interest in developing new strategies for the surface modification of basalt fibres to enhance the fibre/matrix adhesion and make basalt fibres a viable green alternative to glass fibres.

1.2. Fibre/matrix interface

The interface is the common border surface that constitutes the bond between the matrix and the reinforcement. It plays a critical role in FRPs as it controls the load transfer from the matrix to the reinforcement and thus determines the final structural performance of the composite [72], [73]. The load transfer capability of the interface depends on the fibre/matrix adhesion which requires accurate tailoring to guarantee a composite material with the desired properties. Good interfacial adhesion is required to achieve high stiffness and strength, while a relatively weak bond generally enhances energy absorbing performances for impact resistance [74]. Given the key role of the interface, special attention has been paid to understanding the microstructural mechanisms of interfacial adhesion, which include physical-chemical and frictional contributions. It is worth noting that the process of forming interfacial bonding produces a local change in the properties of the fibre and the matrix creating a region with distinct properties from the bulk fibre and matrix. The term *interphase* was therefore introduced in the 1970s to expand the interface concept to a three-dimensional region, with its own defined thickness, in which the chemical, physical and mechanical properties vary continuously or in a stepwise manner from the reinforcement to the matrix [75], [76]. A schematic illustration of the interface and interphase concepts is shown in Figure 1.1.

The nature of the bonding at the fibre/matrix interface is a complex subject and it is specific to each fibre/matrix system as it depends not only on the chemical nature of the two phases but also on the fibre morphology and the diffusivity of the elements in each constituent. Interfacial adhesion can be generally attributed to several mechanisms, often acting collaboratively to produce the final bond. These mechanisms include adsorption and wetting, electrostatic attraction, chemical bonding, inter-diffusion, and mechanical

bonding as well as low energy interactions such as hydrogen bonding and van der Waals forces.

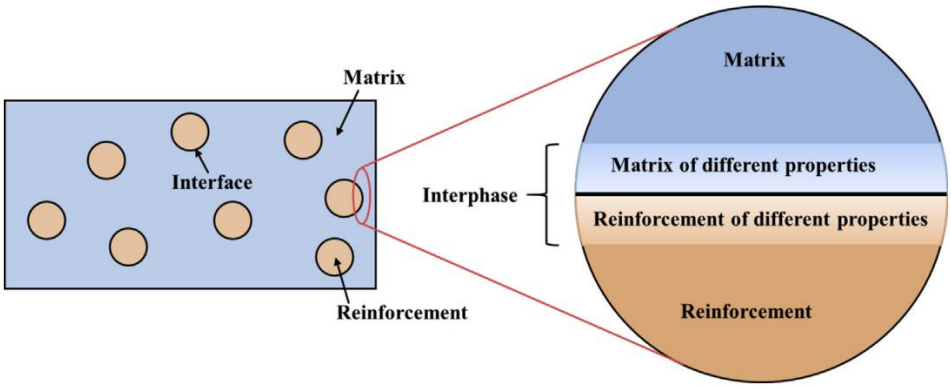

Figure 1.1 Schematic illustration of the concepts of fibre/matrix interface and interphase [77].

1.2.1. Adsorption and wetting

The theory of interactions between solids and liquids is of primary importance when studying adhesion mechanisms at the fibre/matrix interface. In fact, a good wettability of the fibres by the polymer matrix, i.e., the ability of the liquid matrix to spread on the fibre solid surface, is required during the impregnation phase of composite manufacturing [78]. Based on Dupré equation (Eq. 1.1), wettability can be quantitatively expressed as the thermodynamic work of adhesion of a liquid to a solid:

$$W_a = \gamma_s + \gamma_L - \gamma_{SL} \tag{1.1}$$

Where γ_s and γ_L are the surface free energy of the solid and of the liquid, respectively, and γ_{SL} is the free energy at the solid-liquid interface. W_a is defined as the work required to separate two phases having a common interface and, thus, is a measure of interfacial adhesion due to wetting: the higher the work of adhesion, the stronger the bonding.

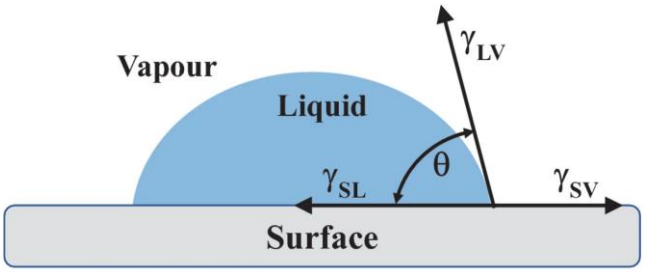

Figure 1.2 Schematic illustration of a liquid droplet on a solid surface.

The wetting properties of a liquid towards a solid surface are also described by the contact angle, that is formed at the equilibrium by a liquid droplet placed on a solid surface (Figure 1.2). The resolution of forces in the point where the three phases (solid, liquid, and vapour) are in contact is dependent on the surface and interfacial energies according to Young's equation (Eq. 1.2):

$$\gamma_{SV} = \gamma_{SL} + \gamma_{LV} \cos\theta \tag{1.2}$$

Where γ_{SV} is the surface free energy at the solid-vapour interface, γ_{SL} at the solid-liquid interface, γ_{LV} at the liquid-vapour interface and θ is the contact angle. Based on the value of the contact angle, liquids can be classified in *wetting*, when the contact angle is lower than 90°, and *non-wetting*, when the contact angle is higher than 90°. By combining the equations 1.1 and 1.2, Young-Dupré equation is obtained:

$$W_a = \gamma_{LV}(1 + \cos\theta) \tag{1.3}$$

Therefore, the work of adhesion can be experimentally determined by knowing the contact angle and the liquid surface energy. Interfacial bonding due to wetting is generated by very short-range interactions of electrons on the atomic scale that depends on van der Waals interactions (dispersive forces) and on the polar attractions of Lewis acids and bases. The surface energy of the liquid can be calculated according to Owens and Wendt equation (Eq. 1.4):

$$\gamma_s + \gamma_L - \gamma_{SL} = 2\sqrt{\gamma_s^d \gamma_L^d} + 2\sqrt{\gamma_s^p \gamma_L^p} \tag{1.4}$$

Where γ_s^d and γ_s^p are the dispersive and polar components of the surface free energy of the solid (reinforcement), and γ_L^d and γ_L^p are the dispersive and polar components of the surface free energy of the liquid (matrix).

1.2.2. Electrostatic attraction

Electrostatic attraction contributes to interfacial adhesion when there is a difference in electrostatic charge between fibre and matrix surfaces. The force of the bonding is determined by the charge density. Compared to the other interaction mechanisms, the electrostatic attraction can be already active at relatively longer distances, having a distance range of the order of centimetres [79]. However, when the materials are in intimate contact, its contribution is typically small unless suitable coupling agents are first applied on the fibre surface [75], [80].

1.2.3. Chemical bonding

A chemical bonding at the interface can be formed by chemical reactions between compatible chemical groups on the fibre and matrix surfaces. As the fibres and the polymer matrices are often dissimilar in nature, coupling agents are often added to the formulation of the fibre protective coating (i.e., sizing) to promote the formation of chemical boding across the interface, thus improving the adhesion and compatibility of the two different materials. The use of coupling agents is efficient for this purpose as they possess, at one end of their molecule, a functional group that can react with the compatible chemical group on the fibre surface and, at the other end, a functional group compatible with the matrix. A typical example is the use of silane agents for glass and basalt fibres as they contain a functional group that can react with the hydroxyl groups of the fibre surface and another group, such as vinyl, that can react with the epoxy groups of the matrix [81]. Similarly, maleic anhydride-based agents are used to enhance the interaction between vegetable fibres and polymer matrices [82].

1.2.4. Mechanical bonding

Mechanical interlocking or anchoring between the fibre and the matrix can be promoted by surface irregularities of the fibres, such as pits, corrugations, and crevices. The strength of the bonding is closely related to the fibre surface roughness: the rougher the surface, the higher the fibre/matrix bond area, and hence, the higher the adhesion strength. This type of mechanism is commonly exploited in carbon fibre-polymer matrix composites. The carbon fibre is subjected to surface oxidation treatments which increase the fibre surface roughness, thus favouring the mechanical anchoring with the matrix [83]. As regards natural fibres, their distinctive irregular and non-homogenous surface allows a mechanical interlocking with the polymer matrix [84]. The strength of this type of bonding is likely to be more significant in longitudinal shear than in transverse tension, in which is likely to be relatively weak unless many re-entrant angles are produced on the fibre surface. Grafting various nanomaterials, e.g. carbon nanotubes [13], ZnO nanorods [85], on the fibre surface has been demonstrated to increase the surface roughness and enhance the mechanical interlocking. Particularly, 1-dimensional carbon nanotubes with a radial orientation are especially effective in providing a bonding in the transverse direction in addition to the longitudinal one [86].

1.2.5. Inter-diffusion

The inter-diffusion mechanism in FRPs is commonly observed at the interfacial region between the polymeric matrix and the polymeric sizing applied on the fibre surface after fibre manufacturing. The sizing formulation usually contains a polymer, referred to as film former, whose molecular chains can diffuse into the matrix, and vice versa, the matrix can diffuse into the sizing, due to high compatibility of the film former with the polymeric matrix [74], [87]. The bonding is governed by a thermodynamic equilibrium and its strength depends on the number of diffused macromolecules, on the amount of entanglement and on the energy of the chemical bonds involved. The molecular migration involved in the interdiffusion mechanism produces an interphase of substantial thickness, with a change of chemical, physical and mechanical properties from those of both the bulk fibre and the bulk matrix [75].

Chapter 2.

Hierarchical fibre-reinforced composites

Despite the widespread use of FRPs as structural components in various industrial fields, the early onset of damage due to debonding at the fibre/matrix interface remains a critical issue [3]. Contrarily to the excellent in-plane tensile properties, laminate FRPs suffer from weak compression and out-of-plane properties, especially delamination resistance [88]. In this context, the hierarchical architecture of many natural materials, such as plant cell walls, animal shells and bones, has provided inspiration for a new class of synthetic composite materials, in which a nanoscale reinforcement is employed alongside microscale reinforcing fibres. The interaction across multiple length scale provides hierarchical materials with unique structural properties, such as combined high strength and toughness even arising from weak constituents [4]. Furthermore, the introduction of nanomaterials at the fibre/matrix interface, e.g. anchored to the fibre surface, creates nano-engineered 3D interfacial regions (interphases) with enhanced adhesion properties. Among nanomaterials, carbon nanostructures (CNSs), including graphene, carbon nanofibres (CNFs) and particularly carbon nanotubes (CNTs), are considered the most attractive candidate nanofillers for developing hierarchical FRPs. Thanks to their unique mechanical, chemical, thermal and electrical properties [7], CNTs allow to implement additional functions in FRPs, such as the ability to store electrical energy, sense damage, resist lightning strikes [7], [89], [90] and remediate the environment [9]. CNT-based hierarchical FRPs are therefore emerging as a new generation of high-performance structural composites with enhanced fibre/matrix interfacial adhesion and additional functionalities, meeting the requirements of a wider class of applications compared to conventional fibre-reinforced composites.

2.1. Fabrication techniques

Two approaches have been used to incorporate CNTs in FRPs, either dispersing them into the polymer matrix, or anchoring them to the fibre surface. These approaches will be

described in the following paragraphs with a focus on fibre modification which is the strategy investigated in this research work.

2.1.1. Matrix modification with CNTs

The matrix modification approach has the advantage of simplicity and compatibility with standard manufacturing techniques, as it involves the shear-mixing of CNTs into the resin and the impregnation of the CNT-modified matrix into the fibre preform. While the fibre-dominated in-plane properties are scarcely affected by the introduction of CNTs, the matrix-dominated properties are significantly improved. Gojny et al. [91] reported a 20% increase in the matrix-dominated interlaminar shear strength (ILSS) of a glass-fibre reinforced composite by introducing 0.3 wt% of amino-functionalised double-wall carbon nanotubes in the epoxy matrix. Moreover, the introduction of CNTs provided the glass-fibre reinforced composite with electrical conductivity, showcasing a multifunctional opportunity of CNT incorporation. The mechanical and functional properties of the composite have been shown to depend on the loading and dispersion of CNTs into the matrix [92]. However, the maximum CNT amount is strongly limited by the consequent increase in resin viscosity, while the homogeneous dispersion is hindered by CNT agglomeration [93] and filtering against the fibre preform during the impregnation process [94]. Agglomeration sites act as stress concentration points, thus reducing the overall mechanical performance of the composite. Consequently, most researchers focused on the latter approach of attaching the CNTs directly to the fibre surface, producing the so-called *fuzzy* or hierarchical fibres.

2.1.2. Fibre modification with CNTs

Compared to the dispersion in the polymer matrix, the reinforcement modification with CNTs allows to incorporate higher CNT loadings, alleviates the issue of agglomeration [88], and typically provides higher enhancement of interfacial adhesion [95], [96]. In fact, thanks to the high aspect ratio of CNTs, their incorporation onto the fibre surface notably increases the fibre/matrix contact area, thus enhancing the intensity of van der Waals interactions at the interface [97], [98]. Contact angle measurements have shown a good

wettability of different polymer matrices, including epoxy resins, towards hierarchical fibres. Qian et al. [98] measured an increase in the BET surface area from 0.12 ± 0.01 m^2/g of pristine silica fibres to 4.21 ± 0.38 m^2/g of CNT-grafted silica fibres, which resulted in excellent wettability of the CNT-grafted fibres with the poly(methyl methacrylate) (PMMA) matrix. In addition, the fibre/matrix interfacial bond is strengthened by the mechanical interlocking between the CNTs and the matrix. Zeng et al. [99] demonstrated that the high aspect ratio of CNTs favours the interlock between the fibre and the matrix, resulting in increasing modulus and strength of glass-fibre reinforced polymers with increasing CNT aspect ratio, until reaching a plateau at an aspect ratio of 1300 due to CNT agglomeration. Suitable CNT functionalization has also been shown to promote the formation of a chemical bonding, further improving the interfacial adhesion [100].

The various methods to apply CNTs on the surface of reinforcing fibres include dip-coating, spray coating, electrophoretic deposition (EPD), chemical grafting and direct growth through chemical vapour deposition (CVD). The dip-coating process is the simplest and most cost-effective method to produce *fuzzy* fibres involving the dispersion of CNTs in an aqueous or non-aqueous dipping medium through mechanical stirring or ultrasonication. By immersing the fibre in the CNT dispersion, a CNT-containing containing sizing is applied to the fibre surface, as schematically illustrated in Figure 2.1a. Incorporation of CNTs into sizing formulations has been proved to enhance the surface roughness of the fibre, provide local stiffness at the fibre/matrix interface, and introduce functional opportunities for sensing applications. However, agglomeration of poorly dispersed CNTs can produce a non-uniform coating, thus limiting the effectiveness of the dip-coating method. Spray coating is another widely used coating technique (Figure 2.1b). Zhang et al. [101] used a spray coating method to deposit CNTs on carbon fibre prepregs, demonstrating a significant increase in the out-of-plane mechanical properties of carbon fibre laminates even at a relatively low CNT loading (0.047 wt%). Methanol was used to disperse CNTs and, after spray coating, was evaporated by heating. The method provided good spatial control and allowed the formation of a CNT network on the fibre surface leading to excellent sensing signals for potential applications as structural health monitoring systems.

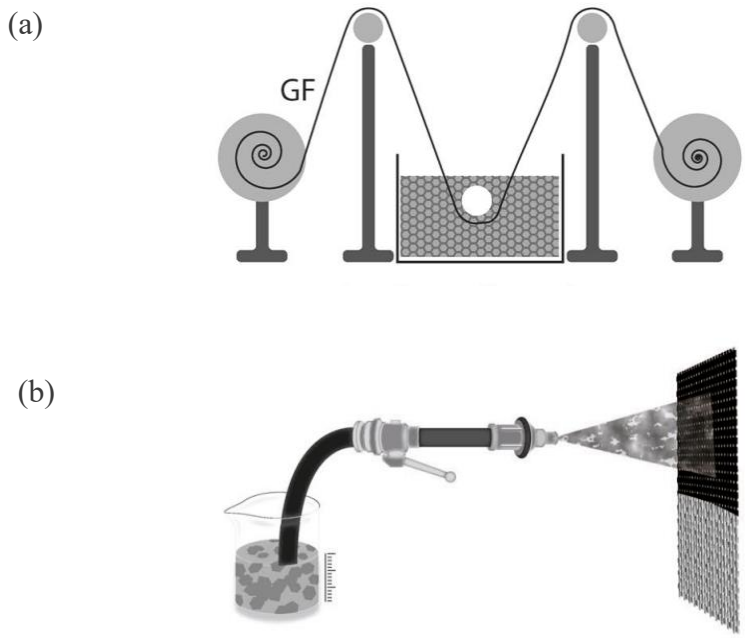

Figure 2.1 Schematic of different coating techniques for CNT incorporation: (a) dip-coating; (b) spray-coating [92].

Despite their simplicity, cost-effectiveness, and applicability to various substrates, the coating methods offer limited interfacial strength due to weak physical adsorption between CNTs and the fibre surface. Moreover, they allow scarce control over the orientation of CNTs, leading to the deposition of randomly oriented CNTs lying in the plane of the fibre surface. The efficiency of CNT deposition on fibres can be improved by promoting a chemical bonding between the CNTs and the fibre surface with an approach named chemical grafting. Chemical grafting can be achieved either by chemical reaction between functionalized CNTs and the reactive groups on the fibre surface or by using a coupling agent to bridge the bond between the fibre and the CNTs. An example of the former approach involves the chemical modification of the hydroxyl groups into amine groups on the glass fibre surface and oxidative treatments via wet chemistry to produce -COOH and -OH groups on the CNTs. As a result, an amine coupling can be easily achieved by reaction between the amine groups of the glass fibres and the carboxyl ones of the CNTs, as schematically displayed in Figure 2.2 [102]. Xiong et al. [103] prepared a CNT-modified carbon fibre reinforcement by dip-coating using a silane coupling agent (3-glycidyl ether oxy-propyl trimethoxy silane, KH560) as the bridge

between carbon fibres and CNTs. Good interfacial adhesion with epoxy resin was achieved as demonstrated by contact angle measurement and IFSS measured by micro-droplet debonding test. Another example of the use of a coupling agent as bridge between CNTs and carbon fibres reported by Chen et al. [104] is illustrated in Figure 2.3. Moreover, the grafting density of the CNTs, which is usually scarce with conventional coupling agents, can be increased by exploiting a layer-by-layer grafting technique, as reported by Zhao et al. [14].

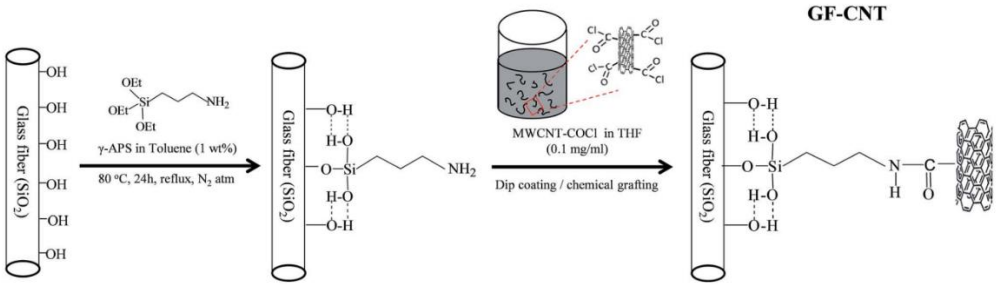

Figure 2.2 Schematic illustration of the experimental preparation of CNT-grafted glass fibres detailing the formation of covalent bonds [102].

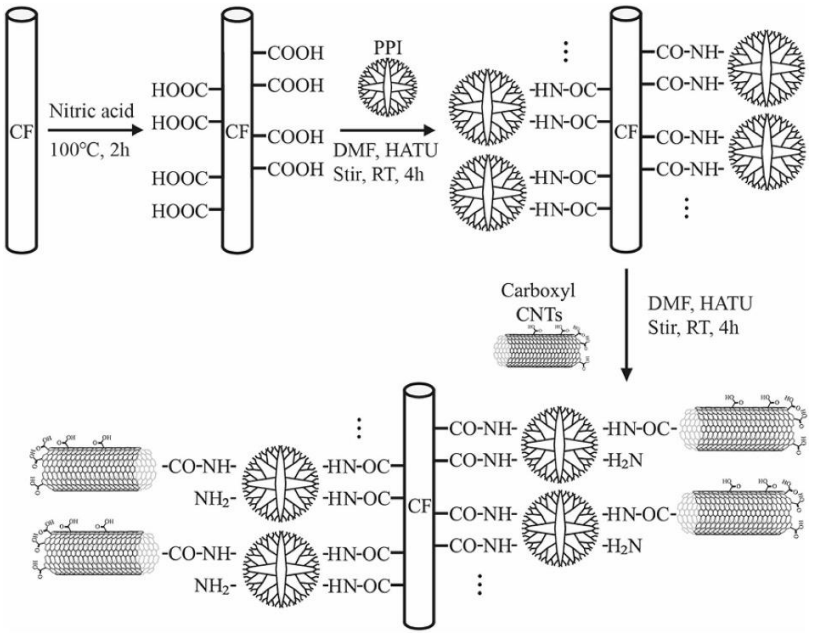

Figure 2.3 Schematic for the preparation of CNT-grafted carbon fibres detailing the use of poly(propylene imine) (PPI) as bridging agent [104].

In electrophoretic deposition (EPD), charged CNTs are stably dispersed in a solvent and made to migrate towards the substrate under the effect of an electric field in a two-electrode cell. In general, the EPD method requires conductive substrates, such as metallic or carbon fibres, as the voltage is applied between the substrate and a counter electrode. Zhang et al. [5] and Haghbin et al. [105] demonstrated its applicability to non-conductive glass fibres by employing two parallel copper plates as cathode and anode and mounting the fibres on the deposition electrode (the anode) (Figure 2.4). By comparing the coating quality obtained through the EPD process to the one obtained by dip-coating, Zhang et al. [5] observed that the EPD method produced a more homogeneous CNT coverage leading to higher interfacial shear strength with epoxy and lower scatter in the electrical properties for damage sensing applications. Numerous studies showed that EPD configuration in parallel electrodes only leads to the deposition of randomly oriented CNTs on the fibre substrate, thus limiting the potential transverse reinforcement in the final composite material. To achieve the deposition of vertically aligned CNTs (VA-CNTs), Li et al. [86] employed a coaxial cylindrical electrode with the carbon fibre as the cathode (Figure 2.5). This configuration allowed to tune the alignment degree of CNTs by controlling the deposition voltage, dispersion time, and CNT concentration in dispersion. However, the application of a similar configuration to non-conductive fibres remains challenging.

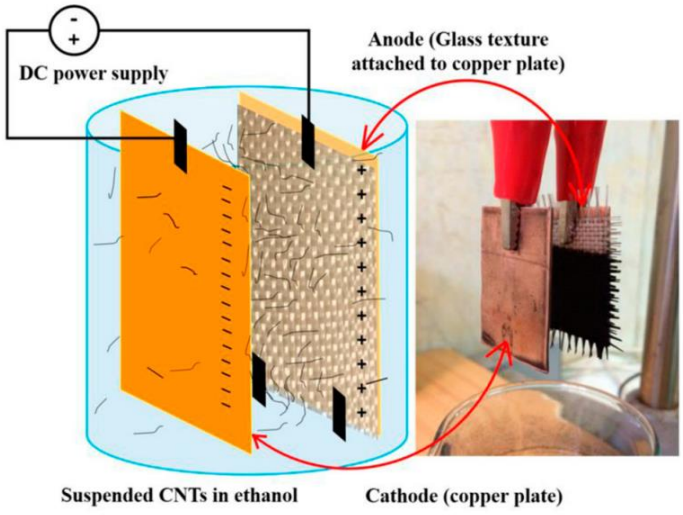

Figure 2.4 Experimental set-up for the electrophoretic deposition of CNTs on non-conductive glass fibre preform [105].

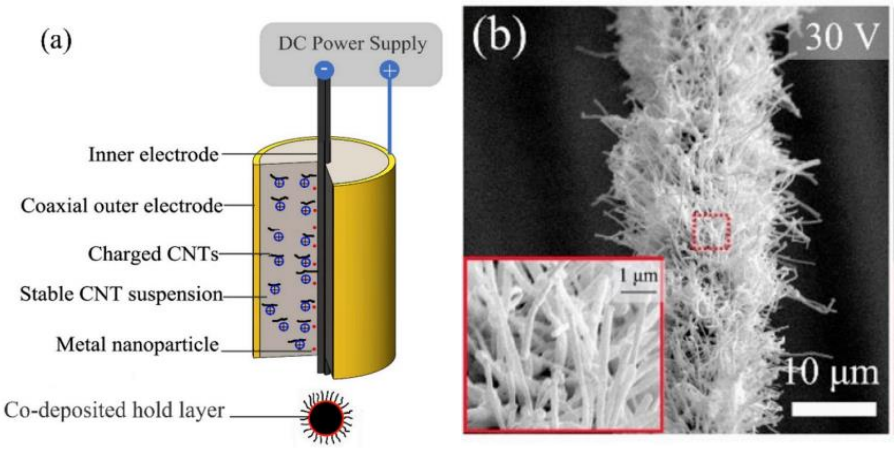

Figure 2.5 (a) Schematic of the coaxial electrode for EPD deposition of VA-CNTs; (b) representative FESEM image of CNT/carbon fibre hierarchical reinforcement obtained at a deposition voltage of 30 V [86].

In this context, the direct growth through chemical vapour deposition (CVD) emerges as the only strategy to allow an excellent control over the orientation and density of CNTs by properly tuning the process parameters. The *in-situ* growth of high loadings of radially aligned CNTs has been achieved on a variety of fibre substrates, including carbon, glass, basalt, and alumina fibres. Briefly, the direct synthesis of CNTs on the fibre surface is achieved from a carbon-rich vapour phase generated by the decomposition of a carbon feedstock, usually a hydrocarbon gas. To catalyse the decomposition of the carbon source and seed the CNT growth, the fibre surface is covered by nanoparticles of transition metals such as Fe, Ni, and Co. Therefore, prior to the CVD growth, a catalyst precursor is deposited on the fibre surface and then reduced in hydrogen atmosphere in the CVD chamber to generate active catalyst nanoparticles. Some works have attempted to integrate all the steps required in the CVD process into a continuous production line, demonstrating its potential scalability [16], [18], [19]. De Luca et al. [16] developed an open-ended growth reactor and produced fuzzy quartz fibres in a continuous fashion, as schematically summarized in Figure 2.6.

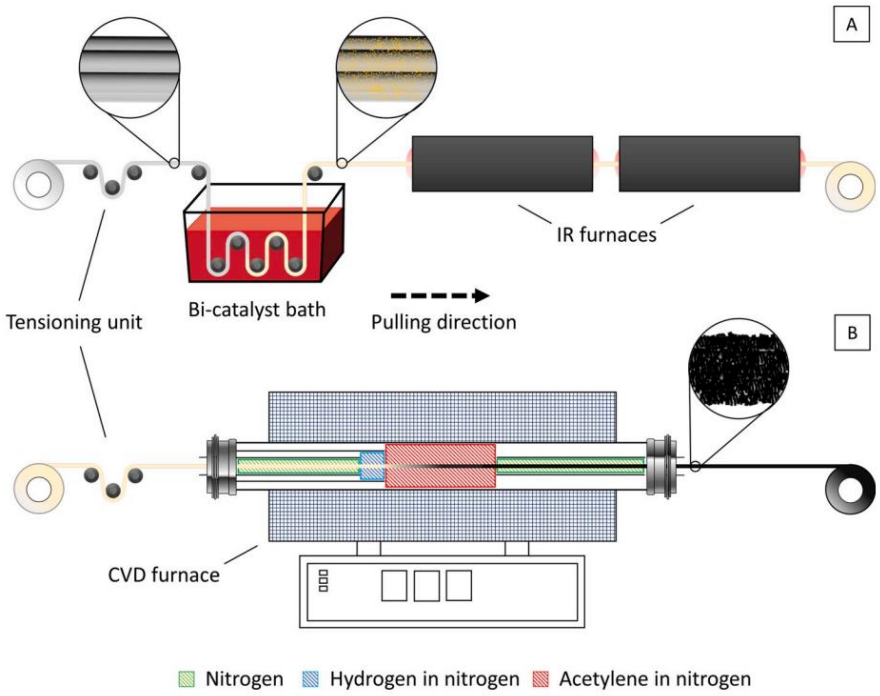

Figure 2.6 Schematic illustration of an experimental set-up for the continuous CVD synthesis of CNTs on quartz fibres. The process consists of two lines: (a) the catalyst precursor deposition line; (b) the open-ended CVD set-up for the CNT synthesis on the catalyst-decorated quartz fibres [19].

2.2. Mechanical and interfacial properties of CNT-based hierarchical FRPs

The incorporation of CNTs into conventional fibre-reinforced polymers is expected to improve the mechanical performance of the composite material thanks to their high specific stiffness and strength and, particularly, to the enhancement of fibre/matrix interfacial properties, which reduces stress concentrations and the initiation and propagation of interfacial cracks.

Wu et al. [106] recently reviewed the mechanical properties of CNT-based hierarchical FRPs, in terms of tensile and flexural strength and modulus, based on the literature in the year span 2010-2022. These properties are summarized in Figure 2.7 as the ordinate of each graph in comparison to the properties of the pristine FRPs, reported as the abscissa.

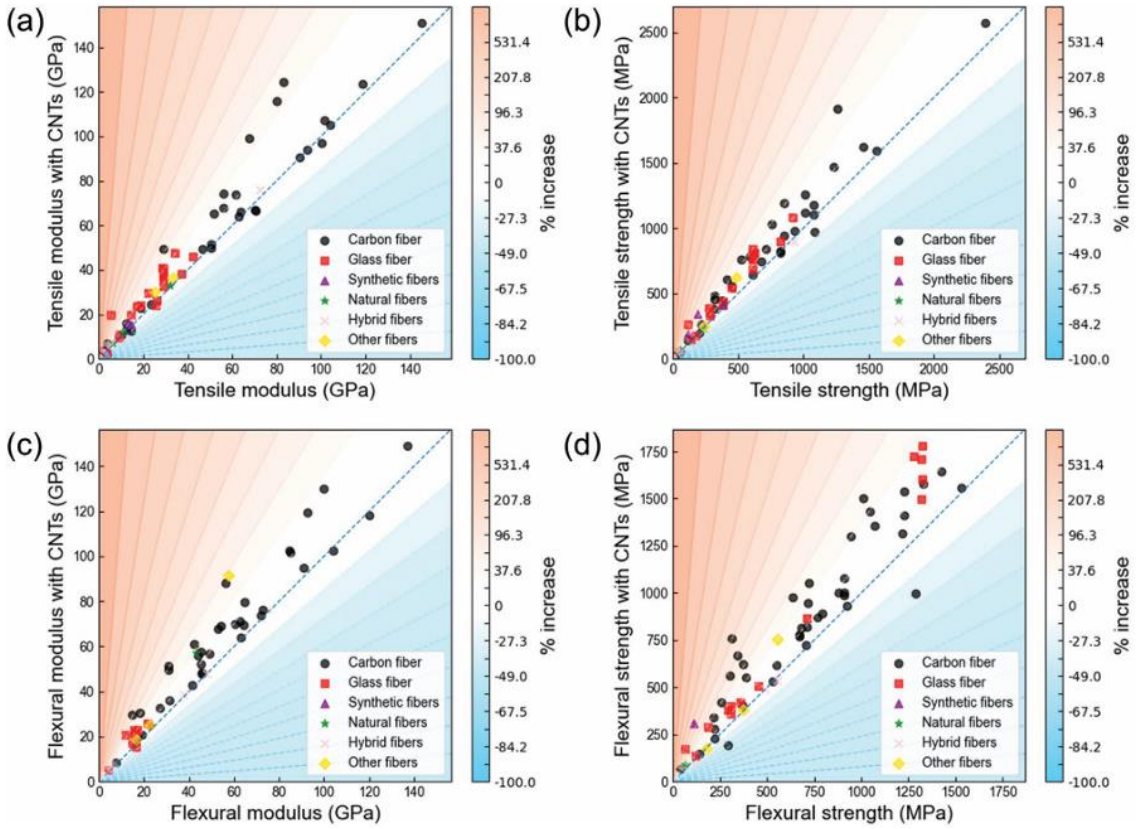

Figure 2.7 Mechanical properties of CNT-based hierarchical FRPs: a) tensile modulus, b) tensile strength, c) flexural modulus and d) flexural strength. Each graph reports the mechanical properties of the pristine FRPs on the x-axis and the properties of CNT-FRPs on the y-axis. FRPs are grouped into 6 categories according to the fibre types, which are carbon fibre, glass fibre, synthetic fibre (including polymer based fibres such as aramid fiber and ultra-high molecular weight polyethylene), natural fibres (including fibres of vegetable origin such as jute fibre and flax fibre), hybrid fibres (when two types of fibres are used together) and other fibres (including basalt fibre, alumina fibre, stainless wire, and brass wire), respectively. The colour bar indicates that a darker colour represents a greater increase in the tensile/flexural modulus/strength. The detailed data and the references are reported in [106].

The incorporation of CNTs was found to significantly increase these four properties compared to the pristine composite material for almost all the reported data, as they mainly fall in the region of the graph above the diagonal line. Nevertheless, a few studies reported a negative effect of the introduction of CNTs, which are generally attributed to poor processing, in particular to the inhomogeneous dispersion of CNTs in the matrix [107], [108]. In fact, as previously discussed, the homogeneous incorporation of CNTs in

the matrix is often hindered by self-filtration issues [94] and CNT agglomeration [93], which limit the effectiveness of CNT incorporation compared to CNT grafting on the fibre surface. Besides, different methods of producing CNT-modified fibres may also modify the percentage of improvement of the mechanical properties. Rong at al. [109] compared CNT-FRPs made through CVD and through chemical grafting, reporting a 20% higher tensile strength and 15% higher flexural strength for CNT-FRPs produced through the former method, which may be attributed to the radial orientation of CNTs grown by CVD that can more effectively strengthen the interface [109]. However, the effectiveness of the direct growth of CNTs on reinforcing fibres might be strongly limited by the degradation of the mechanical properties of the fibre substrate due to the exposure to the high temperatures required for the CVD synthesis of CNTs. An example was reported by Yildiz et al. [110], who measured a 24% decrease in the tensile strength of epoxy composites reinforced with CNT-modified glass fibres produced through direct CVD growth, as a result of the 42% decrease in the tensile strength of CNT-modified glass fibres following CVD at 650 °C. In this case, the incorporation of CNT in the epoxy matrix was found to be more effective, leading to an improvement by 17% in the tensile strength of the resulting composite material.

As the tensile properties of the fibre reinforcement play an important role in determining the mechanical properties of the resulting FRP composite, the degradation of these properties (i.e., tensile strength and modulus) following the direct CVD growth of CNTs is a major issue for the development of high-performance structural composite materials.

2.2.1. Tensile properties of CNT-modified fibres

CNT growth temperatures, generally ranging from 600 to 1000 °C, are not suitable for temperature sensitive substrates. This is a major issue in the direct growth on reinforcing fibres, as the initial mechanical properties of the fibre substrate are often degraded by exposure to the high temperatures and reactive conditions used during CNT growth. For example, carbon fibres are easily attacked by oxygen at temperatures as low as 400 °C and undergo severe strength degradation when heated above 550 °C in both hydrocarbon containing and inert atmospheres [20]. Moreover, common catalyst materials diffuse into

the graphene grains of carbon fibres at high temperatures, causing surface damage and even higher strength degradation. Glass fibres, due to their relatively low softening temperatures (~600 °C for E-glass) and their degradation of mechanical properties at temperatures as low as 250 °C [21], [111], are typically considered not well suited for direct CNT growth. Basalt fibres and quartz fibres are generally more high-temperature resistant than glass fibres [22]–[24] in terms of higher operating temperature limit (~650 °C for basalt and ~1200 °C for quartz compared to ~460 °C for E-glass), and higher softening temperatures (1050 °C for basalt, 1710 °C for quartz), therefore showing better chances to survive a CVD growth process. Nevertheless, recent studies have highlighted a similar degradation pattern of tensile strength for basalt and glass fibres after a thermal conditioning at medium-high temperatures. As reported by Sarasini et al. [67] and Lilli et al. [29], basalt fibres undergo a strength loss of around 75% following heat-treatments at 600 °C. Even in the case of quartz fibres, a strength loss of more than 50% of their original tensile strength was reported after exposure at 760 °C for 30 minutes in N_2 [19]. Also, Zheng et al. [30] found the tensile strength of quartz fibres to decline sharply after 10-hour exposure at 600, 700, 800 and 900 °C in air atmosphere.

The issue of thermal degradation of glass and basalt fibres has been widely investigated in the literature. Several damage mechanisms, classified as surface and structural phenomena, have been proposed to address the issue of thermal strength degradation of these fibres. The two main surface phenomena are sizing removal [15] and thermally induced diffusion of water [16]. Thermal exposure can also cause structural relaxation of the anisotropic silica network structure originated by the high drawing stress during the fibre fabrication [112], [113]. As a consequence, the loss of the mechanical strength of glass and basalt fibres is usually accompanied by increases in the room-temperature density and Young's modulus of heat-treated fibres [67], [114], [115].

As regards quartz fibres, limited research has been carried out. Only Zheng et al. [30] studied the morphology, surface structure and tensile strength of quartz fibres after 10-hour exposure in the temperature range 600-900 °C in air atmosphere. Based on scanning electron microscopy (SEM), transmission electron microscopy (TEM), X-ray diffraction (XRD), and tensile tests, they revealed the formation of nanometre crystallites on the fibre

surface, which are considered to produce new surface defects, leading to strength retention up to only 1/30 of the fibre original mechanical strength after exposure at 900 °C. However, whether the bulk fracture properties of quartz fibres are affected by thermal exposure is not detailed.

2.2.2. Interfacial and interlaminar properties

The main purpose of the incorporation of CNTs in conventional fibre-reinforced composites materials lies in the optimization of fibre/matrix interfacial adhesion for enhancing the structural performance of resulting composite materials. As described in section 1.2 of Part I – State of the art, the quality of the bonding at the fibre/matrix interface determines the efficiency of the stress transfer between the matrix and the fibres and depends on different microstructural mechanisms. The introduction of CNTs can act on one or more of these mechanisms and enhance the resulting interfacial adhesion. For instance, the dispersion of CNTs in the polymer matrix can enhance the fibre/matrix wettability via changes in the matrix surface tension properties [74]. Similarly, CNT modification of the fibre surface might affect the fibre surface free energy and the consequent wettability by the polymer matrix [11]. Modifications of CNTs with functional groups can lead to the formation of chemical bonding with those of the matrix or on the fibre surface [108]. Furthermore, introducing CNTs on the fibre surface is expected to promote mechanical interlocking mechanisms by increasing the surface roughness and fibre/matrix contact area [116].

The improvement of interfacial properties of CNT-based hierarchical composites compared to conventional FRPs has been extensively characterized in the literature by performing experimental characterizations both at the single fibre level and at the composite level. In the former case, the strength of fibre/matrix adhesion is expressed in terms of interfacial shear strength (IFSS), usually characterized by micro-debonding tests, fibre pull-out tests, fibre fragmentation tests, or fibre push out tests, whereas in the latter case, the salient interfacial properties refer to the interlaminar shear strength (ILSS) which is usually measured through compression shear or short beam shear tests.

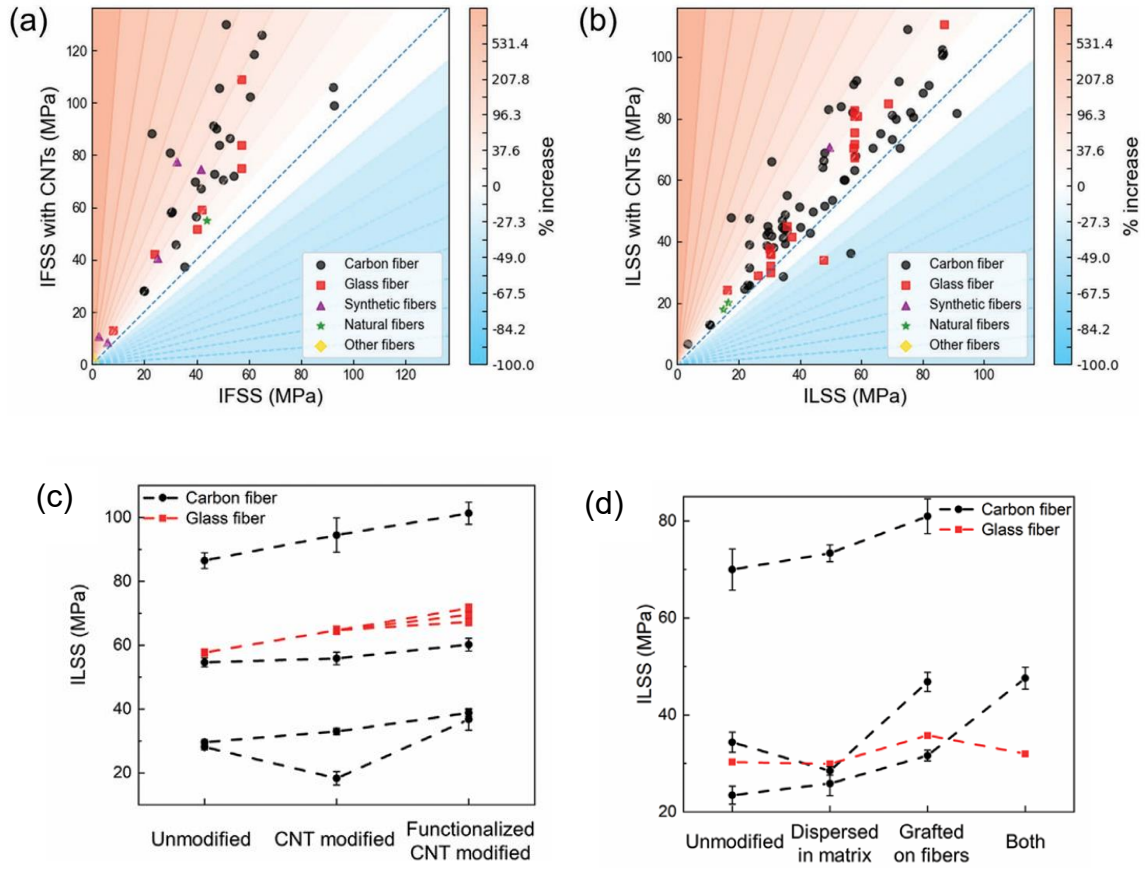

Figure 2.8 Interfacial properties of CNT-based hierarchical FRPs (plotted as the ordinate) compared to pristine FRPs (plotted as the abscissa), demonstrating the effect of CNT incorporation: a) IFSS, b) ILSS, c) effects of CNT functionalization on ILSS of CNT-based hierarchical FRPs, d) effects of the incorporation process of the CNTs on ILSS of functionalized CNT-FRPs. The detailed data and the references are reported in [106].

Figure 2.8 reports a summary of the interfacial properties of CNT-based FRPs compared to pristine FRPs [106]. Most of the composites exhibited greatly enhanced interfacial properties after the incorporation of CNTs. As shown in Figure 2.8c, further enhancements in ILSS can be obtained by functionalizing the CNTs, e.g. amino-functionalized [117] or carboxyl-functionalized CNTs [118]. Compared to dispersions in the matrix, the incorporation of CNTs on the fibre surface was found to produce a more significant increase in the interlaminar properties at similar CNT contents (Figure 2.8d). Additionally, the orientation of CNTs on the fibre surface seem to be an important factor for enhancing the IFSS, with larger improvements achieved in the case of vertically

oriented CNTs compared to randomly oriented CNTs [86], as they can extend deeper into the matrix promoting mechanical interlocking and transverse reinforcement.

2.3. Functional properties of CNT-based hierarchical FRPs

With extraordinarily high mechanical and lightweight properties, CNTs are considered an ideal structural reinforcement for composite materials, whereas their intrinsic functional properties (e.g., high electrical and thermal conductivities) can enlarge the use of hierarchical FRPs to many application fields, including sensors [119], electromagnetic interference (EMI) shielding [120], structural health monitoring [8], energy storage and harvesting [10].

The incorporation of highly conductive nanofillers, such as CNTs, in FRPs was reported to form a continuous path which enables the traveling of free electrons and conduct the electricity, conferring electrical properties such as conductivity, EMI shielding, and sensing, to an otherwise non-conductive composite material [10]. As an example, He et al. [121] studied the electrical conductivity of epoxy composite reinforced with CNT-modified glass fibres. The CNTs were directly grown with a radial orientation on the fibre surface through the CVD method. This study revealed an increase in the electrical conductivity of the composite material with the increase of the weight fraction of the CNTs on the fibre surface, leading to in-plane and through-plane electrical conductivities of 100 and 3.5 S m^{-1}, respectively, with 7 wt.% CNTs. The electrical properties of CNTs could be exploited also in composite materials reinforced with carbon fibres which, despite having high in-plane conductivity, often show relatively low through thickness electrical conductivity [122] and are susceptible to lightning strikes [123]. Using this approach, Sawi et al. [94] reported an improve in the through-thickness electrical conductivity of unidirectional carbon fibre-reinforced composites by one order of magnitude, while the conductivity in the other two directions did not change significantly.

CNT-decorated quartz fibres were demonstrated by De Luca et al. [19] to provide electrical conductivity and a piezoresistive response to quartz fibre-reinforced epoxy composites, offering sensing capabilities which are particularly useful for structural health monitoring applications. As regards basalt fibres, Sarasini et al. [36] measured an

electrical conductivity of ~260 S m^{-1} for basalt fabrics decorated with long vertically-aligned CNT forests synthesised through direct CVD growth.

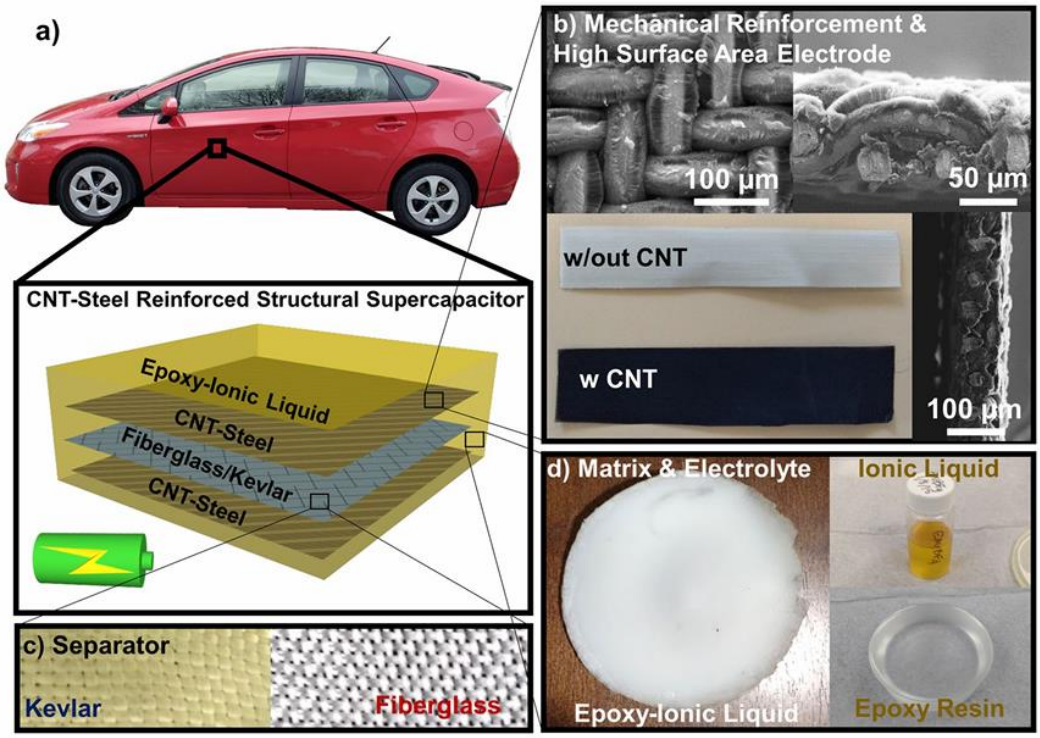

Figure 2.9 Design of the CNT reinforced structural supercapacitor proposed by Muralidharan et al. [131]. (a) Schematic showing the structural supercapacitor with the vision of a reinforced composite material that could be used in a vehicle chassis. (b) SEM and optical images of a CNT-steel mesh. d) Photograph of fiberglass and Kevlar separators. (c) Photographs of the epoxy-ionic liquid electrolyte on the left and the individual components on the right.

Owing to the increasing concern on environmental issues of recent years, including the shortage of water resources and soil contamination, carbon nanomaterials are getting more and more attention of researchers due to their unique physical-chemical and electrochemical properties which can be exploited for the development of highly efficient technologies for environmental remediation activities, i.e., water and soil decontamination [9], [124]. Particularly, carbon nanotubes, even coupled to iron-based nanoparticles [125], were demonstrated to have great potential for the removal of various pollutants from wastewaters, including heavy metal ions, organic dies and other recalcitrant pollutants [126], due to their superior adsorption, photocatalytic and

electrocatalytic capabilities [127], [128]. Anchoring these nanomaterials to reinforcing fibres in FRPs can prevent their dispersion in water and ecosystem during environmental remediation activities. On the other side, due to the peculiar chemical and electrochemical properties of CNTs, CNT-based hierarchical composites also represent promising materials to be used as electrode [129] or membrane [130] in electrochemical processes.

In addition to the environmental remediation application, the electrochemical properties of CNTs have attracted a huge interest for making structural energy storage composites, including batteries, fuel cells, and supercapacitors [132], [133]. In these structural electrochemical devices, the traditional electrochemical functions (i.e., energy storage or harvesting) are embedded into load-bearing FRP composite structures. These materials could potentially be used in electric vehicles, aerospace, marine, and satellites, allowing for consistent weight reductions and enhanced system performances. Specially, supercapacitors are promising energy storage systems, as they can store large amounts of electrical energy. They are composed of two conducting plates soaked in an electrolyte and separated by a very thin insulator. Due to their high surface area and electrical conductivity, CNTs are desirable materials as electrodes for supercapacitor applications [134], [135] while their incorporation in FRPs can lead to the development of capacitors with both load bearing and energy storage capabilities, referred to as structural supercapacitors. A possible configuration for a structural supercapacitor was proposed by Shirshova et al. [136], who assembled two modified carbon fabric electrodes, separated by a glass fabric, infused with a multifunctional polymeric electrolyte. Another study reported a supercapacitor fabricated by using dense, aligned CNTs grown on stainless steel mesh as electrodes separated by Kevlar or fiberglass mats in an ion conducting epoxy electrolyte matrix [131]. The resulting energy storage composite, shown in Figure 2.9, exhibited high mechanical properties combined with an energy density up to 3 mWh/kg.

Chapter 3.

Carbon Nanotubes

3.1. Structure and Properties

Carbon nanotubes (CNTs) are allotropes of carbon composed of one or more graphene sheets rolled up into a seamless cylinder [137], [138]. When composed of a single graphene sheet, CNTs are referred to as single-walled (SW)-CNTs, while multi-walled (MW)-CNTs are composed of multilayers of graphene sheets with an interlayer spacing of 0.34 nm. The diameters of SWCNTs and MWCNTs are typically in the range of 0.4-3 nm and 5-20 nm, respectively, although MWCNT diameter can exceed 100 nm [139]. A schematic representation of SWCNTs and MWCNTs is displayed in Figure 3.1.

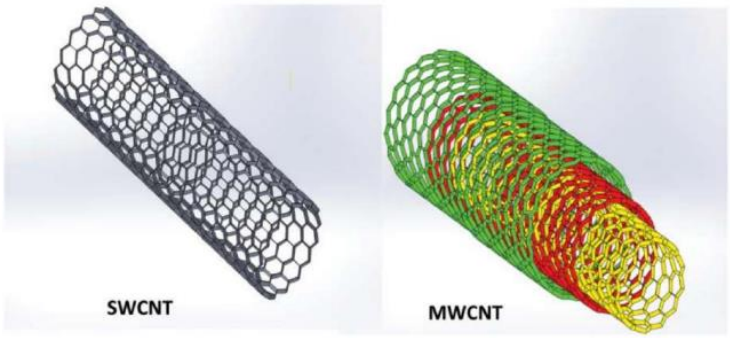

Figure 3.1 Schematic representation of the structure of SWCNTs and MWCNTs [140].

The length of CNTs fluctuates from less than 100 nm to several centimetres [141]. Consequently, CNTs feature superior length/diameter ratios (10^2-10^4) which contribute to the unique properties of this material. Sometimes, the ends of CNTs appear closed, as shown in Figure 3.2. In the case of SWCNTs, the closing is made of hemifullerenic elements, formed by pentagonal and hexagonal rings, while more complex geometries are observed for MWCNTs [142].

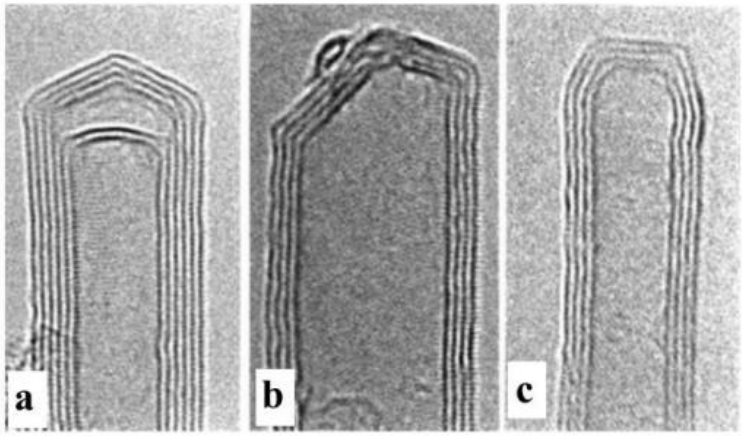

Figure 3.2 TEM micrographs of CNTs: (a-c) MWCNTs with closed ends. The parallel lines are the cross-sections of the sidewalls of concentric cylinders. Diameters of MWNTs are typically on the order of 10–20 nm [141].

In terms of mechanical properties, CNTs are among the strongest and most resilient existing materials. Elastic moduli of the order of 1 TPa and tensile strengths approaching 100 GPa, which are higher than any industrial fibre, have been predicted for individual MWCNTs [143], [144]. The high intrinsic tensile strength of CNTs is due to their hexagonal lattice with sp^2-hybridation, corresponding to a higher bonding energy (614 kJ/mol) than sp^3-bonds [140]. However, structural defects can reduce the measured tensile strength, which typically lies in the range 25-66 GPa [143].

As regards the electrical conductivity, MWCNTs can be either metallic, semiconductor or small-gap semiconductor depending on the tube chirality, i.e. the orientation of the exagonal lattice with respect to the tube axis, and can carry current densities up to 100 MA/cm^2 [145]. Moreover, thermal conductivities as high as 3000 W/m K have been reported, which are superior to the thermal conductivity of diamond [146].

3.2. Synthesis through Chemical Vapour Deposition (CVD)

The synthesis of CNTs is generally achieved through three main techniques, which are schematically summarized in Figure 3.3:

- laser ablation,
- arc-discharge,

- chemical vapour deposition (CVD).

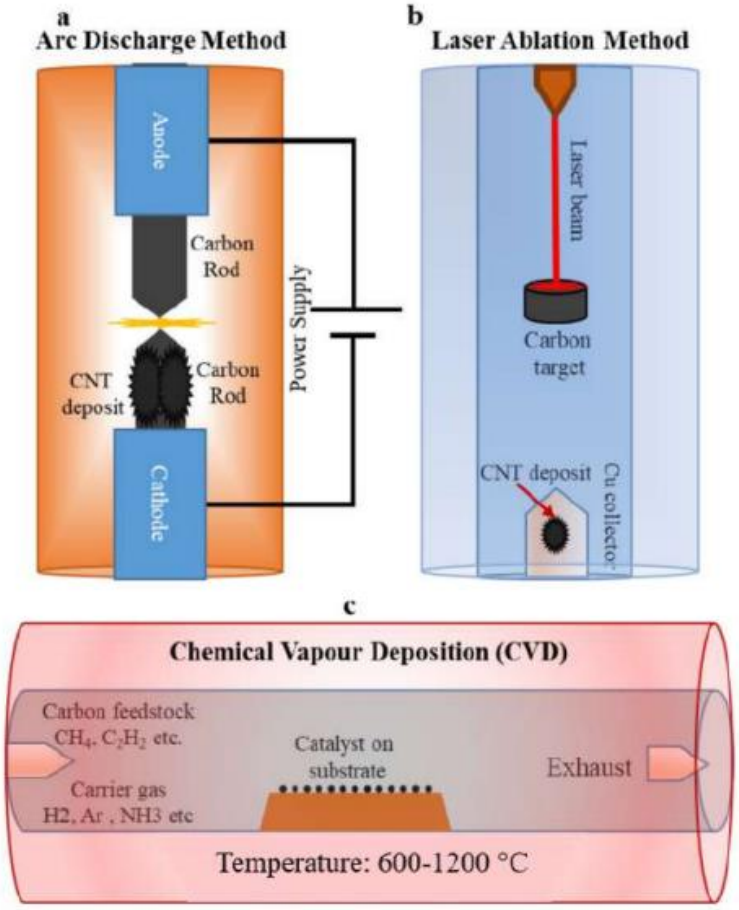

Figure 3.3 Schematic representation of the main methods for the synthesis of CNTs: (a) arch discharge, (b) laser ablation, (c) chemical vapour deposition (CVD).

In arc discharge and laser ablation techniques, high temperatures (3000-4000 °C) promote the evaporation of a solid carbon source and CNTs are synthesized upon condensation, whereas the CVD methods involves the decomposition of volatile organic molecules on metallic catalyst nanoparticles in the temperature range of 600-1200 °C [138], [147]. Although higher crystallinity of CNTs can be achieved through arc discharge and laser ablation, the high energy involved and the requirement of a large solid state carbon target limit the use of these methods as large scale industrial processes. On the other hand, the CVD methods offer higher yield and purity of CNTs at relatively low temperatures along with the unique ability of producing organized CNT architectures (e.g., vertically aligned

forests) at desired substrate locations (Figure 3.4), thus being the preferred option for large scale production [6].

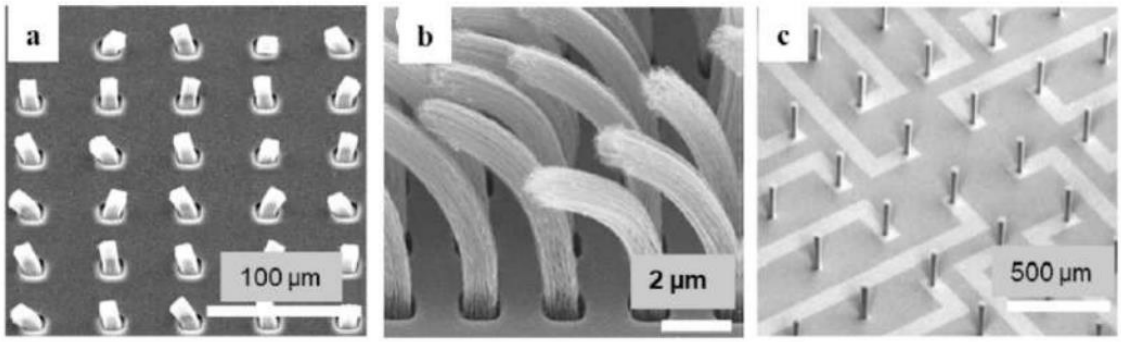

Figure 3.4 SEM images of aligned CNTs grown at selected substrate locations [6].

CVD is an established and versatile technique, enabling the use of hydrocarbon feedstocks in any state (solid, liquid or gas) and the growth on various substrates [148]. It was developed throughout the years in different forms depending on the method of energy delivery, including thermal CVD (TCVD) [149], plasma-enhanced CVD (PE-CVD) [150], photo-thermal CVD [147], laser assisted CVD [151] and many others. Regardless of the used method, the CVD process requires the presence of catalyst nanoparticles, generally transition metals such as Fe, Ni, and Co, allowing hydrocarbon decomposition at a lower temperature than the spontaneous decomposition temperature of the hydrocarbon and acting as nucleation sites for CNT growth. The catalyst can be either pre-deposited on the substrate (supported catalyst method) or introduced directly as vapour into the reaction chamber where, at suitable temperature, liberates metal nanoparticles *in-situ* (floating catalyst method).

The CVD process on a supported catalyst requires preliminary catalyst preparation followed by the actual synthesis of CNTs. A thin film of usually 0.5-10 nm of catalyst precursor is deposited either by physical vapour deposition (PVD) techniques or solution-based methods, such as spin coating, spray coating, dip coating or drop casting [152]. The catalyst-coated substrate is placed inside the reaction chamber and active metal nanoparticles are produced upon exposure for 10-60 minutes at 550-900 °C in a reducing gas environment, typically H_2 or NH_3 [153]. This step is crucial for producing the proper template of catalyst nanoparticles, seeding the subsequent CNT growth. While high

temperatures promote the de-wetting of the catalyst film into nano-sized islands, the reduction of the metal precursor is accomplished by the reducing atmosphere. The size and distribution of nanoparticles depend on temperature, duration, gas flowrate and original thickness of the catalyst film. After the annealing step, the carbon source is introduced in the chamber for typically 15-60 minutes and CNT are grown on the substrate [137]. Growth temperature, hydrocarbon flowrate, duration and catalyst nanoparticle size and distribution affect the resulting diameter, length, number of walls, quality, density, and spatial arrangement of carbon nanotubes.

Although CNT growth mechanism is still debated, the most widely accepted general mechanism is illustrated in Figure 3.5.

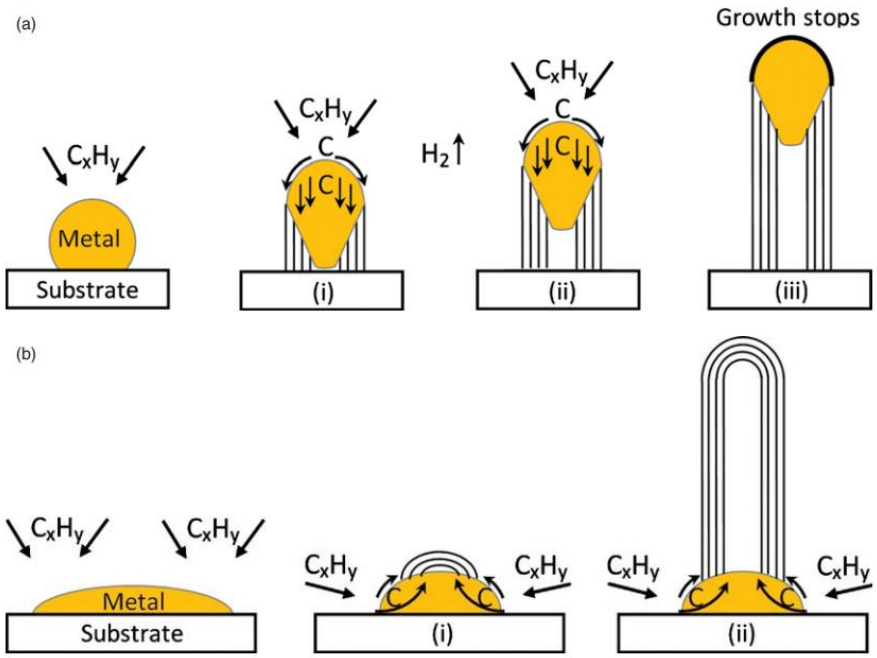

Figure 3.5 Schematic of the growth mechanism of CNTs: (a) tip-growth model, (b) base-growth model [153].

The decomposition of the hydrocarbon gas occurs on the surface of catalyst nanoparticles, leading to carbon diffusion in the metal and precipitation in the form of a cylindrical sp^2 structure upon reaching the solubility limit at that temperature [154]. The catalyst nanoparticle can be either lifted with the growing nanotube or remain attached to the substrate. These conditions are referred to as tip-growth or base-growth modes,

respectively, and the occurrence of one or the other has been explained with catalyst-substrate adhesion [153]. A weak interaction, corresponding to a contact angle higher than 180° between the catalyst particle and the substrate surface, leads to carbon precipitation on the bottom of the nanoparticle which is pushed off the substrate (Figure 3.5a(i)). The growth proceeds until the top surface of the catalyst is available for fresh hydrocarbon decomposition (Figure 3.5a(ii)) and stops when the metal is fully covered with excess carbon (Figure 3.5a(iii)). In contrast, when catalyst/substrate interaction is strong, carbon emerges from the top surface of the particle (Figure 3.5b(i)), crystallizing as a hemispherical dome (the most favourable closed carbon network on a spherical particle) which extends in the form of a seamless graphitic cylinder (Figure 3.5b(ii)) with the catalyst at its root.

The catalytic activity of catalyst materials is believed to depend on the diffusion and solubility of carbon within the catalyst. The most used catalyst materials, i.e., Fe, Ni, and Co, possess high solubility and diffusion rate of carbon at high temperatures [155]. Moreover, nanometre-sized particles are supposed to offer strong adhesion to the carbon atoms of the growing nanotube, determining the formation of high curvature tubular structures of CNTs with diameters dictated by those of the nanoparticles [152], [156]. Proper catalyst size is crucial for achieving CNT growth. Small nanoparticles with a narrow size distribution are required for the growth of SWCNTs, while too large nanoparticles may lead to the growth of amorphous carbon nanofibers or other carbon nanostructures.

The growth of SWCNTs or MWCNTs can be also controlled by selecting the proper process temperature and carbon feedstock. Temperatures required for the synthesis of SWCNTs (900-1200 °C) are generally higher than those for the synthesis of MWCNTs (600-900 °C) [157], [158]. This indicates a higher formation energy of SWCNTs, likely due to the smaller diameter determining a higher curvature and, thus, a higher deformation energy. At high temperatures, many hydrocarbons used for the growth of MWCNTs, such as acetylene, ethylene, and benzene, are unstable and have high pyrolysis rates which lead to the undesired deposition of large amounts of amorphous carbon. Consequently,

SWCNTs are usually synthesized from methane or carbon monoxide, which possess a relatively high thermal stability [153].

3.3. Low Temperature Synthesis

As discussed in section 2.2.1 of Part I – State of the art, lowering CVD temperatures is essential to achieve the direct functionalization of reinforcing fibres without compromising their inherent mechanical properties. Furthermore, CNT growth at low temperatures is attractive for many other potential applications in which a temperature sensitive substrate is involved, including flexible electronic devices, integrated circuit interconnects, through Si vias and sensors [159]–[162]. To address this issue, many strategies have been proposed in the literature, involving the use of bi- or tri-metallic catalysts [163], multi-temperature-zone CVD systems [164], reactive species promoting the decomposition of the carbon feedstock, e.g., through oxidative dehydrogenation reactions [165], or plasma assistance [166].

3.3.1. Thermal CVD

The selection of suitable reaction species with low decomposition temperature is the first aspect to be considered to lower CNT growth temperatures. While the decomposition of methane, the most stable hydrocarbon, is only thermodynamically favoured at temperatures above 600 °C, the change in free energy of formation for ethylene, acetylene, and benzene is negative at temperatures as low as 200 °C (Figure 3.6a). Experimentally, methane requires temperatures above 850 °C because of slow reaction kinetics, whereas the temperature ranges for CNT growth with acetylene and ethylene commonly are 500-750 °C and 650-850 °C, respectively [154]. Magrez et al. [165] exploited the oxidative dehydrogenation of acetylene instead of its pyrolysis by adding CO_2 to the gas mixture in stoichiometric amounts. The addition of CO_2 favoured the reaction thermodynamically (Figure 3.6b), extending the temperature range for CNT growth to 300-750 °C on various temperature-sensitive substrates, including carbon fibres.

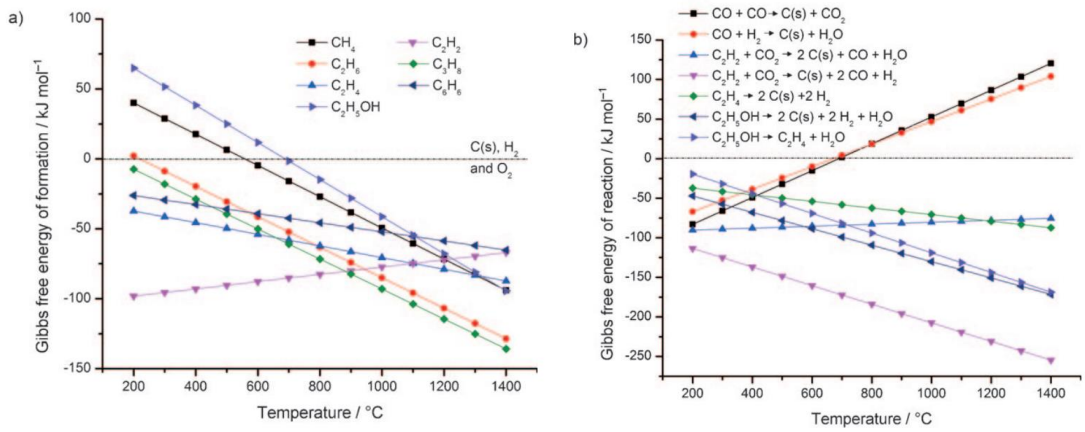

Figure 3.6 Gibbs free energy of formation for various carbon precursors, normalized to the number of atoms in the precursor. (b) Gibbs free energy for oxidative dehydrogenation of acetylene and other typical reactions: CO disproportionation, water gas shift, pyrolysis of ethylene. The energies are normalized to the number of solid carbon atoms [154].

Along with the reaction species, suitable catalyst systems must be selected to seed CNT growth at low temperature. In the work by Magrez et al. [165], the growth was performed both through a Fe-based catalyst and through a bi-metallic Fe-Co catalyst system. Halonen et al. [33] investigated the decomposition of various carbon feedstocks (acetylene, methanol, xylene, cyclopentene oxide, and tetrahydrofuran) on different catalyst systems, composed of Fe, Ni, Co, and their bi- and tri-metallic alloys. Low temperature CNT growth at 400 °C was achieved only when bi-metallic Co–Fe and tri-metallic Ni–Co–Fe catalysts were used, with methanol or acetylene as carbon precursors. In the case of individual catalysts, only Co was found to be active below 500 °C for the decomposition of oxygenates precursors, such as cyclopentene oxide and methanol. Although the role of multi-catalyst systems is still not well understood, their catalytic activity and CNT growth rate at low temperature has been proved to be significantly higher than those of individual metal catalysts. Recently, Yao et al. [163] explored the use of different bi- and tri-metallic combinations of Fe, Co, Ni for CNT growth at low temperatures (350-400 °C) on carbon fibres, effectively reducing the etching effect of the catalyst caused by high temperatures. A strong relationship between the type of catalyst and the loading and graphitization degree of as-grown CNTs was highlighted, with the Fe-Co showing the highest graphitization degree but low catalytic efficiency as opposed

to the Fe-Ni-Co system showing the highest catalytic efficiency and lowest graphitization degree. Although carbon nucleation was observed at temperatures as low as 350 °C, the decrease of temperature caused a decrease in the graphitization degree and loading amount of CNTs. In general, carbon nanostructures grown at low temperatures have lesser yield, more scattered distribution, and poorer graphitization, which may affect the resulting mechanical and functional properties. Therefore, although most research works focused on using traditional catalysts, namely Fe, Co, and Ni, and their combinations, the introduction of new catalyst materials with higher catalytic efficiency at low temperatures has attracted significant attention in recent years. Cartwright [167] and Fan [168] et al. found that trace addition of Cu to the Fe catalyst can significantly enhance its catalytic activity below 500 °C, while Su et al. [169] showed that the activity of the Co catalyst benefits from the addition of small amounts of sulphur. More recently, Li et al. [34] introduced the use of Na as a catalyst in the oxidative dehydrogenation reaction between C_2H_2 and CO_2 demonstrating CNT growth below 500 °C on a range of substrates including carbon fibres, alumina fibres, Si wafers and Ti sheets. Copper has also been shown to be catalytically active towards the growth of various carbon nanostructures, including carbon nanofibers [170], multi-walled [171] and single-walled CNTs [157]. Specially, Cu has been found to catalyse the growth of amorphous carbon nanofibres at temperatures as low as 250 °C [35], becoming a promising option for low temperature growth of carbon nanomaterials on temperature sensitive substrates. Recently, Cui et al. [172] adopted an equimolar Cu-Ni nanoalloy to grow carbon nanofilaments on carbon fibres for interfacial adhesion improvement. Thanks to the combination of the low temperature catalysis of Cu and the high depositing efficiency of Ni, the growth was achieved at temperatures as low as 300 °C.

Other strategies to lower CVD growth temperatures include engineering solutions such as using a multi-zone CVD system, where the decomposition of the carbon feedstock is performed in a higher temperature zone, whereas the growth of CNTs is conducted in a lower temperature zone. Nessim et al. [164] employed a three-zone furnace using ethylene as carbon precursor. The sample was kept in the third zone of the furnace where MWCNTs were grown for 45 min at a substrate temperature of 500 °C, while the gas was pre-heated at a temperature of 770 °C in the first two zones.

3.3.2. Plasma-Enhanced CVD

Plasma-enhanced chemical vapour deposition (PE-CVD) uses electrical power at a sufficiently high voltage to dissociate and ionize the carbon precursor gas at low temperature. This generates a glow discharge plasma consisting of electrons, ions, photons, highly reactive radicals, and a fraction of undissociated source gas. Such plasma environment enhances the reactivity of the processing gas and supplies part of the energy required for the chemical reactions involved in CNT growth (i.e., carbon diffusion through the catalyst nanoparticles, carbon precipitation, and crystallization in a cylindrical network), allowing lower operating temperatures. Particularly, whereas in thermal CVD a high activation energy must be overcome on the catalyst surface for dehydrogenation of the carbon source, in PE-CVD this barrier is only partially present as the plasma directly provides highly reactive, (partially) dehydrogenated species to the catalyst [173]. The plasma also possibly affects the catalyst nanoparticles during the growth, enhancing the carbon solubility [174]. In addition, a distinctive aspect of PE-CVD is the interaction with the electric field which offers the unique advantage of controlling the alignment of CNTs, resulting in the conformal growth of straight and aligned CNTs on substrates of different geometry, as demonstrated by Bower et al. [32] (Figure 3.7).

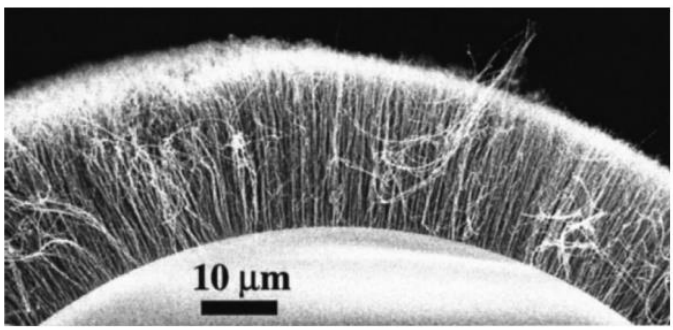

Figure 3.7 PE-CVD-induced conformal growth of aligned CNTs on the surface of an optical fibre (diameter of 125 μm) [32].

Therefore, PE-CVD allows lower operating temperatures while maintaining reasonable growth rates, quality, and alignment of CNTs. Katagiri et al. [175], [176] demonstrated the growth of aligned MWCNT forests at temperatures as low as 400 °C on Co catalyst

nanoparticles deposited on a $Si/SiO_2/TiN$ substrate. As-grown CNTs exhibited good structural quality as confirmed by TEM analysis. The growth of even more densely packed and aligned MWCNT forests was subsequently achieved by the same group by developing a multi-step plasma-based CVD method with the focus on controlling the nanoparticle formation step through plasma assistance [177]. Li et al. [178] reported the PE-CVD growth of dense vertically aligned CNTs on a conductive titanium silicide substrate using a multi-layer Ni/Al/Ni catalyst. After annealing for 10 min in a H_2:N_2 mixture (3:1), MWCNTs with an average diameter of 20 nm were grown at a rate of 120 nm/min using 35 sccm of CH_4 and 200 W plasma power. Other examples of PE-CVD synthesis of vertically-aligned CNTs have been reported at temperatures as low as 300 °C on metal, silicon, and silica substrates, predominantly intended for electrical applications [31], [179], [180]. Boskovic et al. [181] even achieved the growth of carbon nanofibers at room temperature by entirely substituting the requirement of thermal energy with the plasma decomposition of methane on a Ni-based catalyst. It is worth noting that the plasma itself can contribute to heat the substrate, thus deviating the real growth temperature from the controlled one unless the input power is extremely low [182]. Based on this consideration, Meyyappan [183] argued that many works reporting low temperature PE-CVD may be misleading due to inaccurate or not mentioned measurement of the substrate temperature. However, the effectiveness of PE-CVD in performing CNT growth at low substrate temperature was accurately demonstrated by Hofmann et al. [184] using temperature labels as calibration standards. They reported the growth of vertically aligned carbon nanofibres at a substrate temperature of 120 °C using acetylene/ammonia gas mixture and a plasma power of only 18 W.

As regards reinforcing fibres, the PE-CVD technique has been proposed to deposit thin polymeric coatings, especially for its better control over the film thickness and uniformity compared to commercial sizing methods [28], [185]. Only a limited number of studies adopted the PE-CVD technique to grow carbon-based nanomaterials, most of them focusing on carbon fibres. Sha [186] and Zhang et al. [187] reported the growth of vertical graphene and randomly-oriented CNTs on carbon fibres using PE-CVD at 400 °C and 450 °C, respectively. Both studies reported a significant increase in IFSS with epoxy, while preserving the fibre tensile strength.

Despite numerous interesting growth results at low temperatures, some challenges may obstacle the commercial application of PE-CVD. In fact, the use of high voltages causes energetic ion bombardment which could damage the substrate or even etch the deposited material [188]. One solution is the use of remote PE-CVD systems, in which the plasma is generated in a chamber separated from the deposition chamber or, more generally, is not in direct contact with the substrate [189]. Moreover, in some cases, plasma etching can be even desirable as it can be exploited for the selective growth of CNTs with narrow diameter and chirality distributions, as reported by Zhang et al. [190]. The main disadvantage of PE-CVD lies in the low pressures (between 10^{-4} and 10^{-3} bar) at which the plasma is generated, which require the use of a high vacuum system and a more sophisticated reactor to contain the plasma. As a result, PE-CVD setup is often more expensive than thermal CVD systems. However, the higher cost of the equipment can be outweighed in applications where temperature sensitive substrates are involved and low temperature growth of CNTs with desired properties cannot be met by conventional thermal CVD. Moreover, examples of PE-CVD at atmospheric pressure have been reported, such as atmospheric radio-frequency discharge and dielectric barrier discharge, with the advantage of no need of expensive vacuum pumps and of reduced ion bombardment, due to the more frequent collisions between ions at higher pressure that make them lose most of their energy [191].

PART II – MATERIALS AND METHODS

PART II – MATERIALS AND METHODS

Chapter 1.

Materials

1.1. Reinforcement materials

In this research work, two fibre materials were selected as substrates for CNT synthesis. A continuous roving of quartz fibres (Quartzel® C14 1600 QS1318) with a nominal fibre diameter of 14 μm and a linear density of 1600 tex supplied by Saint-Gobain and a plain-woven basalt fabric (220 g/m^2) provided by Basaltex (BAS 220.1270.P) with an average fibre diameter of 14 μm. In both cases, the fibres were sized with a commercial sizing tailored for epoxy resins.

1.2. Catalyst precursors

The catalyst precursors for the CVD processes on quartz fibres were iron (III) nitrate nonahydrate ($Fe(NO_3)_3 \cdot 9H_2O$, ≥98%) and copper(II) acetate monohydrate ($Cu(CH_3COO)_2 \cdot H_2O$, ≥98%). Such precursors were dissolved in 2-propanol ($(CH_3)_2CHOH$, ≥99.5%) and acetonitrile (C_2H_3N, ≥99%), respectively. NaOH (by Sigma Aldrich, reagent grade ≥98%) was dissolved in water for chemical pre-treatment of the basalt fabric.

1.3. Liquids for wetting analysis

Four liquids were selected for the tensiometric tests: n-hexane, water, diiodomethane and an epoxy resin. N-hexane (Sodipro) was chosen to measure the wetted perimeter of tested fibres, as it is a totally wetting liquid. The reference liquids, i.e., water, diiodomethane and the epoxy resin (InfuGreen 810 provided by Sicomin, France) were chosen for the highly polar character of water and the highly dispersive character of diiodomethane,

while the epoxy resin was chosen to calculate the work of adhesion with a potential matrix material. Their chemical-physical properties at room temperature (20 °C), including the surface tensions, the polar and dispersive components, and the viscosity, are listed in Table 1. 2. As the resin surface tension is considered to be barely affected by the mixing in of the hardener [192], only the base resin was used in order to avoid polymerization and time dependant changes in the fluids properties.

Table 1. 2 Surface free energy and its components at 20 °C for the test liquids.

Solvent	**Viscosity η (mPa s)**	**Surface free energy (mJ/m^2)**		
		Tot, γ_L	**Dispersive, γ_L^d**	**Polar, γ_L^p**
Water	1.00	72.8	21.8	51
Epoxy Resin	142	48.4	48.4	0
Diiodomethane	2.76	50.8	48.5	2.3
n-Hexane	0.32	18.4	18.4	0

1.4. Materials for electrochemical tests

Sodium sulphate (Na_2SO_4, ≥99.0%), used in the support electrolyte for electrochemical tests, was supplied by Sigma Aldrich (Milano, Italy).

The homemade conductive bio-polymer film (Pol) was produced using solvent-casting and solvent evaporation techniques. Starch was dissolved in distilled water and stirred for 30 minutes at 95 °C to achieve complete gelatinization. The ionic liquid [EMIM-Cl] was then added as a plasticizer, and the mixture was heated at the same temperature until homogeneous. The solution was partially cooled to 65 °C, poured into a Petri dish, and dried slowly in an oven at 45 °C before being left to dry at room temperature.

Chapter 2.

Synthesis of carbon nanotubes

2.1.Pre-treatments

Prior to the CVD process, different pre-treatments were carried out on the fibre substrates depending on the catalyst used. Iron and copper catalyst precursors were deposited on the surface of quartz fibres through a dip-coating method. To achieve the deposition of the Fe-based catalyst precursor, bundles of as-received fibres (around 50 mm-long) were dipped into a 50 mM solution of iron(III) nitrate nonahydrate in 2-propanol for 5 minutes. The Cu-based precursor was deposited on as-received fibre bundles after complete evaporation of a 5 mM solution of copper(II) acetate monohydrate in acetonitrile. In this case, the fibres were placed on a glass rack at the bottom of a crystallizer, i.e., a laboratory glass container with a wide base to foster solvent evaporation and allow the formation of uniformly sized crystals of the solute. Both dipping processes were carried out at room temperature, and, after the deposition, the fibres were allowed to dry at room temperature overnight. As regards the fibres coated with the Cu catalyst precursor, an additional oxidation step, consisting in a heat treatment at 300 °C for 1 hour in air atmosphere, was carried out prior to the CVD synthesis process to promote the decomposition of copper(II) acetate monohydrate into a mixture of Cu, CuO, and Cu_2O. For the synthesis on basalt fibres with *in-situ* catalyst generation approach, basalt fabrics samples (2x2 cm) were chemically etched in a 2M NaOH-aqueous solution for 3 hours at room temperature and, afterwards, dried on a rack at room temperature.

2.2.CVD synthesis protocols

Thermal and plasma-enhanced CVD syntheses were carried out at the INFN TITAN Laboratory of Sapienza University of Rome, displayed in Figure 2.10. The pre-treated fibre samples were placed on the heating element of the CVD apparatus (Figure 2.10b),

consisting of a high vacuum reaction chamber, with the base pressure in the low 10^{-7} mbar range, equipped with a radiofrequency (RF)-plasma module with a gas-shower cathode.

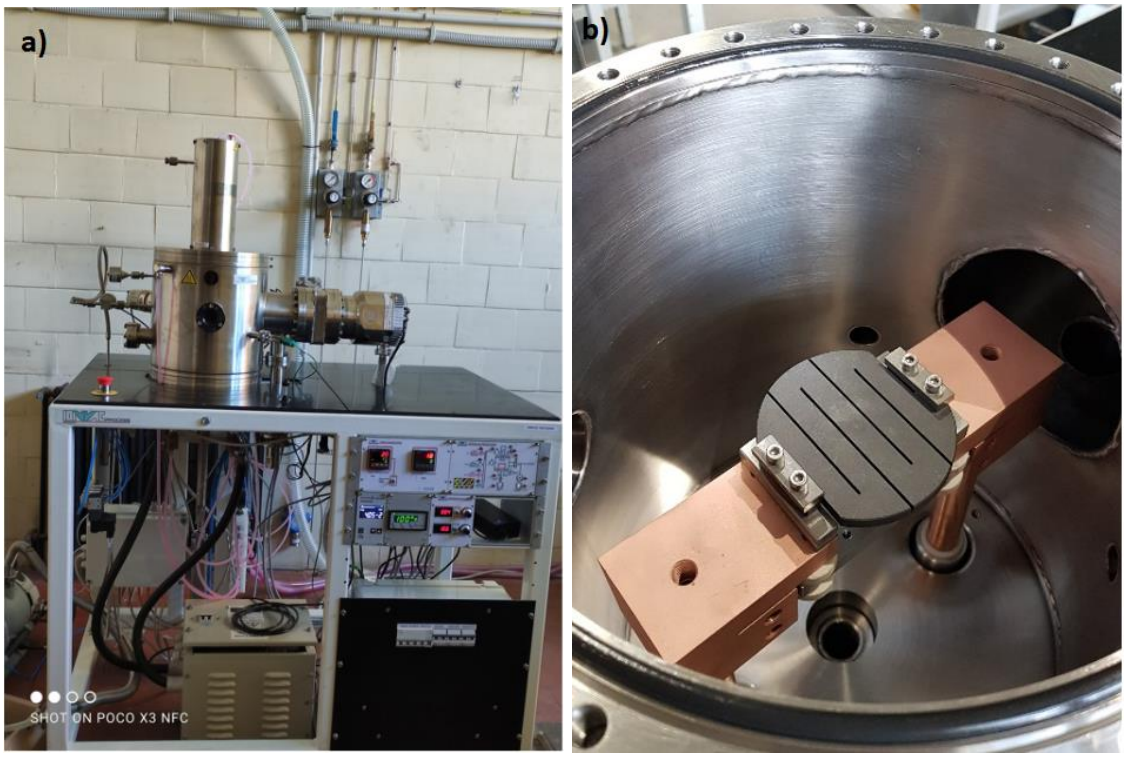

Figure 2.10 (a) Titan Lab CVD chamber; (b) detail of the heating element inside the CVD chamber.

Two thermocouples were used to monitor the temperature during the process: one inside the heating element, which corresponded to the set temperature, the other one measuring the substrate temperature. It is worth noting that, while for basalt fabric samples the second thermocouple was anchored to the top surface of the fabric substrate, in the case of quartz fibre bundles, due to their small thickness, the second thermocouple was placed on the top surface of the heating element. This configuration was considered to provide a good approximation of the temperature experienced by quartz fibre samples, as they were in close contact with the surface of the heating element. As the present work focusses on mitigating the temperature experienced by the substrate during CVD growth, the discussion will refer to the temperature values detected by the second thermocouple.

The CVD process was composed of two main stages: (i) a thermal annealing step, during which high temperatures and a H_2 atmosphere were exploited to reduce the catalyst

precursor and produce evenly-distributed active catalyst nanoparticles seeding the subsequent growth; (ii) the actual synthesis (or growth) step, where acetylene was introduced as a carbon source and, in the case of PE-CVD, a highly energetic plasma was generated. The operative parameters, i.e., heating rate to the target temperature, gas flow rates, times, partial pressures, and temperatures of each stage were optimized for each catalyst system based on a well-established growth procedure for the growth of vertically aligned CNTs via thermal CVD on different substrates [36], [158], [193]–[196]. The optimized parameters for each fibre substrate and catalyst system are listed in Table 2.1. After the growth step, the chamber was allowed to cool down to room temperature under the base pressure.

Table 2.1 CVD parameters optimized in this research work depending on the substrate (i.e., quartz or basalt fibres), catalyst system (i.e., Fe, Cu, or in-situ Fe) and CVD method used (i.e., T-CVD, or PE-CVD), including annealing and growth temperatures (T), heating conditions up to the target annealing temperature, gas flow rates and partial pressures during annealing and growth, annealing and growth dwelling time (t), and plasma power.

Sample	**Method**	**Annealing**				**Growth**			
		T [°C]	**Heating**	**Gas flow rates and partial pressures**	**t [min]**	**T [°C]**	**Gas flow rates and partial pressures**	**t [min]**	**Plasma Power [W]**
Quartz fibres, Fe catalyst	T-CVD	520, 620	200 °C/min in vacuum	H_2: from 170 to 300 sccm at 30 sccm/min, up to a partial pressure of $8 \cdot 10^{-1}$ mbar	4	540, 640	C_2H_2: 300 sccm H_2: 0 sccm, up to a partial pressure of 50 mbar	10	-
	PE-CVD	520, 620	200 °C/min in vacuum	H_2: from 170 to 300 sccm at 30 sccm/min, up to a partial pressure of	4	540, 640	C_2H_2: 20 sccm H_2: 0 sccm, up to a partial pressure of 3 mbar	10	50

				$8 \cdot 10^{-1}$ mbar					
Basalt fibres, *in-situ* Fe catalyst	PE-CVD	420, 460, 485	200 °C/min in vacuum	H_2: from 170 to 300 sccm at 30 sccm/min, up to a partial pressure of $8 \cdot 10^{-1}$ mbar	8	480, 510, 580	C_2H_2: 20 sccm H_2: 0 sccm, up to a partial pressure of 3 mbar	14	50
Quartz fibres, Cu catalyst	T-CVD	420, 510	50 °C/min in H_2 atmosphere: 0 to 300 sccm at 30 sccm/min up to a partial pressure of $8 \cdot 10^{-1}$ mbar	H2: 300 sccm	18	420, 510	H2: 150 sccm C2H2: 20 sccm Total pressure: 5 mbar	30	-
	PE-CVD	420, 510	50 °C/min in H_2 atmosphere: 0 to 300 sccm at 30 sccm/min up to a partial pressure of $8 \cdot 10^{-1}$ mbar	H2: 300 sccm	18	420, 510	H2: 120 sccm C2H2: 60 sccm Total pressure: 5 mbar	30	30

Chapter 3.

Characterization methods

3.1. Fibre heat treatment

To evaluate the effects of thermal exposure on the mechanical properties of quartz fibres, a tube furnace (Lenton Thermal Designs Ltd., Hope, UK) was used for heat-treating bundles of as-received quartz fibres in air atmosphere for 1 hour. The heat treatments were performed at temperatures of 600, 700, and 800 °C, typically required for the synthesis of CNTs through traditional thermal chemical vapour deposition (CVD) processes. Finally, the fibres were removed from the furnace and allowed to cool down at room temperature.

The mechanical properties of fibres following the CVD processes optimized in this work were evaluated after exposure of as-received fibres to the exact thermal cycle and gas flow experienced during the synthesis, described in section 2.2 of Part II – Materials and Methods. The catalyst pre-treatment step was omitted in this case to avoid the growth of CNTs and, thus, facilitate the handling of single fibres when preparing tensile test samples.

3.2. Single fibre tensile testing

Tensile tests were conducted following ASTM C1557 [197] standard procedure. Single fibres were carefully extracted by hand from the fibre bundles or fabrics and glued onto a card tab with a central cut-out window equal to the gauge length (Figure 3.8). Afterwards, the average fibre diameter was evaluated using an optical microscope Nikon Eclipse 150L equipped with Lucia Measurement image analysis software. A Zwick/Roell Z010 tensile machine equipped with a 100 N range load cell was used for the tests, which were carried out at room temperature, in displacement control and with a 2 mm/min crosshead speed.

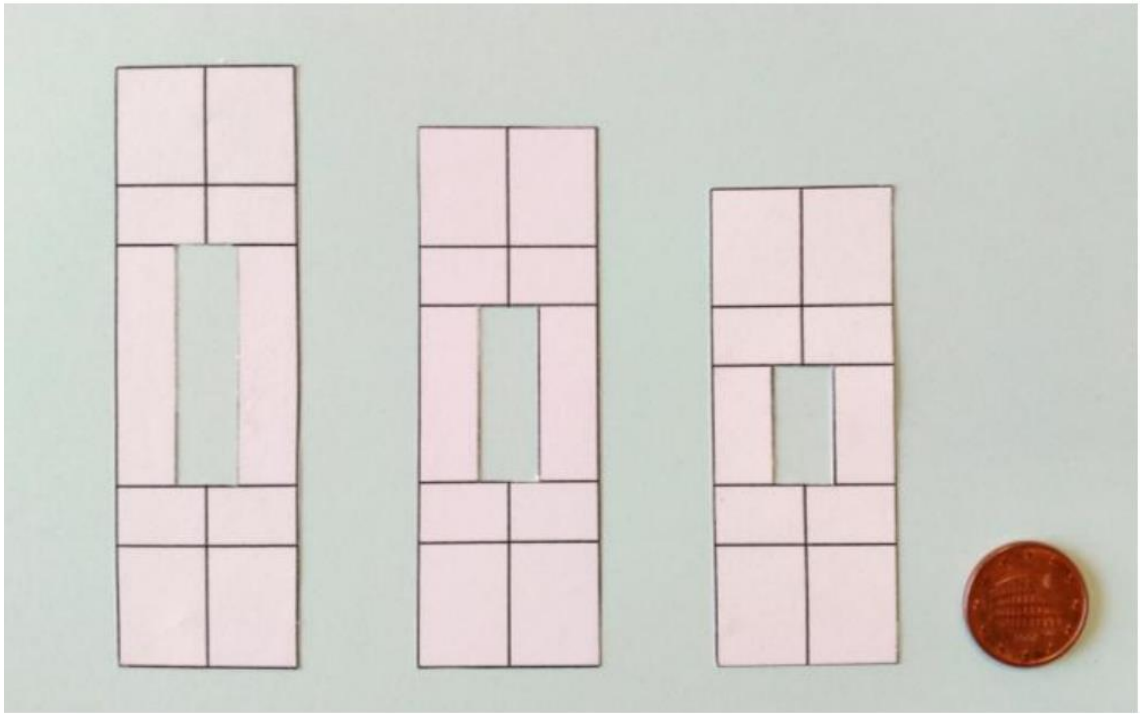

Figure 3.8 Card tabs used as supports for tensile tests samples. The central cut-out window is equal to the gauge length, i.e., 20, 30 or 40 mm.

The actual fibre elongation in the gauge length was determined by subtracting the displacement associated with the system compliance, i.e., the contribution by the load train system and specimen-gripping system to the total crosshead displacement, from the total crosshead displacement. The system compliance was calculated according to ASTM C1557 [197] by obtaining the force versus displacement behaviour of as-received fibres at three different gauge lengths, namely 20 mm, 30 mm and 40 mm. Once the system compliance was evaluated, heat-treated and CVD-treated fibre samples were tested at a gauge length of 20 mm. At least 20 valid tests were obtained for each set of fibres.

Ceramic fibres, including quartz and basalt fibres investigated in this work, usually possess a distribution of strengths rather than a unique value, requiring statistical tools to be analysed [198]. In this work, a two-parameter Weibull distribution, which can be applied when one population of flaws is responsible for the fibre failure, was employed for statistically analyse the dispersion of the tensile strength and Young's modulus values according to equation 3.1:

$$F(\sigma) = 1 - \exp\left[-\left(\frac{\sigma}{\sigma_0}\right)^m\right] \quad (3.1)$$

where $F(\sigma)$ is the cumulative probability of failure at the applied stress σ, m is Weibull modulus (also referred to as shape parameter) and σ_0 is a scale parameter, corresponding to the 63.2 percentile of the distribution.

The maximum likelihood estimation method was used to estimate the parameters of the Weibull distribution, i.e., m and σ_0, for each set of tested fibres. In addition, 90% confidence intervals (CI) and the unbiased estimates of Weibull moduli, m_u, were calculated according to the standard ISO 20501:2019. The probability of failure (F) in the graphical representation of $ln\{ln[1/(1-F)]\}$ against $ln(\sigma)$ was estimated according to equation 3.2:

$$F_j = \frac{j-0.5}{N} \quad (3.2)$$

where N is the number of tested fibres and j is the rank of the jth data point [199].

3.3. Thermogravimetric analysis (TGA)

A SetSys Evolution (Setaram Instrumentation) thermogravimetric analyser was used to measure the evolution of the mass as-received quartz fibres with temperature. The fibres were heated up to 800 °C at 10 °C/min in a nitrogen atmosphere.

3.4. Density measurement

To evaluate possible variations of the fibre density following thermal exposure, the density of both as-received and heat-treated quartz fibres was measured through helium pycnometry (AccuPyc II 1340).

3.5. X-ray diffraction (XRD) analysis

To assess the effects of thermal exposure on the fibre structure and reveal the possible occurrence of crystallization phenomena in amorphous quartz fibres, a Philips X'Pert PRO powder diffractometer (Cu_{K1} α radiation = 1.54060 Å, Cu_{K2} α radiation = 1.54443 Å) was used to perform X-ray diffraction (XRD) analyses on as-received and heat-treated

quartz fibres. XRD patterns were collected at room temperature in the range of 2θ = 10°-70° with a scan step 2θ = 0.02° and scan rate of 1°/min.

3.6. Mechanical characterization at the nanoscale

This work adopted high-speed nanoindentation and pillar-splitting experiments for high-resolution mapping of the mechanical properties and fracture toughness assessment over polished cross-sections of single fibres. Throughout the experimental, optimization of testing parameters has been focused on the ceramic fibres, discarding non-optimized data subsequently acquired for the embedding epoxy resin matrix (required for mounting purposes of the fibres on their exposed cross-sections). In fact, to ensure a structurally stable alignment of the single fibre with the nanoindentation instrument testing axis, fibre bundles were embedded in an epoxy matrix, ensuring accurate planar positioning of their cross-sectional area to the mounted free surface.

To acquire set point information on the load-indentation depth relationship for high-speed mapping and basic information on the variation of hardness and elastic modulus as a function of thermal treatment conditions, 5 x 5 grid nanoindentation experiments, centred over single fibres, were performed through a G200 Nano-indenter (KLA Corporation) equipped with a Berkovich tip. Tests were conducted using the Continuous Stiffness Measurement (CSM) mode [200] to a maximum penetration depth of 200 nm. The machine frame stiffness and tip area function were calibrated by performing measurements on a certified fused quartz reference sample, according to ISO 14,577 standard. Low modulus and hardness data were discarded as associated with the mounting resin.

3.6.1. High-speed nanoindentation mapping

High-speed nanoindentation mapping [201], [202] was performed over at least three fibres per sample for high-throughput mapping of mechanical properties and identification of local heterogeneities distribution over the polished cross-section of as-received and heat-treated quartz fibres. The method, based on the same principles as the standard Oliver-Pharr one [200], benefits from specific improvements in the measurement

hardware, electronics, and data management, allowing to realize a vast number of tests in short times (from 1 to 5 s for a complete load-unload sequence). A two-dimensional map of hardness and elastic modulus represents the main output of a high-speed nanoindentation experiment. The maps were conducted in load-control mode to achieve precise repeatability of the indents, being the instrument, a force-controlled one. The target load for testing was extracted by previously acquired load-indentation depth relationships from CSM data quasi-static nanoindentation, allowing achievement of an average indentation depth on the ceramic fibre of ~80 nm. Details on loads and indentation depths for each sample are presented in Table 3.1. The spacing between the indents followed a $1/5^{th}$ of the target depth rule, as per standard allowed for ceramic materials by the detailed studied on high-speed mapping by Vignesh et al. and Phani et al., discussing the minimum required spacing, as a function of material properties, to avoid mutual interactions between plastic zones of the indents [203], [204].

Table 3.1 High-speed nanoindentation testing parameters and average indentation depth reached.

Sample	**Target load (μN)**	**Average indentation depth (nm)**
Non-treated	800	85.5
600 °C	800	81.9
700 °C	700	82.4
800 °C	700	82.3

Experiments were accomplished using a G200 nanoindenter (KLA Corporation, Oak Ridge, TN, USA) equipped with a standard Berkovich tip. High-speed grid indentations with lateral extensions of $20 \times 20\ \mu m$ (Figure 3.9) were realized, centred on each fibre, with accurate positioning for each indent at $1/5^{th}$ of the reached indentation depth ensured by a nano-positioning NanoVision stage (Physik Instrumente (PI) GmbH & Co.) available on the instrument. Considering the maximum indentation depth achieved of 80 nm, 500 nm laterally resolved maps were obtained, with a total number of indents, on average, of 1936.

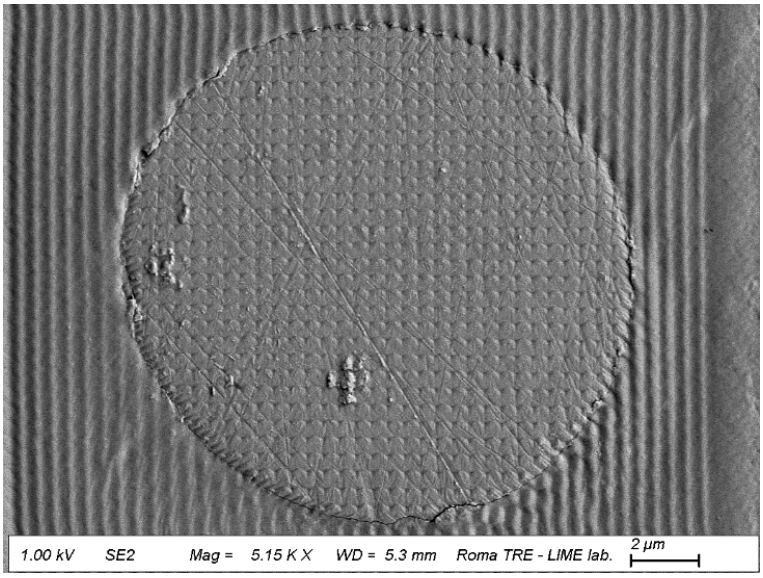

Figure 3.9 Representative load-controlled nanoindentation high-speed map performed over a quartz fibre cross-section. Data over the matrix has been discarded due to the optimization of spacing performed for quartz mechanical properties assessment.

The machine compliance and indenter area function were calibrated before and after each specimen on a certified Fused Quartz reference sample by employing the same high-speed methodology (same dynamical testing conditions of the performed maps) with varied loads.

After performing the experiments, data filtering of hardness and elastic modulus 2D maps was applied to exclude contributions of the polymeric matrix to the determination of local heterogeneities in the fibre. Statistical deconvolution algorithms based on probability distribution function (PDF) and k-means clustering were used to evaluate property variations within the fibre. The probability distribution of each indentation hardness and elastic modulus data set was fitted with a multi-variate gaussian distribution function (PDF) according to a well-established procedure [205], [206]. At the same time, k-means clustering followed the proposed procedure by Vignesh et al. [203].

3.6.2. Fracture toughness measurements via pillar-splitting

The pillar splitting method, a nanoindentation-based methodology presented and optimized by Sebastiani et al. [207]–[210], was employed to analyse the micro-scale

fracture toughness of single quartz fibres. Pillar splitting is based on the sharp nanoindentation of pillars, produced by focused ion beam (FIB) micro-milling, that are loaded till rupture during subsequent sharp nanoindentation testing. Fracture toughness is easily calculated through the following equation (Eq. 3.3) by only measuring the pop-in (failure) indentation load needed to fracture the pillar:

$$K_c = \gamma \frac{P_c}{R^{3/2}} \tag{3.3}$$

Where K_c is the fracture toughness (MPa·√m), P_c is the critical load for unstable pillar failure (mN), R is the measured pillar radius (μm), and γ is a dimensionless coefficient calculated by Finite Element Modelling (FEM). A previous work [211] has presented the variation of such coefficient for a wide range of material properties (H/E ratio and Poisson's ratio), as well as for a range of sharp indenter angles (including the most used Berkovich and Cube-Corner indenters). A remarkable benefit of this method is that (a) the measurement of the crack length is not required since the crack is spontaneously nucleated during the indentation process, and (b) there is no effect of residual stresses, which are released as the pillar fabricated by the FIB milling process [207], [212]. The γ coefficient was extracted from high-speed mapping values averaging elastic modulus and hardness within the relevant corresponding areas to the position of the FIB milled pillars.

In this work, pillars having a diameter (D) of 4.06 μm and an aspect ratio $h \,/\, D \geq 1$ were milled at the centre of defect-free single fibres. A multi-step semi-automated procedure was used for FIB milling through a Helios Nanolab 600 FIB/SEM microscope (ThermoFisher Scientific). This procedure involved a coarse milling phase, with a current of 0.46 nA and an ion beam voltage of 30 kV, and a final multi-step polishing and edge sharpening phase at 28 pA and 30 kV (Figure 3.10a). Some pillars were FIB-sectioned after fabrication, as shown in Figure 3.10b, to accurately measure the diameter and taper angle and investigate the presence of pre-existing cracks in the sample material.

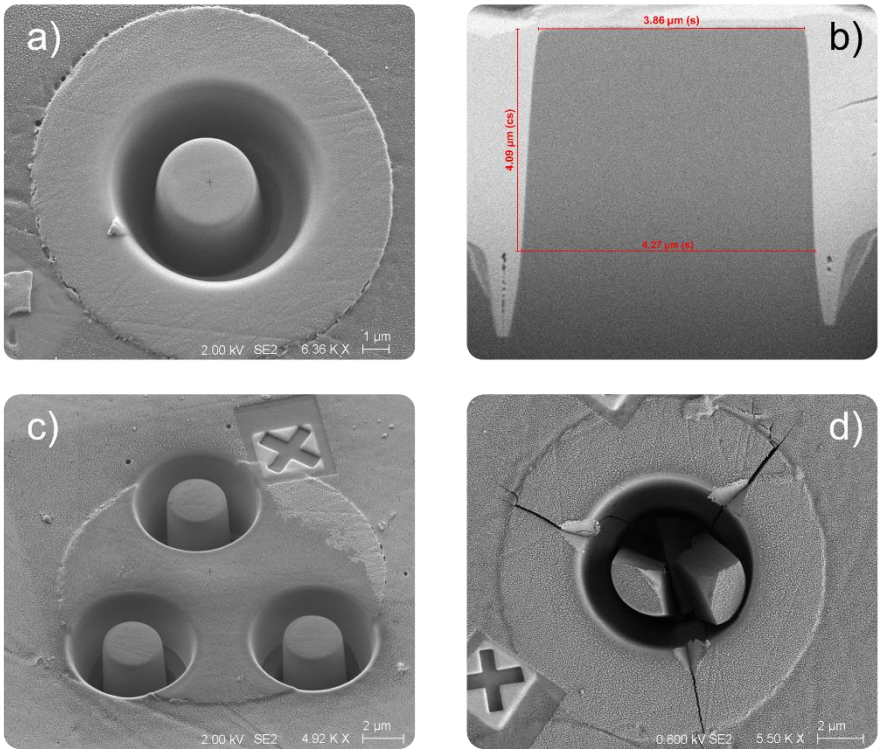

Figure 3.10 The micro-pillar splitting methodology involved a) fabrication of 4 µm diameter pillars at each fibre centre using a standardized procedure for reproducibility and b) FIB cross-sectioning to assess the shape and tapering angle. c) Carousel of micro-pillars having 3 µm diameter at fibres edge to evidence gradients from edge to centre of fracture toughness. d) Representative post-mortem image of a micro-pillar.

Before splitting, fibre push experiments were conducted to ensure that applied loads were far from the critical shear ones for the fibre-matrix slip at the interface. As evidenced in Figure 3.11, the latter occurs when the load-displacement curve of an indented fibre deviates consistently from the ideally expected quadratic behaviour. For the present study, the events were registered within a range of applied loads between $82 \div 90\ mN$, while the highest critical load for splitting recorded corresponded to $\sim 19\ mN$, thus being $1/5^{th}$ of the critical share one.

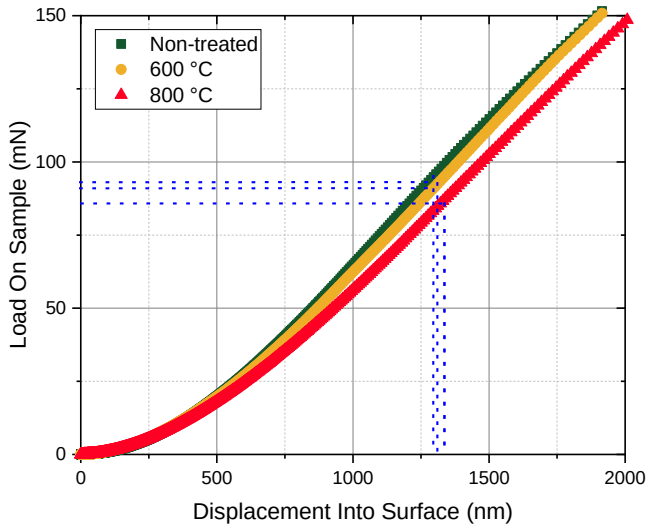

Figure 3.11 Representative Load On Sample versus Displacement Into Surface curves for a fibre-pushing experiment performed using a Berkovich tip. Highlighted are the shifts from an ideally quadratic loading behaviour corresponding to the beginning of the sliding phenomenon of the fibre to the embedding resin.

Pillar splitting tests were carried out by means of a Keysight G200 nanoindenter, equipped with a Cube-Corner indenter, fully calibrated on a Fused Quartz reference, according to the standard ISO 14577-1-2-3. A constant strain rate of 0.05 1/s was used until achieving unstable failure of the pillar, corresponding to a pop-in event in the load-displacement curve. The splitting of at least five pillars were performed to determine the fracture toughness at the fibre centre. It is worth mentioning that residual imprints and cracks in the fibre, as shown in Figure 3.10d, correspond to events occurring after the splitting of the central pillar and are due to abrupt precipitation of the indenter towards the substrate, subsequently to the pop-in event. To investigate fracture toughness dependence upon diametral positioning, pillars with a diameter of 3 µm were realized on single fibre peripheral areas following the described fabrication principles (Figure 3.10c).

3.7. Scanning electron microscopy (SEM)

Morphological and chemical investigations of the lateral and fracture surfaces of fibres were performed through a Mira3 field emission scanning electron microscope (FESEM)

by Tescan equipped with an energy dispersive X-ray (EDS) detector (Octane Elect, by EDAX-AMETEK). Non-conductive samples, e.g., as-received and heat-treated fibres, were sputter coated with gold prior to investigation.

3.8. Transmission electron microscopy (TEM)

Transmission electron microscopy (TEM) was used for the characterization of individual CNTs grown on fibres and of thin lamellae of heat-treated fibres and CNT-modified fibres. Sample preparation of thin lamellae by focused ion beam (FIB) is described in section 3.8.1, while TEM sample preparation for the investigation of individual CNTs is described in section 3.8.2. Finally, section 3.8.3 provides details on the TEM investigation.

3.8.1. TEM sample preparation by focused ion beam (FIB)

Heat treated quartz fibres, not covered by CNTs, were coated with a 20 nm thick layer of Pt-Pd (80:20 ratio between Pt and Pd) by a Cressington Sputter Coater prior to FIB preparation to make the surface electrically conductive. The CNT-coated quartz fibres were loaded directly into the FIB without any additional coating.

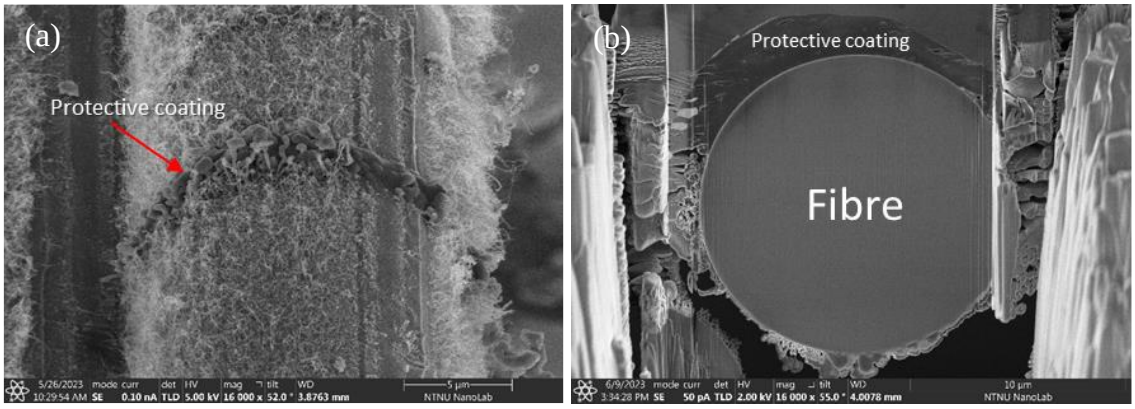

Figure 3.12 FIB preparation of a thin lamella of CNT-modified quartz fibres: a) detail of the carbon protection layer, b) as-prepared lamella.

Sample preparation of thin lamellae by FIB was performed with a Helios UX G4 from Thermo Fisher Scientific. To avoid ion-beam damage in the region of interest, a ~3 µm thick layer of carbon was deposited on top of the sample as a protection layer (Figure

3.12a). The first part of the protection layer was deposited by electron beam assisted deposition. The region of interest was cut out and transferred to a Cu half-grid by standard lift-out technique. The lamellae were mounted as flags, by Pt deposition, to one of the middle posts on the Cu grid. All coarse thinning were then performed with 30 kV acceleration voltage for the Ga^+ ions. Final thinning was first done at 5 kV and then 2 kV voltage on either side of the lamellae to minimize ion-beam induced surface damage. A representative as-prepared lamella is displayed in Figure 3.12b.

3.8.2. TEM sample preparation of individual CNTs

CNT-coated quartz and basalt fibres were dispersed in pure isopropanol and ultrasonicated for 10 – 15 min. Afterwards, a droplet of the obtained dispersion was transferred to a Cu TEM grid coated with a lacey, amorphous carbon film.

3.8.3. TEM characterization

The FIB prepared lamellae were plasma cleaned for 30 s just before the samples were loaded into the TEM to remove possible hydrocarbon contamination on the sample surface. On the other hand, the individual CNTs dispersed on lacey, amorphous carbon support films were loaded directly into the TEM column without any additional plasma cleaning to avoid removing the support film and to avoid modifying the CNTs.

Transmission electron microscopy (TEM) was performed with a double spherical aberration corrected cold FEG JEOL ARM 200FC, which was operated at 200 kV. This instrument is equipped with a large solid angle Centurio detector, covering a 0.98 sr solid angle, for energy dispersive X-ray spectroscopy (EDS) and a GIF Quantum ER spectrometer for electron energy loss spectroscopy (EELS). EDS and EELS were done simultaneously in scanning transmission electron microscopy (STEM) mode.

3.9. Raman spectroscopy

To investigate the quality of the obtained CNTs, Raman spectroscopy was performed using a micro-Raman dispersive spectrometer (SENTERRA, Bruker Optik GmbH) equipped with a CW diode pumped solid state laser (532 nm, 5 mW, 10 scans, resolution

0.5 cm^{-1}). Based on the determined I_D/I_G intensity ratio, the in-plane crystallite dimensions (L_a) were obtained applying the following equation (Eq. 3.4) [213]:

$$\frac{I_D}{I_G} \approx 0.0063\, L_a^2 \tag{3.4}$$

3.10. Atomic force microscopy (AFM)

The investigation of the surface topography of fibres was carried out through a MFP-3D Infinity atomic force microscope supplied by Asylum Research (Santa Barbara, USA) and set in tapping mode. A single fiber was fixed on AFM support for testing. A silicon probe (AC160TS-R3) with a resonant frequency of ≈300 kHz and a spring constant of ≈25 N/m was used. Scan rate was set to 1 Hz and topographies of 3 × 3 μm^2 with a resolution of 256 × 256 pixels were obtained. Three different zones for each fiber were analyzed. Three-dimensional data of the fiber's surface were plotted using IGOR Pro 6.27 software. Finally, data obtained by AFM were post-processed with the open source software Gwiddion to obtain topographic descriptors, including Root Mean Square (RMS) roughness, arithmetic mean roughness, maximum peak height, and maximum pit depth.

3.11. Tensiometric tests

Wettability tests were performed through a tensiometer K100SF (Kruss, GmbH) in different reference liquids following a recently developed procedure for the reliable determination of fibre wetting properties [192]. In fact, tensiometric methods were reported as the most convenient for measuring the contact angles of singles fibres, providing information in static and dynamic conditions. A tensiometer measures the capillary force F (mN) when a single fibre is immersed vertically in a test liquid of known surface tension γ_L, corresponding to the meniscus mass m (g) formed by the liquid around fibre. According to Wilhelmy equation (Eq. 3.5), the fibre/liquid contact angle θ_e (°) can be obtained if the wetted perimeter p (μm) of the fibre is known:

$$F = mg = \gamma_L p \cos\theta_e \tag{3.5}$$

Due to the heterogeneity of CNT-modified fibre diameters, the wetted perimeter p was assessed beforehand for each tested fibre by using n-hexane which is a totally wetting liquid, implying that $\cos\theta_e = 1$. In addition, three test liquids were selected for this study: water, diiodomethane, and a representative bio-based epoxy resin.

For the determination of the contact angle between the single fibre and the reference liquids, single quartz fibres were dipped vertically at a velocity of 1 mm/min in a vessel containing the test liquid up to at least 3− 4 mm immersion depth (advancing mode). When immersion is completed, the fibre is maintained in contact with the liquid in a static position during 60 s to reach an "equilibrium state". At equilibrium, the capillary force is measured and the corresponding static contact angle θ_e is derived from the Eq. 3.5. Then, the fibre is withdrawn from the liquid (receding mode). Tensiometric tests were carried out on five samples for each type of fibre and test liquid. In addition to the static contact angle measurement, advancing and receding angles were also determined considering the mean capillary force over at least 60 s of each mode. However, only the static contact angle was used for the surface energy determination, being ideally the closest to the equilibrium contact angle.

To determine the surface free energy γ_S of single quartz fibres and its polar and dispersive components γ_S^p and γ_S^d (mJ/m^2), the Owens and Wendt approach [214] based on Eq. 3.6 was coupled with the definition of contact angle according to Young-Laplace equilibrium (Eq. 3.7):

$$\gamma_s + \gamma_L - \gamma_{SL} = 2\sqrt{\gamma_s^d \gamma_L^d} + 2\sqrt{\gamma_s^p \gamma_L^p} \tag{3.6}$$

$$\cos\theta_e = \frac{\gamma_S - \gamma_{SL}}{\gamma_L} \tag{3.7}$$

These equations can then be rewritten as follows (Eq. 3.8):

$$\frac{\gamma_L(1+\cos\theta_e)}{2\sqrt{\gamma_L^d}} = \sqrt{\gamma_s^p}\left(\frac{\sqrt{\gamma_L^p}}{\sqrt{\gamma_L^d}}\right) + \sqrt{\gamma_S^d} \tag{3.8}$$

Considering the left hand-side term as the Y ordinate, and the fraction in brackets in the right hand-side term as the X abscissa, the obtained equation (Eq. 3.8) was used for the linear regression of the values of the static contact angles with the test liquids (θ_e) along with the liquid surface free energy (γ_L) and its dispersive (γ_L^d) and polar (γ_L^p) components. Consequently, the slope and the y-intercept of the linear fit allowed to determine the surface free energy of the fibre, as they are respectively the square roots of its polar and dispersive components.

Afterwards, based on the surface free energy of the fibres and surface tension of the epoxy resin, the work of adhesion of each fibre set with the epoxy resin was calculated to predict the wettability and quality of adhesion at the fibre/matrix interface. Different approaches were adopted to calculate the work of adhesion (W_a), namely Young-Dupré equation (Eq. 3.9), Owens, Wendt, Rabel and Kaelble (OWRK) approach (Eq. 3.10), and Wu approach (Eq. 3.11):

$$W_a = \gamma_{LV}(1 + cos\,\theta) \tag{3.9}$$

$$W_A' = 2 \times \left(\sqrt{\gamma_S^d \times \gamma_L^d} + \sqrt{\gamma_S^p \times \gamma_L^p}\right) \tag{3.10}$$

$$W_A'' = 4 \times \left(\frac{\gamma_L^d \gamma_S^d}{\gamma_L^d + \gamma_S^d} + \frac{\gamma_L^p \gamma_S^p}{\gamma_L^p + \gamma_S^p}\right) \tag{3.11}$$

The work of adhesion W_A' (mJ/m2) derived from the Owens and Wendt approach (Eq. 3.10) is based on the geometric mean of dispersive and polar components of the liquid surface tension and solid surface free energy, whereas Eq. 3.11 derived from the Wu approach is based on the harmonic mean of dispersive and polar components of the liquid surface tension and solid surface free energy.

3.12. Electrochemical tests

The electrochemical properties of CNT-modified fibres were assessed by following two different approaches. As described in section 3.12.1, CNT-decorated quartz fibres were tested in wet conditions to investigate their potential application as cathode materials for the electrochemical generation of hydrogen peroxide, an environmentally friendly

oxidant which finds extensive application in the field of environmental remediation [215]. On the other hand, a detailed electrochemical characterization was carried out in dry conditions (section 3.12.2) on CNT-modified basalt fibres to gain a comprehensive understanding of the electrochemical characteristics of the samples and their potential applications. These measurements enabled the evaluation of the materials' conductive and reactive properties, charge transfer capacity, electrical resistance, and stability.

3.12.1. Tests in wet conditions

An Amel 2051 potentiostat/galvanostat (Amel, Italy) was used for the electrochemical characterization of CNT-modified quartz fibres to verify the ability of the carbon-based material to catalyse the electrochemical production of hydrogen peroxide according to the reaction (Eq. 3.12):

$$O_2 + 2H_3O^+ + 2e^- \rightarrow H_2O_2 + 2H_2O \quad (3.12)$$

The experimental apparatus consisted of a two-chamber cell separated by a Nafion 324 cation exchange membrane. Each chamber was stirred with a magnetic bar and contained a volume of 100ml of a 0.05 M Na_2SO_4 aqueous solution as the support electrolyte. The anode was a rectangular platinum electrode, while the cathode was made of a bundle of CNT-decorated quartz fibres with an average length of 5 cm. Tests were performed at room temperature (T=21±2 ºC), with a constant current intensity ranging from 2 to 25 mA, and a continuous oxygen flow in the cathodic chamber. During the tests, the concentration of H_2O_2 in the cathodic solution was measured at selected reaction times using the Merck reflectometric kit based on a specific peroxidase reagent (detection limit 0.2 mg/L).,

The current efficiency, defined as the ratio of the experimentally produced species to the amount theoretically predicted by the Faraday's law, was calculated according to Eq. 3.13:

$$CE\ (\%) = \frac{nFCV}{It}\ 100 \quad (3.13)$$

where n is the stoichiometric number of transferred electrons, F is the Faraday constant (96,485 C mol^{-1}), C is the concentration of the considered species in bulk solution (M), V is the catholyte volume (l), I is the current intensity (A) and t is the electrolysis time (s).

3.12.2. Tests in dry conditions

A symmetric electrochemical cell was assembled for the electrochemical characterization of basalt fabric samples functionalized with vertically aligned carbon nanotubes (VA-CNTs) using steel disks as electrodes. The materials to be tested, i.e., two CNT-modified basalt fabric samples, were inserted between the electrodes in two different setups, as illustrated in Figure 3.13: (i) a single layer of either the polymer film (Pol) or the functionalized basalt fabric (Bs-NT) was placed between the metal electrodes (Figure 3.13a); (ii) two functionalized basalt fabrics, separated by a polyethylene film (PE), were placed between the electrodes (Figure 3.13b). In the last configuration, the polyethylene film featured a window through which a homemade conductive bio-polymer film (Pol) was inserted. The procedure for the preparation of the bio-polymer film (Pol) is described in section 1.4 of Part II − Materials and Methods.

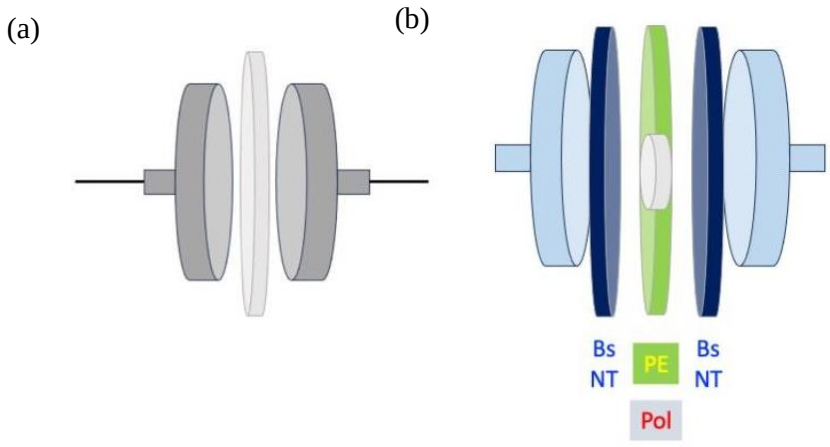

Figure 3.13 The two setups used for electrochemical tests : (a) a single layer of either the polymer film (Pol) or the CNT-decorated basalt fabric (Bs-NT) placed between the metal electrodes; (b) two CNT-decorated basalt fabrics, separated by a polyethylene film (PE), placed between the electrodes. In the second setup, a homemade conductive bio-polymer film (Pol) was inserted in a central window of the polyethylene film.

Electrochemical tests were conducted at room temperature using the Metrohm Autolab PGSTAT204 apparatus. The tests performed included: i) potentiodynamic polarization (section 3.12.2.1), ii) electrochemical impedance spectroscopy (section 3.12.2.2), and iii) cyclic voltammetry (section 3.12.2.3).

3.12.2.1. Potentiodynamic polarization

Potentiodynamic polarization is a technique for analyzing the corrosion state of materials which provides information on electrode processes such as corrosion rates, susceptibility to pitting, passivity, etc. The technique is based on scanning the potential around the open circuit potential value with extremely low scanning speed (mV s^{-1}) to work in quasi-stationary conditions. When the potential of metals in solution is moved away from the open circuit potential, the oxidation and reduction reactions are no longer in equilibrium, leading to a phenomenon known as electrode polarization, which generates an electric current. Shifting the potential toward positive values results in anodic polarization, initiating oxidative processes. Conversely, shifting the potential toward negative values results in cathodic polarization and reductive processes. The effects of polarization are illustrated in a graph where the magnitude of the generated current (typically displayed on a logarithmic scale) is plotted as a function of the applied potential. A typical anodic polarization graph is shown in Figure 3.14.

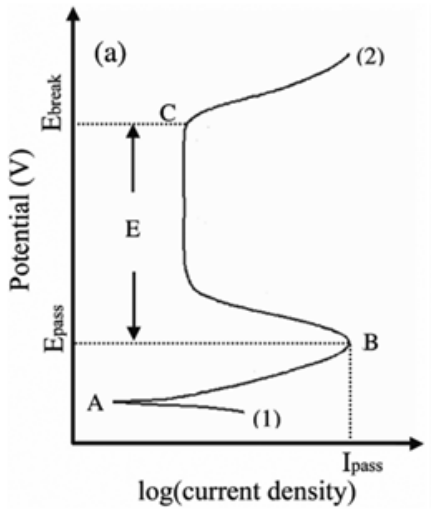

Figure 3.14 Example of a polarization curve.

Point A represents the point where oxidation and reduction are in equilibrium (E_{corr}). As the potential is shifted increasingly positive, a current is generated due to the anodic reaction from the oxidation of the material. This region where oxidation occurs is known as the active region. For some materials, as the potential continues to increase, a segment with a very low and constant current may be observed, caused by passivation, which refers to the formation of a protective layer on the surface (often an oxide layer in metals). Further increasing the potential beyond what is often referred to as the breakdown potential may cause part of the coating to break, resulting in a rapid increase in current. This phenomenon is known as pitting. However, the increase in current is not always associated with pitting; in some cases, it may be due to transpassive dissolution, while for certain alloys, it may be attributed to oxygen evolution.

The operating conditions for the polarization tests are as follows: the potential difference between the two electrodes varies at a rate of 2 mV/s, starting from E_1 = 0 V and proceeding to E_2 = -0.3 V, and finally to E_3 = +0.3 V. Only the system's response within the potential range of -0.3 to +0.3 V will be reported.

3.12.2.2. Electrochemical impedance spectroscopy (EIS)

Impedance spectroscopy is an investigative technique that highlights the kinetics of processes occurring in an electrochemical system. It characterizes surface changes under specific conditions and adapts system parameters to achieve desired effects on the surface. This technique involves applying a small sinusoidal voltage signal (typically between 1 and 10 mV) superimposed on a predetermined potential and measuring the resulting current that flows through the cell. If the relationship between voltage and current is linear—meaning the current signal has the same frequency as the input signal but a different phase—the cell behavior can be analyzed in terms of impedance. Impedance represents a circuit's ability to oppose current flow and is analytically expressed as the ratio of voltage to current.

An electrochemical cell is typically a nonlinear system due to the variety of processes involved. However, when the excitation amplitude is very small, the system behaves linearly. By analyzing the system's impedance as a function of frequency, information can

be obtained about variations in internal dynamics that modify the chemical and physical characteristics of the system. These variations may include electron transport across the interface, charge transport resulting from the application of an external potential that generates an electric field gradient, flows of agglomerated atoms due to defects in the electrolyte, and material transport driven by concentration gradients or convection. EIS also allows for assessing the potential for corrosion processes and their rates. Frequency scanning is typically performed over a range from 100 kHz to 1 mHz.

The results of these measurements are often presented graphically, with the most common formats being the Nyquist and Bode diagrams. Bode plots illustrate the behavior of the impedance modulus and phase as a function of the logarithm of the frequency, allowing for the representation of large variations in impedance values and their correlation with frequency. Nyquist plots represent impedance in the complex plane using polar coordinates. In this representation, at a given frequency, the impedance modulus is depicted as a vector, while the phase corresponds to the angle between the vector and the horizontal axis. This allows for a quick qualitative interpretation of the electrochemical system's behavior, although it does not provide information on frequency. The Nyquist plot is particularly useful when there is no substantial variation in the impedance modulus with frequency.

The operating conditions for the impedance tests are as follows: at a potential of E = 0.0 V, an AC amplitude of ±10 mV is applied over a frequency range of $1 \cdot 10^{+5}$ Hz – 1 Hz.

3.12.2.3. Cyclic voltammetry (CV)

Cyclic voltammetry is a versatile voltammetric analysis technique based on measuring the current that flows through an electrode immersed in a solution containing electroactive species (which can be oxidized or reduced) when subjected to a change in potential.

The potential applied to the working electrode, relative to a reference electrode that maintains a constant potential, consists of a triangular wave with a slope dependent on the scan rate (scanning speed) (Figure 3.15). Typical scan rates range from 5 to 1000 V/s. By subjecting an electrochemical cell to this type of potential stress, an exchange of

electrons is induced between the electrode and the electroactive species, allowing for the monitoring of the associated current during the oxidation and reduction processes (or viceversa).

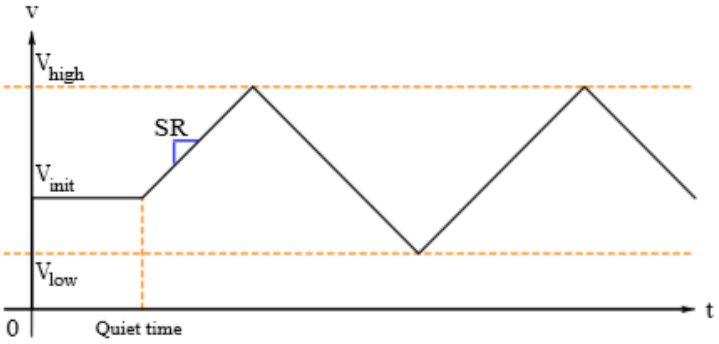

Figure 3.15 Potential trend over time in a cyclic voltammetry. Two cycles are represented in this graph.

To perform an analytical-quantitative analysis, it is essential to consider redox processes, in which the intensity of the current through the electrode depends primarly on how the electroactive species reach it. Among the three processes that facilitate the movement of species in solution —convection, migration, and diffusion— only diffusion can be directly correlated with the concentration of the electroactive species. To ensure that the electroactive species primarily move by diffusion, several conditions must be met: the temperature must be kept constant, the solution should not be stirred, and a supporting electrolyte must be used to prevent the migration of charged electroactive species under the analytical conditions. Additionally, it is important to consider redox processes where the rate at which the chemical species reaches the electrode is much slower than the rate of electron exchange between the electrode and the solution. In this scenario, the system is controlled by mass transfer.

The behavior of the current as a function of potential variation is represented in the so-called voltammogram (or cyclic voltammogram), as shown in Figure 3.16.

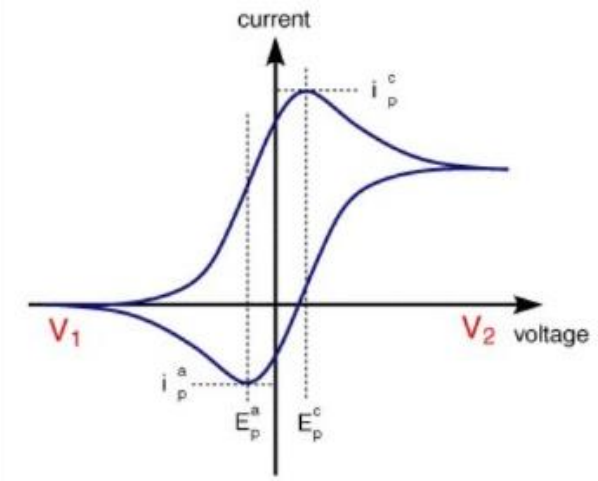

Figure 3.16 Example of a ciclovoltammogram.

The behavior of the current when moving towards less positive potentials shows that the decrease in potential leads, according to the Nernst equation (Eq. 3.14), to a reduction in the concentration of the oxidized species on the surface of the electrode:

$$E = E^{\circ} + \frac{[Ox]^n}{[Red]^m} \tag{3.14}$$

This generates a concentration gradient that, once the standard potential is surpassed, results in the diffusion of the oxidized species toward the area of lower concentration, namely the bulk of the solution (Figure 3.17).

A cathodic faradaic current is then recorded, whose magnitude increases until all the species on the electrode's surface are reduced, bringing the concentration of the oxidized species at the electrode surface to zero. As the reduced species diffuse from the solution to the electrode, an increase in the solution volume at the electrode's surface occurs, slowing the diffusion rate of the oxidized species and resulting in a current decrease. When the scan slope is reversed and the potential increases, the reduced species generated in the previous half-cycle are present on the electrode surface, while the oxidized species are abundant in the bulk of the solution. The increase in potential leads to a decrease in the concentration of the reduced species at the electrode surface, resulting in the diffusion of the species toward the bulk of the solution. Thus, there will be an increase in the

concentration of the oxidized species at the electrode surface, leading to an increasing anodic current.

It is important to note that when a negative potential is applied to the electrode and the concentration of positive ions in the solution is high, an electric double layer is formed that acts like a capacitor. Consequently, a capacitive current flow is generated, which adds to the faradaic current. Therefore, the current recorded before E^O can be associated with the capacitance of the electrode-solution interface.

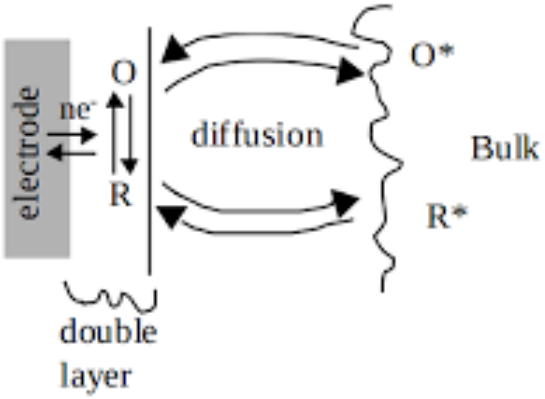

Figure 3.17 Schematic for the formation of the condensed layer.

The curve obtained has a closed-cycle trend, characterized by the presence of both an anodic and a cathodic wave for reversible systems. In contrast, for irreversible systems, one of the two waves is absent. Chemical reversibility is used to determine whether the analyte is stable during the reaction and can be subsequently re-oxidized. Electrochemical reversibility refers to the kinetic transfer of electrons between the electrode and the analyte. An electrochemical process is considered reversible if equilibrium is established immediately during any change in applied potential, which occurs when there is low resistance to electron transfer. Processes in which electron transfer is rapid and that respond to the Nernst equation are often referred to as "Nernstian." Conversely, a process is classified as irreversible if the electron transfer occurs much more slowly than the scan rate, preventing the concentration predicted by the Nernst law from being established at the electrode surface, as equilibrium between the concentrations is not quickly attained. If the reduction process is both chemically and electrochemically reversible, the peak-to-

peak separation between the anodic and cathodic peaks remains fixed at 57 mV at 25°C (relative to the scan rate), with a half-height width of 59 mV. In the case of a reversible process, an increase in the scan rate leads to a reduction in the diffusion layer, resulting in an increase in current. Conversely, when the scan occurs slowly, the diffusion layer has more time to develop, and the measured current will be lower. To ensure that an electrode behaves as Nernstian as possible, it is advisable to use low scan rates; this allows for a greater likelihood that electronic transfer will occur more quickly than diffusion, especially when the current is low. For a reversible process, the current peak always occurs at the same voltage value, regardless of the scan rate. The position of this peak is characteristic of the specific reaction taking place at the electrode surface. In a reversible process, the ratio of anodic to cathodic current is unity. In contrast, for a chemically and electrochemically non-reversible process, the separation of the potential peaks and the position of the current peak vary as a function of the scan rate. For these processes, the position of the current peak also varies as a function of the reduction rate constant (K_{red}) because the current takes longer to respond to a change in potential.

The operating conditions for the cyclic voltammetry tests included a potential range of +1.0 to -1.0 V and scan rates of 5, 10, 50, 100, and 200 mV/s.

PART III – RESULTS AND DISCUSSION

PART III – RESULTS AND DISCUSSION

Chapter 1.

Effect of thermal treatment on the mechanical properties of quartz fibres

The degradation of the mechanical properties of most reinforcing fibres after high-temperature exposure is one of the major drawbacks of the direct growth of carbon nanotubes (CNTs) through chemical vapour deposition (CVD) as a strategy for improving the mechanical performance of polymer composites and introducing multifunctionalities. In fact, the temperatures involved in the CVD process (≥600 °C) often have detrimental effects on the mechanical properties of the fibre substrates. The most severe thermal degradation is observed in the case of E-glass fibres, which exhibit appreciable strength losses at temperatures as low as 250 °C [216]. Furthermore, the strength of E-glass fibres has been found to drop by 50–70% over the temperature range of 450–600 °C [37], [111], [115], [217]. Similarly, basalt fibres undergo a strength loss of around 75% following heat treatments at 600 °C [29], regardless of the higher operating and softening temperatures of basalt fibres (~650 °C and 1050 °C, respectively) compared to E-glass fibres (~460 °C and 600 °C, respectively).

Quartz fibres, also known as ultrapure silica glass fibres, are designed to withstand service temperatures much higher than E- or S-glass fibres. Therefore, they are proposed in this research work as a promising candidate for the direct growth of CNTs. However, whilst the thermal degradation of general-purpose glass fibres and basalt fibres has been widely investigated in the literature, limited research has been conducted on quartz fibres. Recently, De Luca et al. [19] achieved a uniform coverage of carbon nanotubes (CNTs) on quartz fibres resulting in both a 12% improvement of IFSS and a piezo-resistive response suitable for strain-sensing applications. Nevertheless, they detected a 50%

decrease of the tensile strength of the fibres exposed to 760 °C for 30 minutes in N_2, suggesting the need for a more thorough investigation to clarify the effects of exposure to typical CVD temperatures on the mechanical properties of quartz fibres and understand the damage mechanisms at play.

The effects of exposure to medium-high temperatures (600, 700, 800 °C) on the mechanical properties of single quartz fibres are investigated in this chapter as a baseline for the subsequent exploration of the synthesis of CNTs on quartz fibre substrates, presented in the following chapters of this research work. The variations of tensile strength, Young's modulus, Weibull parameters, density, fracture toughness, surface morphology and microstructure are provided as a function of heat-treatment temperature and the possible controlling mechanisms are discussed.

1.1. Tensile properties of single quartz fibres

The tensile properties of as-received fibres were characterized through single fibre tensile tests at three different gauge lengths, namely 20 mm, 30 mm, and 40 mm. Table 1.3 summarises the results of the tensile tests in terms of average values and corresponding standard deviations. As typically observed for ceramic materials [67], [218], [219], the measured tensile strengths and strains at failure were highly dependent on the gauge length, following a decreasing trend with increasing gauge length. This is the manifestation of a dimension effect typical of brittle materials, which can be related to the higher probability to encounter more severe flaws as the tested volume increases [218]. On the other hand, Young's modulus showed no clear dependence on the gauge length, as supported by previous works on ceramic fibres [67], [218], [219].

Table 1.3 Results of tensile tests for as-received (R.T.) and heat-treated single quartz fibres in terms of average values (average value/standard deviation).

Heat-treatment temperature (°C)	Gauge length (mm)	Diameter (µm)	Tensile strength (MPa)	Young's modulus (GPa)	Strain at failure (%)
R.T.	20	14.3/0.3	1974.5/364.4	75.5/3.1	2.6/0.5
R.T.	30	14.6/0.4	1277.0/293.0	67.2/3.6	1.9/0.5
R.T.	40	14.6/0.4	1136.0/275.4	74.1/3.4	1.5/0.4
600	20	14.7/0.4	506.4/118.6	71.7/3.8	0.7/0.2
700	20	14.5/0.7	464.5/118.4	66.5/3.4	0.7/0.2
800	20	14.0/0.4	274.3/74.7	73.4/3.9	0.4/0.1

To evaluate the influence of exposure to typical CVD temperatures on the mechanical behaviour of quartz fibres, heat treatments at 600 °C, 700 °C and 800 °C for 1 hour were carried out in air atmosphere, and further tensile tests were performed on the heat-treated fibres, maintaining a constant gauge length of 20 mm. The outcomes of these tests, summarized in Table 1.3, revealed a strength drop by approximately 74% after heat treatment at 600 °C which is comparable to the one reported for general-purpose glass fibres and basalt fibres at 600 °C [21], [37], [67], [111], [115], [217]. As the heat-treatment temperature increased, a decreasing trend of the mechanical strength was observed, with strength losses of approximately 76% and 86% for quartz fibres heat-treated at 700 °C and 800 °C, respectively. These values are in good agreement with those from previous studies [30], [220]–[223], highlighting that high-temperature exposure can seriously compromise the mechanical response of quartz fibres.

To identify the possible damage mechanisms, tensile test data were further analysed using a two-parameter Weibull distribution whose characteristic parameters, estimated through the maximum likelihood estimation (MLE) method, are reported in Table 1.4. Weibull plots of tensile strength and Young's modulus (Figure 1.3 and Figure 1.4) indicate that a unimodal Weibull function well describes the tensile test data, as the values are arranged according to a linear trend. This implies the existence of a single-flaw population

responsible for the failure of quartz fibres [218] irrespective of the gauge length (Figure 1.3) and heat-treatment temperature (Figure 1.4). Therefore, it can be assumed that high-temperature exposure did not change the nature of the defects but could affect their severity and homogeneity, as it can be qualitatively deduced by the detected variations of the Weibull parameters (Table 1.4) [48]. In fact, the decreasing trend of the characteristic strength values, as observed for the average strength values, suggests an increase in the average size of critical defects following heat treatment. On the other hand, the similar values of $m_{\sigma,u}$ and the highly overlapping confidence intervals indicate no significant difference in shape parameter between the distributions, suggesting that the same flaw types were active in all sets of tested samples.

Table 1.4 Weibull distribution parameters estimated through MLE for as-received (R.T.) and heat-treated single quartz fibres. Confidence intervals (CI) at 90% and the unbiased estimate of the shape parameters ($m_{\sigma,u}$, $m_{E,u}$) are provided for both tensile strength and Young's modulus.

Heat-treatment temperature (°C)	**Gauge length (mm)**	**Tensile strength - m_σ [90% CI]**	**Tensile strength –$m_{\sigma,u}$**	**Tensile strength – σ_0 [90% CI] (MPa)**	**Young's modulus – m_E [90% CI]**	**Young's modulus – $m_{E,u}$**	**Young's modulus – E_0 [90% CI] (GPa)**
R.T.	20	6.2 [4.3, 7.8]	5.8	2125.3 [1989.0, 2273.3]	29.9 [20.9, 37.6]	27.9	77.0 [75.9, 78.0]
R.T.	30	5.0 [3.6, 6.3]	4.7	1391.1 [1287.6, 1504.6]	20.6 [14.7, 25.7]	19.4	68.9 [67.6, 70.2]
R.T.	40	4.9 [3.0, 5.8]	4.1	1243.8 [1121.8, 1381.5]	24.9 [16.5, 32.0]	22.9	75.6 [74.2, 77.1]
600	20	5.1 [3.8, 6.1]	4.8	552.7 [519.0, 588.9]	17.5 [13.3, 21.1]	21.1	73.6 [72.2, 74.9]
700	20	4.4 [3.4, 5.4]	4.3	510.0 [475.4, 547.6]	21.0 [16.1, 25.4]	20.2	68.1 [67.1, 69.1]
800	20	4.3 [3.0, 5.5]	4.0	302.1 [273.4, 334.4]	17.9 [12.2, 22.8]	16.6	75.3 [73.5, 77.1]

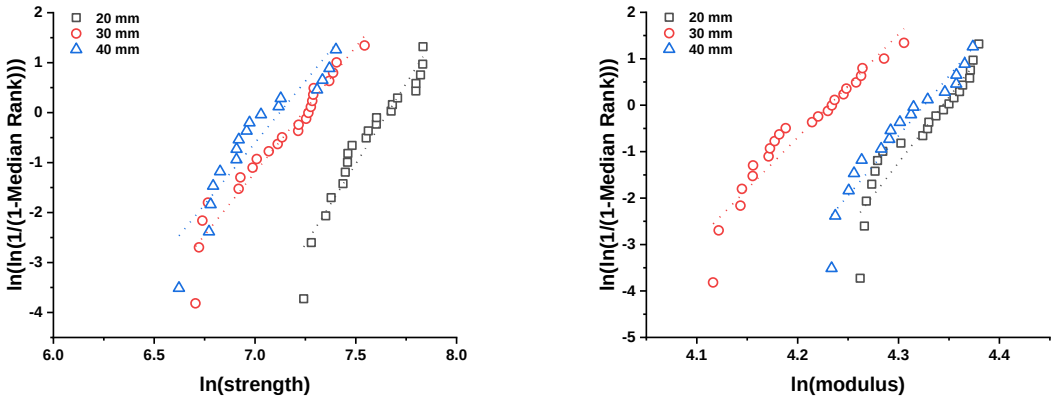

Figure 1.3 Weibull plots of (left) the tensile strength and (right) Young's modulus of single quartz fibres as a function of gauge length.

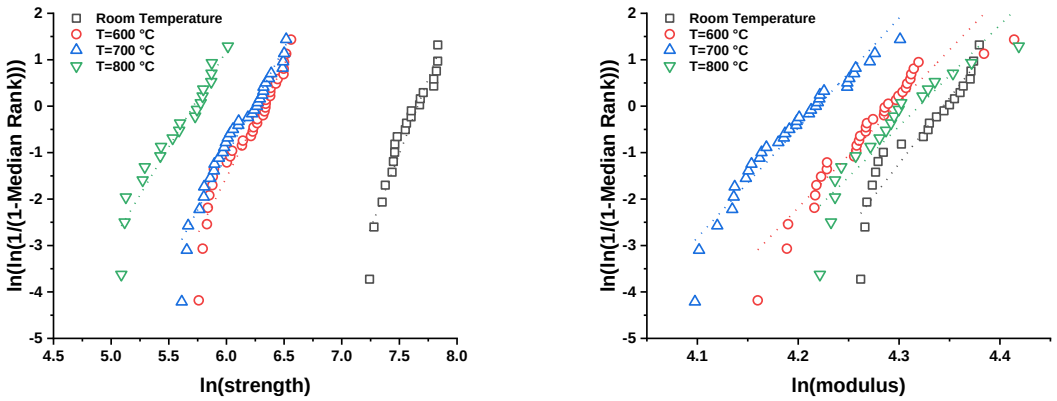

Figure 1.4 Weibull plots of (left) the tensile strength and (right) Young's modulus of single quartz fibres as a function of heat-treatment temperature.

1.2.Morphological characterization

To determine the nature and the location of the critical fracture origin, the fracture surfaces of tested fibred were analysed by scanning electron microscopy (SEM) after tensile tests. As shown in Figure 1.5, a peculiar morphology, typical of the fracture mechanism of brittle materials [29], [216], [224], was detected regardless of heat-treatment temperature. This characteristic morphology, schematically shown in Figure 1.6, features three distinct regions, i.e., mirror, mist, and hackle zone, originated by changes in the crack propagation rate during fibre breakage. As the fracture occurs, the

first region generated around the critical flaw is the mirror zone, which appears smooth and featureless. Under load, the growth rate of the crack increases until it becomes unstable, producing a dimpled surface, i.e., the mist zone. Finally, the crack branches out producing a rough region, i.e., the hackle zone [216]. Based on the location of the mirror zone, highlighted with a white dashed line in the representative SEM micrographs in Figure 1.5, it can be concluded that the fracture originated from the fibre surface (rather than within the bulk). This reveals that superficial flaws are responsible for fibre breakage regardless of heat treatment temperature. Heat treatment was found to affect only the size of the mirror zone, which increased with heat-treatment temperature and with the reduction in tensile strength. This is in accordance with previous findings by Feih et al. [216] who reported that the tensile strength of glass fibres, σ_f, is related to the size of the mirror zone according to the following equation 1.1:

$$\sigma_f = A_m(d_m)^{-0.5} \tag{1.1}$$

where d_m is the mirror depth and A_m is referred to as mirror constant and is generally related to the fracture toughness of the material.

No signs of visible flaws were detected at the fracture origin. While it is possible that the sputtered gold coating – even if very thin – may have obscured such features, the difficulty of characterizing the fracture-triggering flaw on the fibre fracture surfaces is also to be considered, with no flaws observed at the origin for the majority of the mirror regions examined in literature [225], [226].

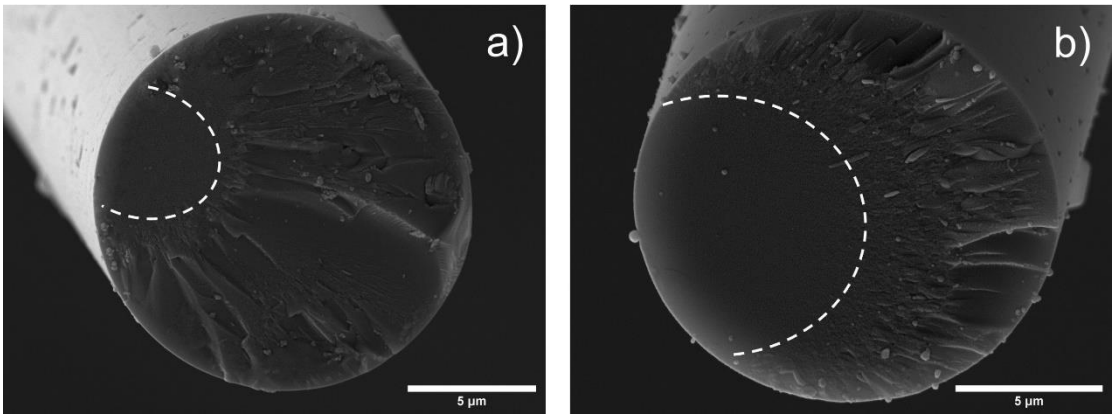

Figure 1.5 SEM micrographs of the fracture surfaces of (a) untreated quartz fibres and (b) heat-treated quartz fibres at 800 °C. The mirror zone is highlighted with a white dashed line.

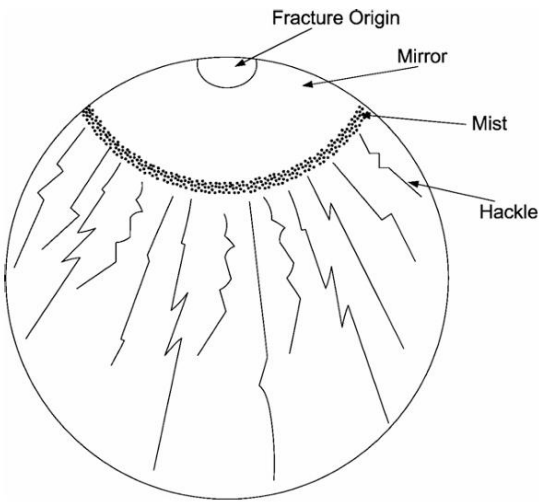

Figure 1.6 Schematic representation of the fibre fracture surface [21].

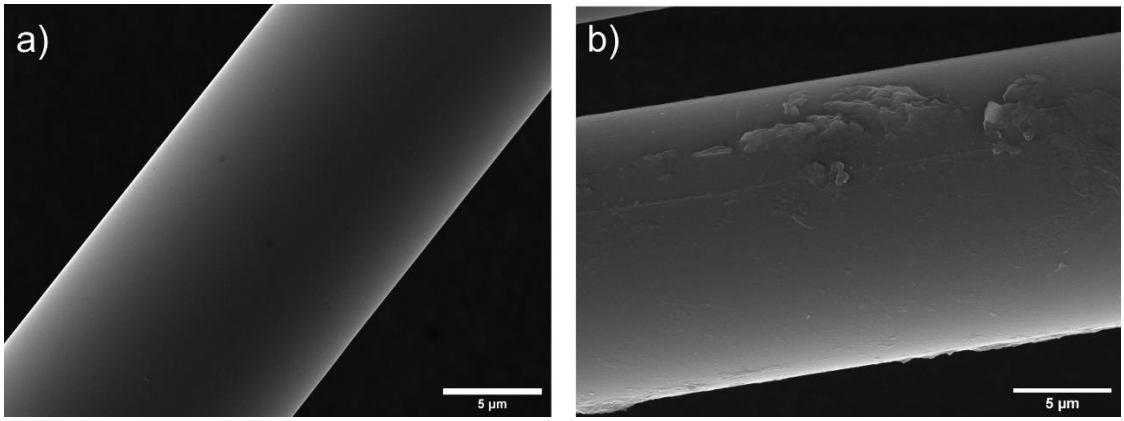

Figure 1.7 SEM micrographs detailing the lateral surface of (a) untreated and (b) heat-treated (800 °C) quartz fibres.

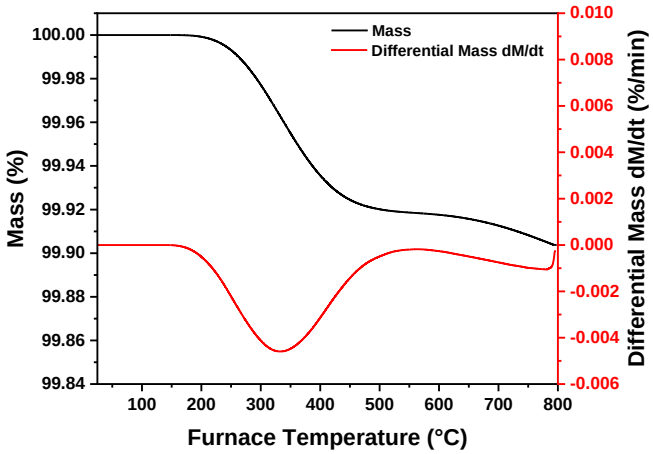

Figure 1.8 TGA and DTG curves from thermogravimetric analysis performed on as-received quartz fibres.

It is worth noting that possible superposition of a certain amount of bending onto the tensile loading may be produced by inaccuracies in the alignment between the fibre and the loading direction. While the effect of the misalignment on the value of the tensile strength can be neglected at the gauge lengths used in this research work [227], a certain amount of bending can enhance the predominant failure from the surface and mask the failure from the volume defects. Nevertheless, the failure of brittle fibres, such as glass and basalt fibres, is often reported to be governed by surface flaw distributions [21], [29], [67], [217], making it reasonable to assume it also valid for quartz fibres.

SEM investigation of the lateral surface of as-received quartz fibres (Figure 1.7a) revealed a quite smooth morphology, which can be ascribed to the presence of a commercial epoxy resin-compatible sizing. On the other hand, Figure 1.7b shows the occurrence of some surface irregularities after heat treatment. As reported by Thomason [228], the organic materials in epoxy-compatible glass fibre sizings are rapidly decomposed and volatilized in the temperature range 250-500 °C [21], [228]. The possible occurrence of sizing degradation was therefore investigated through thermogravimetric analysis (TGA) performed on as-received quartz fibres. As shown in Figure 1.8, a total weight loss amounting to less than 0.1% of the initial weight was detected up to 800 °C. The derivative thermogravimetric (DTG) curve reveals that most of the weight loss occurred in the temperature range of 150-550°C, with a maximum degradation rate at 330 °C.

These findings are in line with the hypothesis of sizing degradation, which can be considered as one of the main factors determining quartz fibre strength loss, as usually reported for glass fibres [111], [115]. In fact, the presence of an organic sizing on the fibre surface is known to exert a flaw-healing effect, increasing the fibre tensile strength by "filling" the defects on the fibre surface [48]. On the other hand, the loss of protective sizing exposes the inherent fibre flaws, with consequent reduction of the fibre strength. Moreover, removing the protective sizing exposes the fibres to mechanical handling damage, which is at play during the removal of single fibres from heat-treated bundles. However, it is worth noting that the exposure of the inherent flaws and mechanical handling damage due to sizing degradation should affect the strength of all heat-treated fibres to the same extent, suggesting the existence of fundamental thermal effects responsible for the further strength losses detected with increasing temperature.

1.3. Structural characterization

When exposed to high temperatures, the amorphous structure of quartz fibres can undergo devitrification phenomena [112] with consequent volume changes that compromise the original structural integrity of the fibres. Therefore, crystallization phenomena are often reported as the main factor determining the degradation of the mechanical properties of quartz fibres [229]. Compared to bulk quartz glass, the small diameter and high surface energy of quartz fibres promote the surface nucleation of crystal, thus allowing crystallization at lower temperatures (1100-1435 °C). It is noteworthy that Zheng et al. [30] observed the formation of nanometre-ordered regions localized at the fibre surface after prolonged exposure (10 hours) at temperatures as low as 700 °C and the nucleation of surface nanometre crystallites at 900 °C. In the present study, diffraction analysis (XRD) revealed that quartz fibres exhibited an amorphous structure up to 800 °C (Figure 1.9). As it cannot be easily identified with the XRD method, the possible occurrence of localized crystallization phenomena was investigated at the nanoscale through transmission electron microscopy (TEM). This analysis, performed on thin cross-sections of 800°C-treated quartz fibres (Figure 1.10), did not show any evidence of localized crystallization nor segregation phenomena in the region below the fibre surface, revealing a homogeneous chemical composition and amorphous structure towards the fibre core.

These results strengthen the hypothesis of a failure mechanism that occurs predominantly at the fibre surface, as no structural ordering processes nor segregation phenomena seem to take place in the fibre bulk.

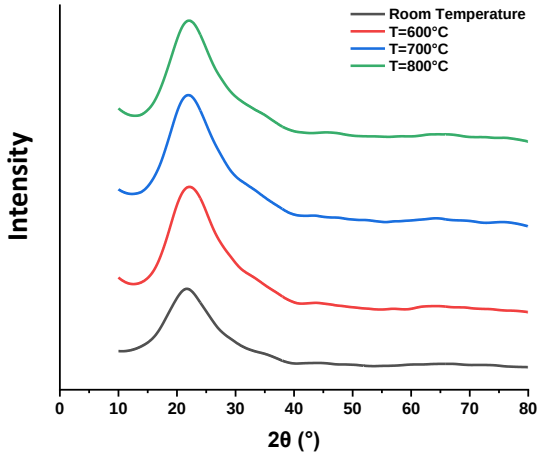

Figure 1.9 X-ray diffraction patterns for untreated and heat-treated quartz fibres.

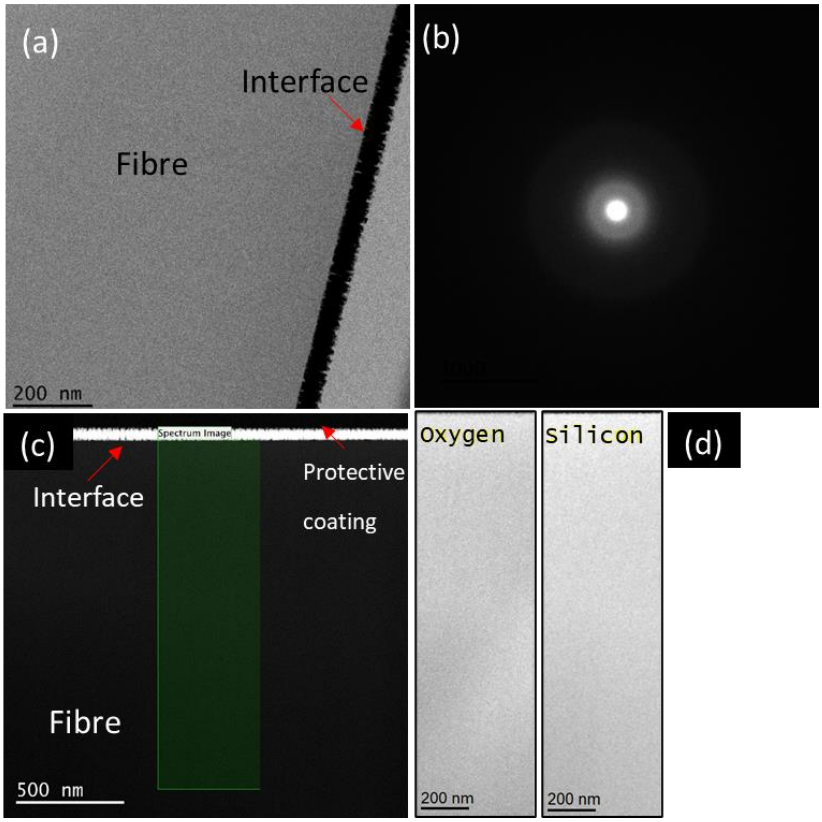

Figure 1.10: (a) Bright field TEM micrograph and (b) electron diffraction pattern from a quartz fibres heat-treated at 800 °C for 1 hour in air atmosphere; (c) HAADF STEM micrograph and (d) EELS map of O and Si.

Indirect evidence of this is provided by the measured Young's modulus which, unlike tensile strength, was hardly affected by thermal exposure, implying no bulk modification phenomena being involved, as supported by a previous work on quartz fibres [223]. On the contrary, an increase in stiffness with increasing temperature has been commonly reported for general-purpose glass fibres and basalt fibres [29], [67], [113]–[115] due to a thermally-induced structural relaxation phenomenon occurring in the bulk of the fibre. Consequently, the density of glass and basalt fibres was found to increase after thermal exposure. Regarding quartz fibres, Table 1.5 shows no significant variations in the measured fibre density, confirming that no relevant bulk modification occurred.

Table 1.5 Density of untreated and heat-treated quartz fibres expressed as average value/standard deviation.

Temperature (°C)	**Density (g/cm^3)**
R.T.	2.218/0.043
600	2.212/0.019
700	2.209/0.015
800	2.243/0.029

To address the complex issue of quartz fibre thermal degradation, the thermal and mechanical history of the fibre should also be taken into account. During manufacturing, the drawing stresses and rapid cooling rates produce structural anisotropy and excess enthalpy due to changes in the Si-O-Si bond angles and deformations in the silica network, respectively. These effects have been previously addressed to explain the greater strength of glass fibres than bulk glass. Conversely, exposure to high temperatures causes the structural relaxation of internal deformation states, with anisotropy relaxation occurring more quickly and at lower temperatures compared to enthalpy relaxation. According to Feih et al. [21], this behaviour is consistent with a surface-controlled mechanism for strength loss, as structural relaxation proceeds more rapidly at the fibre surface than within its bulk. Additionally, water from the degradation of the silane-based sizing or absorbed onto the glass surface has been shown to facilitate surface structural relaxation by attacking the silica network through thermally activated stress corrosion. As

observed by Lilli et al. [29] for basalt fibres, this phenomenon can produce radial gradients of the mechanical properties of heat-treated fibres. Therefore, to reveal potential structural heterogeneities and further examine whether bulk changes contribute to the thermally induced decay in quartz fibre strength, high-speed nanoindentation and pillar-splitting experiments were carried out for the high-resolution mapping of the mechanical properties and the assessment of the fracture toughness across the fibre cross-section.

1.4. Mechanical characterization at the nanoscale

Figure 1.11 and Figure 1.12 illustrate the data of the elastic modulus and hardness obtained from the high-speed nanoindentation mapping of representative fibre cross-sections in relation to the heat-treatment temperature. Moreover, Figure 1.13 reports high-speed nanoindentation maps for the elastic modulus over hardness ratio. These high-resolution mechanical maps offer preliminary qualitative evidence of the absence of gradients in the mechanical properties of the fibres across their cross-sectional areas for all four treatment conditions examined. Nevertheless, a pronounced gradient in both elastic modulus and hardness is observed at the interface between the embedding matrix and the fibres, showing an increase from the outer layer to the core. This effect is generally attributed to artifacts resulting from indents that span both phases, leading to a mixed mechanical response.

To further investigate potential differences in the fibre nanoindentation response, a comparison was made between quasi-static nanoindentations conducted at the fibre centre and mechanical data obtained by averaging values from central circular areas (4 μm in diameter) from each mapping (Figure 1.14). Apart from discrepancies between the results from continuous stiffness measurement (CSM) nanoindentation and high-speed mapping—arising from the intrinsic differences between the constant low strain rate used in one method and the significantly higher (at least one order of magnitude greater), non-

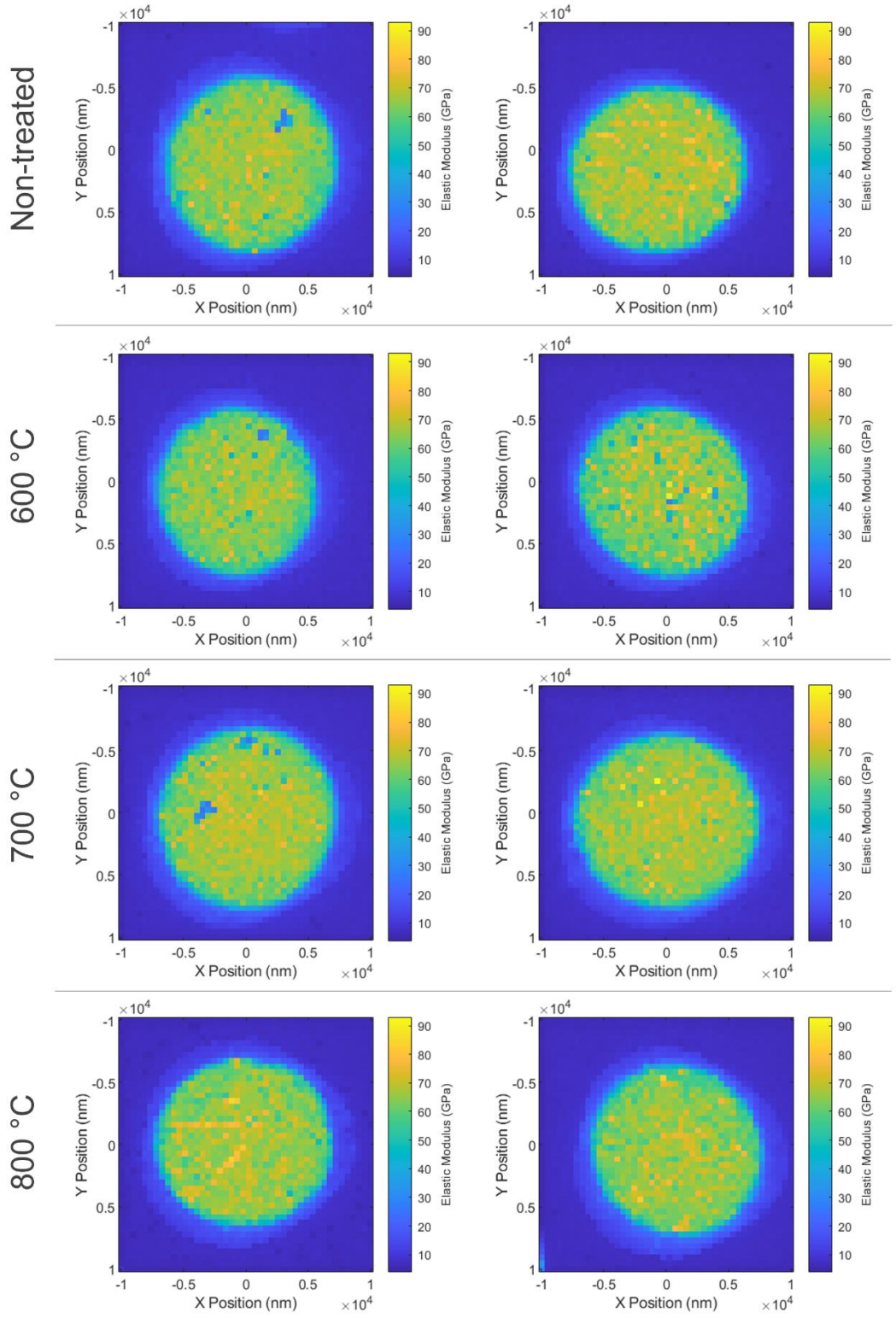

Figure 1.11 Representative high-speed nanoindentation maps for the elastic modulus as a function of the heat-treatment temperature.

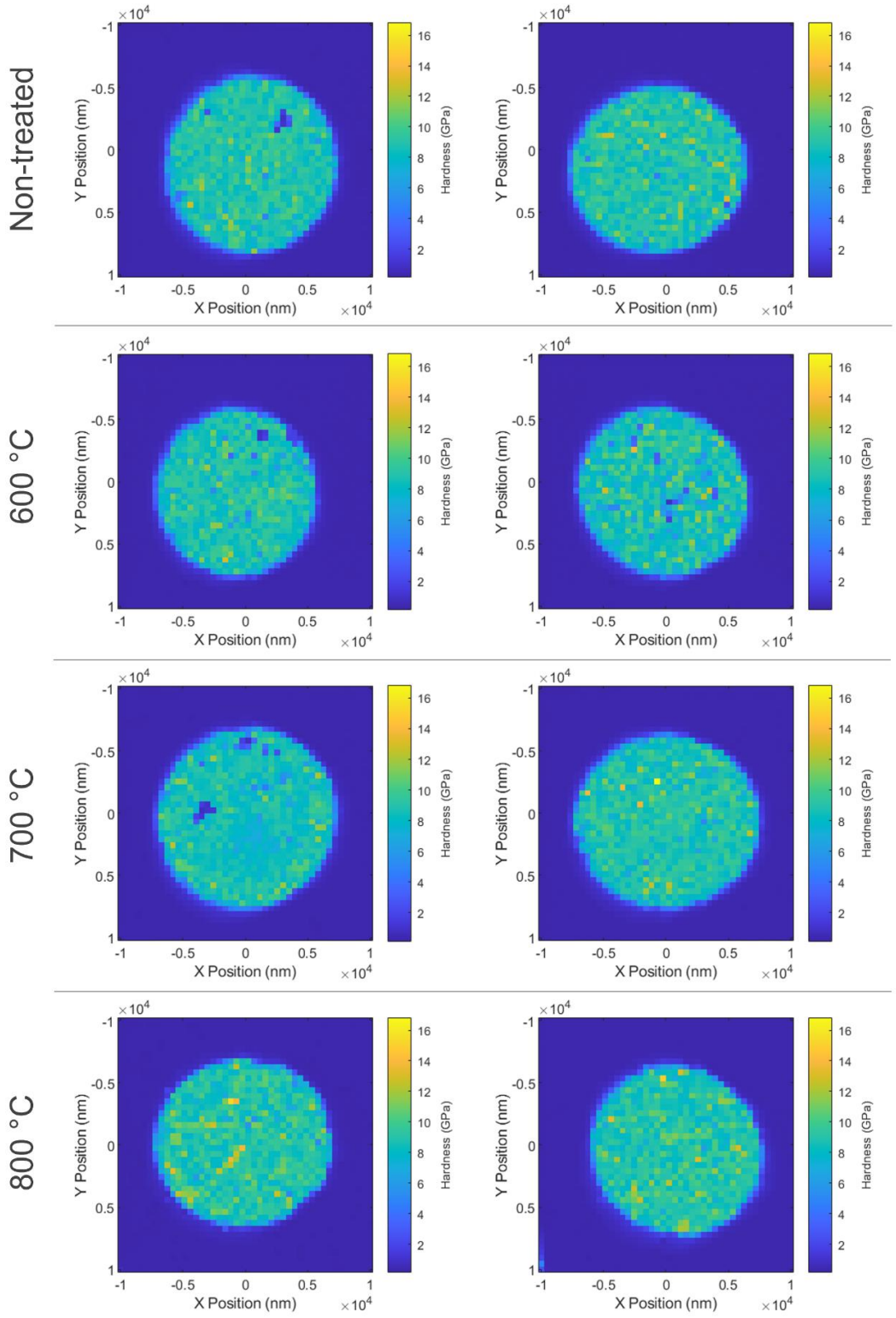

Figure 1.12 Representative high-speed nanoindentation maps for the hardness as a function of the heat-treatment temperature.

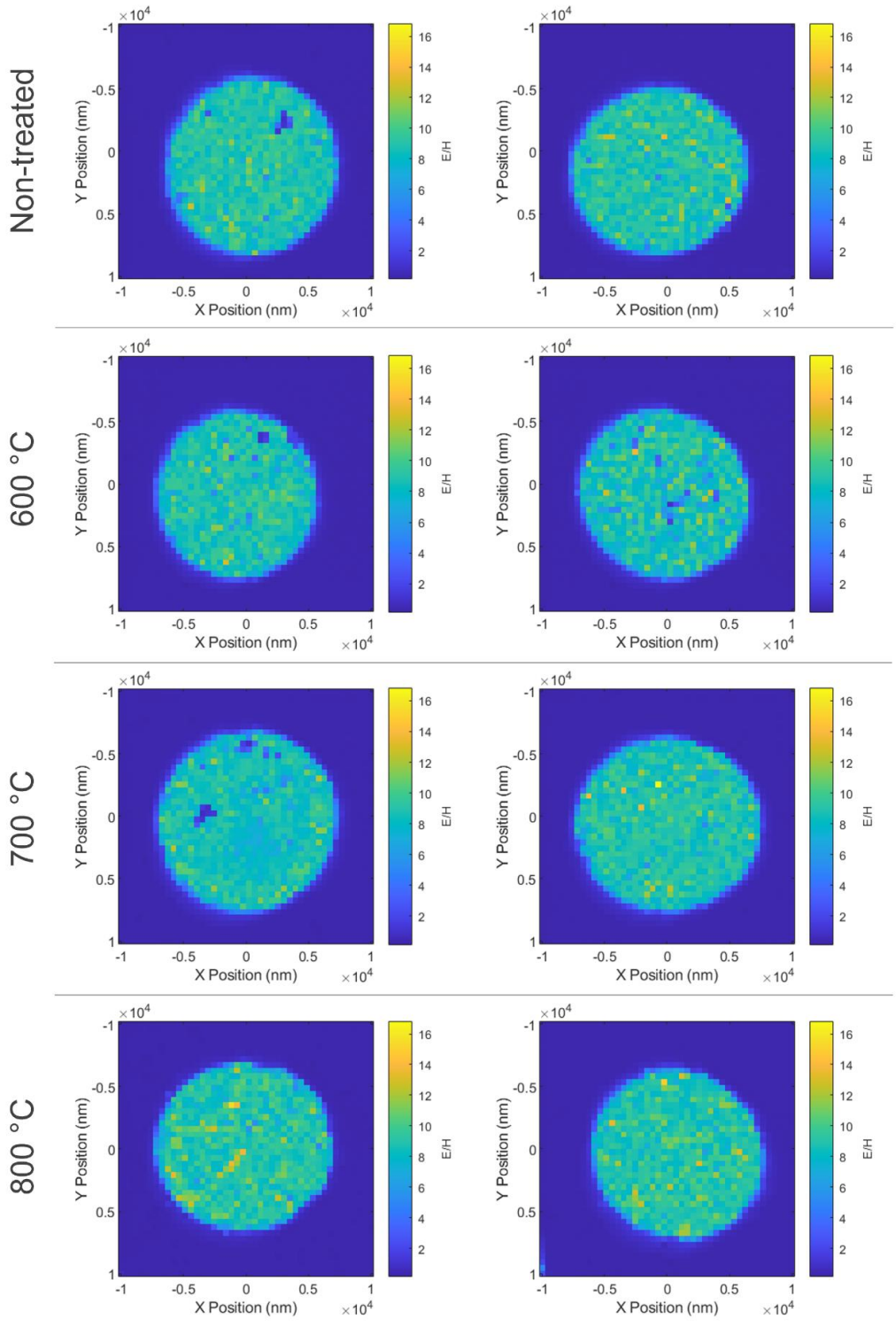

Figure 1.13 Representative high-speed nanoindentation maps for the elastic modulus over hardness ratio. The averaged values over dimensions corresponding to fabricated pillars diameters in each position used for calculation have been extracted from those values.

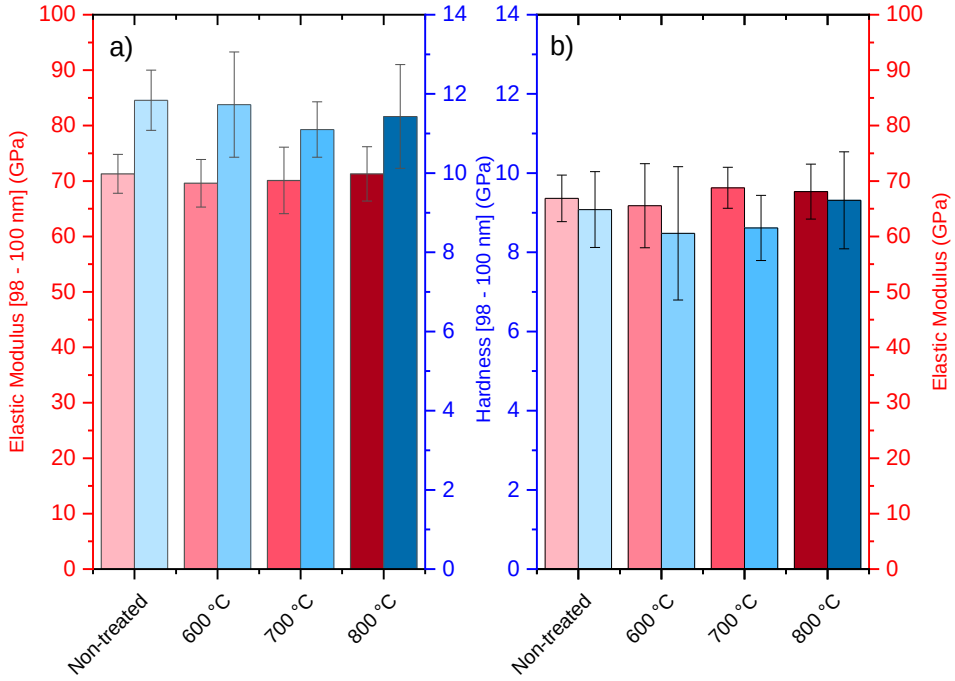

Figure 1.14 Elastic modulus and Hardness values from nanoindentation experiments as calculated from a) Continuous Stiffness Measurements averaged across multiple tests over several fibres and b) data extrapolation from multiple high-speed maps at the fibre centre (in a lateral dimension whose position corresponds to the positioning of the pillars and their diameter).

Table 1.6 Mechanical properties of the quartz fibres as a function of the thermal treatment identified via Continuous Stiffness Nanoindentation experiments.

Sample	**Elastic Modulus (GPa) [98 - 100 nm]**	**Hardness (GPa) [98 - 100 nm]**	**E/H**
Non-treated	71.30 ± 3.50	11.84 ± 0.76	6.20 ± 0.48
600 °C	69.60 ± 4.30	11.73 ± 1.33	5.93 ± 0.76
700 °C	70.10 ± 6.00	11.1 ± 0.70	6.31 ± 0.67
800 °C	71.30 ± 4.90	11.43 ± 1.31	6.23 ± 0.83

Table 1.7 Mechanical properties of the quartz fibres as a function of the thermal treatment identified via data averaging high-speed nanoindentation maps over more than two fibres in areas corresponding to the positions of the pillars (fibres centre).

Sample	Elastic Modulus (GPa)	Hardness (GPa)	E/H
Non-treated	66.9 ± 4.2	9.1 ± 0.9	7.4 ± 0.9
600 °C	65.5 ± 7.6	8.5 ± 1.7	7.7 ± 1.7
700 °C	68.8 ± 3.7	8.6 ± 0.8	8.0 ± 0.9
800 °C	68.1 ± 4.9	9.3 ± 1.2	7.3 ± 1.1

constant straining in the other—no statistically significant differences were found for the fibres as a function of heat-treatment temperature, nor for the elastic modulus or hardness values for both quasi-static (Table 1.6) and high-speed mapping (Table 1.7). These analyses at the nanoscale support the macroscopic findings from single fibre tensile tests, although the differing absolute values of Young's modulus must be attributed, also in this case, to the distinct nature of the two techniques [29].

Probability Distribution Function (PDF) deconvolutions, able to identify at least two distinct mechanical phases based on elastic modulus and hardness responses, were applied to the fibre cross-sections to gain a deeper understanding of potential gradient formation and quantify it within a statistically robust framework. As detailed in Figure 1.15, no significant differences were observed in quartz response. Although the PDF distributions were effectively reconstructed in all cases using a multivariate bi-Gaussian approach—indicating the effective presence of two phases in the mechanical response—the differences in their values and the related standard errors suggest that the identified two phases are more likely related to randomly distributed defects or localized crystalline regions rather than a consistent microstructural gradient that could alter the two populations of searched phases by more than 5%. Additionally, Figure 1.16 reports the results of the k-means clustering analysis, which identifies the position of the average and standard error values for the two mechanical phases within the fibre cross-section. The analysis indicates that no specific mechanical sub-structures were formed, reinforcing the

hypothesis that the observed clustered differences arise from randomly distributed sub-surface features.

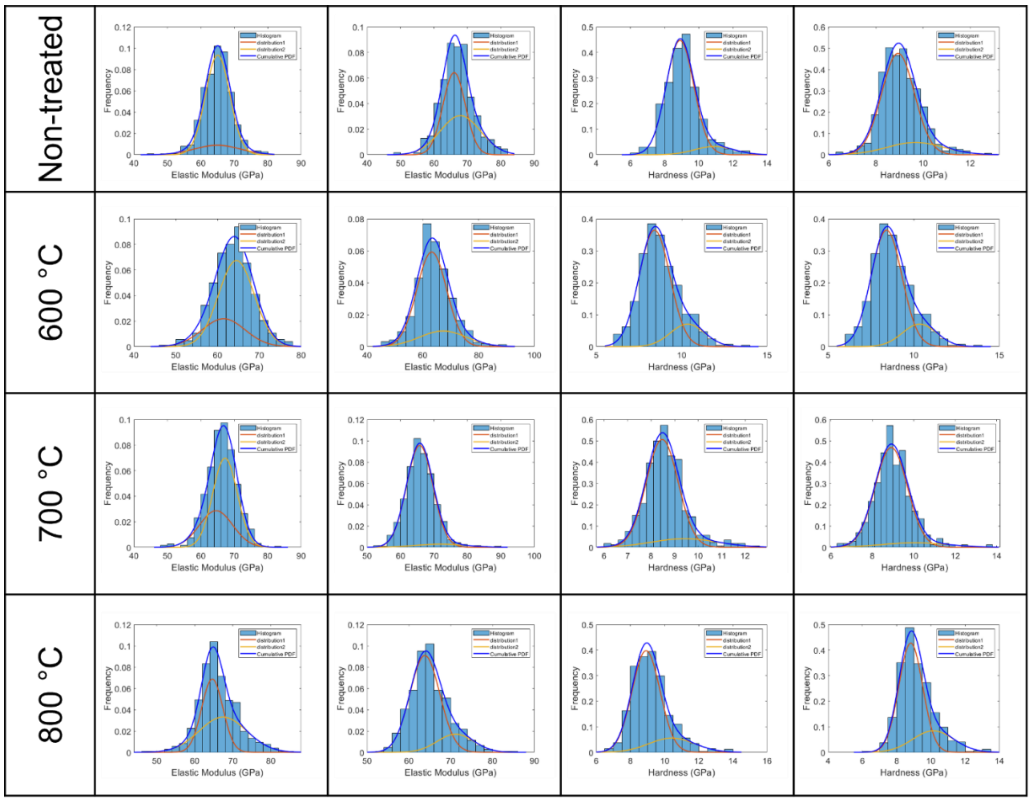

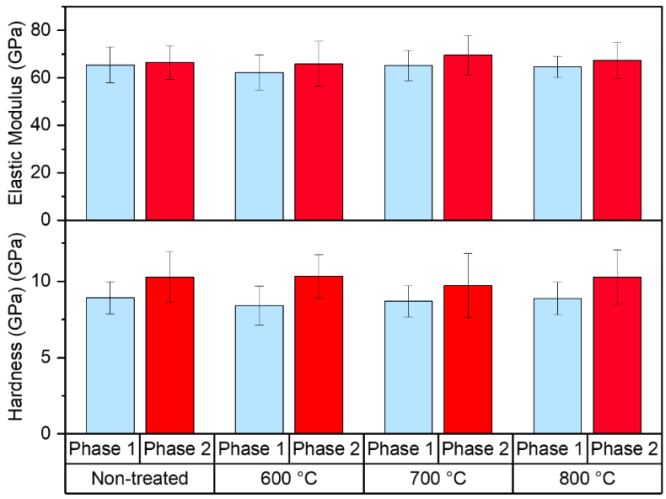

Figure 1.15 Probability Distribution Function (PDF) deconvolutions to investigate the presence of secondary mechanical phases arising from the heat treatment (due to crystalline domain formation). The analysis region has been limited to 90% of the fibre's diameter to their centre to avoid computation of matrix-fibre interface properties.

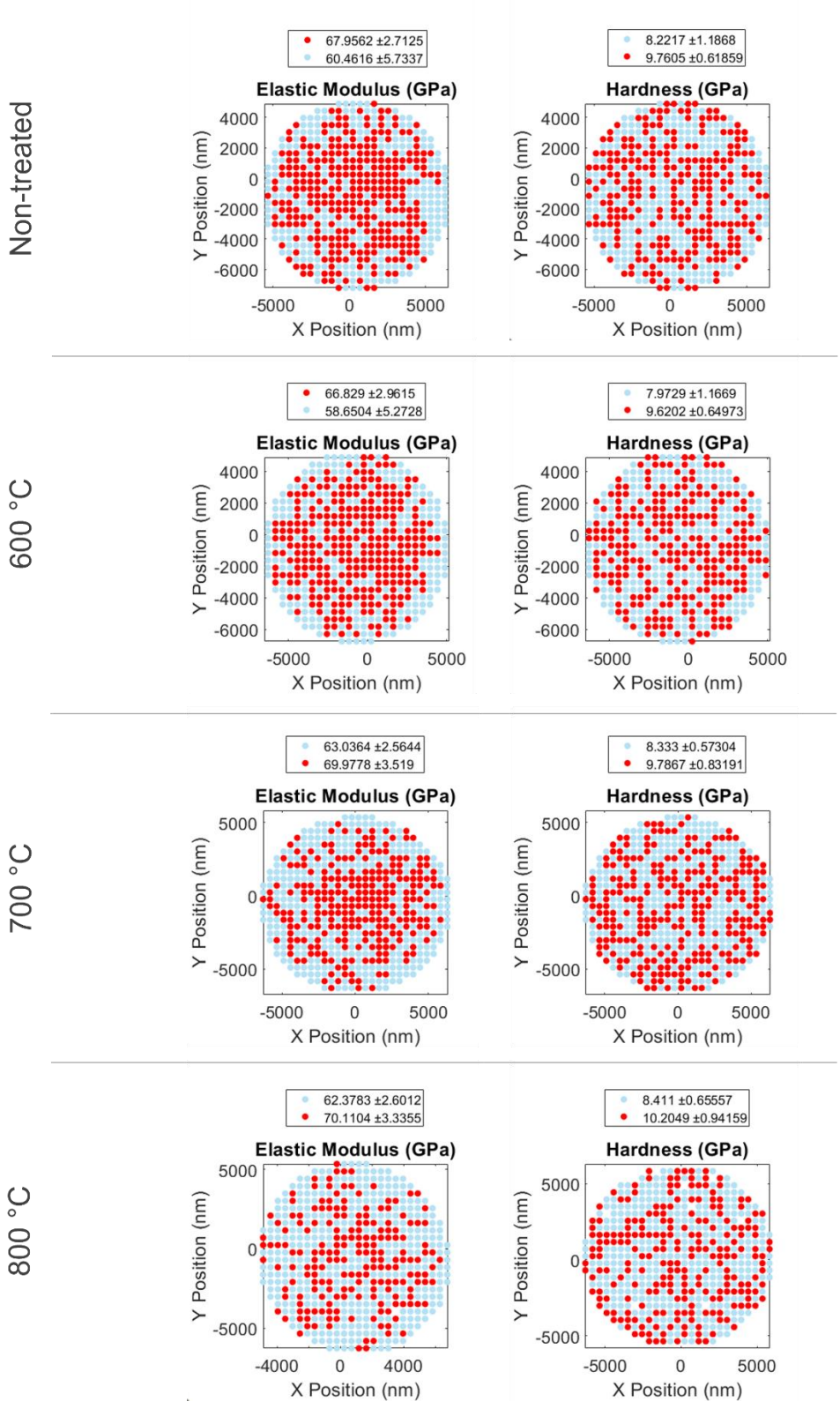

Figure 1.16 K-means clustering to study secondary phases (two targeted clusters) distributions within the fibres compared with PDF deconvolution data from Figure 1.15.

Prior to the drawing process, glass melts contain randomly oriented defects, such as striae, microbubbles, and anisotropic inhomogeneous domains, which are frozen-in in fibres during thermal quenching [112], [230]. The randomly distributed clustered values of elastic modulus and hardness observed across the cross-sections of quartz fibres, therefore, are likely to reflect these frozen-in defects. This observation still aligns with previous findings of a failure governed by surface flaws, although the bulk defects may be thought as potential sources of fracture. In fact, the axial stress applied during the drawing process promotes a preferential alignment of flaws along the fibre axis, significantly lowering the probability of fracture initiation from bulk defects. Furthermore, the long-range preferential orientation of these flaws is unlikely to be altered by thermal exposure below the glass transition temperature, as a viscous state would be needed [112]. Consequently, it is reasonable to conclude that the fibre bulk is dotted with anisotropic defects irrespective of the heat-treatment conditions, which are not expected to control the fibre failure.

To further examine the effect of thermal treatment on the bulk properties of quartz fibres, pillar-splitting experiments were performed for determining possible variation in the fracture toughness of quartz fibres from the non-treated case to the heat-treated ones. Figure 1.17 presents representative data from the Load versus Displacement-Into-Surface curves of micro-pillar splitting tests aimed at evaluating the fracture toughness of individual quartz fibres at their centre. This involved the use of both CSM and high-speed mapping data, the latter derived from specific areas at the fibre centre and having lateral dimensions equal to the diameter of the pillars. From this data, a reproducible and precise burst in the displacement could be seen for each population of fibres corresponding to the critical splitting event; its average value is seen to increase with the treatment temperature. Being the diameters equal and reproducible with each pillar and having reported no statistically significant variations in the E/H response of the fibres with temperature (as well as within the cross-sectional area: see Figure 1.13) on which the calibration coefficient γ is dependent, this directly translates into an increase of the fracture toughness values from the untreated fibres to those treated at 800 °C. Indeed, as evidenced in Figure 1.18, a statistically significant increment of ~9% exists in the K_c values for the two set of fibres (Table 1.8).

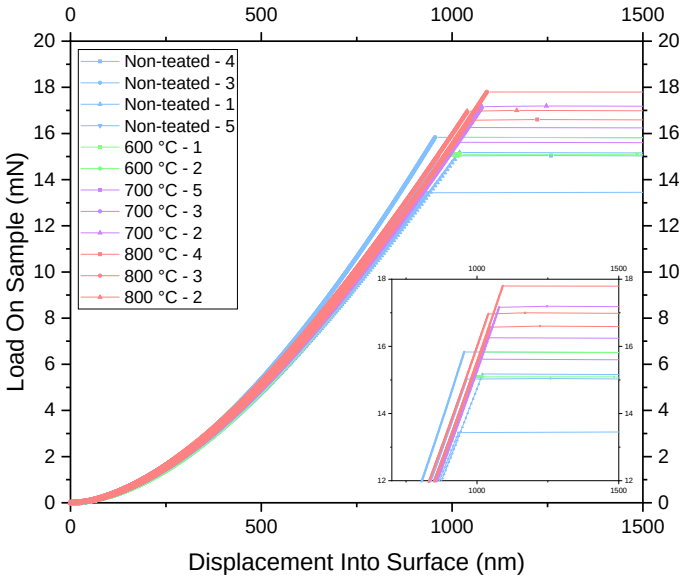

Figure 1.17 Load On Sample versus Displacement Into Surface curves corresponding to representative micro-pillar splitting experiments performed on the fibres samples. The inset magnifies differences into the pop-in event corresponding to pillar-splitting for each heat-treated population.

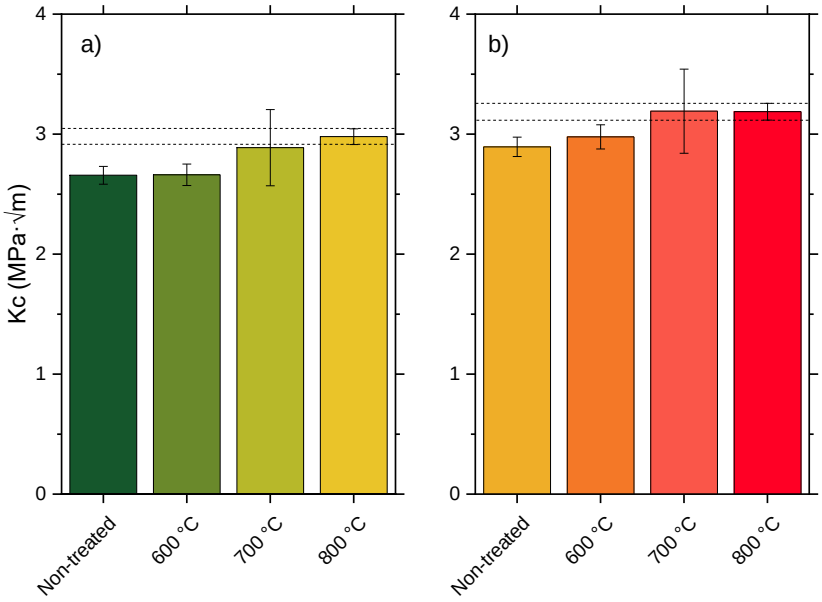

Figure 1.18 Fracture toughness as a function of the thermal treatment obtained from micro-pillar splitting experiments. Comparison between values of the γ coefficient as obtained from a) continuous stiffness measurements at the centre of the fibres and b) values obtained from high-speed data points corresponding to pillar positions at the fibre centre.

Table 1.8 Critical loads (Pc), calibration coefficients and fracture toughness values as calculated from experiments at the centre of the fibres from two evaluation procedures for the mechanical properties (i.e., Continuous Stiffness Measurements and High-speed nanoindentation mapping).

Sample	**P_c (mN)**	**γ (CSM)**	**γ (High-speed)**	$K_c\ (MPa\sqrt{m})$ CSM	$K_c\ (MPa\sqrt{m})$ High-speed
Non-treated	14.87 ± 4.19	0.501745	0.546467	2.65 ± 0.07	2.89 ± 0.08
600 °C	15.46 ± 0.52	0.498667	0.557899	2.66 ± 0.89	2.97 ± 0.10
700 °C	16.34 ± 0.77	0.511834	0.565716	2.88 ± 0.31	3.19 ± 0.35
800 °C	16.95 ± 0.37	0.509192	0.544761	2.97 ± 0.06	3.18 ± 0.06

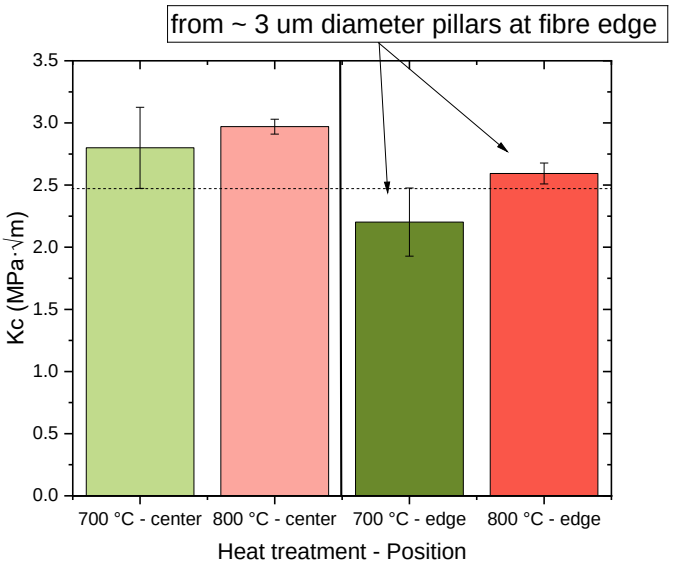

Figure 1.19 Fracture toughness trends at the fibre edge were reported compared with values from bigger pillars fabricated at the centre. The rising trend of fracture toughness with treatment temperature is consistent also for the edge of the fibres, while lower values compared to 4 μm diameter pillars depend upon increasing positioning error for lower diameters and size effects.

In contrast, Feih et al. [217] identified a unique K_c value for E-glass fibres, regardless of the heat-treatment temperature, while Lilli et al. [29] observed a consistent increase in the K_c of heat-treated basalt fibres—up to 22% of the original value—using both single-edge notch tension (SENT) and pillar-splitting methods. In both studies, possible variations in K_c serve as indicators of the occurrence or not of bulk structural modifications, which are supported by changes in Young's modulus and fibre density and, in Lilli's work, by the occurrence of structural heterogeneities across the fibre cross-section. Notably, having reported no significant changes in the material-specific coefficient γ (which pertains to the elastic-plastic properties of the material), the increase in fracture toughness measured in this study is not dependent upon specific variations of the elastic and plastic responses, relying instead on triggered modifications in the crack propagation resistance due to treatment.

Further experiments were conducted to elucidate this trend as a function of the diametral position of the probed volume (micro-pillar). Tests on micro-pillars machined at the fibre edge—where the diametral dimensions were intentionally reduced compared to those fabricated at the pillar centre to enhance the resolution—revealed a similar trend, as illustrated in Figure 1.19, showing an increase in K_c values from the 700 °C treatment to the 800 °C treatment. Although these values cannot be directly compared to those from larger diameters due to increasing positioning errors —as a function of the pillar diameter— and size effects when reducing the lateral size of a test, they still align reasonably well with the results from the centre. This observation reinforces earlier conclusions that the mechanical properties do not exhibit a significant gradient from the edge to the centre of the fibre, aside from those related to mixed indentation responses, as previously mentioned.

The temperature-dependent changes in fracture toughness indicate that quartz fibres are indeed influenced by exposure to temperatures ranging from 600 to 800 °C. This effect occurs uniformly throughout the fibre cross-section, without creating radial gradients. While further research is needed to fully understand this phenomenon, its relationship with the strength reduction is noteworthy. According to classic fracture mechanics, particularly Griffith's theory [231], a decrease in fibre strength can be due to either a

reduction in fracture toughness or an increase in the severity of flaws, whether in size or shape. Therefore, enhancing crack propagation resistance should theoretically improve the fibre tensile strength. However, the extent of the improvement in K_c measured in this work is not sufficient to compensate for the significant strength reductions observed, which may arise from extrinsic critical-sized flaws.

Considering that, in pillar-splitting experiments the critical size of the crack depends solely on its initiation under the indenter tip and unstable propagation due to pillar-edge-dominated effects. The measured material-intrinsic increase in crack propagation resistance (intrinsic for the probed pillar volume) does not contradict the findings from the other investigations included in this research. It is reasonable to assume that the mechanism primarily responsible for strength degradation is mainly active at the surface of quartz fibres, potentially involving the thermally activated growth of pre-existing flaws and the emergence of new, more severe defects.

In conclusion, although showing a strength degradation behaviour similar to general-purpose glass fibres and basalt fibres [21], [29], [37], [67], [111], [115], [217], the bulk properties of quartz fibres seem to be less affected by thermal exposure, remaining relatively stable after heat treatment up to 800 °C. The thermal-induced reduction in strength of quartz fibres can be attributed to surface-controlled mechanisms which involve the exposure and growth of inherent flaws following the loss of protective sizing, as well as the potential formation of new, more severe defects whose negative effect on the tensile strength cannot be offset by the slight improvement in crack propagation resistance. Mechanical handling damage, relaxation of structural anisotropy and water attacking, all acting at the surface of quartz fibres, are proposed as possible damage mechanisms, requiring future investigations to be verified.

Chapter 2.

Thermal and plasma assisted synthesis of CNTs

The synthesis of CNTs through chemical vapour deposition (CVD) usually requires process temperatures above 600 °C [153] which can deteriorate the mechanical properties of temperature-sensitive substrates [147], including most reinforcing fibres, such as carbon [20], glass [111] and basalt fibres [67]. In the previous chapter, a significant decay of the mechanical strength following thermal exposure above 600 °C was assessed in the case of quartz fibres. Achieving the growth of CNTs at lower temperatures, therefore, becomes of major importance to produce hierarchical quartz fibres with preserved mechanical properties for applications in high-performance structural composite materials.

To address this issue, the use of a plasma-enhanced (PE)-CVD technique is proposed in this chapter as it exploits a highly energetic plasma during the synthesis step to supply some of the energy for the chemical reactions involved in CNT growth. The morphology and structure of CNTs obtained through PE-CVD on quartz fibres are compared to the ones obtained through a conventional thermal CVD method both at high temperatures (above 600 °C) and at low temperatures (below 550 °C). Furthermore, a detailed characterization of the catalyst morphology is included and discussed in relation to the CNT morphology observed under the different process conditions. A traditional Fe-based external catalyst is used in this investigation, whereas the use of innovative catalyst systems will be introduced in the following chapter.

2.1. CNT synthesis conditions

The growth of CNTs on quartz fibres was investigated through two different CVD methods, namely a traditional thermal-based (T-CVD) synthesis and a plasma-assisted (PE-CVD) technique, with the aim of comparing them in terms of CNT morphology and lower temperature limit for the synthesis of CNTs under the adopted process conditions.

The selection of the parameters for the catalyst deposition step and CVD process was based on previous studies reporting the thermal [36], [158], [194]–[196] and PE-CVD [193] syntheses of vertically aligned (VA)-CNTs on various substrates. This particular morphology, consisting of highly dense aligned arrays of aligned CNTs, was taken as a benchmark as it represents a highly ordered organization of CNTs and is often considered as the best type of CNTs among all known forms [232], [233].

Prior to CVD synthesis, a Fe-salt catalyst precursor was deposited on the fibre surface by dip-coating in a 50 mM-solution of iron nitrate nonahydrate. The dip-coating process parameters were selected based on the works by Lilli et al. [234] and Yamamoto et al. [235], where the growth of dense VA-CNT forests was achieved on basalt and alumina fibres, respectively.

Table 2.2 Substrate temperatures measured during the annealing and synthesis step of both Fe-catalysed thermal CVD (T-CVD) and plasma enhanced CVD (PE-CVD) processes performed on quartz fibres.

Method	Annealing Temperature [°C]	Synthesis Temperature [°C]
T-CVD	620	640
PE-CVD	620	640
T-CVD	520	640
T-CVD	520	540
PE-CVD	520	540

As-coated fibres were then subjected to a two stage CVD process: (i) firstly, the fibre samples were annealed in hydrogen atmosphere with the twofold aim of reducing the catalyst precursor to its active metallic state and triggering the de-wetting of the catalyst film and the nucleation of iron-based nanoparticles working as a template for subsequent CNT growth [236]; (ii) afterwards, the actual CNT synthesis (or growth) step was performed with acetylene as a carbon source. The process parameters used for each step in the case of thermal and plasma-enhanced CVD, i.e., the duration, flow rates, partial pressures of gases and plasma power, are detailed in section 2.2 of Part II – Materials and Methods. The temperatures selected for each step and CVD process are detailed here-in

and summarized in Table 2.2. It is worth noting that, as one of the main purposes of this research work is to mitigate the effects of temperature on the substrate, the reported values refer to the temperature experienced by the substrate during the process, measured with a thermocouple as described in section 2.2 of Part II – Materials and Methods. In the following discussion, each process will be referred as: "METHOD" followed by "annealing temperature/synthesis temperature", e.g., T-CVD 620/640 °C.

As a benchmark for the CVD growth on quartz fibres, a well-established thermal CVD process was performed on dip-coated fibres at temperatures above 600 °C (T-CVD 620-640°C). This synthesis protocol, optimized for the Fe-catalysed growth of vertically-aligned (VA)-CNTs on silicon and fused silica flat substrates [149], [158], [237] at the Sapienza-INFN CVD facility, was previously adopted for the growth of VA-CNT forests on basalt fabrics [36]. Afterwards, a PE-CVD process was carried out at the same process temperatures (PE-CVD 620-640 °C) under the process conditions optimized by Yadav et al. [193] to highlight the effect of plasma on the resulting CNT morphology. It is worth noting that the plasma assistance was introduced only during the synthesis step, while a thermal annealing was adopted for all the CVD processes. Therefore, although the presence of plasma during the synthesis is expected to allow a reduction in the synthesis temperature by providing part of the energy for the decomposition of the carbon feedstock and CNT growth, the formation of correctly sized catalyst nanoparticles during the annealing stage remains an essential condition for CNT growth and depends on the temperature of the substrate surface [147]. Therefore, to investigate a lower temperature synthesis through thermal and PE-CVD, the annealing temperature was first reduced to 520 °C and the catalyst morphology after this step was investigated and compared to the one obtained at 620 °C. Afterwards, the catalyst template produced at 520 °C was subjected to a thermal CNT growth at 640 °C (T-CVD 520-640 °C) under the same synthesis conditions found effective for the higher temperature annealing to verify its suitability for the synthesis of CNTs. Once demonstrated that lowering the annealing temperature to 520 °C can still lead to the synthesis of CNTs, the synthesis temperature was reduced to 540 °C and both thermal (T-CVD 520-540 °C) and plasma assisted (PE-CVD 520-540 °C) syntheses were carried out at temperatures below 550 °C.

2.2. Morphological characterization of CNT-modified fibres

A detailed morphological analysis was conducted on quartz fibres subjected to the different CVD growth treatments. Scanning electron microscopy (SEM), transmission electron microscopy (TEM) and Raman spectroscopy were used to compare the effects of different CVD methods and process temperatures in terms of CNT arrangement and coverage density on the fibre surface as well as length, diameter, growth mechanism and structural quality of the obtained CNTs.

Figure 2.11 reports representative micrographs from the SEM investigation carried out on quartz fibres following CVD at high temperatures (T-CVD 620/640 °C and PE-CVD 620/640 °C). An abundant coverage of the fibre surface with long (up to 80 μm) arrays of aligned CNTs was achieved after T-CVD 620/640 °C. This outcome confirms the transferability of the selected synthesis protocol, previously optimized for the synthesis of VA-CNTs on silicon and silica flat substrates and on basalt fibres, to substrates of different materials (silicon, silica, basalt) and geometry (flat substrates or fibres). The growth of CNTs on quartz fibres was previously reported in the work by Jin et al. [238], where short CNTs with a radial orientation were synthesized in the temperature range 600-750 °C. Long VA-CNTs forests were grown on quartz fibres for the first time by De Luca et al. [223] using a Fe-Ni catalyst system. They observed that a prolonged dwell time in the synthesis zone of the furnace at 760 °C (up to 30 minutes) led to the growth of longer CNTs organized in a so-called Mohawk morphology, while a shorter dwell time produced a uniform 200 nm-thick carpet of CNTs. The splayed Mohawk arrangement, in which a single fibre features two or more arrays of VA-CNTs oriented perpendicularly to its surface, is typical of substrates of similar geometry [232], [235]. During the growth, CNTs are forced to grow perpendicularly to the substrate surface due to proximity (also known as crowding) effects generated by Van der Waals interactions between nearby CNTs. This growth mechanism leads to the formation of uniform VA-CNT carpets on flat surfaces [149], [158], [237] whereas on fibre substrates the growth proceeds with a radial orientation until CNTs become longer than the fibre diameter and van der Waals interactions among nearby CNTs split them into two or more arrays, generating a typical Mohawk morphology [232], [235].

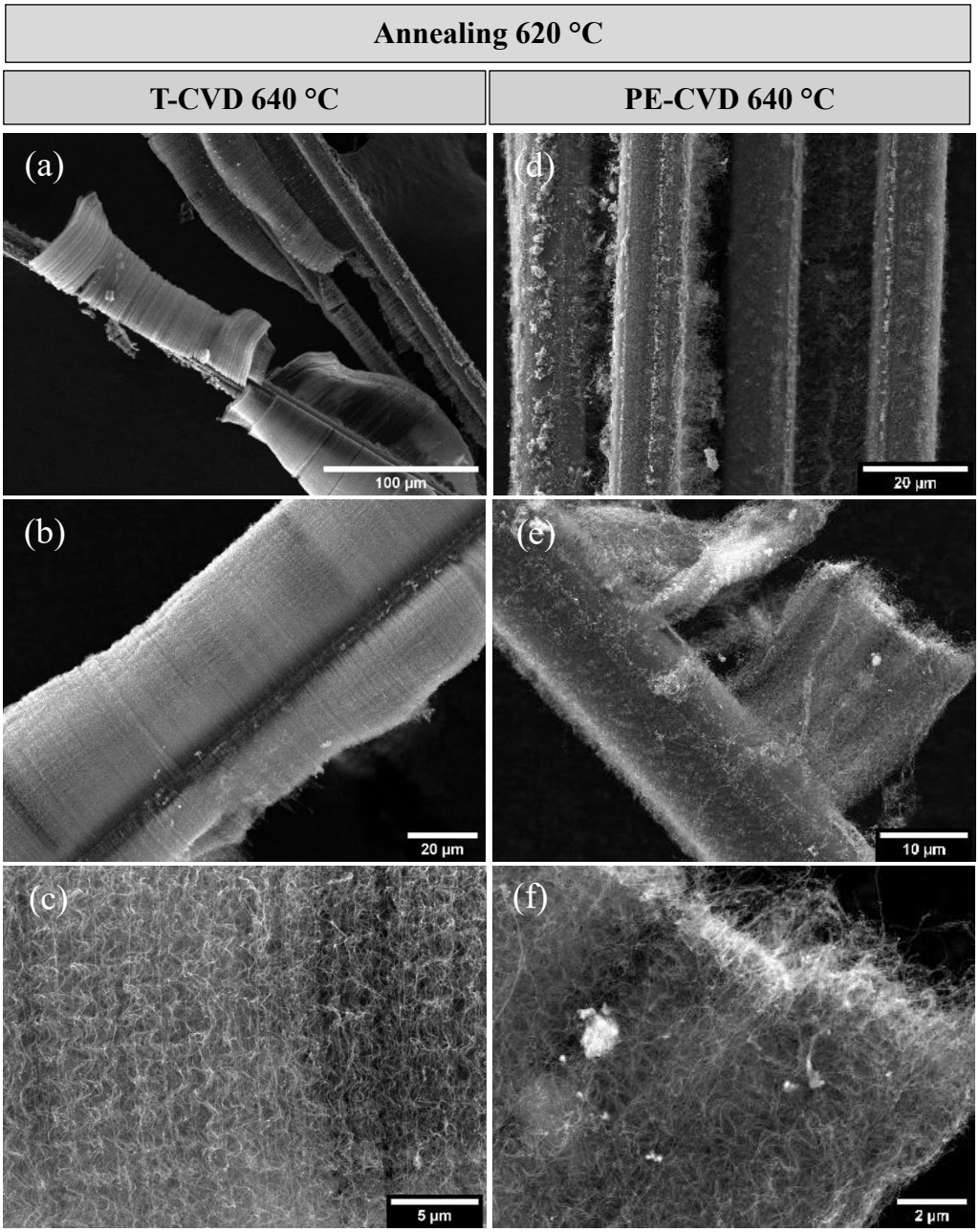

Figure 2.11 SEM micrographs at different magnifications of CNTs grown on quartz fibre surface through annealing at 620 °C and growth at 640 °C: (a, b, c) T-CVD; (d, e, f) PE-CVD.

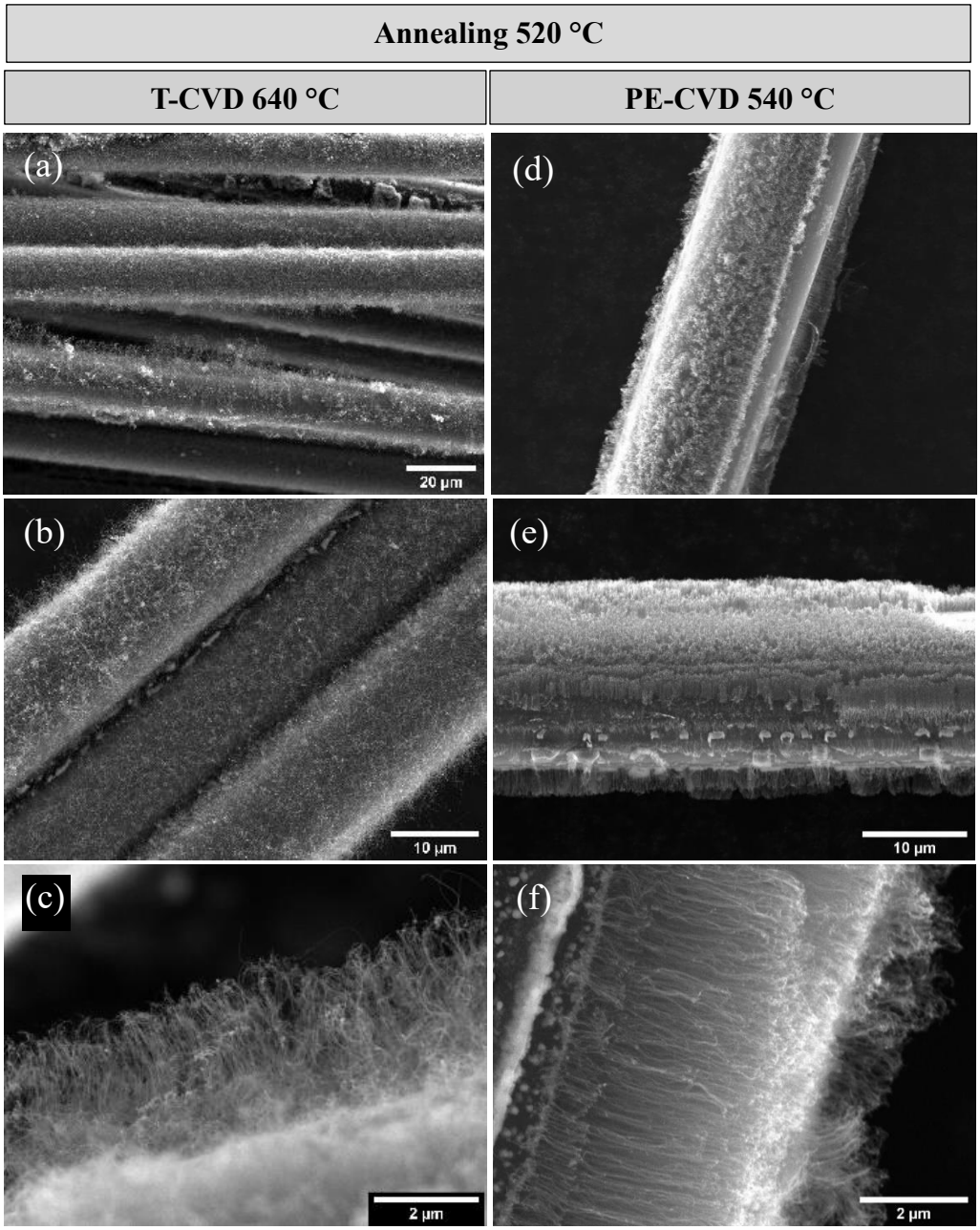

Figure 2.12 SEM micrographs at different magnifications of CNTs grown on quartz fibre surface through annealing at 520 °C and: (a, b, c) growth at 640 °C via thermal CVD; (d, e, f) growth at 540 °C via PECVD.

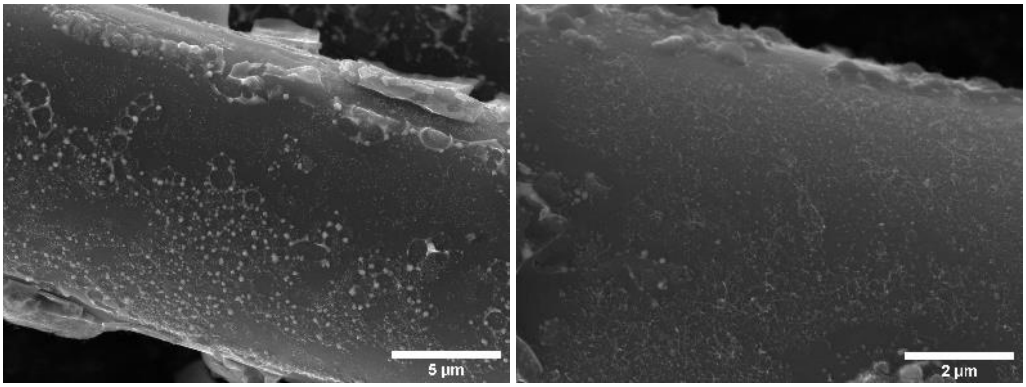

Figure 2.13 SEM micrographs detailing the surface morphology of quartz fibre after annealing at 520 °C and growth at 540 °C via thermal CVD.

As shown in Figure 2.11d-f, a more disordered and less homogeneous morphology was obtained through the PE-CVD 620/640 °C process, with fibres covered either by CNT forests or shorter randomly oriented CNTs. Unlike the CNT arrays grown through the thermal process, the CNT arrays grown by PE-CVD were much shorter, reaching a maximum of 20 µm. The process parameters of this process were selected based on the work by Yadav et al. [193] for the growth of VA-CNTs on Si wafers through PE-CVD. Similarly to this work, Yadav et al. [193] observed a shorter length compared to that of the thermal CVD synthesis which explained with the significantly lower flow rate of hydrocarbon gas (18 sccm compared to the 300 sccm of the thermal synthesis) resulting from the optimization of the process parameters in the PE-CVD synthesis step at a plasma power of 50 W. This explanation could apply also for the present work as the same flow rates as those used by Yadav et al. [193] were used both in the case of the thermal and the PE-CVD syntheses. Another possible explanation can be found in the lower growth rate caused by plasma etching during the PE-CVD synthesis [239], [240]. In fact, it is important to note that plasma is usually employed for both the deposition of thin conformal films and for etching, depending on the choice of conditions. Counterintuitively, in order to deposit carbon nanostructures a PE-CVD reactor must be operated in the etching, rather than deposition, regime to avoid thin-film formation and consequent catalyst poisoning. The competition between nanotube growth versus etching therefore must be taken into account as an additional factor compared to thermal CVD which affects the growth rate and, thus, the final length of as-grown CNTs.

To investigate the opportunity of reducing the process temperature, a thermal process was first performed with an annealing temperature of 520 °C while the synthesis temperature was kept at 640 °C (T-CVD 520/640 °C). The rationale for this process was to verify the formation of a suitable distribution of correctly sized catalyst nanoparticles at 520 °C which could effectively act as a template for the growth of CNTs. The abundant coverage of CNTs obtained through the T-CVD 520/640 °C process, displayed in Figure 2.12a-c, confirmed this hypothesis, demonstrating the possibility of growing CNTs on a Fe catalyst layer annealed at 520 °C. The CNTs grown through T-CVD 520/640 °C did not show any Mohawk arrangement, being shorter than the previous samples (up to 3 μm) and with a random orientation.

When the growth temperature is reduced to 540 °C (T-CVD 520-540 °C), the thermal growth of CNTs is no longer achievable, except for sparse CNT sprouts surrounded by large catalyst islands (Figure 2.13), confirming the well-known temperature limit of conventional thermal Fe-catalysed CVD.

On the other hand, a well-organized morphology of radially aligned CNTs was obtained through low-temperature PE-CVD (PE-CVD 520/540 °C), as displayed in Figure 2.12. This outcome confirms PE-CVD as an effective technique for achieving CNT growth at temperatures below 550 °C, thus mitigating the thermal conditions to which the substrate is exposed during the process. Short CNTs with a length fluctuating from 1 to 3 μm were obtained, probably due to the combination of low temperature and the above-mentioned low acetylene flow rate optimized in the PE-CVD process. Contrarily to the curly and highly entangled CNTs grown through the other processes, CNTs produced by PE-CVD 520/540 °C appear to be straight and well aligned, with a low tortuosity of the single tubes, in accordance with the findings by Yadav et al. [193].

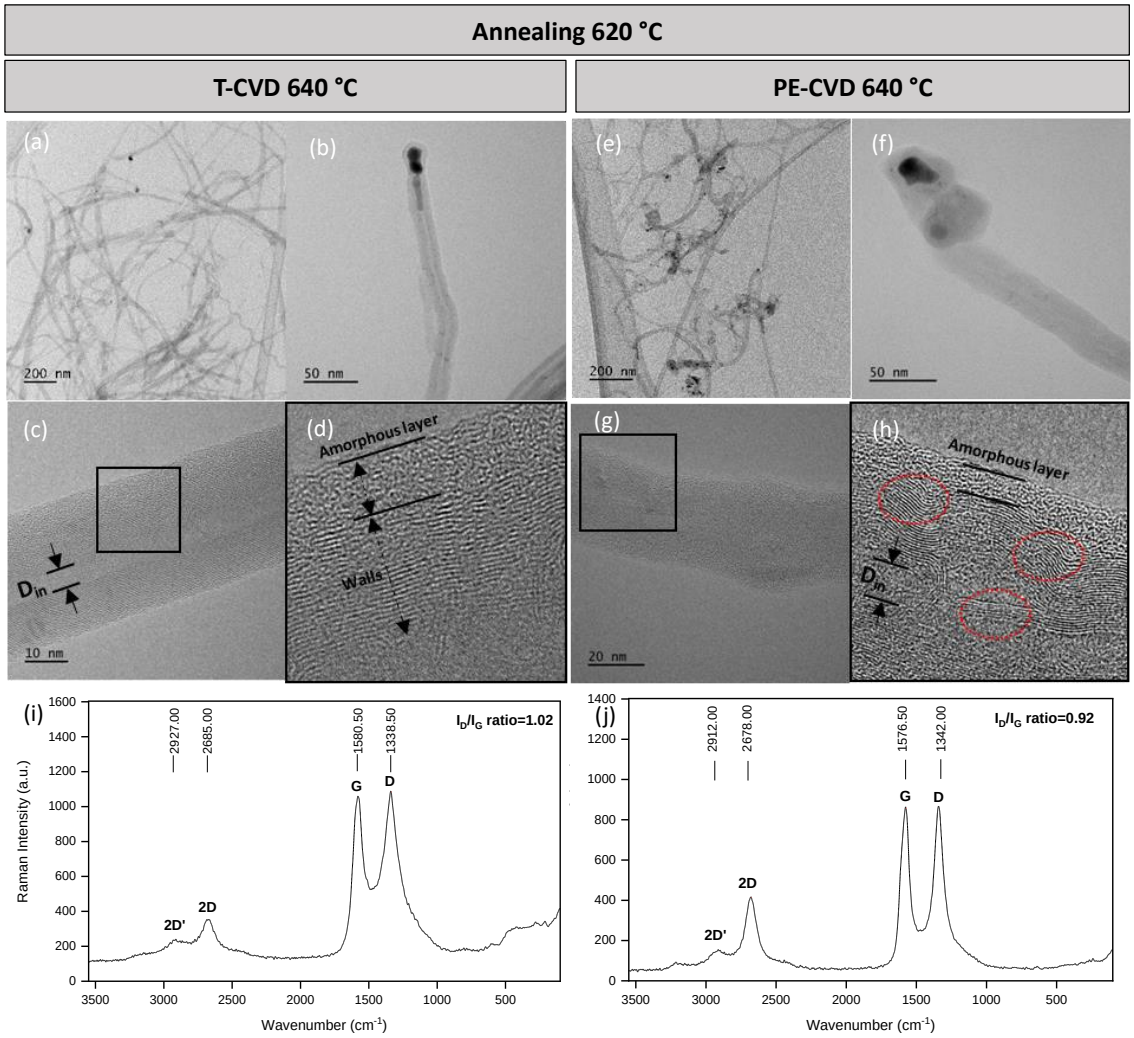

Figure 2.14 (a-h) Bright field (BF) TEM micrographs at different magnification of multi-walled CNTs (MWCNTs) grown at high temperature on quartz fibres (annealing at 620 °C and growth at 640 °C): (a-d) T-CVD; (e-h) PE-CVD. Raman spectra for quartz fibres decorated with MWCNTs grown by (i) T-CVD and (j) PE-CVD. 2D-peaks, G-peaks, D-peaks and corresponding I_D to I_G ratios are included.

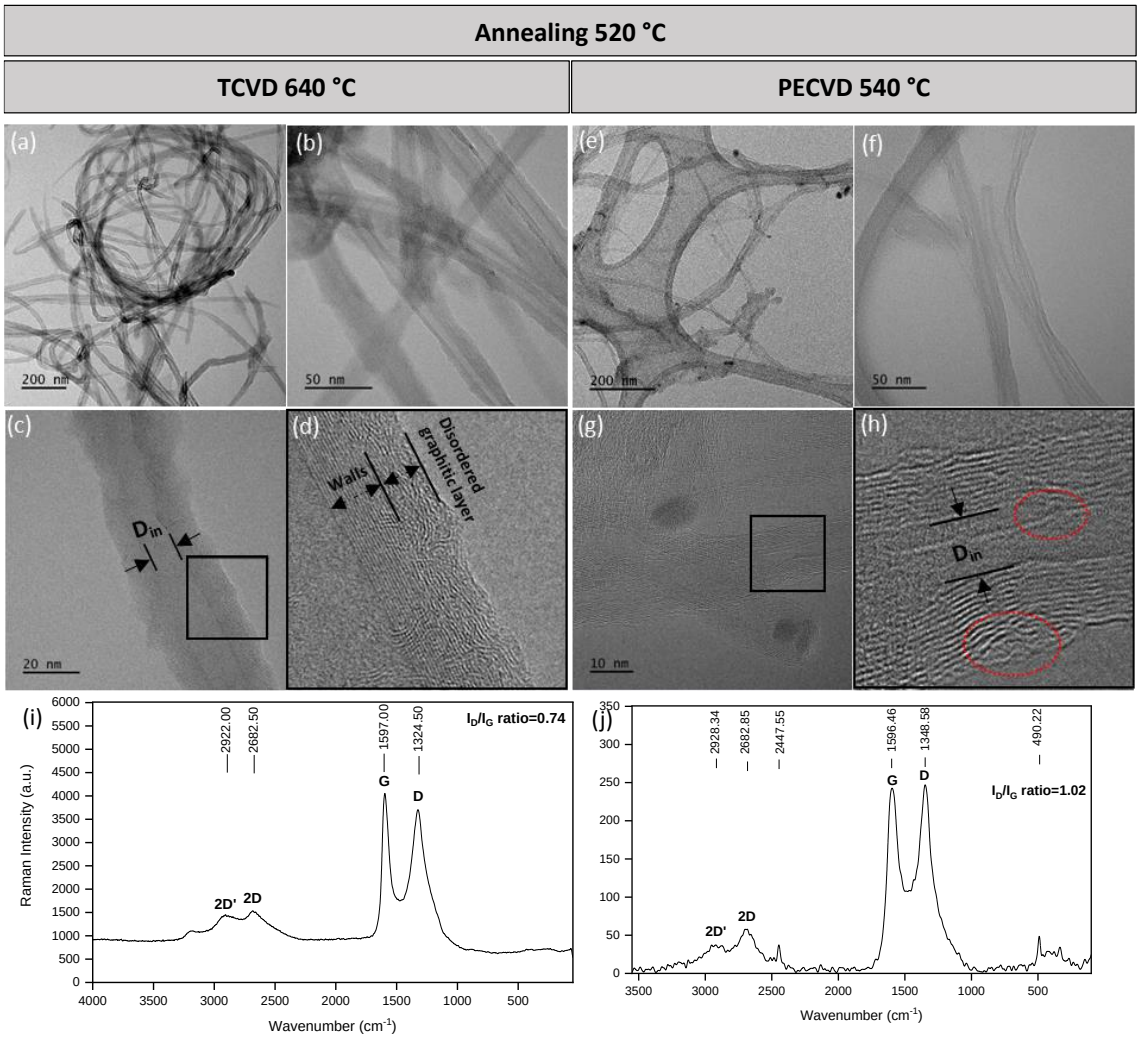

Figure 2.15 (a-h) BF TEM micrographs at different magnification of multi-walled CNTs (MWCNTs) grown on quartz fibres following low temperature annealing (520 °C for 4 minutes) and growth through: (a-d) T-CVD at 640 °C; (e-h) PE-CVD at 540 °C. Raman spectra for quartz fibres decorated with MWCNTs grown by (i) T-CVD and (j) PE-CVD. 2D-peaks, G-peaks, D-peaks and corresponding I_D to I_G ratios are included.

The morphology and structure of individual CNTs produced by the different CVD processes were analysed by TEM after dispersion in isopropanol and ultrasonication. TEM micrographs (Figure 2.14 and Figure 2.15) show the formation of multi-walled carbon nanotubes (MWCNTs) for all samples, with average diameters around 20 nm for CNTs synthesized at 640 °C, i.e., T-CVD 620/640 °C, PE-CVD 620/640 °C, T-CVD 520/640 °C, regardless of the annealing temperature (Table 2.3). Contrarily, MWCNTs

with smaller outer diameters (12 nm) were produced through PE-CVD 520/540 °C (Figure 2.15e-h). The average diameter of CNTs was found to correspond to the measured average size of iron nanoparticles seeding the growth (Table 2.3). The existence of a correlation between the size of the catalyst nanoparticles and the CNT diameter is widely accepted in the literature [152], [156]. Therefore, information about the size distribution and size uniformity of the catalyst nanoparticles can be deduced from the diameter distribution of as-grown CNTs. By looking at the standard deviations of the measured CNT diameters, it can be assumed that, despite the comparable average diameters produced through high temperature syntheses (i.e., T-CVD 620/640 °C, PE-CVD 620/640 °C and T-CVD 520/640 °C), the wider distribution of CNT diameters produced through PE-CVD 620/640 °C and T-CVD 520/640 °C reveals a non-uniform size of Fe nanoparticles seeding the growth. Similarly, although CNTs with smaller outer diameters are produced through PE-CVD 520/540 °C, the relatively large scatter of values suggests the presence of non-uniformly sized nucleation sites. A detailed investigation of the catalyst morphology after the dip-coating, annealing and growth step is included in section 2.3.

Table 2.3 Properties of individual MWCNTs grown on quartz fibres at different synthesis conditions: outer diameter, D_{out}, inner diameter, D_{in}, outer/inner diameter ratio, D_{out}/D_{in}, Fe nanoparticle maximum size, D_1, Fe nanoparticle minimum size, D_2. Each property is measured from TEM micrographs on at least 40 tubes and reported in terms of average value (standard deviation).

Annealing Temperature [°C]	**Growth Temperature [°C]**	**Growth method**	**D_{out} [nm]**	**D_{in} [nm]**	**D_{out}/D_{in}**	**Fe nanoparticle D_1 [nm]**	**Fe nanoparticle D_2 [nm]**
620	640	T-CVD	19.2 (4.8)	5.5 (2.0)	3.7 (1.0)	20.9 (9.2)	13.3 (4.4)
		PE-CVD	19.8 (8.3)	5.6 (2.2)	4.5 (3.4)	18.2 (9.4)	12.4 (5.6)
520	640	T-CVD	20.9 (6.8)	7.4 (1.7)	2.8 (0.9)	19.1 (3.9)	12.6 (5.5)
	540	PE-CVD	12.2 (4.5)	4.5 (2.2)	2.8 (0.8)	13.7 (7.3)	9.0 (4.0)

Based on the location of the nanoparticle inside the tube, i.e., either at the tip or at the bottom of the CNT, it is possible to distinguish the CNT growth mechanism, as the catalyst nanoparticle can be either lifted with the growing nanotube (tip-growth mechanism) or remain attached to the substrate during the synthesis (base-growth mechanism) [153]. Catalyst nanoparticles were mostly seen at the tip of CNTs for all investigated samples, revealing that a tip-growth mechanism was the predominant mechanism for CNT growth irrespective of the synthesis method (i.e., thermal or plasma assisted) and process temperatures. Particularly, as a tip-growth mechanism was detected for both thermal and plasma assisted CVD at the same process temperatures (i.e., T-CVD 620/640 °C, PE-CVD 620/640 °C), it can be concluded that a change in the synthesis method did not change the growth mode, which is more strictly related to the adhesion with catalyst and substrate [153], the catalyst nanoparticle size [241], or the variation of the process parameters, including the plasma power [242].

In addition to the presence of catalyst nanoparticles at the tip of CNTs, longer column-like iron particles were often found in the cavities of CNTs, as previously observed for CNTs grown on basalt fibres by Sarasini et al. [36]. This can be ascribed to the forces exerted by the walls of the growing nanotube, which might deform the catalyst particle and even arrest its lifting [163]. Interestingly, this phenomenon was more often observed for CNTs grown with high-temperature annealing, particularly following PE-CVD 620/640 °C. This seems to relate to the higher average outer diameter/inner diameter ratio (Table 2.3), as a narrower core is expected to exert stronger forces on the catalyst particles during the growth, thus favouring the encapsulation of the catalyst along the tube. On the other hand, CNTs grown with low-temperature annealing (T-CVD 520/640 °C and PE-CVD 520/540 °C) showed hollow cavities with the catalyst found mainly at the tip, corresponding to an outer/inner diameter ratio much lower than the one obtained after T-CVD and PE-CVD at 620/640 °C.

As regards the CNT structural quality, the Raman spectra of quartz fibres after thermal CVD and PE-CVD at high temperature (620-640 °C) are shown in Figure 2.14i-j. The observed spectral features, typical of most graphite-like (sp^2) carbon materials, include a mode around 1580 cm^{-1} (G-band), which is related to the graphitization of the sample, a

defect-induced mode around (D-band), and two second-order modes of lower intensity (2D and 2D') at around 2700 cm^{-1} and 2900 cm^{-1} [243], respectively. The values (around 0.9-1.0) of the intensity ratio between the D and G bands (I_D/I_G) indicate a relatively low graphitic ordering [244], as supported by the TEM observation of defect-rich CNTs and of the presence of an amorphous carbon layer covering the tubes (Figure 2.14), which contributes to increase the intensity of the D-band and broadens the peaks [213]. In addition, the value of the I_D/I_G ratio can be used to determine the size L_a of a nanocrystal with ordered sp^2 C-C bonds [245], which was estimated to be around 12 Å for both samples.

The Raman spectra for the CNT-decorated fibres after the low-temperature syntheses (T-CVD 520-640 °C and PE-CVD 520-540 °C) show similar features to the high-temperature processes, with a value of the I_D/I_G ratio equal to 1.02 for the PE-CVD 520-540 °C process and to 0.74 for the T-CVD 520-640 °C case (Figure 2.15i-j). The values of the I_D/I_G ratio for the samples investigated in this work compares quite favourably with the ones reported by De Luca et al. [223], ranging from 0.73 to 0.90, for CNTs grown on quartz fibres via thermal CVD at 760 °C. It is worth noting that the presence of amorphous carbon, being a mixture of sp^3, sp^2, and sp^1 sites, contributes to the D-band, making it difficult to interpret the reduction in the I_D/I_G ratio of the T-CVD 520-640 °C sample as a change in the defect density of the CNTs [244]. The TEM investigation (Figure 2.15) provides further information, showing well-graphitized but highly defective CNTs that, unlike the other samples, are no longer covered by amorphous carbon, but by disordered graphitic layers. Due to the lower I_D/I_G ratio, the in-plane crystallite size L_a of the T-CVD 520-640 °C sample was calculated as 10.9 Å, while for the PE-CVD 520-540 °C case it was around 12 Å, similarly to the samples following the high-temperature CVD processes.

2.3. Catalyst morphology

The morphology of the catalyst on the substrate surface is known to play an important role in the synthesis of CNTs, determining whether the growth is possible and influencing the resulting CNT morphology [153], [156]. In sight of this, the evolution of the catalyst

morphology on quartz fibre surface was investigated after each step of the synthesis process, i.e. catalyst pre-deposition by dip-coating, H_2-annealing pre-treatment, and CNT growth. SEM, energy dispersive spectroscopy (EDS), atomic force microscopy (AFM), TEM, scanning transmission electron microscopy (STEM) and electron energy loss spectroscopy (EELS) analyses were performed to disclose possible catalyst-related mechanisms behind the CNT morphologies observed under the different process conditions.

Figure 2.16 shows the surface morphology of dip-coated quartz fibres investigated through simultaneous SEM and EDS analyses. Abundant deposition was achieved in the form of clusters, with a morphology comparing quite favourably with the one observed in the reference studies [234], [235].

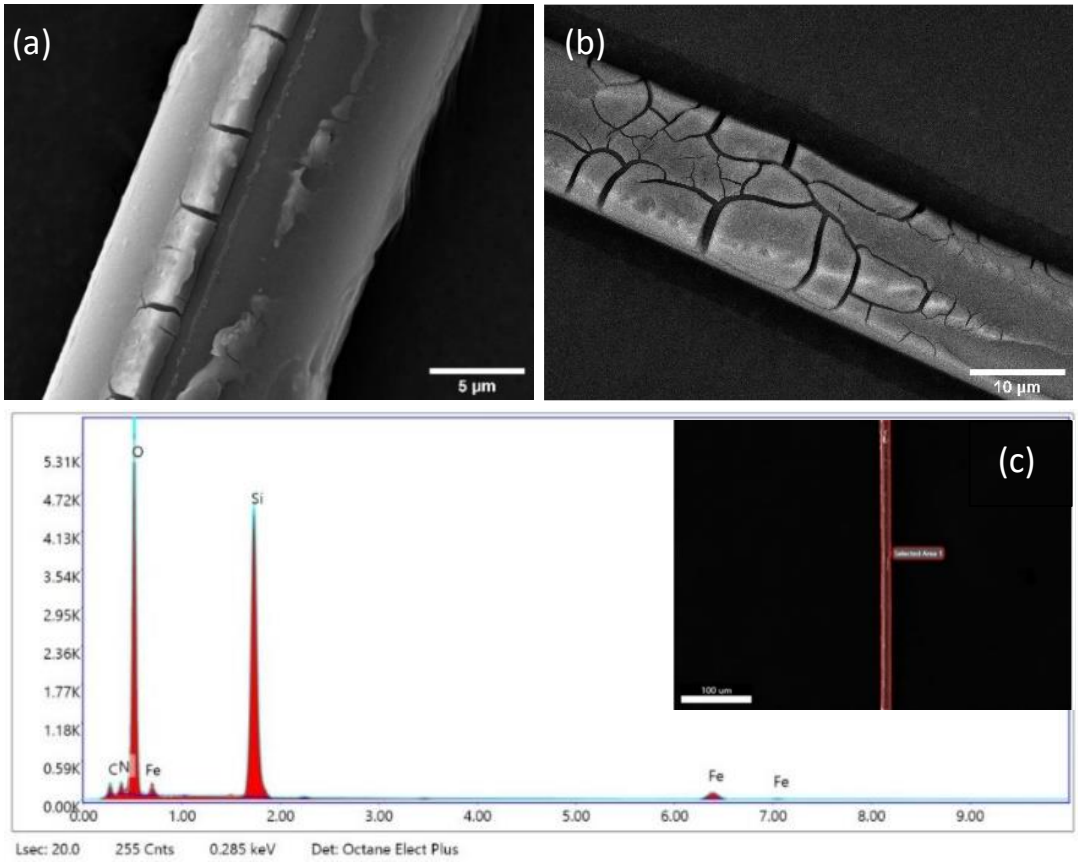

Figure 2.16 (a, b) SEM micrographs of dip-coated quartz fibres; (c) EDS spectrum for a portion of a dip-coated quartz fibre displayed on the right-hand side.

SEM (Figure 2.17a) and AFM investigations (Figure 2.18a,b and Figure 2.19a) of the fibre surface after the annealing step at 620 °C reveal the formation of a dense and homogeneous distribution of catalyst nanoparticles. This catalyst morphology is directly related to the observed alignment of CNTs in forests following T-CVD 620/640 °C, as a sufficiently dense distribution of uniformly sized nucleation sites is a necessary condition for generating proximity effects which guide the growth in a common direction [232], [233], as previously discussed. In the case of PE-CVD 620/640 °C, the growth of VA-CNT forests occurs only in some portions of the fibre surface, while other regions feature randomly oriented CNTs. A similar morphology was attributed by Yamamoto et al. [235] to the coarsening of evenly distributed catalyst nanoparticles into larger size clusters after long annealing durations, with consequent non-uniformity and diminution of nanoparticle density. As reported by Amama et al. [246], the coarsening of catalyst nanoparticles can take place not only during the annealing step, but also during the growth. The occurrence of coarsening phenomena is supported by the larger scatter of diameters of CNTs synthesized through PE-CVD 620/640 °C compared to the thermal counterpart. These phenomena might be related to the higher energy input which, analogously to the exposure to higher temperatures [247], enhanced the mobility of nanoparticles promoting the diffusion of atoms from small to large particles or even the coalescence of whole nanoparticles to form new bigger ones [248].

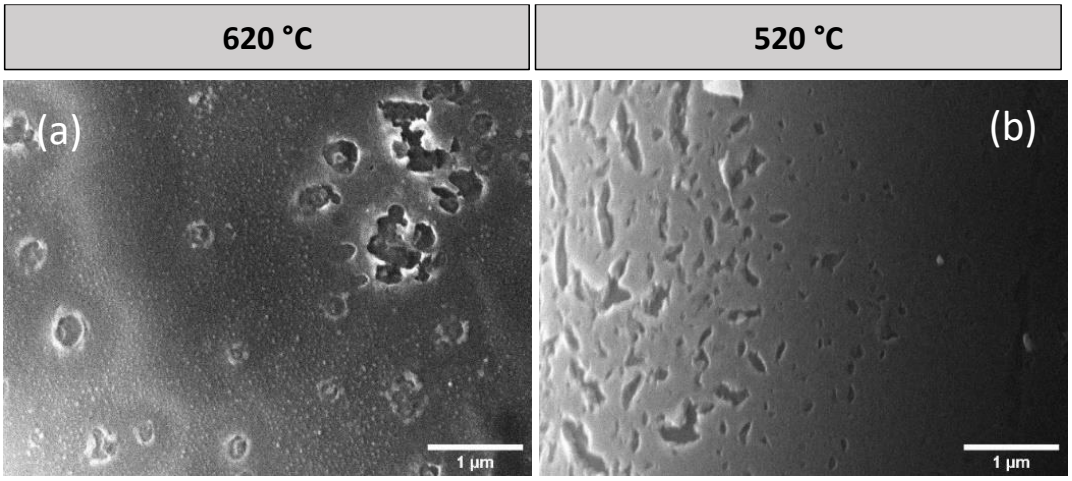

Figure 2.17 SEM micrographs of quartz fibre surface after the 4-min annealing step in hydrogen atmosphere at (a) 620 °C and (b) 520 °C.

As opposed to the higher temperature annealing, SEM investigation after annealing at 520 °C showed no obvious formation of catalyst nanoparticles, with the fibre surface mainly covered by an almost continuous layer of iron (Figure 2.17b). The discontinuities in the catalyst film seem to suggest that the low-temperature annealing led only to the beginning of Fe film instability which eventually causes the restructuring into catalyst islands driven by a decrease in free energy due the weak interaction between Fe and the SiO_2 substrate [249]. AFM investigation (Figure 2.18c,d and Figure 2.19b) provided further details on the catalyst morphology revealing that, in fact, the de-wetting of the catalyst film began at 520 °C, leading to the formation of sparse and unevenly distributed nanoparticles. Furthermore, AFM data analysis revealed a slight reduction in the surface roughness values compared to fibres annealed at 620 °C (Table 2.4).

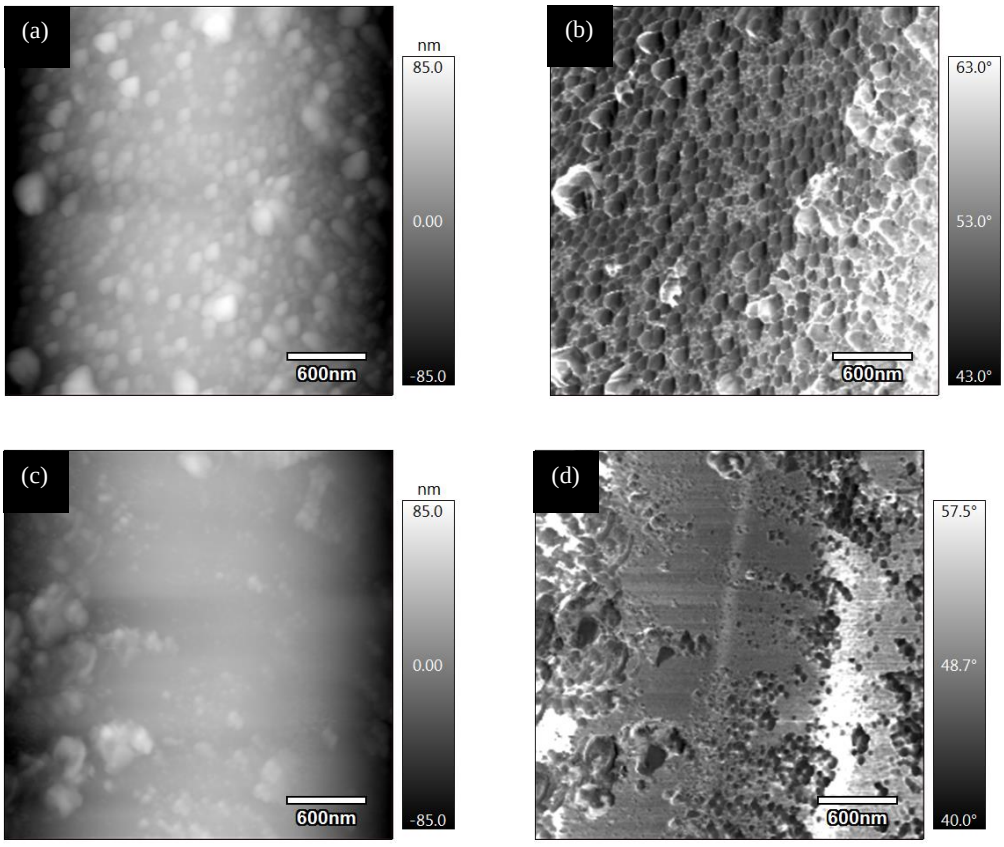

Figure 2.18 (a, c) AFM-topography and (b, d) AFM-phase images of quartz fibres after the 4-min annealing step in hydrogen atmosphere at (a,b) 620 °C and (c,d) 520 °C.

Table 2.4 Roughness measurements for annealed quartz fibres in terms of average values (standard deviations).

Annealing Temperature (°C)	**RMS roughness [nm]**	**Mean roughness (arithmetic) [nm]**	**Maximum peak height [nm]**	**Maximum peak depth [nm]**
620	10.7 (2.2)	6.9 (1.4)	86.1 (24.5)	-29.3 (-10.0)
520	8.9 (1.9)	6.3 (1.7)	73.7 (27.6)	-34.4 (-8.2)

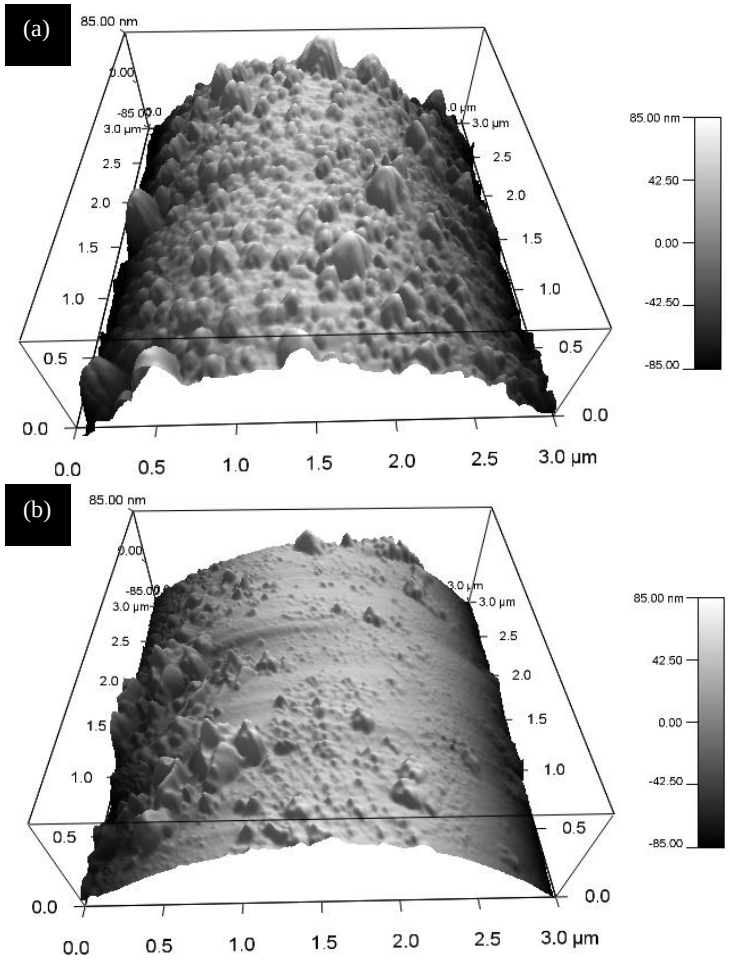

Figure 2.19 3D rendering of AFM images detailing the surface topography of quartz fibres after the 4-min annealing step in hydrogen atmosphere at (a) 620 °C and (b) 520 °C.

Despite the low density of catalyst nanoparticles produced through annealing at 520 °C, an abundant coverage of CNTs was obtained through T-CVD 520/640 °C. This suggests the formation of correctly sized Fe nanoparticles, confirming previous observations that exposure above 600 °C of a Fe layer reduced at lower temperatures triggers the rapid de-wetting of the Fe film into catalyst nanoparticles [247]. However, the random orientation of CNTs indicates a relatively low density of nucleation sites [235], whereas the large scatter of diameter values indicates a non-uniform nanoparticle size. It is likely that, by the time the carbon source decomposition and the carbon precipitation as CNTs began, the catalyst evolution did not reach a steady state of stable-sized nanoparticles and CNT nucleation and growth proceeded at different rates determined by the different nanoparticle sizes [250], thus leading to a disordered growth.

The abundant CNT growth obtained through PE-CVD 520/540 °C suggests that the energy supply through plasma exerted a similar effect to the exposure above 600 °C, triggering the formation of suitable iron nanoparticles for CNT growth. Accordingly, the relatively high value of the standard deviation of measured diameters reveals a non-uniform size of nucleation sites, likely due to their formation during the growth step caused by the low-temperature annealing. A distinctive feature of CNTs grown through PE-CVD 520/540 °C is the low tortuosity of single CNTs. The density of the nucleation sites is known to affect the tortuosity of CNTs, with more densely packed CNTs being more aligned and straighter than CNTs with lower density [247]. In addition, the presence of an electric field during plasma assisted synthesis is known to foster the alignment of the tubes by orienting the growing CNT perpendicularly to the fibre surface, in the direction of the electric field lines [32], [251]. The observed morphology is therefore expected to arise from a combination of these two factors.

To shed light on this issue, the catalyst morphology after the syntheses through T-CVD 620-640 °C and PE-CVD 520-540 °C was investigated by means of a detailed TEM analysis at the CNT/fibre interface. High-resolution bright field (BF) TEM micrographs

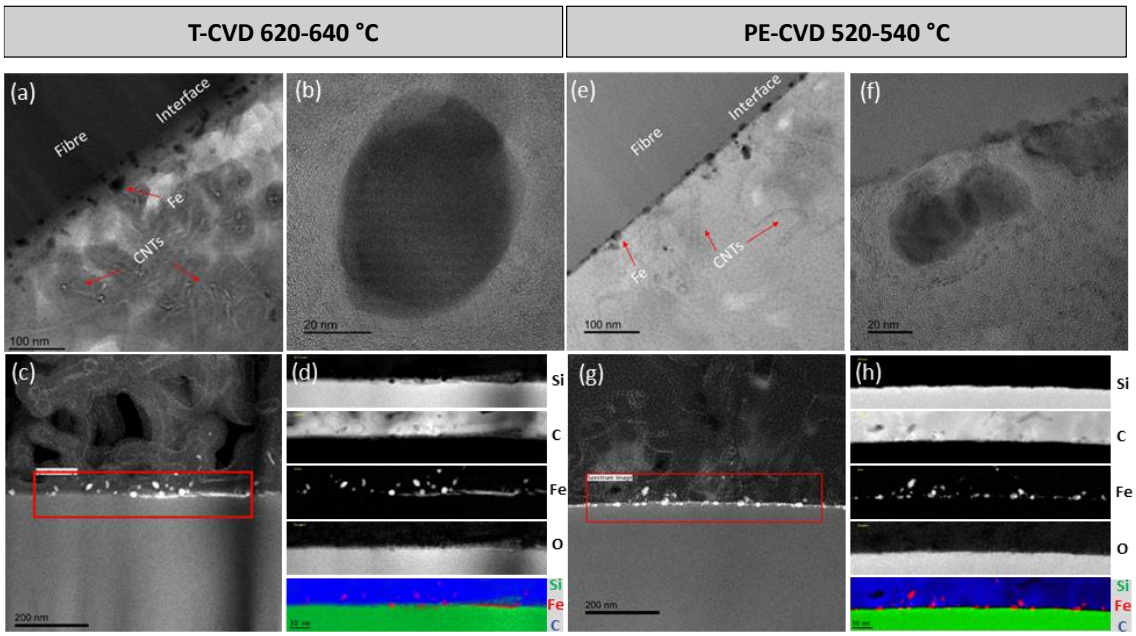

Figure 2.20 TEM characterization of the fibre/CNTs interface after (a-d) the T-CVD 620-640 °C and (e-h) the PE-CVD 520-540 °C process: (a, e) BF TEM micrographs at the interface; (b, f) higher magnification TEM micrographs detailing a catalyst nanoparticle located at the fibre/CNTs interface; (c, g) HAADF STEM micrographs and (d, h) EELS maps at the interface.

(Figure 2.20a, e) show numerous CNTs embedded in the carbon protection layer, which was applied during sample preparation to prevent the sample surface from being damaged by the FIB. Despite the tip growth mechanism, catalyst nanoparticles were mainly observed at the fibre surface as most CNT tips were probably cut during FIB milling due to the random orientation of the tubes in the selected area. Catalyst particles found at the fibre surface suggest that not all catalyst particles nucleated CNTs. As a confirmation, BF TEM micrographs at higher magnification (Figure 2.20b, f) revealed that the catalyst nanoparticles found at the fibre surface were encapsulated by graphitic multilayers, which are known to cause catalyst inactivity [236]. This is in accordance with previous studies [252]–[254] where, by comparing the number density of catalyst nanoparticles prior to the growth to the number density of as-grown CNTs, they concluded that only a fraction of catalyst nanoparticles was active for CNT growth. Although the iron nanoparticles at the fibre surface were not effectively used as nucleation sites for the growth of CNTs, their size, density and distribution give crucial information about the catalyst morphology

during the growth. To further evidence iron nanoparticle distribution, high angle annular dark field (HAADF) STEM mode (Figure 2.20c, g) was adopted as the contrast scales almost with the atomic number squared, showing the heavy iron atoms as bright contrast spots. Moreover, EELS mapping corresponding to the different elements, i.e., Si, C, Fe, O, was performed in the regions highlighted in the HAADF images (Figure 2.20d, h). These analyses confirmed the formation of a uniform dispersion of catalyst nanoparticles after the PE-CVD synthesis at 520-540 °C, demonstrating that the energy supply through plasma and heating was enough both to complete the nanoparticle formation and to trigger the CNT growth. Compared to the thermal process optimized at high temperatures (T-CVD 620-640 °C), nanoparticles of smaller average size and with a more dense and homogeneous distribution were observed on the fibre surface, in accordance with the average CNT diameters measured through TEM analysis on dispersed CNTs. The low-temperature synthesis, therefore, allowed for good dispersion of smaller catalyst nanoparticles due to slower progression of Ostwald ripening at low temperatures [247], leading to a more controlled and aligned growth.

Chapter 3.

Synthesis of CNTs with innovative catalyst systems

In the previous chapter, the potential of PE-CVD for the low temperature CNT synthesis has been investigated on quartz fibres in the presence of a conventional Fe-based catalyst pre-deposited on the fibre substrate. In addition to exploiting a plasma environment to foster hydrocarbon decomposition and chemical reactions during the CVD synthesis step, the selection of alternative catalyst systems with higher catalytic efficiency at low temperatures is a promising strategy to reduce CVD temperature conditions.

In this chapter, two innovative approaches are proposed for catalysing the synthesis of CNTs on different fibre substrates (i.e., basalt and quartz fibres) and studied in combination with both thermal and PE-CVD synthesis techniques. The selected catalyst systems consist in: (i) an *in-situ* catalyst generation approach, exploiting the native iron content of the basalt substrate as a catalyst, without the addition of any external catalyst; (ii) a copper-based catalyst, previously demonstrated to be catalytically active towards the growth of carbon nanofibers at temperatures as low as 250 °C [35].

3.1. *In-situ* catalyst generation

While the addition of an external catalyst precursor is required for most fibre substrates, the chemical composition of basalt fibres, classified as iron-rich aluminosilicate systems, suggests that their inherent iron oxide content (typically around 5-10 %) might be exploited as an *in-situ* catalyst. This is expected to provide the intriguing advantages of reducing the number of processing steps as well as a more homogeneous distribution of the catalyst nanoparticles, thus overcoming the well-known issues of uneven deposition of the catalyst precursor following the solution dip-coating step [255] and the coarsening of catalyst nanoparticles at high temperatures [247].

In a recent work, Sarasini et al. [36] proposed a possible mechanism for the *in-situ* catalyst generation on basalt fibres, reported in Figure 3.18. The chemical composition of basalt

fibres includes oxides acting as glass network modifiers (i.e., FeO, TiO_2, CaO, Na_2O, K_2O, MgO) that can freely diffuse in the network structure, and oxides like Al_2O_3 and Fe_2O_3, which act as either glass network formers or network modifiers. When the fibre surface is subjected to a corrosion attack, part of the siloxane bonds of the glass network breaks with consequent silicates migration in the solution and enrichment of the fibre surface with other oxides, including iron oxides [256]–[258]. The first step of the *in-situ* catalyst generation approach, therefore, requires an alkaline (or acidic) pre-etching of the basalt substrate to promote the exposure of iron oxides on the fibre surface. Afterwards, the formation of active nucleation sites for the subsequent CNT growth is promoted through an annealing treatment at high temperatures (above 700 °C) in hydrogen atmosphere. Two essential phenomena are believed to occur during this step: (i) the reduction of Fe^{2+} ions to active Fe^0 nucleation sites on the fibre surface exposed to the hydrogen atmosphere [259] assisted by (ii) an outward diffusion of Fe^{2+} towards the fibre's surface [260]–[262]. In fact, the non-equilibrium hyperquenched structure of basalt fibres, resulting from the manufacturing process, stores significant amounts of energy which are expected to be released during high-temperature exposure through structural rearrangements of the glass network [112], [263]–[265]. The diffusion and segregation of small-sized Fe^{2+}, therefore, is driven by the resulting lower network distortion [262]. Finally, the *in-situ* catalysed growth of CNTs is achieved at high temperatures (above 700 °C) in C_2H_2 atmosphere.

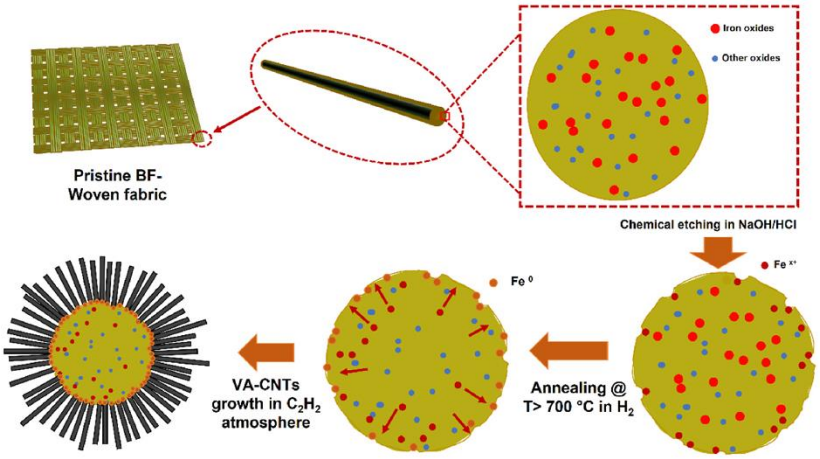

Figure 3.18 Mechanism proposed by Sarasini et al. [36] for the growth of CNTs on basalt fibres with in-situ catalyst generation.

3.1.1. CNT synthesis conditions

Reported for the first time by Forster et al. [15] and afterwards by Chang et al. [266], the *in-situ* catalyst generation approach was optimized in the work by Sarasini et al. [36], where a uniform growth of highly dense vertically aligned (VA)-CNTs on basalt fabrics was reported for the first time by employing a thermal CVD process with annealing at 720 °C and synthesis at 740 °C. As such high temperatures are known to seriously affect the mechanical response of basalt fibres [29], [67], [262], a PE-CVD method was adopted in this research work to achieve the synthesis of CNTs at temperatures below 600 °C. The parameters of the CVD process were optimized based on those found effective for the PE-CVD growth on quartz fibres, as described in the previous chapter. Details of the optimized process parameters (i.e., the duration, flow rates, partial pressures of gases and plasma power) are reported in section 2.2 of Part II – Materials and Methods. It is worth noting that the plasma assistance was employed only during the growth step to provide part of the energy for hydrocarbon decomposition and CNT formation, while the first step of the CVD process consisted in a thermal annealing. Therefore, it was necessary to explore the effects of reducing the annealing temperature on the *in-situ* catalyst generation approach.

To optimize a low temperature synthesis process, the effects of the annealing and synthesis temperature on the CNT morphology were separately assessed. In particular, a constant synthesis temperature below 600 °C (i.e., 580 °C) was initially set, while the annealing temperature was progressively reduced to identify the minimum temperature required for the effective activation of the native iron of basalt fibres as a catalyst. The investigated annealing temperatures are 485, 460 and 420 °C. Prior to the synthesis process, all basalt samples were pre-treated in a mild alkaline environment (2M NaOH-aqueous solution for 3 hours at room temperature) according to the conditions optimized by Sarasini et al. [36] for the pre-etching of the basalt surface.

Once identified the lower temperature limit for the annealing step, the effects of lowering the synthesis temperature were assessed by carrying out two different PE-CVD processes: i) PE-CVD with annealing at 460 °C and synthesis at 510 °C; ii) PE-CVD with annealing at 420 °C and synthesis at 480 °C. It is worth noting that the reported temperatures correspond to the substrate temperatures measured through a thermocouple anchored to

the top surface of the fabric substrate, as detailed in section 2.2 of Part II – Materials and Methods. This temperature takes into account the deviations of the actual growth temperature from the controlled one derived from the well-known exothermic decomposition of acetylene [267] and plasma heating [182], which contribute to increase the substrate temperature during the synthesis step. For the processes PE-CVD 460/510 °C and PE-CVD 420/480 °C, therefore, the temperature difference between the annealing and synthesis steps must be ascribed only to these inevitable heating effects, as a constant operating temperature was set through the CVD chamber equipment for both the annealing and growth steps.

The temperatures selected for each step and CVD process are summarized in Table 3.2. In the following discussion, each process will be referred as: "METHOD" followed by "annealing temperature/synthesis temperature", e.g., PE-CVD 485/580 °C.

Table 3.2 Substrate temperatures measured during the annealing and synthesis step of different plasma enhanced CVD (PE-CVD) processes performed on basalt fabrics.

Method	Annealing Temperature [°C]	Synthesis Temperature [°C]
PE-CVD 485/580 °C	485	580
PE-CVD 460/580 °C	460	580
PE-CVD 420/580 °C	420	580
PE-CVD 460/510 °C	460	510
PE-CVD 420/480 °C	420	480

3.1.2. Morphological characterization of CNT-modified fibres

Figure 3.19 reports representative SEM micrographs at different magnifications detailing the morphology of CNT-modified basalt fabrics following PE-CVD at annealing temperatures of 485, 460 and 420 °C and constant synthesis temperature of 580 °C. An abundant and homogeneous growth of VA-CNT forests was observed for the first two processes (PE-CVD 485/580 °C and PE-CVD 460/580 °C) with an average length of VA-CNT arrays equal to 34.5 ± 5.8 μm and 29.5 ± 4.5 μm, respectively. This morphology is completely comparable with the one reported by Sarasini et al. [36] for basalt samples

subjected to thermal CVD above 700 °C, demonstrating that the plasma power introduced during the synthesis step was able to compensate entirely for the temperature difference in terms of energy needed for the growth. However, when the annealing temperature is reduced to 420 °C, a homogeneous coverage is no longer achieved, with the growth of sparse and shorter VA-CNT arrays having an average length of 14.9 ± 3.1 μm.

The different morphologies obtained by varying the annealing temperature give important information about the catalyst activation during the annealing step. The observed arrangement of CNTs into arrays of aligned tubes is directly related to the formation of densely packed nucleation sites, i.e., catalyst nanoparticles, forcing the tubes to grow in a common direction due to van der Waals interactions between nearby CNTs [232]. As basalt samples with annealing at 485 °C and 460 °C were homogeneously covered by VA-CNTs, with an abundant growth both on the surface and through the thickness of the fabric sample, it is reasonable to assume that a high density of active catalyst nucleation sites was achieved all over the sample. On the other hand, the poor coverage observed for the sample with annealing at 420 °C suggests a lower density and less uniform distribution of active nucleation sites, indicating that the annealing at 420 °C was probably not sufficient to completely activate the iron catalyst into suitable-sized and evenly distributed nanoparticles. Considering the proposed mechanism for the *in-situ* catalyst generation, the main factors behind the inhomogeneous activation of the catalyst might be either an insufficient reduction or diffusion rate at low temperatures. Based on studies on the reduction of iron oxides in H_2 atmosphere through temperature-programmed reduction (TPR) experiments, the reduction of iron oxides usually occurs in the temperature range 400-600 °C [268]–[270]. The time for full reduction of hematite (Fe_2O_3) particles (grain size around 1-2 μm) in isothermal conditions was reported to be about 7 minutes and 5 minutes at temperatures of 429 °C and 472, respectively, whereas times exceeding 60 minutes were required at temperatures below 360 °C [271]. Similar results were reported also for the reduction of magnetite (Fe_3O_4) [272]. The annealing time of 8 minutes selected in this work is therefore expected to be sufficient for the complete reduction of the iron oxides on the surface of basalt fabrics. On the other hand, it is likely that the outward diffusion of Fe^{2+} occurs over a longer time scale at 420 °C,

due to the smaller driving force for structural rearrangements of the glass network [273], [274].

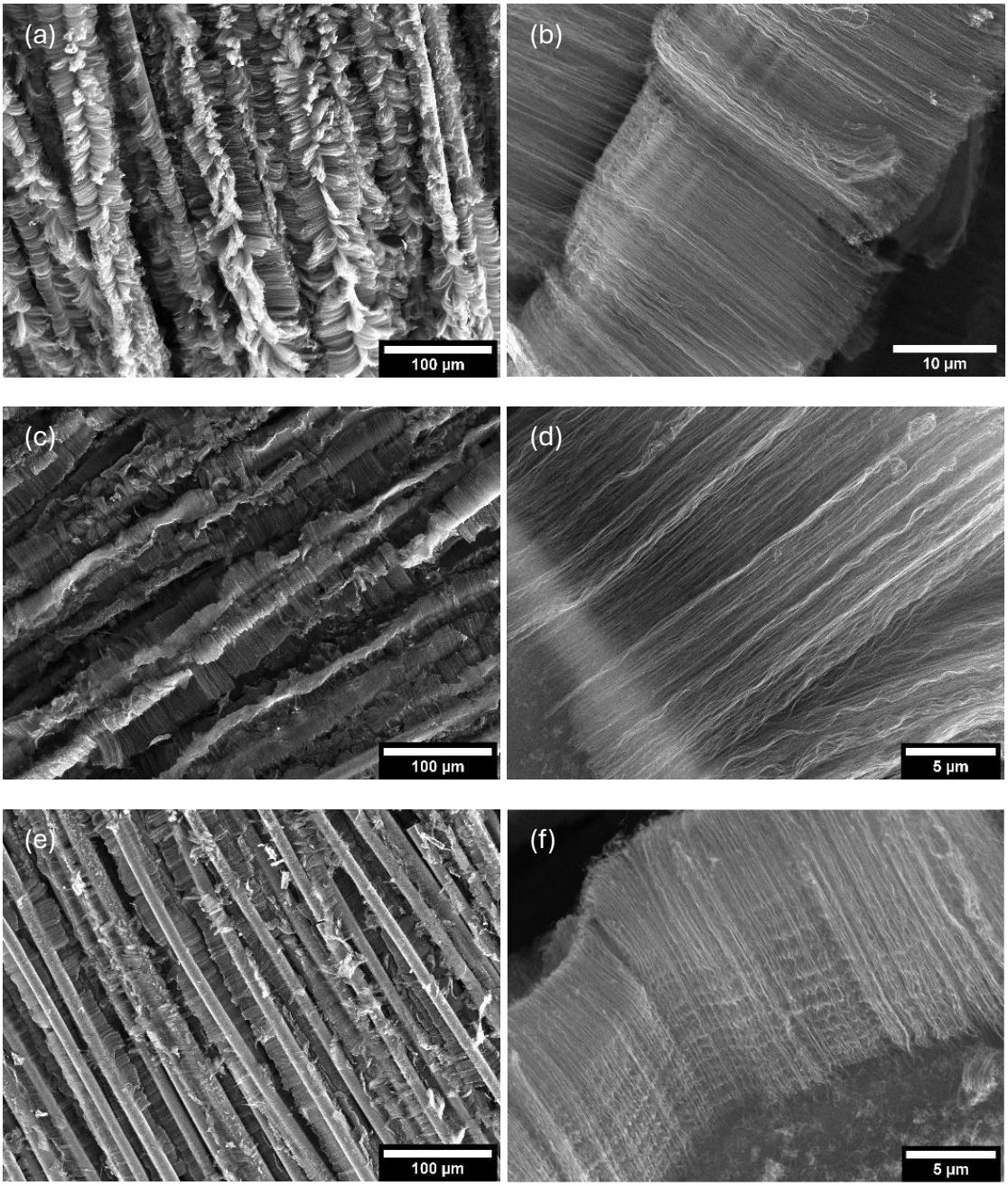

Figure 3.19 SEM micrographs detailing the morphology of CNT-modified basalt fabrics after PE-CVD with varying annealing temperatures: (a-b) 485 °C; (c-d) 460 °C; (e-f) 420 °C. The growth temperature was equal to 580 °C for all samples.

In this hypothesis, the iron diffusion is considered as the rate-limiting step. Consequently, while the iron exposed on the fibre surface after the alkaline treatment was readily available to be reduced when exposed to the hydrogen flow, the low diffusion rate of Fe^{2+} possibly hindered the new supply of iron to the basalt surface, thus leading to a less dense CNT coverage.

As observed by Tolga Gul [247], the density of the catalyst nanoparticles also affects the tortuosity of individual tubes in the VA-CNT forest. By comparing the higher magnification SEM micrograph in Figure 3.19b,d to the one reported by Sarasini et al. [36], it can be assumed that in both cases the density of nanoparticles was sufficient to guarantee the growth of well-aligned CNTs. In contrast, a higher tortuosity of CNTs was observed for the sample with annealing at 420 °C (Figure 3.19f), thus supporting the hypothesis of a lower density of nucleation sites.

By varying the annealing temperature, it has been demonstrated that a uniform distribution of active iron nucleation sites can be produced at temperatures as low as 460 °C through the *in-situ* catalyst generation approach.

The morphologies resulting from the two processes at lower synthesis temperatures, i.e., PE-CVD 460/510 °C and PE-CVD 420-480 °C are displayed in the representative SEM micrographs in Figure 3.20. As shown in Figure 3.20a-b, the PE-CVD process at 460/510 °C led to an abundant and homogeneous growth of VACNTs forests, similar to the one observed after PE-CVD at 460/580 °C and 485/580 °C. On the other hand, the lower temperature process led to an inhomogeneous CNT coverage (Figure 3.20c-d), providing further evidence of the incomplete activation of the *in-situ* catalyst following annealing at 420 °C. Average CNT lengths of 32.5 ± 3.4 µm and 15.5 ± 2.9 µm were measured for PE-CVD 460/510 °C and PE-CVD 420/480 °C, respectively. Interestingly, these values compare quite favourably with the corresponding values measured after PE-CVD at the same annealing temperature but higher synthesis temperature (i.e., 460/580 °C and 420/580 °C, respectively). These findings seem to indicate a significant effect of the annealing temperature not only on the distribution of CNTs but also on their length, regardless of the synthesis temperature. It is worth noting that, despite the low density of CNTs observed on samples produced with PE-CVD at 420/480 °C and 420/580 °C, the CNTs grew with a radial alignment that cannot be explained by the density of the catalyst

distribution alone. In this case, the radial orientation and relatively low waviness of the tubes evidence the effect of plasma which, along with the catalyst distribution, contributes to the final CNT morphology and orientation. In fact, as reported by Bower et al. [32] and observed for PE-CVD on quartz fibres in the previous chapter of this thesis, the presence of plasma can exert an aligning effect on the growing CNTs in the direction of the electric field lines, which are oriented perpendicularly to the fibre surface.

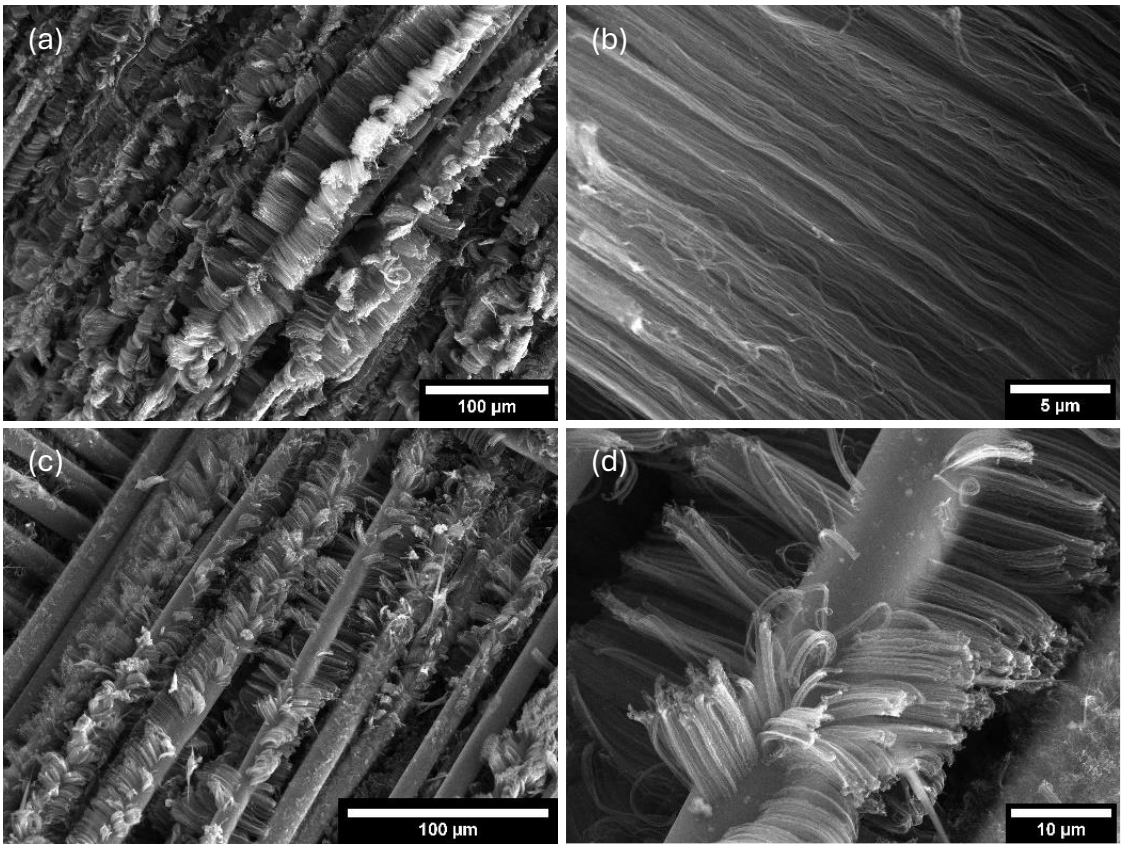

Figure 3.20 SEM micrographs detailing the morphology of CNT-modified basalt fabrics after low temperature PE-CVD: (a-b) annealing at 460 °C and growth at 510 °C; (c-d) annealing at 420 °C and growth at 480 °C.

The investigation of the effects of the annealing and synthesis temperatures during PE-CVD with *in-situ* catalyst generation revealed the PE-CVD process with annealing at 460 °C and synthesis at 510 °C as the best option for achieving a homogeneous CNT growth at low temperatures. This process led to a CNT morphology completely comparable to the thermal counterpart reported in [36] with a consistent temperature reduction which is

expected to mitigate the strength loss experienced by the basalt substrate. On the other hand, using a lower annealing temperature (420 °C) led to a non-uniform coverage of shorter CNTs, identifying a lower temperature limit under the selected process conditions.

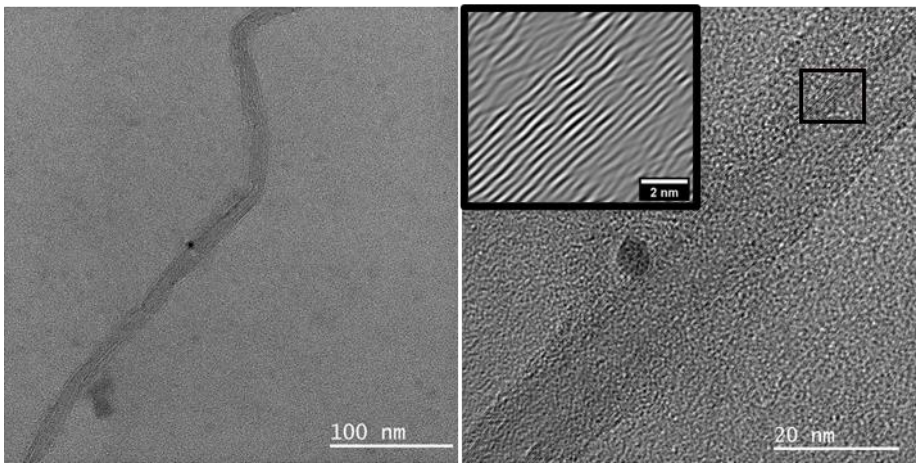

Figure 3.21 TEM micrographs of CNTs grown on basalt fabric through PE-CVD at 460/510 °C (annealing temperature/synthesis temperature).

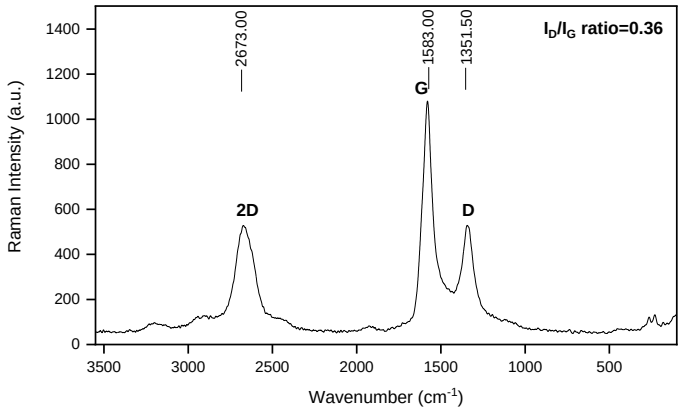

Figure 3.22 Raman spectrum of CNT-modified basalt fabric after PE-CVD at 460/510 °C (annealing temperature/synthesis temperature).

Being the best investigated option, CNTs produced through PE-CVD 460/510 °C were further characterized through TEM and Raman investigations. As-grown CNTs were analysed by TEM after dispersion in ethanol and ultrasonication in order to evidence their local structure. Figure 3.21 displays typical TEM micrographs at different magnifications,

showing well graphitized multi-walled CNTs with diameters ranging from 10 to 17 nm. In terms of structural quality, the Raman spectrum of the basalt fabrics with CNTs is shown in Figure 3.22, where typical spectral features of most graphite-like (sp^2) carbon materials are present, including a mode around 1580 cm^{-1} (G-band), a mode around 1340 cm^{-1} (D-band), and a second-order mode of lower intensity (2D) around 2700 cm^{-1}. The ratio between D and G bands (I_D /I_G), which are respectively related to the defect and the crystallization degree of the sample, offers a qualitative measure of the defect density in CNTs, with higher values indicating a lower graphitic ordering [243]. A value of 0.36 was obtained for the basalt sample subjected to PE-CVD at 460/510 °C, indicating a better structural quality than the one reported by Sarasini et al. [36] for CNTs grown on basalt through thermal CVD at 720/740 °C and *in-situ* catalyst generation, having a value of the I_D /I_G ratio of 0.69. Although low synthesis temperatures usually lead to high structural defects [275], the obtained value is also significantly lower than the values reported by Kinoshita et al. [276], ranging from 0.56 to 0.79, for thermal syntheses at 700 °C with acetylene as carbon precursor and an external catalyst. The relatively low defect density might be a result of the combination of the high density of active catalyst sites and the use of a PE-CVD technique which contributed to the concerted growth of VA-CNT arrays with good alignment and structural quality.

3.2. Copper-based catalyst

Copper catalysts are extensively used at an industrial scale because of their high activity and selectivity to catalyse a wide range of reactions of commercial importance. These reactions, often involving hydrocarbons or other carbon-containing compounds, e.g., CO and CO_2, either as reactants or products, include methanol synthesis from CO or CO_2, the water-gas shift reaction, methanol steam reforming, oxidative methanol reforming, oxidation of CO, oxidation of hydrocarbons, oxidation of volatile organic compounds (VOCs) [277]–[279]. Although copper was initially thought to be inactive towards the growth of CNTs, in the last decade many works have demonstrated the growth of different carbon nanostructures through Cu-catalysed CVD, including multi-walled [171] and single-walled CNTs [157]. Although the main application of copper in this field is in the synthesis of graphene at very high temperatures (>900 °C) [280], [281], Cu has also

become a promising option for the synthesis of carbon nanostructures at low temperatures. In fact, Zhang et al. [170] demonstrated its activity towards the growth of carbon nanofibers and carbon nanocoils at temperatures as low as 200 °C and 250 °C, respectively. As regards the direct growth on reinforcing fibres, copper has been employed as a catalyst for the growth on carbon fibres to avoid the well-known deteriorating mechanism caused by the most common metallic nanoparticles, e.g., Fe, due to the diffusion of metal atoms into the graphite grains of carbon fibres [172], [282]. Furthermore, the use of innovative catalysts, including copper, was investigated by Lilli et al. [234] for the growth of different carbon nanostructures, including carbon nanocoils and nanofibers, on basalt fibre substrates at temperatures below 500 °C.

In this context, this research work investigates the use of a copper-based catalyst on quartz fibres, proposing it as an alternative method to Fe-catalysed PE-CVD for the synthesis of CNTs at temperatures below 550 °C. The Cu-catalysed synthesis is investigated both through thermal CVD and in combination with the PE-CVD technique.

3.2.1. CNT synthesis conditions

To achieve the Cu-catalysed synthesis on quartz fibres, a careful tuning of the operative parameters of each process step was carried out, starting with the selection of a suitable catalyst precursor and its deposition on as-received quartz fibres through dip-coating. Based on the works by Acauan [35] and Lilli [234] et al., reporting the copper-catalysed synthesis of various carbon nanostructures on carbon and basalt fibres respectively, a solution of copper acetate monohydrate in acetonitrile was employed for the dipping step. The concentration, immersion time, and temperature of the solution were systematically varied to achieve a homogeneous coverage of the fibre surface with the catalyst precursor, as investigated through simultaneous SEM and EDS analyses. The best results were obtained after complete evaporation of a 5 mM-solution at room temperature in a crystallizer, i.e., a laboratory glass container that has a wide base to allow for greater evaporation of the solvent and formation of uniformly sized crystals of the solute. This strategy was preferred to the conventional dip-coating procedure, in which the fibres are immersed in the solution and withdrawn after a certain immersion time, to overcome the

operator-induced variability of the results derived from a non-controlled withdrawal speed, an important parameter influencing the thickness and morphology of the deposited film as much as the immersion time, coating solution concentration, and temperature [255].

Once the optimal conditions for the deposition of the catalyst precursor were identified, the activity of copper towards the synthesis of carbon nanostructures was assessed under the CVD process parameters previously optimized for the Fe-catalysed thermal synthesis (T-CVD 620/640 °C). An intermediate oxidation step was introduced prior to the CVD process to promote the decomposition of the Cu salt and foster the formation of active metal nanoparticles during the annealing stage of the CVD process. Using a tubular oven, the Cu-salt dip-coated quartz fibres were treated at 300 °C for 1 hour in air atmosphere to decompose copper(II) acetate monohydrate into a mixture of Cu, CuO, and Cu_2O. These conditions were selected based on the work by Lin et al. [283] who studied the thermal decomposition of copper(II) acetate monohydrate in air at temperatures up to 500 °C, revealing that the decomposition is complete at temperatures around 300 °C, while higher temperatures lead to the gradual oxidation of Cu and Cu_2O to CuO. The thermal decomposition of Cu precursors, including copper acetate and copper nitrate, is a common practice for the preparation of active Cu^0 catalyst nanoparticles for various industrial reactions and is generally followed by the reduction of the oxide phase formed during thermal decomposition [277], [284]. As the reduction of CuO and Cu_2O to Cu is a highly exothermic process, great care is required to avoid local overheating and sintering of active crystallites at high temperatures with consequent loss of surface area, which adversely affects the performance of the catalyst. Therefore, at an industrial level, the catalyst is reduced by being slowly heated in a controlled flow rate of hydrogen. Similarly, a hydrogen flow was introduced in the CVD chamber during heating up to the annealing temperature and a relatively slow heating rate of 50 °C/min was selected.

Once the possibility of achieving a Cu-catalysed growth was confirmed under the process conditions optimized for the iron catalyst, the CVD processing parameters of the T-CVD 620/640 °C process, i.e., the processing temperature, duration, and flow rates of both the annealing and synthesis steps, were adjusted to identify the suitable conditions for a low

temperature Cu-catalysed growth. In fact, there are a few differences between Cu and Fe that suggest that the CVD conditions of the Cu-catalysed processes should be distinct from those catalysed by Fe. According to the most accepted mechanism for the growth of CNTs, an active catalyst should have some solubility of carbon in solid solution to allow C atoms to dissolve into the metal nanoparticle and precipitate out in the form of a cylindrical graphitic structure. The Cu–C binary phase diagram confirms the solubility of carbon in the Cu solid solution, but with a solubility much lower than in Fe [285]. Moreover, Cu possesses a lower catalytic activity for the decomposition of the carbon feedstock [155]. This suggests the need for a slower supply of carbon (i.e., lower acetylene flow rate, during the synthesis) to avoid catalyst poisoning due to the rapid precipitation of amorphous carbon. As a direct consequence of the slower carbon supply, longer synthesis durations are required to achieve the same CNT loading.

In addition to the different solubility of carbon and catalytic activity for hydrocarbon decomposition, it is reasonable to expect a different de-wetting behaviour of Cu than Fe, due to factors including the different interaction of Cu with silica and diffusion at the Cu-SiO_2 interface [286], [287], which suggests that distinct annealing conditions should be adopted for the formation of a suitable distribution of active nanoparticles acting as a template for CNT growth.

Based on these considerations, a careful tuning of the annealing and synthesis parameters, i.e., processing temperature, duration, and flow rates, was carried out leading to the identification of the optimal parameters for the Cu-catalysed thermal growth of CNTs at 510 °C, as reported in section 2.2 of Part II – Materials and Methods. Once the optimal growth conditions were achieved, the effects of further temperature reduction (420 °C and 320 °C) and of plasma assistance were evaluated. It is worth noting that, compared to the previously optimized Fe-catalysed synthesis processes on both quartz and basalt fibres, longer annealing and synthesis durations were required to achieve the Cu-catalysed growth, resulting in a total process duration of ~1 hour (considering also the time required for heating to the annealing temperature) compared to the ~15 minutes required for the Fe-catalysed syntheses on quartz fibres and ~25 minutes required for the PE-CVD growth on basalt fibres. Moreover, the presence of hydrogen during the synthesis step was found

to be necessary to improve the yield of nanostructure growth and avoid catalyst coalescence.

3.2.2. Morphological characterization of CNT-modified fibres

Prior to CVD growth, copper acetate monohydrate was deposited on the fibre surface by dip-coating as a catalyst precursor. The morphology of dip-coated fibres, resulting from the tuning of the process parameters, is shown in Figure 3.23a along with the EDS spectrum (Figure 3.23c) corresponding to a portion of the fibre surface shown in Figure 3.23b.

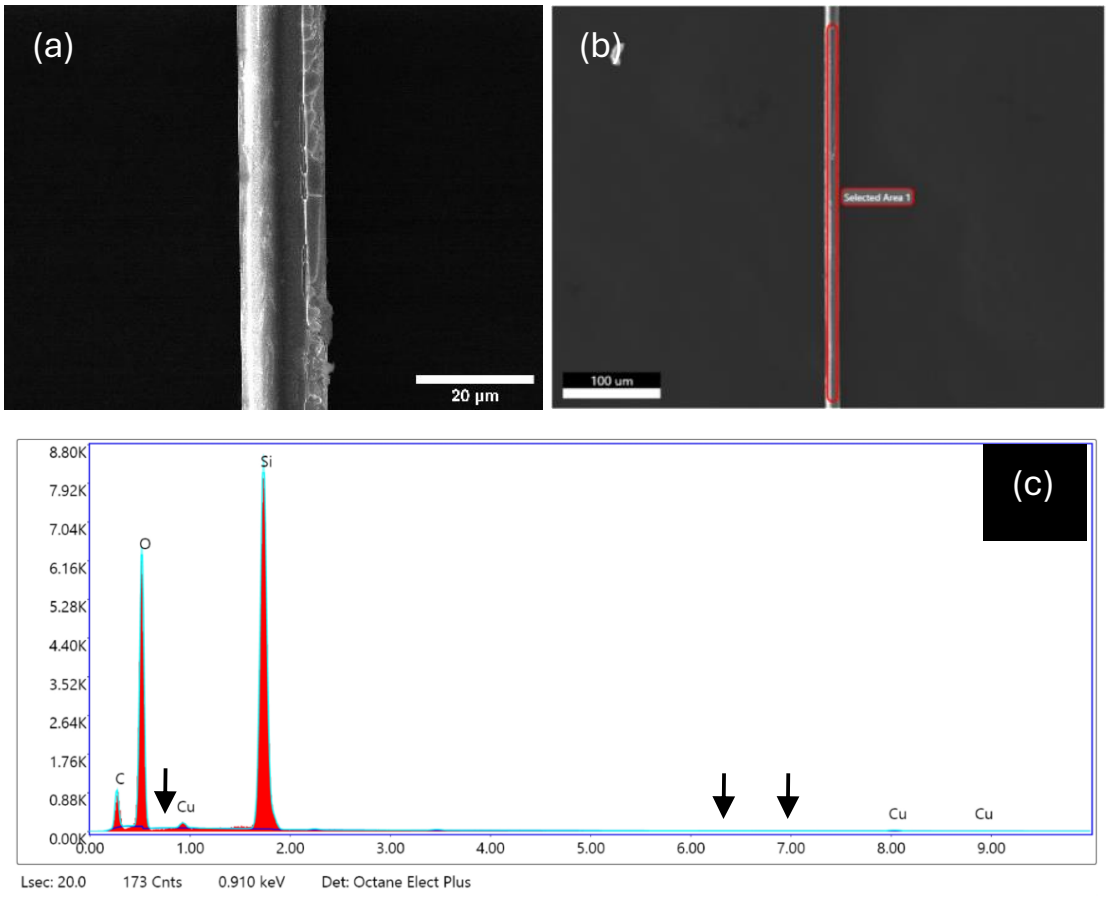

Figure 3.23 (a) SEM micrograph of a Cu-salt dip-coated quartz fibre; (b) a portion of a dip-coated quartz fibre selected for EDS analysis; (c) EDS spectra for a dip-coated quartz fibre. The arrows denote the peak positions of Fe element, and no signal was found in the corresponding position.

The characteristic peaks of Cu in the EDS spectrum confirm the deposition of the catalyst precursor on the fibre surface while, as evidenced by the arrows, no Fe or other metal elements which normally can catalyse CNT growth were present on quartz fibre surface. A uniform coverage of the fibre surface was successfully achieved at the optimized dip-coating conditions, as revealed by the representative SEM micrograph in Figure 3.23a.

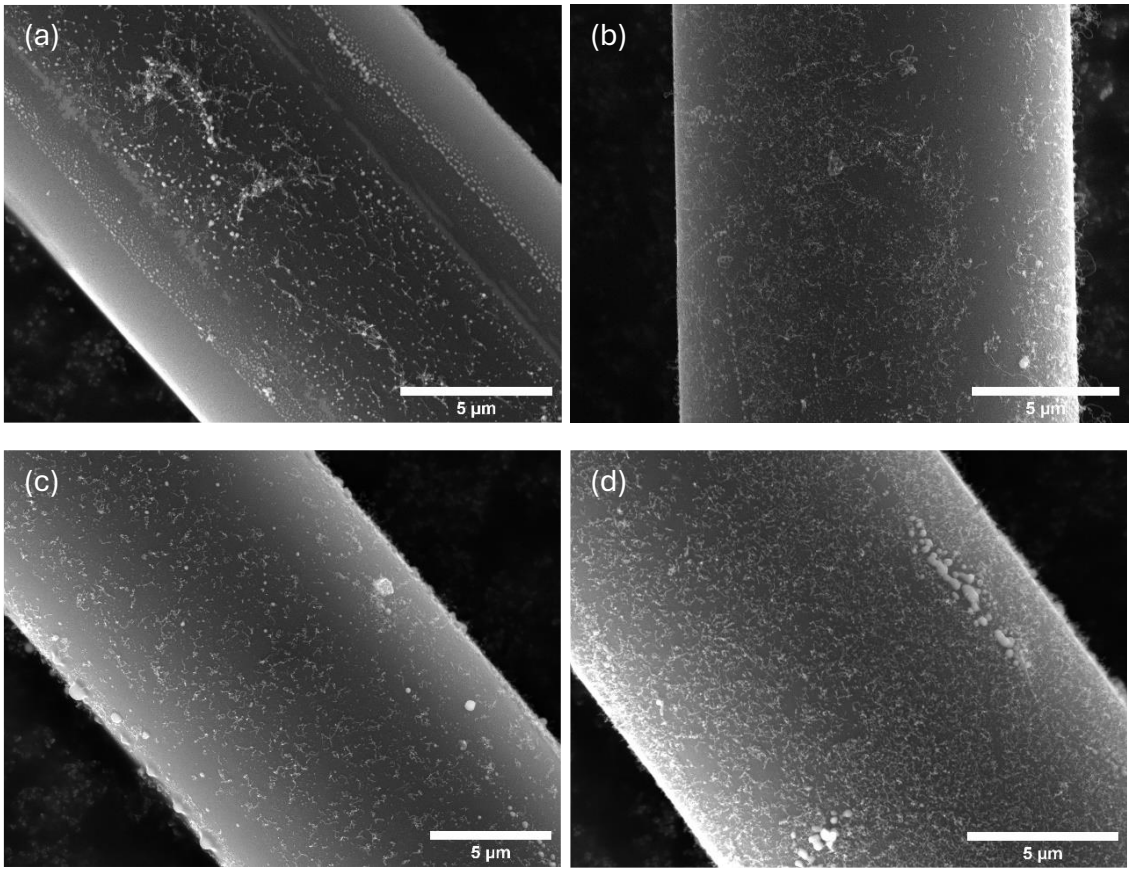

Figure 3.24 Representative SEM micrographs detailing the morphology of the carbon nanostructures grown on quartz fibres following (a) Cu-catalysed T-CVD 620/640 °C (process conditions optimized for Fe-catalysed growth), (b) Cu-catalysed T-CVD 620/640 °C preceded by an intermediate oxidation step, (c) Cu-catalysed T-CVD 620/640 °C with hydrogen flow during heating at a heating rate of 50 °C/min, (d) Cu-catalysed T-CVD 620/640 °C with both the pre-oxidation step and slow heating in hydrogen flow.

To assess the possibility to grow CNTs onto quartz fibres using Cu as a catalyst, CVD conditions were left unchanged from those previously found to be effective for Fe-catalysed thermal growth (T-CVD 620/640 °C) discussed in Chapter 2 of Part II – Results

and Discussion. Despite non-uniform, the presence of some CNT sprouts on the fibre surface (Figure 3.24a) confirmed the catalytic activity of Cu for the synthesis of carbon nanostructures while suggesting that different CVD conditions should be used. Therefore, as discussed in section 3.2.1, an intermediate oxidation step was introduced before CVD and a hydrogen flow was injected during heating up to the target annealing temperature. These strategies improved the uniformity and density of the CNT coverage as shown in the representative SEM micrographs in Figure 3.24b-d. Finally, by adjusting the CVD process parameters, i.e., processing temperature, duration, and flow rates of both the annealing and synthesis steps according to the considerations reported in section 3.2.1, a protocol for the Cu-catalysed thermal synthesis of CNTs was optimized at temperatures as low as 510 °C (T-CVD 510 °C).

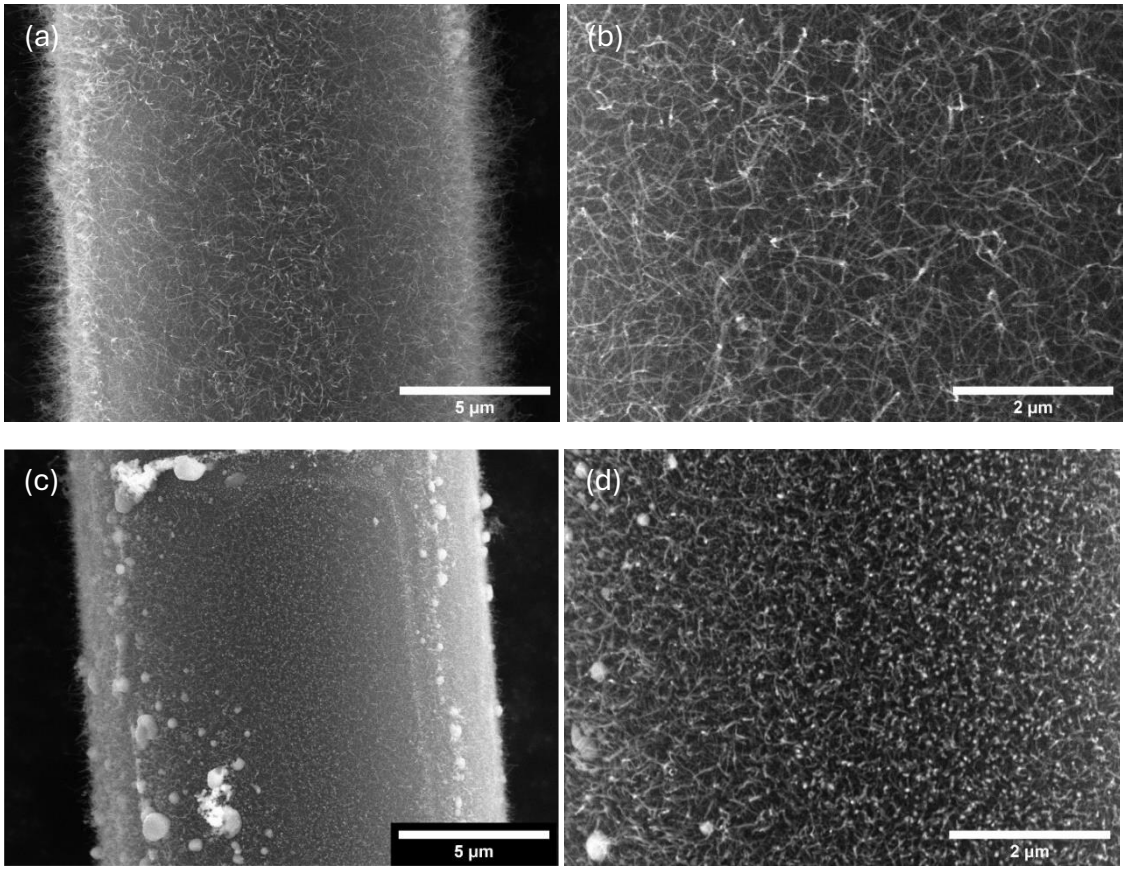

Figure 3.25 Representative SEM micrographs at different magnification detailing the morphology of the carbon nanostructures grown on quartz fibres following Cu-catalysed (a, b) T-CVD 510 °C, and (c, d) T-CVD 420 °C.

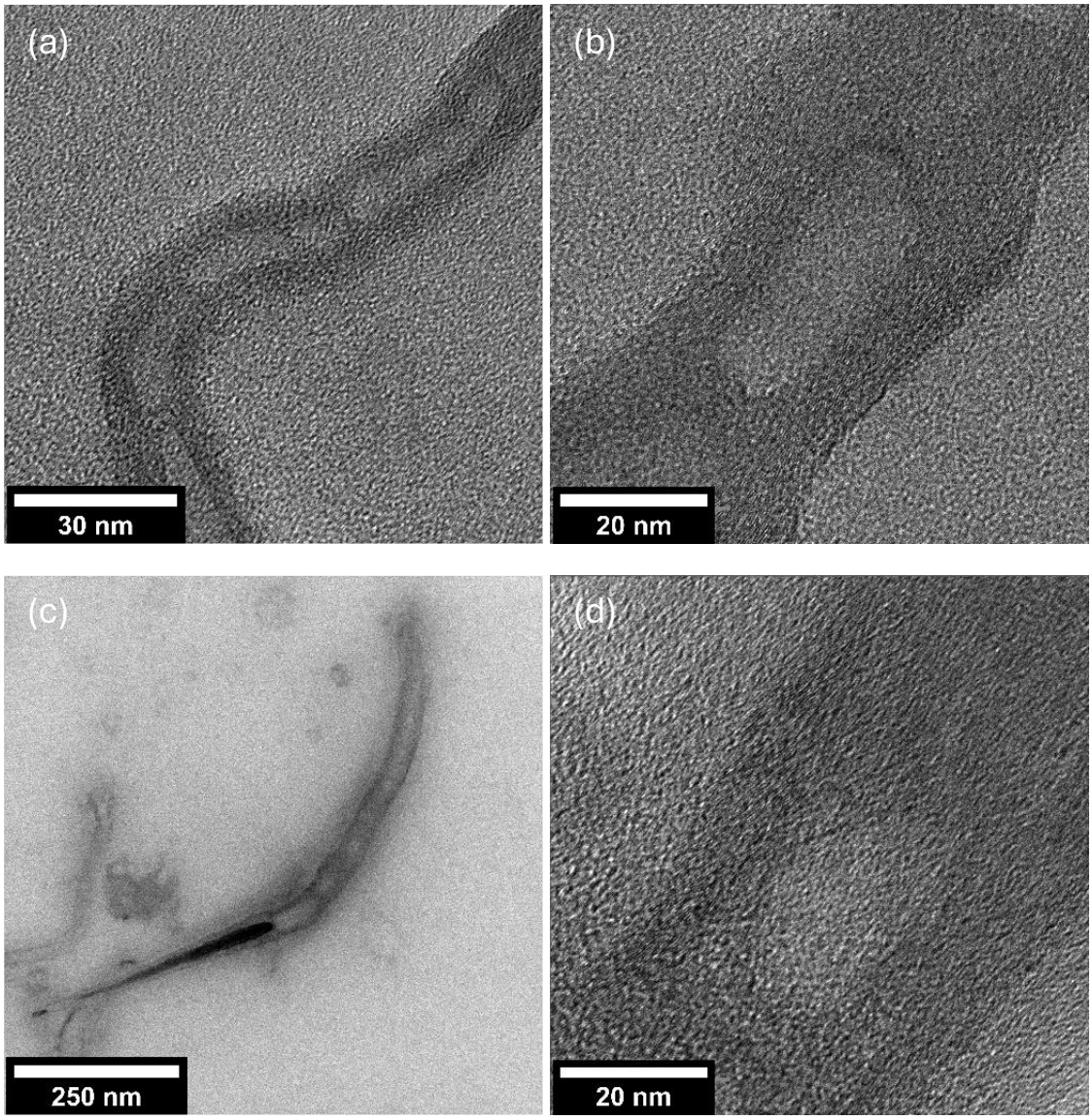

Figure 3.26 BF TEM micrographs at different magnification of bamboo-type CNTs grown on quartz fibres following Cu-catalysed (a, b) T-CVD 510 °C, and (c, d) T-CVD 420 °C.

An abundant and dense coverage of relatively short (~2 μm) randomly oriented CNTs was achieved on quartz fibre surface through T-CVD 510 °C, as detailed in Figure 3.25a-b. The growth of carbon nanostructures was also achieved at 420 °C under the same process conditions (T-CVD 420 °C), while a further reduction to 320 °C did not lead to any growth (data not shown). As displayed in Figure 3.25c-d, a homogeneous submicrometric-thick (~0.2 μm) layer of CNTs was synthesized through thermal CVD at 420 °C. TEM investigation of individual nanostructures synthesized through T-CVD 510

°C and T-CVD 420 °C revealed the formation of bamboo-type CNTs (Figure 3.26), featuring a stacked cups structure which resembles the compartmentalized structure of a bamboo stem [239]. The CNT diameter, having an average value of 24.7 ± 7.5 nm for T-CVD 510 °C and 23.4 ± 10.0 nm for T-CVD 420 °C, was found to decrease towards the tip, where the inner cavity was often filled by a severely elongated Cu nanoparticle, as revealed by the simultaneous STEM and EDS analyses reported in Figure 3.27.

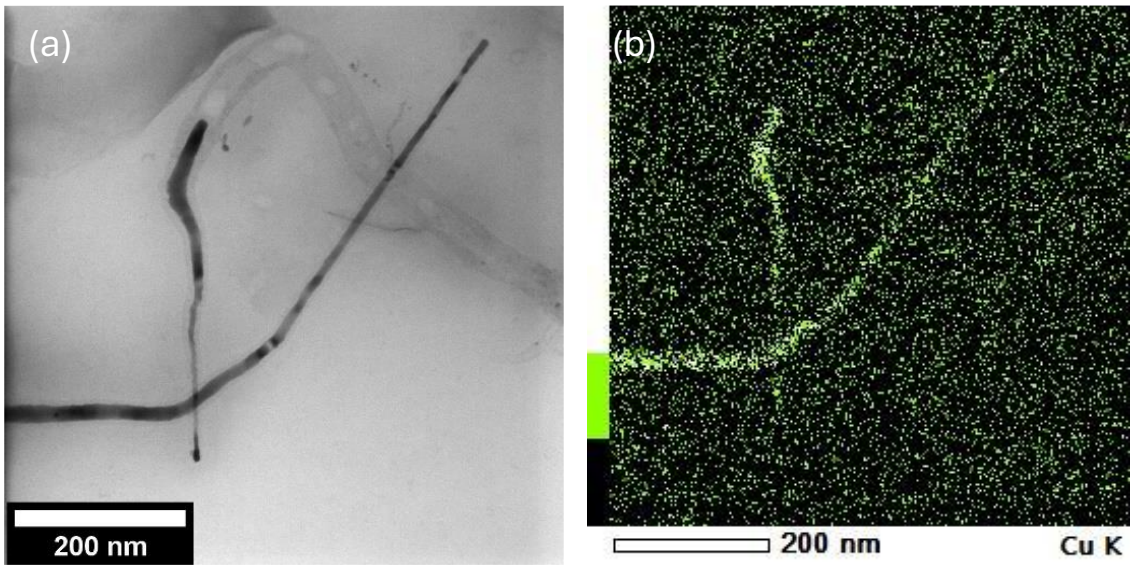

Figure 3.27 Representative (a) STEM micrographs and corresponding (b) EDS map of Cu detailing the elongated copper catalyst inside the CNT cavity after T-CVD 420 °C.

The presence of a Cu particle at the tip of the CNT revealed a tip-growth mechanism, which was often reported in the literature for the Cu-catalysed growth on silica substrates due to the weak interaction of Cu with the SiO_2 substrate [155], [285]. The elongation of the catalyst nanoparticle along the tubes was found to be more pronounced than the one observed for the iron catalyst, discussed in section 2.2 of Part III – Results and Discussion, indicating a high tendency of the Cu catalyst to deform under the forces exerted by the walls of the growing nanotube. The significant elongation of the Cu catalyst was related to the peculiar bamboo-like CNT morphology by Cui et al. [282] who achieved the Cu-catalysed growth of this kind of CNTs at 650 °C. According to the proposed mechanism, during CNT growth the Cu particle is lifted upward and elongated while the walls of the tubes are formed around its tail. When the bottom of the tail is lifted by the rising particle,

a transversal wall known as “bamboo joint” is left inside the growing tube. The repetition of this mechanism during the growth is believed to lead to the formation of the bamboo-like structure [282].

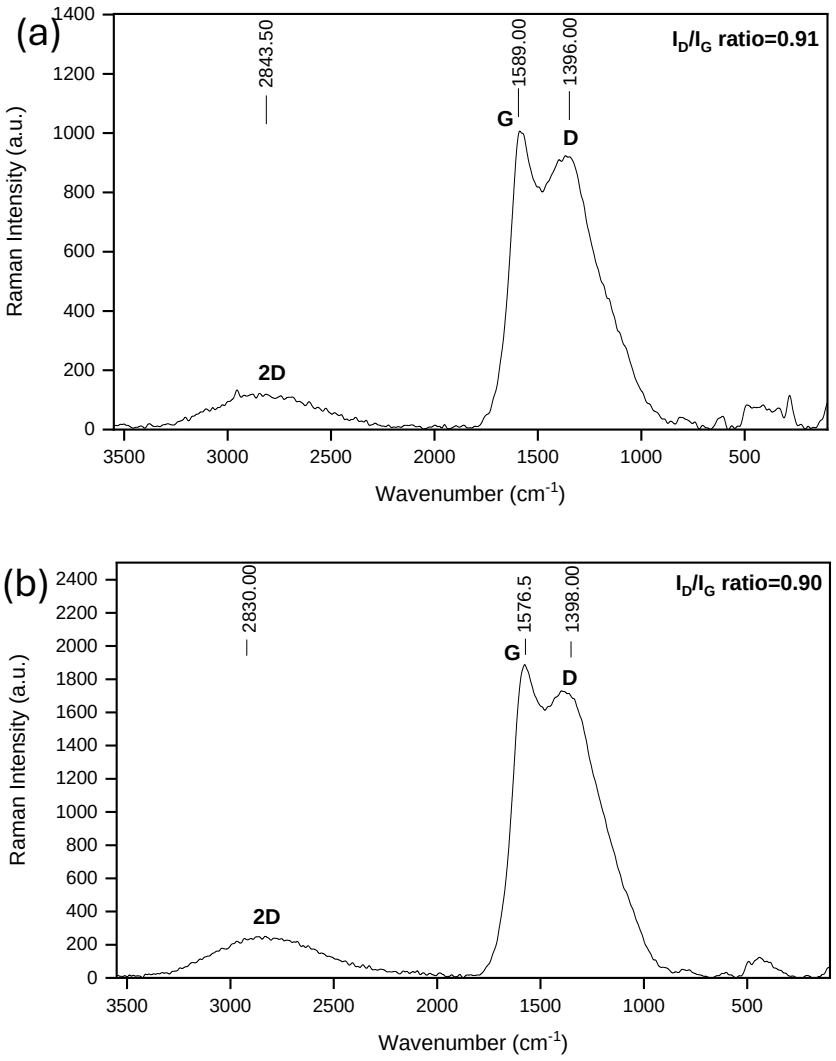

Figure 3.28 Raman spectra for quartz fibres decorated with bamboo-type CNTs grown by Cu-catalysed (a) T-CVD 510 °C and (b) T-CVD 410 °C. 2D-peaks, G-peaks, D-peaks and corresponding I_D to I_G ratios are included.

The occurrence of different types of carbon nanostructures, including bamboo-type CNTs, helical structures and amorphous nanofibres, was highlighted by numerous works in the literature when the CVD temperature is below the conventional 600–700 °C [288], [289]. However, while previous works on the Cu-catalysed synthesis below 550 °C

reported the growth of amorphous or poorly graphitized nanofibers [35], [170], [290] , which are distinguished from other nanostructures as they do not feature any internal hollow cavity, a graphitic structure appears to be present in the nanostructures synthesized in this work, with crystalline planes mainly arranged parallel to the CNT axis except for the ones constituting the bamboo joints (Figure 3.26b, d). Accordingly, Raman spectra (Figure 3.28) revealed the characteristic features of graphite-like (sp^2) carbon materials (G-band ~1580 cm^{-1}, D-band ~1340 cm^{-1} and 2D-band ~2700 cm^{-1}). The broadening of the peaks compared to CNTs grown through Fe-catalysed CVD reflects the higher degree of structural disorder [291]–[293] due the decrease of cluster (condensed benzene rings) sizes, higher cluster distribution and stress, and broadening of chemical bonding [294].

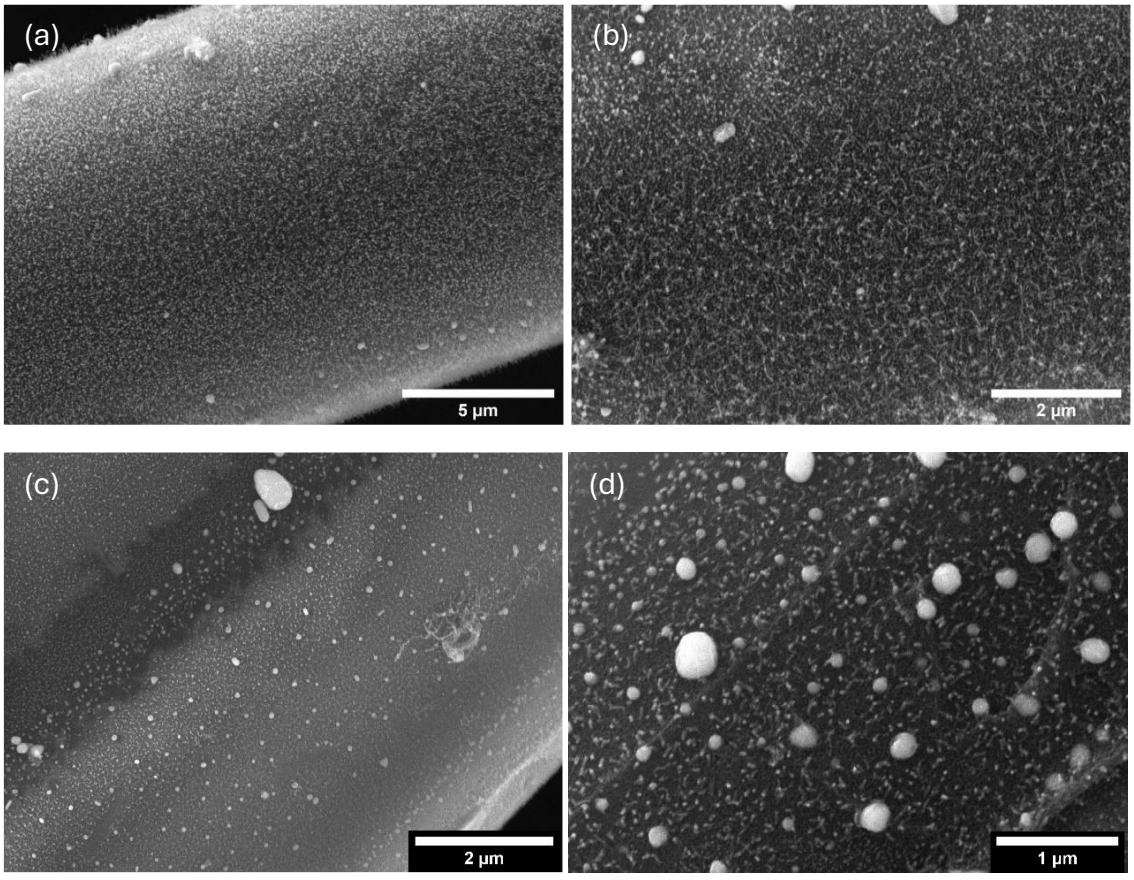

Figure 3.29 Representative SEM micrographs at different magnification detailing the morphology of the carbon nanostructures grown on quartz fibres following (a, b) PE-CVD 510 °C, and (c, d) PE-CVD 420 °C.

These outcomes demonstrate the ability of the copper catalyst to catalyse the synthesis of CNTs at much lower temperatures compared to Fe-based catalyst systems. In fact, the Fe-catalysed thermal growth on quartz fibres was only possible at temperatures above 600 °C, while plasma assistance was required to achieve the synthesis below 550 °C (PE-CVD 520/540 °C), as discussed in section 2.2 of Part III – Results and Discussion. Also, the *in-situ* catalyst generation approach developed on basalt fibres, exploiting the native Fe content of basalt, revealed a lower temperature limit for complete catalyst activation (460 °C) and required plasma assistance for the synthesis of CNTs at 510 °C. The obtained results, therefore, proved the possibility to achieve CNT synthesis below 550 °C through Cu-catalysed thermal CVD, providing a viable alternative to the use of PE-CVD.

The effect of the simultaneous use of plasma assistance and Cu catalyst was investigated by introducing a plasma power of 30 W during the synthesis step at 510 °C (PE-CVD 510 °C), as shown in Figure 3.29a-b. By properly adjusting the gas flow rates, the growth of a dense carpet of short nanostructures was achieved. As previously observed for CNTs synthesized through Fe-catalysed PE-CVD on quartz fibres, CNTs with a shorter length (~0.1 μm) were obtained through PE-CVD 510 °C compared to T-CVD 510 °C, supporting the observations of a lower growth rate during PE-CVD previously discussed for the Fe-catalysed syntheses on quartz fibres (see section 2.2 of Part III – Results and Discussion). PE-CVD at lower temperature (PE-CVD 420 °C) led only to the nucleation of sparse, extremely short (up to 80 nm) CNT sprouts under the adopted process conditions (Figure 3.29). TEM investigation on individual carbon nanostructures synthesized through PE-CVD 510 °C revealed the formation of bamboo-type CNTs with average diameters of 27.2 ± 7.2 nm, but with a more irregular structure than the one observed after the thermal processes (Figure 3.30a-b). Moreover, the formation of amorphous carbon nanostructures with diameters exceeding 70 nm and no hollow cavities was also observed (Figure 3.30c-d). Based on these findings, the lower value of I_D/I_G ratio measured in the Raman spectrum of the PE-CVD 510 °C sample (Figure 3.31) can be ascribed to the higher amorphous and disordered character of the nanostructures synthesized through this method, in an opposite trend as compared to highly graphitized materials. As established by Ferrari and Robertson [295], while the G peak intensity represents the in-plane bond-stretching motion of pairs of sp^2 carbon atoms (not requiring

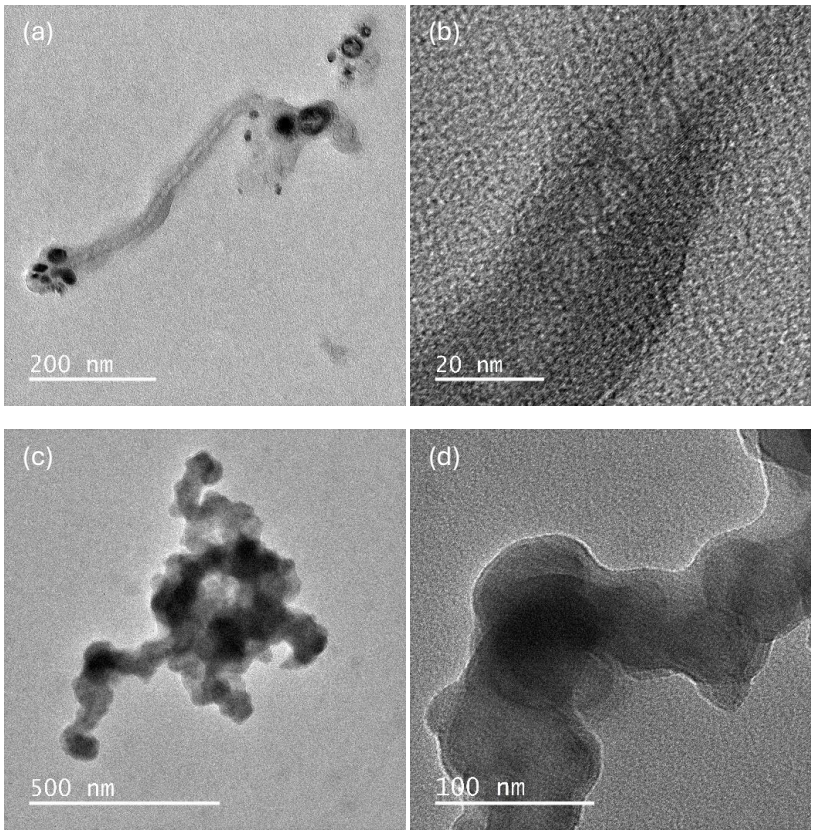

Figure 3.30 BF TEM micrographs at different magnification of (a, b) bamboo-type CNTs and (c, d) amorphous nanostructures grown on quartz fibres following Cu-catalysed PE-CVD 510 °C.

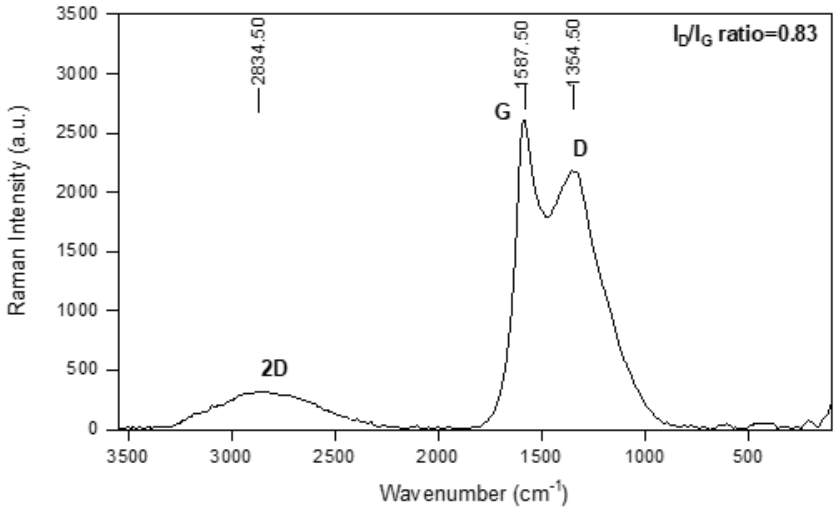

Figure 3.31 Raman spectrum for quartz fibres subjected to PE-CVD 510 °C. 2D-peak, G-peak, D-peak and corresponding I_D to I_G ratio are included.

the presence of sixfold rings), the D peak is a breathing mode of A_{1g} symmetry, and D peak intensity is strictly connected to the presence of aromatic rings. Since this mode is not present in perfect graphite, the D peak increases with disorder for highly graphitized carbon. Conversely, in highly disordered materials, the number of aromatic rings decreases more rapidly than the number of sp^2 carbon atoms, so the D peak intensity becomes smaller than the intensity of the G peak. Therefore, for disordered carbon materials, a decrease of I_D/I_G represents lower quality carbonaceous material (fewer aromatic rings), such as for the sample produced through PE-CVD 510 °C compared to T-CVD 510 °C and T-CVD 420 °C.

Although not optimized, the obtained results confirm the possibility of achieving nanostructure growth by combining the use of a copper catalyst and PE-CVD. However, the additional level of process complexity introduced by plasma assistance compared to thermal CVD suggests the need for a careful optimization of the process parameters specific to the glow discharge in order to achieve an optimal growth [239]. These parameters are expected to affect the catalytic activity of the copper catalyst by influencing the size and distribution of Cu nanoparticles [174], [286] as well as the poisoning rate [239], thus playing a critical role in shaping the outcome of the growth process.

Chapter 4.

Applications of CNT-modified fibres

In this chapter, the properties of CNT-modified fibres are investigated with a focus on two potential application fields: (i) the use as reinforcement for structural composite materials; (ii) the use in electrochemical applications, as those for environmental remediation activities (i.e., electrochemical generation of hydrogen peroxide) and for energy harvesting and storage. Although presented separately, the properties of CNT-modified fibres showcased in this investigation could be exploited simultaneously for the development of high-performance structural composites with integrated multifunctionalies, which meet the requirements of a wider class of industrial applications.

4.1. Structural composite materials

The incorporation of CNTs onto the surface of reinforcing fibres is often reported in the literature as an effective strategy to improve the mechanical properties of the resulting polymer composite material [106]. However, the high temperatures (600 – 1000 °C) required for the direct CVD growth of CNTs often cause a severe degradation of the tensile properties of the fibre substrate, thus limiting or even negatively affecting the mechanical properties of the final composite [110]. In the previous chapters of this research work, different strategies were proposed to achieve the synthesis of CNTs on reinforcing fibres at temperatures below 550 °C, thus mitigating the thermal conditions to which the fibre substrate is exposed. To verify the effectiveness of these strategies in preserving the fibre tensile properties, the mechanical properties of single fibres following the exposure to CVD process conditions are discussed here-in and compared to those of as-received fibres.

In addition to the tensile properties of reinforcing fibres, the adhesion at the fibre/matrix interface plays a key role for the mechanical performance of the resulting composite [72],

[73]. The final bond at the fibre/matrix interface is the result of different microstructural mechanisms, involving physical-chemical and frictional contributions [77]. At the single fibre level, the strength of the bond at the fibre/matrix interface is usually expressed in terms of interfacial shear strength (IFSS), which can be experimentally characterized by several methods, including micro-debonding tests, fibre pull-out tests, fibre fragmentation tests, or fibre push out tests [73]. The advantages of CNT incorporation on the fibre surface in terms of improved interfacial shear strength (IFSS) have been widely reported in the literature, reaching increments of IFSS with epoxy up to 175% [13], [14], [296] compared to commercially sized fibres. The detected improvements in interfacial adhesion have been mainly attributed to the increased surface area and mechanical anchoring derived by CNT introduction on the fibre surface. The wettability of the fibre surface by the polymer matrix is also expected to play an important role for the formation of a strong bonding at the fibre/matrix interface during the impregnation phase of composite manufacturing. However, the effect of CNTs on the fibre wettability has been rarely investigated in the literature, with only a few works focused on CNT-decorated carbon fibres [297], [298]. Consequently, a detailed investigation of the surface and wetting properties of quartz fibres was carried out in this work prior and after CNT introduction. A recently developed tensiometric procedure [192] was adopted to determine the contact angles with different test liquids (water, diiodomethane and epoxy resin), the surface free energy of the fibre and the work of adhesion with an epoxy matrix.

4.1.1. Tensile properties of single fibres

4.1.1.1. Quartz fibres

The deterioration of the mechanical properties of quartz fibres following high temperature exposure was thoroughly investigated in the first part of this research work, as reported in Chapter 1 of Part III – Results and Discussion. After heat treatment in the typical temperature range of thermal CVD (600–800 °C), the tensile strength of quartz fibres was found to lose up to 86% of its original value, while the fibre bulk properties (Young's modulus, hardness, density) were found to be relatively stable up to 800 °C. Therefore, the severe degradation of tensile strength experienced by quartz fibres after high

temperature exposure motivated the development of different strategies for achieving CNT synthesis at lower temperatures.

In Chapter 2 of Part III – Results and Discussion, the use of a PE-CVD technique was proved to allow the synthesis of CNTs on quartz fibres at temperatures as low as 520–540 °C. To evaluate the effects of this process and of the high temperature thermal counterpart, referred to as PE-CVD 520/540 °C and T-CVD 620/640 °C respectively, on the fibre mechanical strength, single fibre tensile tests were carried out on as-received quartz fibres exposed to the CVD process, without any external catalyst deposition. This procedure, allowing to assess the combined effect of temperature and atmosphere on the fibre properties, was adopted to facilitate the handling of single fibres following the synthesis process. In fact, CNT-decorated fibres tend to stick together due to interactions between CNTs, hindering the extraction of single fibres from the fibre bundle for the preparation of tensile testing samples. This issue, combined with the severe fibre strength loss after high temperature exposure, made sample preparation extremely difficult in the case of CNT-modified fibres, which easily break into short fragments during handling. Although the adopted procedure did not involve the preliminary dipping step of the iron catalyst, the effect of this step on the mechanical properties of the fibre are expected to be negligible, in accordance with the findings by Lilli et al. [234] for basalt fibres and by the Luca et al. [223] for quartz fibres.

The results of the tensile tests performed on quartz fibres exposed to the two CVD processes are reported in Table 4.1. High-temperature T-CVD 620/640 °C led to a strength loss of 74%, which compares perfectly with the strength loss observed for quartz fibres heat-treated at 600 °C in air atmosphere, reported in section 1.1 of Part III – Results and Discussion. These outcomes evidence a similar strength degradation effect irrespective of the different gas environments in which the thermal exposure occurred. Similarly to quartz fibres heat-treated in air atmosphere, the thermal strength loss of CVD-treated quartz fibres is expected to arise from sizing degradation and consequent exposure and growth of surface defects at temperatures above 600 °C, while no modifications of the fibre core are likely to occur. As a confirmation, TEM investigation and EELS maps of CNT-decorated fibres (Figure 4.1) did not evidence any localized crystallization nor

segregation phenomena in the region below the fibre surface. In accordance with the findings reported in Chapter 1 of Part III – Results and Discussion for quartz fibres heat-treated in air atmosphere, a totally amorphous structure and a homogeneous chemical composition towards the core were observed for T-CVD-treated quartz fibres. As expected, this suggests that thermal exposure at CVD conditions did not affect the fibre bulk properties (Young's modulus, hardness, density) similarly to what observed for quartz fibres heat-treated up to 800 °C.

Table 4.1 Results of tensile tests for as-received quartz fibres (QFs) and quartz fibres exposed to the CVD protocols optimized for the Fe-catalysed thermal (T-CVD 620/640 °C) and plasma assisted (PE-CVD 520/540 °C) synthesis of CNTs. The results are expressed in terms of average values (average value/standard deviation) and Weibull characteristic parameters.

Sample	**Diameter (μm)**	**Tensile strength (MPa)**	**Characteristic life [MPa]**	**Shape parameter**
As-received QFs	14.3/0.3	1974.5/364.4	2125.3	6.2
T-CVD 620/640 °C	14.8/0.5	518.3/117.8	563.2	5.2
PE-CVD 520/540 °C	14.5/0.6	1888.1/374.7	2042.3	5.7

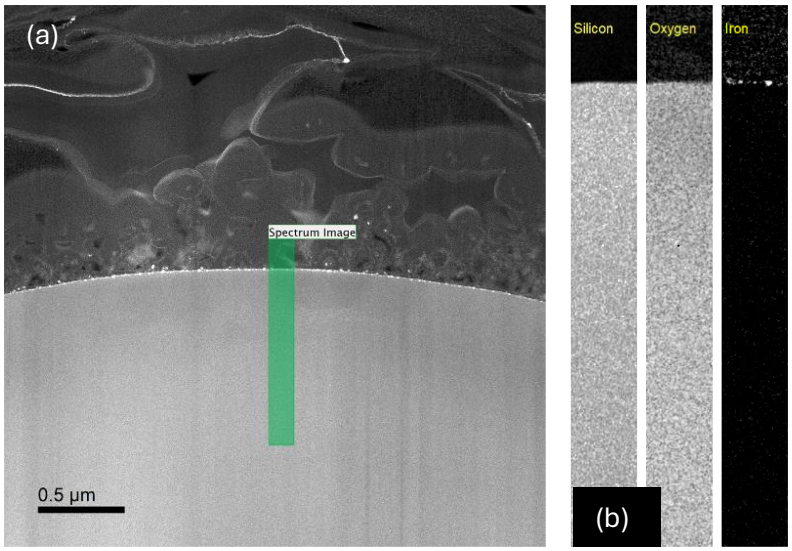

Figure 4.1 (a) HAADF STEM micrograph and (b) EELS map of O, Si and Fe for a CNT-decorated quartz fibre following T-CVD 620/640 °C.

As regards quartz fibres exposed to the PE-CVD 520/540 °C process, a minimal strength loss of around 5% was measured indicating that quartz fibre retained almost entirely their original strength (Table 4.1). This outcome reveals that a temperature reduction of around 100 °C was sufficient to preserve the tensile strength of quartz fibres, demonstrating the effectiveness of the PE-CVD strategy for producing CNT-decorated quartz fibres with preserved mechanical properties.

The dispersion of the tensile strength values was analysed through a two-parameter Weibull distribution. While the values of the characteristic strength vary similarly to the average values of the tensile strength with the thermal treatments, the values of the shape parameter give information about the dispersion of the tensile strength data around the characteristic value. The higher is the value of the shape parameter, the lower is the dispersion of the strength values and, therefore, the higher is the reliability of the material. The shape parameter for the tensile strength of thermally treated quartz fibres (Table 4.1) was found to be lower than the value of as-received quartz fibres, indicating a wider dispersion of experimental data. Higher CVD temperatures led to lower values of the shape parameter, indicating that the temperature reduction allowed by PE-CVD not only preserved the mechanical strength of the fibres but also mitigated the dispersion of tensile strength values, thus leading to a more reliable material.

Table 4.2 Results of tensile tests for as-received quartz fibres (QFs), heat-treated quartz fibres at 300 °C for 1 hour in air (HT 300 °C), and quartz fibres exposed to the CVD protocols optimized for the Cu-catalysed thermal synthesis of CNTs at 510 °C (T-CVD 510 °C) and at 420 °C (T-CVD 420 °C). The results are expressed in terms of average values (average value/standard deviation) and Weibull characteristic parameters.

Sample	**Diameter (µm)**	**Tensile strength (MPa)**	**Characteristic life [MPa]**	**Shape parameter**
As-received QFs	14.3/0.3	1974.5/364.4	2125.3	6.2
HT 300 °C	14.8/0.7	1869.3/408.3	2031.6	5.4
T-CVD 510 °C	14.4/0.5	1150.5/294.7	1261.8	4.6
T-CVD 420 °C	14.7/0.7	1243.9/289.8	1353.3	5.2

The investigation of the tensile properties was extended also to fibres subjected to the CVD conditions optimized for Cu-catalysed thermal growth processes (T-CVD 510 °C and T-CVD 420 °C) reported in section 3.2 of Part III – Results and Discussion. While no external catalyst deposition –expected to have no significant effect on the mechanical properties of quartz fibres as supported by the findings by Lilli et al. [234] for basalt fibres– was carried out on as-received fibres to avoid nanostructure growth, the intermediate oxidation treatment at 300 °C for 1 hour in air atmosphere was performed prior to each CVD process. Table 4.2 reports the average values of the fibre strength measured through single fibre tensile tests on as received quartz fibres, fibres exposed to the pre-treatment at 300 °C, and fibres exposed to both the pre-treatment at 300 °C and the synthesis steps at 510 °C and 420 °C. The results show that the pre-oxidation step was responsible for only a slight decrease (~5%) in the tensile strength of quartz fibres, while a more relevant strength degradation was detected after the CVD processes, with strength losses of ~42% following T-CVD 510 °C and of ~37% following T-CVD 420 °C. These findings confirm that, compared to conventional Fe-catalysed thermal CVD (T-CVD 620/640 °C), the reduction of temperature below 550 °C allowed by the Cu catalyst was able to mitigate the loss of the fibre tensile strength. However, the CVD conditions optimized for the Cu-catalysed syntheses were found to affect the tensile strength of quartz fibres to a greater extent than Fe-catalysed PE-CVD 520/540 °C, despite the lower process temperatures. Moreover, a wider dispersion of experimental data was highlighted by the lower values of the Weibull shape parameter (Table 4.2). These outcomes can be ascribed to the longer duration required for the Cu-catalysed processes (~1 hour) compared to Fe-catalysed PE-CVD 520/540 °C (~15 minutes). In fact, the strength loss is not only dependent on temperature but also on time. As regards glass fibres, a sudden strength drop with time has been reported, followed by a minimum steady state reached after a prolonged exposure that depends on the specific temperature level [21]. Accordingly, in the work by Sarasini et al. [67], a treatment time of 1 hour was selected for basalt fibres to ensure the conditions for steady-state loss at temperatures in the range 200–600 °C. Therefore, it is likely that the ~1 hour exposure during the Cu-catalysed processes –preceded by 1 hour exposure at 300 °C– allowed to reach the minimum steady-

state strength at each treatment temperature (i.e., 300 °C, 420 °C and 510 °C). Conversely, the ~15 min exposure above 500 °C optimized for the Fe-catalysed PE-CVD limited the strength loss due to a shorter duration than that required to reach the steady state. In terms of damage mechanisms, it is likely that such a short exposure limited the loss of the organic sizing and the consequent thermally-induced growth of surface flaws which, on the other hand, are expected to be at play after 1 hour exposure at temperatures of 400–500 °C, in accordance with the thermogravimetric analysis reported in section 1.2 of Part III – Results and Discussion.

4.1.1.2. Basalt fibres

In this work, basalt fibres have been adopted as a substrate for the synthesis of CNTs to demonstrate an innovative catalyst approach, consisting of exploiting the native iron content of basalt as an *in-situ* catalyst for CNT growth, as described in section 3.1 of Part III – Results and Discussion. This approach, referred to as *in-situ* catalyst generation, has been investigated in combination with a PE-CVD technique to achieve the growth of vertically aligned CNTs (VA-CNTs) on basalt fabrics at low temperatures (below 550 °C). After a careful tuning of the process parameters, a uniform coverage of dense VA-CNT forests was obtained at temperatures as low as 460 °C and 510 °C for the annealing step and synthesis step, respectively, as opposed to the temperatures above 700 °C reported in a previous work for the synthesis through thermal CVD [36].

Table 4.3: Results of tensile tests for as-received and thermally-treated single basalt fibres (BFs) in terms of average values (average value/standard deviation) and Weibull characteristic parameters.

Sample	**Diameter (µm)**	**Tensile strength (MPa)**	**Characteristic life [MPa]**	**Shape parameter**
As-received BFs	14.6/1.9	2235.1/286.3	2369.3	7.9
PE-CVD 460/510 °C	14.8/1.3	1452.6/461.3	1612.4	3.6

The effect of the synthesis process, referred to as PE-CVD 460/510 °C, on the mechanical properties of the fibre substrate was assessed through single fibre tensile tests. The results of the tests carried out on single fibres extracted from as-received fabrics and fabrics exposed to the CVD conditions are reported in Table 4.3 in terms of average values, standard deviation and Weibull distribution parameters, i.e., characteristic life and shape parameter. Analogously to the procedure adopted for quartz fibres, described in the previous paragraph (section 4.1.1.1), the basalt substrate was exposed to the CVD environment (i.e., temperature and atmosphere) without any alkaline pre-etching of the fibre surface, in order to avoid the activation of the native iron as catalyst and, therefore, hinder the growth of CNTs during the process. As pointed out for quartz fibres, this procedure discards the effect of the alkaline pre-treatment on the final strength of basalt fibres which, according to Sarasini et al. [36], accounts for a negligible 4% reduction in the average tensile strength.

The results of the tensile tests (Table 4.3) show an average strength loss of 35% for basalt fibres exposed to PE-CVD 460/510 °C. This outcome reveals that, although mitigating the thermal strength loss observed after thermal CVD above 700 °C [36], the exposure to temperatures above 450 °C during the CVD process still caused a non-negligible reduction of the fibre strength. Moreover, Weibull shape parameter was found to decrease by around 55%, indicating a significantly wider dispersion of tensile strength data compared to as-received fibres. This is in accordance with previous studies reporting consistent degradation of the fibre strength at temperatures of 400–500 °C both in inert and air atmospheres [29], [67], [262] as well as a reduction in Weibull shape parameter of over 50% after heat treatment [29].

Xing et al. [262] studied the evolution of the tensile strength of basalt fibres after exposure for 1 hour in the temperature range 100–1000 °C, highlighting a severe drop in the fibre strength at temperatures above 200 °C. The thermal degradation of the fibre strength below 400 °C was mainly ascribed to sizing degradation while higher temperatures are believed to determine structural rearrangements driven by the release of the high potential energy stored in the glass network during extremely rapid cooling in fibre manufacturing. The occurrence of structural changes in the temperature range 400–600 °C was confirmed

by Lilli et al. [29] who observed an increase in the average elastic modulus as well as local radial heterogeneities in the fibre structure and elastic modulus detected though high-speed nanoindentation measurements on the fibre cross-section.

The measured strength loss as well as the occurrence of bulk structural rearrangements differentiates the behaviour of basalt fibres from that of quartz fibres, which exhibited relatively stable bulk properties and a homogeneous structure up to 800 °C as well as a negligible reduction in tensile strength after PE-CVD at 520–540 °C. This highlights a lower temperature resistance of basalt fibres compared to quartz fibres, indicating that lower CVD temperatures should be adopted for preserving the fibre strength. The structural rearrangement phenomena expected to occur in basalt fibres during heat treatment above 400 °C involve the simultaneous relaxation of both excessive enthalpy and structural anisotropy [265], [273] as well as the diffusion and segregation of Fe^{2+} ions [260], [262]. The latter phenomenon is exploited in the *in-situ* catalyst generation approach, which was found to require a minimum temperature of 460 °C to effectively lead to a uniform distribution of active iron nanoparticles seeding CNT growth. This seems to indicate that a certain reduction in tensile strength is inevitable with this approach, as it necessitates process temperatures sufficiently high to trigger structural rearrangements in the glass network of basalt. It is worth noting that the phase separation of iron during the annealing step might also affect the final strength of the fibre, as the presence of iron oxides in the glass network was reported to play a key role for enhancing the mechanical performance of basalt fibres compared to that of glass fibres [68].

4.1.2. Surface free energy and work of adhesion

The investigation of the fibre surface properties was carried out through tensiometric tests on as-received quartz fibres, CNT-modified quartz fibres following PE-CVD 520/540 °C, and CNT-modified quartz fibres following T-CVD 620/640 °C. These samples were selected to showcase not only the effects of CNT modification of the fibre surface but also of different CNT morphologies on the fibre wetting properties in comparison to those of commercially sized fibres. As the characteristic of interest for these samples is the CNT morphology rather than the CVD process used for the CNT growth, CNT-modified

samples will be addressed as: s-CNT-QFs for fibres decorated with short (up to 3 μm) radially aligned CNTs produced through PE-CVD 520/540 °C, and l-CNT-QFs for fibres decorated with long (up to 80 μm) arrays of vertically aligned CNTs. Commercially sized quartz fibres will be referred to as QFs.

Table 4.4 Results of tensiometric tests for commercially sized quartz fibres (QF), quartz fibres decorated with short CNTs (s-CNT-QF), and quartz fibres decorated with long CNTs (l-CNT-QF). The table reports the values of the fibre radius (calculated from the wetted perimeter), and of the advancing (θ_{adv}), receding (θ_{rec}), and static (θ_{stat}) angles for each test liquid, expressed in terms of average values (standard deviations).

	n-hexane	**Water**			**Diiodomethane**			**Epoxy resin**		
Sample	**Radius [μm]**	**θ_{adv} [°]**	**θ_{rec} [°]**	**θ_{stat} [°]**	**θ_{adv} [°]**	**θ_{rec} [°]**	**θ_{stat} [°]**	**θ_{adv} [°]**	**θ_{rec} [°]**	**θ_{stat} [°]**
QF	7.4 (0.4)	80.9 (7.5)	18.9 (8.7)	50.8 (7.9)	55.8 (4.1)	29.9 (11.1)	37.3 (8.5)	64.8 (1.2)	55.3 (3.9)	55.1 (2.6)
s-CNT-QF	8.2 (0.8)	125.3 (15.2)	34.2 (16.7)	83.1 (14.7)	54.6 (6.0)	32.5 (9.3)	38.8 (5.3)	61.3 (6.1)	57.6 (6.1)	54.4 (7.7)
l-CNT-QF	19.7 (9.5)	154.8 (16.9)	82.8 (32.0)	122.1 (14.4)	33.6 (1.5)	21.6 (3.5)	25.2 (5.8)	51.2 (3.8)	39.2 (7.0)	41.6 (8.1)

Table 4.4 reports the average values and standard deviations of the contact angles measured for at least 5 fibres from each set of samples (commercially sized QFs, s-CNT-QFs, l-CNT-QFs) by means of tensiometric tests with three test liquids (water, diiodomethane and epoxy resin), whose surface energies are detailed in section 1.3 of Part II – Materials and Methods. Prior to the measurement, the wetted perimeter was assessed for each tested fibre by using a totally wetting liquid (n-hexane), having a contact angle equal to 0°. The average values of the fibre radius calculated from these tests under the hypothesis of a circular cross-section, reported in Table 4.4, are in accordance with the values measured through optical microscopy for as-received quartz fibres (Table 4.1) and with the CNT length measured through SEM, reported in chapter 2 of Part III – Results and Discussion.

As expected from the theory of wetting [214], the relation $\theta_{adv} > \theta_{stat} > \theta_{rec}$ was found to be respected for all test liquids and fibres, except for the static contact angle of s-CNT-QFs with the resin which is outside this range. This can be a result of the relatively high standard deviation and of the low hysteresis, i.e. the small difference between advancing and receding angles.

The presence of CNTs was found to increase the contact angle with water compared to sized fibres, in agreement with previous observations that CNT films produced by CVD are hydrophobic [299], [300] due to the presence of C–H terminations on their surface [301]. Fibres with longer CNTs exhibited a higher contact angle (122.1°) than shorter CNTs (83.1°), indicating a pronounced hydrophobicity, in accordance with the previously reported superhydrophobic behaviour of VA-CNTs arrays [302]. As regards diiodomethane, no significant difference in contact angle was observed for s-CNT-QFs compared to sized quartz fibres, whereas for l-CNT-QFs the contact angle was found to decrease. Similarly, hardly any difference between the contact angles of sized quartz fibres and s-CNT- QFs was observed in the case of the epoxy resin, while a decrease in contact angle was measured for l-CNT-QFs. This similarity can be related to the mainly dispersive character of both test liquids. The receding and advancing contact angles showed similar trends to the those of the static contact angle. The difference of these two contact angle values, i.e., the contact angle hysteresis, significantly increased for CNT-decorated fibres, particularly with water. This change can be attributed to the increase in chemical surface heterogeneity and surface roughness [298], [303].

Knowing the static contact angles (θ_e) with all the liquids, along with the liquid total surface energy (γ_L) and its dispersive (γ_L^d) and polar (γ_L^p) components, it was possible to plot the X–Y graph from Eq. 4.1 according to Owens and Wendt method, as explained in Section 3.11 of Part II – Materials and Methods.

$$\frac{\gamma_L(1+\cos\theta_e)}{2\sqrt{\gamma_L^d}} = \sqrt{\gamma_s^p}\left(\frac{\sqrt{\gamma_L^p}}{\sqrt{\gamma_L^d}}\right) + \sqrt{\gamma_S^d} \tag{4.1}$$

The obtained graphs are reported in Figure 4.2, while Table 4.5 reports the values of the polar (γ_s^p) and dispersive (γ_S^d) components of the fibre surface free energy, as determined

from the slope and the y-intercept of the linear fit. The correlation coefficient of the linear fit (R^2) was found to be quite close to 1 for sized QFs and s-CNT-QFs indicating that the linear regression well describes the distribution of data (Figure 4.2a-b). Differently, for l-CNT-QF a negative slope of the curve, which has no physical meaning ($\sqrt{\gamma_S^p} \geq 0$), and a relatively low correlation coefficient (around 0.86) were obtained, suggesting that the data are not well fitted by a linear model. As pointed out by Shalel-Levanon et al. [304], the validity of the Owens and Wendt method for the calculation of surface tensions of solids is limited to the range of contact angles for which $\sqrt{\gamma_S^p} \geq 0$ and $\sqrt{\gamma_S^d} \geq 0$. Although the use of a minimum of two liquids, including a totally dispersive one, allows to have a wide range of contact angles that results in physically meaningful solutions, negative values can be obtained for $\sqrt{\gamma_S^p}$ depending on the surface tension components of the liquids as well as on the contact angles. As an example, the graph reported by Shalel-Levanon et al. [304] (Figure 4.3) for two test liquids, i.e., water as the polar one and hexane as the dispersive one, reveals the possible combinations of contact angles for which $\sqrt{\gamma_S^p} \leq 0$. Therefore, it can be concluded that the high hydrophobic character of the l-CNT-QFs (contact angle with water of 122° ca.) combined with a good affinity for totally dispersive liquids as diiodomethane (contact angle of 25° ca.) and epoxy resin (contact angle of 42° ca) cannot be described by the Owens and Wendt method, being outside its validity range, suggesting the need of using either a different combination of test liquids or a different method for determining the surface free energy of this material. Consequently, only the values of the surface free energies calculated for sized quartz fibres (QFs) and s-CNT-QFs will be addressed in this discussion.

a)

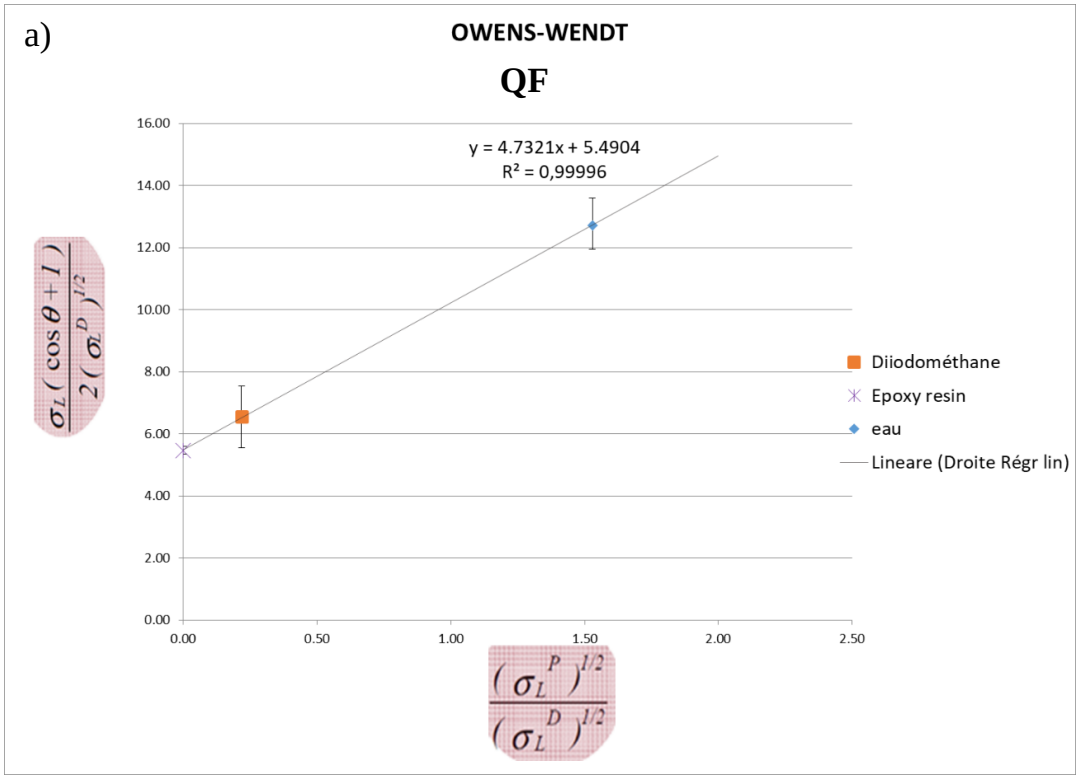
OWENS-WENDT
QF
y = 4.7321x + 5.4904
R² = 0,99996
16.00
14.00
12.00
10.00
8.00
6.00
4.00
2.00
0.00
0.00
0.50
1.00
1.50
2.00
2.50
Diiodométhane
Epoxy resin
eau
Lineare (Droite Régr lin)
$\frac{\sigma_L(\cos\theta+1)}{2(\sigma_L^D)^{1/2}}$
$\frac{(\sigma_L^P)^{1/2}}{(\sigma_L^D)^{1/2}}$

b)

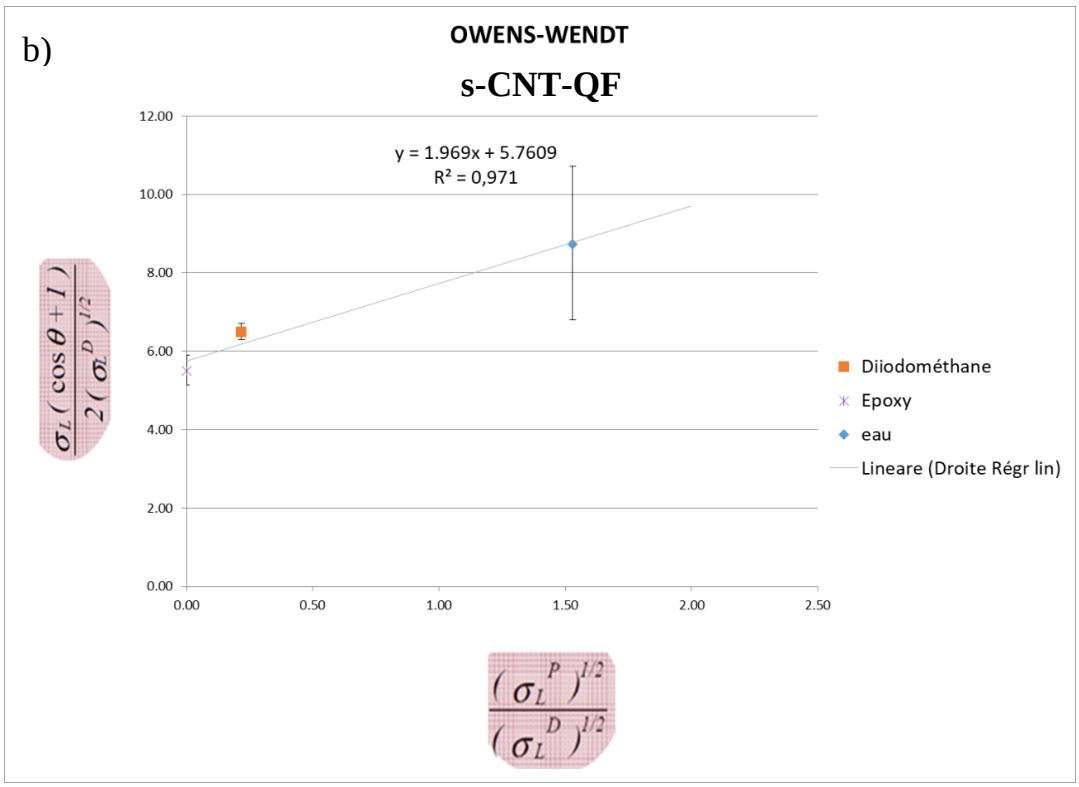
OWENS-WENDT
s-CNT-QF
y = 1.969x + 5.7609
R² = 0,971
12.00
10.00
8.00
6.00
4.00
2.00
0.00
0.00
0.50
1.00
1.50
2.00
2.50
Diiodométhane
Epoxy
eau
Lineare (Droite Régr lin)
$\frac{\sigma_L(\cos\theta+1)}{2(\sigma_L^D)^{1/2}}$
$\frac{(\sigma_L^P)^{1/2}}{(\sigma_L^D)^{1/2}}$

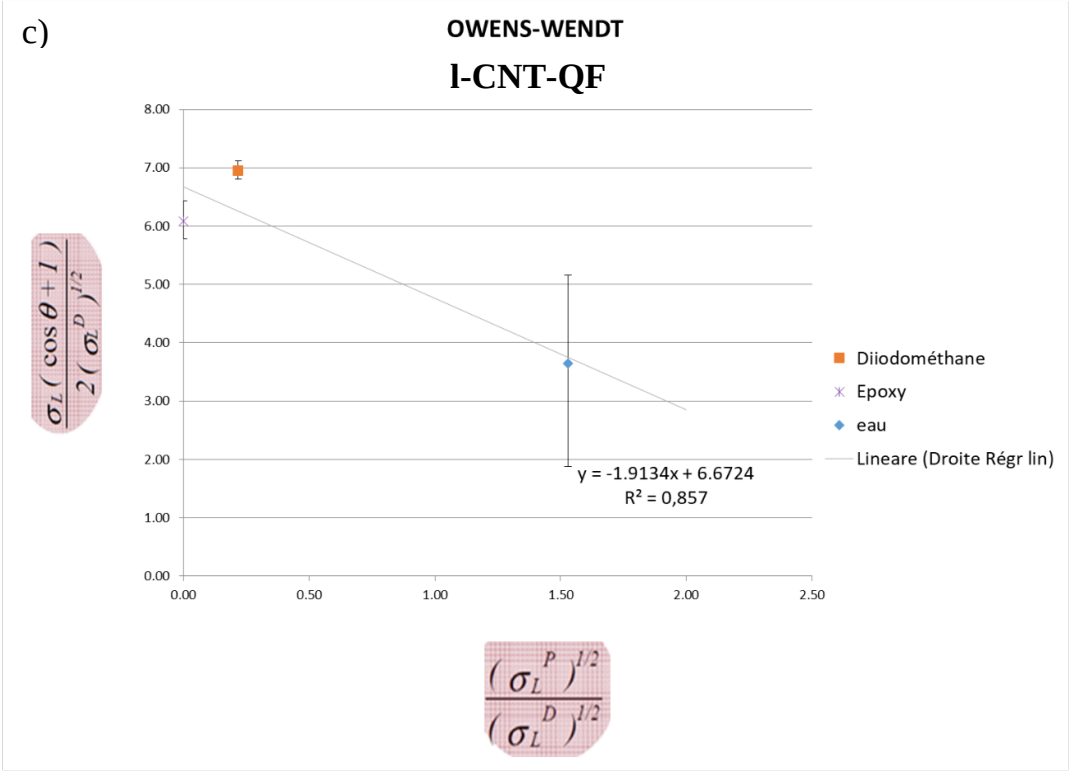

Figure 4.2 Linear fit according to Owens-Wendt equation for (a) sized quartz fibres, (b) quartz fibres decorated with short CNTs (s-CNT-QF), (c) quartz fibres decorated with long CNTs (l-CNT-QF).

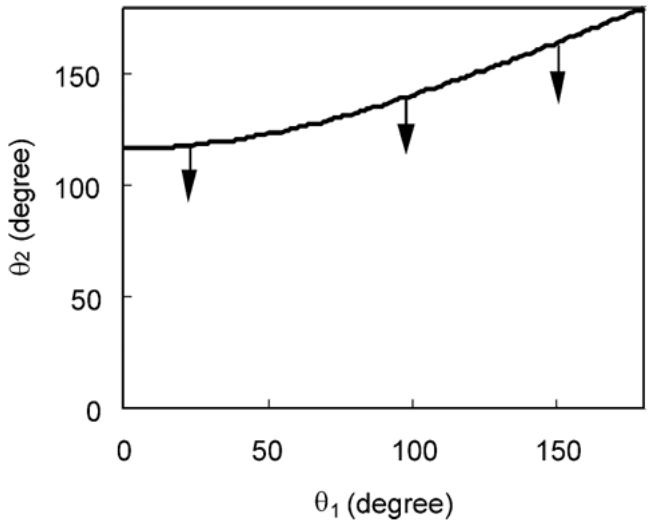

Figure 4.3 Combinations of contact angles that give $\sqrt{\gamma_S^p} = 0$ when hexane and water are used as the testing liquids, and the Owens and Wendt method is used for the calculations. θ1 and θ2 are

the contact angles with hexane and water, respectively. The allowed range, for which $\sqrt{\gamma_S^p} > 0$, is indicated by the arrows [304].

Table 4.5 Fibre surface energy (γ_s) and components (polar, γ_p, and dispersive, γ_d) calculated through Owens-Wendt equation. Work of adhesion (W_a) calculated according to different equations: Owens, Wendt, Rabel and Kaelble (OWRK), Wu and Young-Dupré (Y-D).

Sample	**γ_s [mN/m]**	**γ_p [mN/m]**	**γ_d [mN/m]**	**R^2**	**Dispersivity ratio**	**W_a [mN/m]**		
						OWRK	**Wu**	**Y-D**
QF	52.5 (6.0)	22.4 (4.1)	30.1 (1.9)	0.99996	0.57	76.4 (2.5)	74.3 (3.0)	76.1 (1.8)
s-CNT-QF	37.1 (3.5)	3.9 (4.5)	33.2 (2.4)	0.97114	0.90	80.2 (1.6)	78.8 (1.9)	76.6 (5.2)
l-CNT-QF	-	-	-	0.85693	-	-	-	84.6 (4.5)

Commercially sized quartz fibres have a surface free energy of 52.5 ± 6.0 mJ/m^2 with polar and dispersive components of 22.4 ± 4.1 mJ/m^2 and 30.1 ± 1.9 mJ/m^2, respectively. On the other hand, a total surface free energy of 37.1 ± 3.5 mJ/m^2 was calculated for s-CNT-QFs, which is in good agreement with the values reported in the literature for the surface energy of CNTs [305]–[307]. The obtained values show that the CNTs reduced the polar character of quartz fibres by 83%, while the dispersive component was slightly increased. This resulted in a change in the dispersivity ratio, i.e. the ratio between the dispersive and total surface energy, from 0.57 of sized QFs to 0.90 of s-CNT-QFs. Moreover, the total surface energy was reduced by 29% for s-CNT-QFs compared to untreated fibres. This trend has already been observed for the deposition of carbon nanotubes on carbon fibre surfaces [296], [303], [308].

The wetting behaviour of each set of fibres towards the epoxy resin was further analysed by calculating the work of adhesion W_A, which provides a quantitative measure of the wettability of the fibres towards the matrix and plays a role during processing for the

formation of fibre/matrix bonding within the final composite. The higher the W_A, the better would be the wettability and the quality of the adhesion between fibres and matrix. Three approaches were used to calculate the work of adhesion, based on the following equations:

$$W_a = \gamma_{LV}(1 + cos\,\theta) \tag{4.2}$$

$$W_A' = 2 \times \left(\sqrt{\gamma_S^d \times \gamma_L^d} + \sqrt{\gamma_S^p \times \gamma_L^p}\right) \tag{4.3}$$

$$W_A'' = 4 \times \left(\frac{\gamma_L^d \gamma_S^d}{\gamma_L^d + \gamma_S^d} + \frac{\gamma_L^p \gamma_S^p}{\gamma_L^p + \gamma_S^p}\right) \tag{4.4}$$

where Eq. 4.2 is Young-Dupré (Y-D) equation, Eq. 4.3 is according to Owens, Wendt, Rabel and Kaelble (OWRK) approach, and Eq. 4.4 is according to Wu approach.

According to the Young-Dupré approach (Eq. 4.2), the lower the contact angle the greater the work of adhesion and the wettability between the fibres and the epoxy matrix. Since the contact angles with the epoxy resin and the calculated work of adhesion W_A (Table 4.5) are similar for sized QFs and s-CNT-QFs, the Young-Dupré approach does not allow to discriminate the effect of short CNTs. On the other hand, as expected from the lower value of the contact angle with the resin, the value of Y-D work of adhesion for l-CNT-QFs highlights a higher affinity for the resin than sized QFs. When considering the polar and dispersive components of the surface free energies via the OWRK (Eq. 4.3) and Wu (Eq. 4.4) approaches, a slight improvement (5-6%) in the work of adhesion from the sized case is observed also for s-CNT-QFs. These increases can be ascribed to the higher dispersive character of CNT-modified QFs, which improves the affinity with the mainly dispersive epoxy resin. However, the reduction in total surface energy of s-CNT-QFs counterbalances the increased dispersive character resulting in a limited improvement in the work of adhesion, as previously observed for CNTs deposited on carbon fibres [308].

The results thus show that the introduction of CNTs significantly reduces the polar character of quartz fibres while slightly increasing the dispersive character. This is expected to improve the wettability towards liquids with a mainly dispersive character as confirmed by the increase in the Y-D work of adhesion with the resin for l-CNT-QFs and

the slight increase in the values of W_A for s-CNT-QFs calculated according to OWRK and Wu approaches. Although it was not possible to calculate the fibre surface free energy of l-CNT-QFs with Owens and Wendt method, the contact angles with the different test liquids provided useful information on the effect of density and length of the CNTs on the fibre wetting properties. L-CNT-QFs showed a pronounced hydrophobic behaviour and, as opposed to s-CNT-QFs, a reduction in the contact angles with both diiodomethane and the epoxy resin compared to sized QFs, thus indicating that a dense coverage of long VA-CNT forests leads to a higher affinity for liquids with a mainly dispersive character, as confirmed by the increase in the Y-D work of adhesion with the resin.

This investigation provided an insight into the contribution of CNT modification of the fibre surface to the fibre/matrix interfacial adhesion in terms of physical-chemical interactions. The nanostructuration of the fibre surface with CNTs was found to induce a modification of contact angles and surface free energy which can be ascribed to the modified surface chemistry, the increase of the local roughness and the enhancement of the fibre specific surface area [302]. These factors are expected to contribute to the enhancement of the interfacial adhesion strength along with the well-known effect of mechanical interlocking usually reported in the literature for CNT-modified fibres [100], [298].

4.2. Electrochemical applications

Achieving the surface modification of fibres with CNTs without compromising their mechanical performance paves the way for the design of high-performance composite materials with integrated multifunctionalities. In this section, the electrochemical properties of CNT-decorated fibres are investigated to showcase potential applications of these materials in the field of environmental remediation (through the electrochemical generation of hydrogen peroxide) and other electrochemical devices, particularly those for energy harvesting and storage such as supercapacitors.

Hydrogen peroxide is an environmentally friendly oxidant as it leaves no hazardous residues, finding extensive application in the field of wastewater treatment. Similarly to other carbon-based materials [309], [310], the presence of CNTs can catalyse the

production of hydrogen peroxide through an *in-situ* electrochemical reduction of oxygen [311], a strategy receiving extensive attention to overcome the high energy consumption and use of toxic chemicals of the current production process (the anthraquinone method), as well as the costs and risks associated with H_2O_2 transport, handling and storage. This peculiar property of CNTs could be exploited to extend the application of hierarchical fibre-reinforced polymers to the field of environmental remediation by combining the structural performances of these materials to the environmental remediation functionality.

Furthermore, the peculiar chemical and electrochemical properties of CNTs, coupled with their high electrical conductivity and surface area, may also offer the opportunity to develop multifunctional composite materials with simultaneous mechanical and energy storage/harvesting properties [10]. This could open possibilities for the development of structural electrochemical devices, such as batteries [132] and supercapacitors [131], a research field attracting extensive interest in recent years. In fact, structural electrochemical devices are desirable for applications in electric vehicles, aerospace, marine, and satellites, where they might enhance the system performance while allowing for a massive weight reduction [312]. Moreover, in the form of textiles, CNT-modified fabrics could potentially be used as flexible and stretchable supercapacitors or energy harvesting devices for wearable equipment [313].

4.2.1. Electrochemical generation of hydrogen peroxide

Carbon-based materials, including CNTs, have been demonstrated to be catalytically active towards the electrochemical production of hydrogen peroxide through the 2-electron pathway oxygen reduction reaction (Eq. 4.5):

$$O_2 + 2H_3O^+ + 2e^- \rightarrow H_2O_2 + 2H_2O \quad (4.5)$$

The introduction of CNTs on the surface of reinforcing fibres, therefore, might provide this distinctive characteristic to the hierarchical fibres, opening for potential applications in the field of environmental remediation. A preliminary electrochemical investigation was therefore carried out to verify this functionality for CNT-decorated quartz fibres following the T-CVD 620/640 °C process, because of the presence of a high loading of long CNT forests. A bundle of fibres with a length of around 5 cm and a weight of 71 mg

was used as the cathode. Figure 4.4a reports the results of the hydrogen peroxide electrogeneration tests in terms of the evolution of H_2O_2 concentration with time at different constant current intensities, ranging from 2 mA to 25 mA.

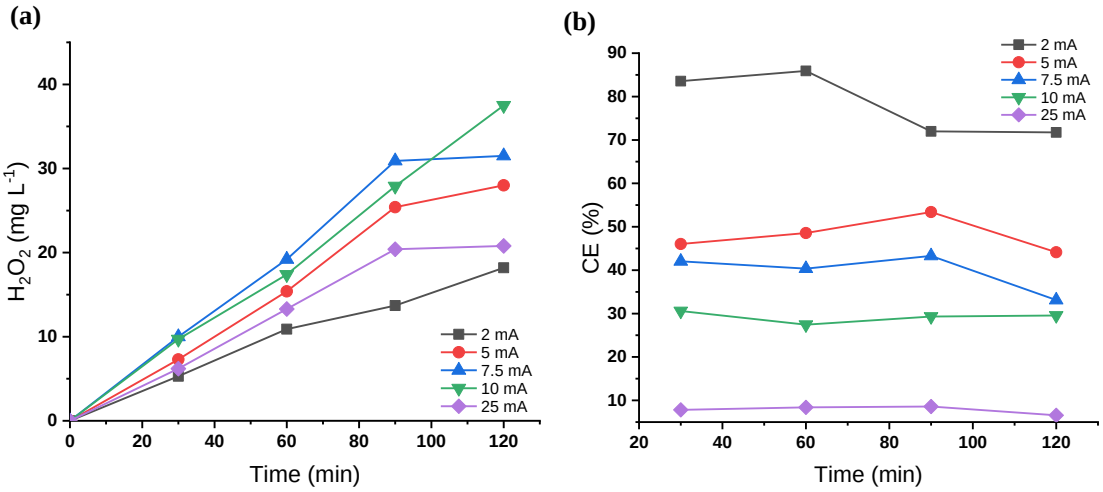

Figure 4.4 Hydrogen peroxide production on CNT-decorated quartz fibre electrode (T-CVD 620/640 °C) at different current intensities: (a) hydrogen peroxide accumulation, (b) current efficiency (CE). Conditions: [Na_2SO_4]=0.05 M; T=21±2ºC, cathode weight= 71 mg.

The results confirm the hydrogen peroxide production functionality of hierarchical quartz fibres, with the highest H_2O_2 concentration equal to 37.5 mg/L detected after 120 min at a current intensity of 10 mA. Furthermore, the calculated current efficiency (CE), whose evolution with time is reported in Figure 4.4b, reveals a performance comparable to that of typical carbon-based electrodes, such as graphite, carbon felt and reticulated vitreous carbon [310], for current intensities within the range 5–25 mA, as well as a maximum current efficiency at 2 mA, with an average value of 78% and a maximum value of 86% calculated after 60 minutes, which compares quite favourably with those reported in previous studies for CNT-based cathodes [314], [315].

The H_2O_2 accumulation curves exhibit a quasi-linear increase in H_2O_2 concentration with time up to 90 minutes, while for longer test durations a plateau seems to occur for most of the current intensities investigated, except for the tests at 2 mA and 10 mA. Accordingly, Figure 4.4b shows a decrease in the current efficiency at 120 min for the tests at 5, 7.5, and 25 mA. This behaviour evidences the occurrence of parasite reactions

that counterbalance H_2O_2 generation. These reactions may include the H_2O_2 reduction (Eq. 4.6), the four-electron oxygen reaction (Eq. 4.7), the hydrogen evolution (Eq. 4.8):

$$H_2O_2 + 2\,e^- \rightarrow 2OH^- \quad (4.6)$$

$$O_2 + 2H_2O + 4\,e^- \rightarrow 4OH^- \quad (4.7)$$

$$4H_2O + 4\,e^- \rightarrow 2H_2 + 4OH^- \quad (4.8)$$

According to Qiang et al. [316], no significant self-decomposition of H_2O_2 (Eq. 4.9) is expected under the process conditions adopted in this study, as it requires higher pH and temperatures:

$$2H_2O_2 \rightarrow 4H_2O + O_2 \quad (4.9)$$

The extent of parasitic reactions tends to increase with higher currents due to increased overpotential and mass transfer limitations, as high currents quickly deplete the available oxygen near the electrode surface, favouring water reduction. Consequently, the current efficiency at the highest tested current value of 25 mA was always below 10%.

Although the highest current efficiency was obtained for a current intensity of 2 mA, a current intensity of 5 mA was used for the following tests as a compromise between the current efficiency and production rate. The hydrogen peroxide production functionality was therefore demonstrated for CNT-decorated quartz fibres following the low-temperature PE-CVD process at 520-540 °C by testing a bundle of CNT-decorated fibres with a weight of 46 mg at a current intensity of 5 mA. The test was repeated also on as-received quartz fibres and Fe dip-coated quartz fibres (data not shown). As expected, no H_2O_2 production nor current flow was detected for samples without CNTs, confirming the sole contribution of CNTs to the H_2O_2 electrochemical generation functionality of hierarchical quartz fibres.

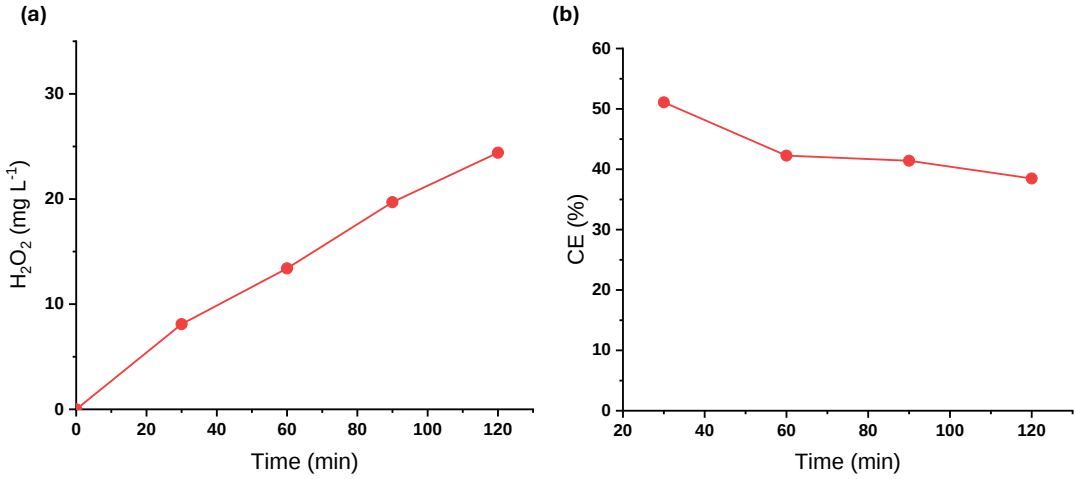

Figure 4.5 Hydrogen peroxide production on CNT-decorated quartz fibre electrode (PE-CVD 520/540 °C): (a) hydrogen peroxide accumulation, (b) current efficiency (CE). Conditions: [Na_2SO_4]=0.05 M; T=21±2ºC, I=5 mA; PE-CVD cathode weight=46 mg.

The test performed on the PE-CVD sample confirmed once again the ability of CNT-decorated fibres to produce H_2O_2 (Figure 4.5a), with a H_2O_2 concentration equal to 24.4 mg/L after 120 minutes and an average faradaic efficiency of 43% (Figure 4.5b). It is worth noting that these results are not directly comparable with the ones obtained for the T-CVD sample, as the different weights and CNT morphologies (i.e., length and density) of the tested samples are expected to produce a difference in the current density experienced by the cathode (i.e., the current per unit of surface area), due to the different total surface area which was not measured during this preliminary investigation. To allow for a comparison between the T-CVD sample and PE-CVD sample, therefore, the results are provided in terms of relative H_2O_2 concentration per weight of cathode in Figure 4.6. This representation of data reveals a slightly higher relative concentration of H_2O_2 for the PE-CVD sample compared to that obtained with the T-CVD cathode. Accordingly, the relative faradaic efficiency per weight of cathode (Figure 4.6b) appears to be higher for the PE-CVD sample. The marked decreasing trend with time might be due to the need for a screening with varying current intensity to identify the best current conditions for the PE-CVD cathode, as a current intensity of 5 mA might not be optimal for this sample. In fact, due to the lower weight of the PE-CVD cathode (i.e., lower number of fibres in the sample) and lower CNT length revealed by the SEM investigation, the total surface area

of this cathode is expected to be lower than that of the T-CVD cathode, resulting in a higher current density which might more easily favour the occurrence of parasite reactions. It is worth noting that the reported results must be intended as a pre-screening highlighting a potential multifunctionality of CNT-decorated quartz fibres. A more detailed investigation will need a measure of the total surface area of the cathodes, for example by using the Brunauer-Emmett Teller (BET) method based on nitrogen adsorption/desorption isotherms [314], [315], which is beyond the purpose of the preliminary investigation carried out in this study. Moreover, further investigation would be needed to comprehensively study the effects of the operative parameters, including current density, pH, temperature, feeding gas, as well as the stability of the electrode following continuous runs, with tests carried out both on single fibres and hierarchical fibre-reinforced composites to assess their suitability as cathodes for H_2O_2 production.

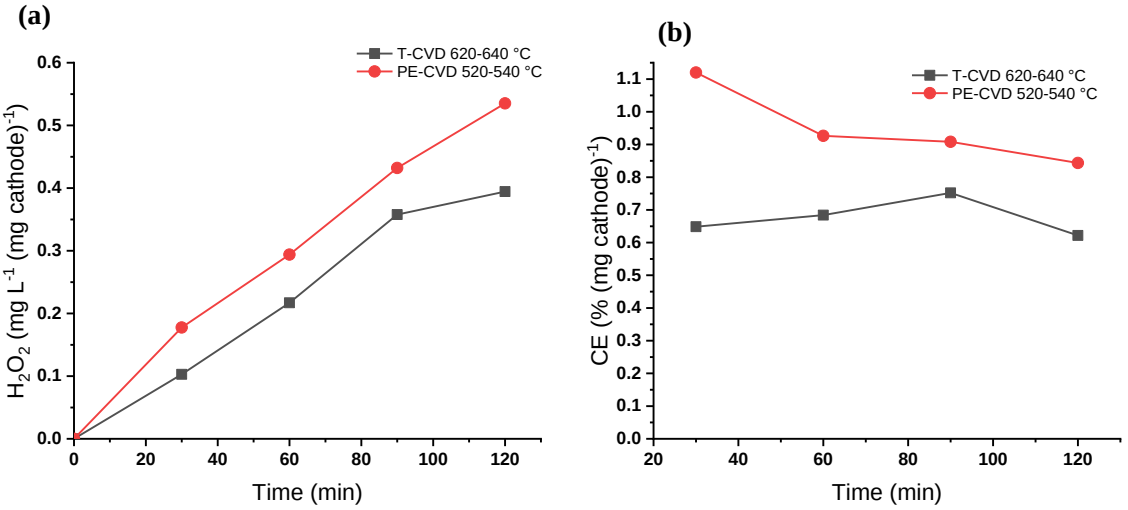

Figure 4.6 Hydrogen peroxide production on CNT-decorated quartz fibre electrode (T-CVD 620/640 °C and PE-CVD 520/540 °C): (a) hydrogen peroxide accumulation per weight of cathode, (b) current efficiency (CE) per weight of cathode. Conditions: [Na_2SO_4]=0.05 M; T=21±2ºC, I=5 mA; T-CVD cathode weight=71 mg; PE-CVD cathode weight=46 mg.

4.2.2. Electrochemical devices

As demonstrated by Sarasini et al. [36], the growth of VA-CNT forests on basalt fabrics is able to confer an electrical conductivity of ~260 S/m to an otherwise insulating

material. In this research work, various electrochemical characterizations, including potentiodynamic polarization, electrochemical impedance spectroscopy, and cyclic voltammetry, were carried out as a preliminary investigation of the electrochemical response of CNT-modified basalt fabrics to uncover possible applications in the field of electrochemical devices.

To this aim, a symmetric electrochemical cell was assembled, as described in section 3.12.2 of Part II – Materials and Methods. The samples to be tested, inserted between the metal electrodes, were: (i) a single layer of either a polymer film (Pol) or the CNT-decorated basalt fabric (Bs-NT); (ii) two CNT-decorated basalt fabrics, separated by a polyethylene film (PE). In the last configuration, a homemade conductive bio-polymer film (Pol) was inserted through a window featured by the polyethylene film.

The first electrochemical test carried out on either the single materials, i.e., the polymer film alone (Pol) and the CNT-decorated basalt fabric alone (Bs-NT), or the assembled system, i.e., the two CNT-decorated basalt fabrics separated by the polymer film (Pol+Bs-NT), was the potentiodynamic polarization test. The potentiostatic curves provide information on the electrochemical stability of the device, as they measure the current over a range around the Open Circuit Potential (OCP) or corrosion potential, using a very slow potential scan. The main parameters of interest are the corrosion potential and the corrosion current, which can be determined by projecting the intersection of the anodic and cathodic branches onto the y-axis (ordinate) and x-axis (abscissa), respectively. The more the potential value is shifted to the left (towards more negative values), the more susceptible to instability the system is. Conversely, lower current values correspond to a more resistant material which is likely to undergo less corrosion phenomena.

As illustrated in Figure 4.7 and Table 4.6, the system composed of basalt and polymer exhibits an intermediate current and has a corrosion potential lower than the components used individually, highlighting that the system is electrochemically resistant at least within the investigated potential range. The branches of the different curves related to the cathodic (left branch) and anodic processes (right branch) do not show consistent changes in slope, as if no corrosive processes or electrochemical degradation are occurring.

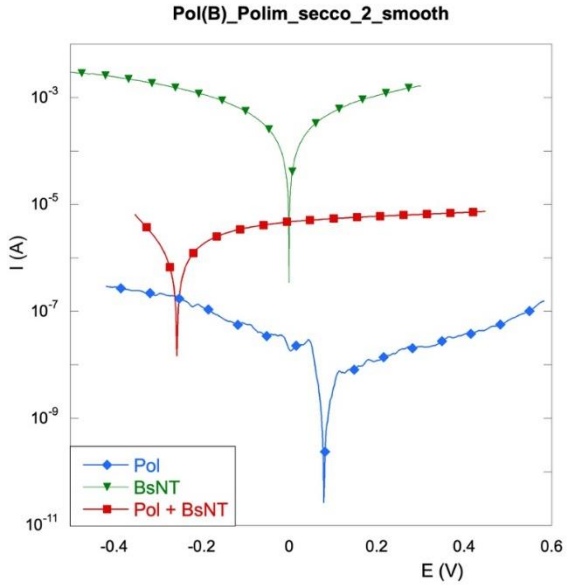

Figure 4.7 Potentiostatic curves.

Table 4.6 Current (I_{corr}) and potential (E_{corr}) values corresponding to the potentiostatic curves.

Sample	E_{corr} [mV]	I_{corr} [mA]
Pol	- 82.9	$3.6 \cdot 10^{-6}$
Bs-NT	- 0.2	$1.4 \cdot 10^{-1}$
Pol+Bs-NT	- 254.2	$7.7 \cdot 10^{-4}$

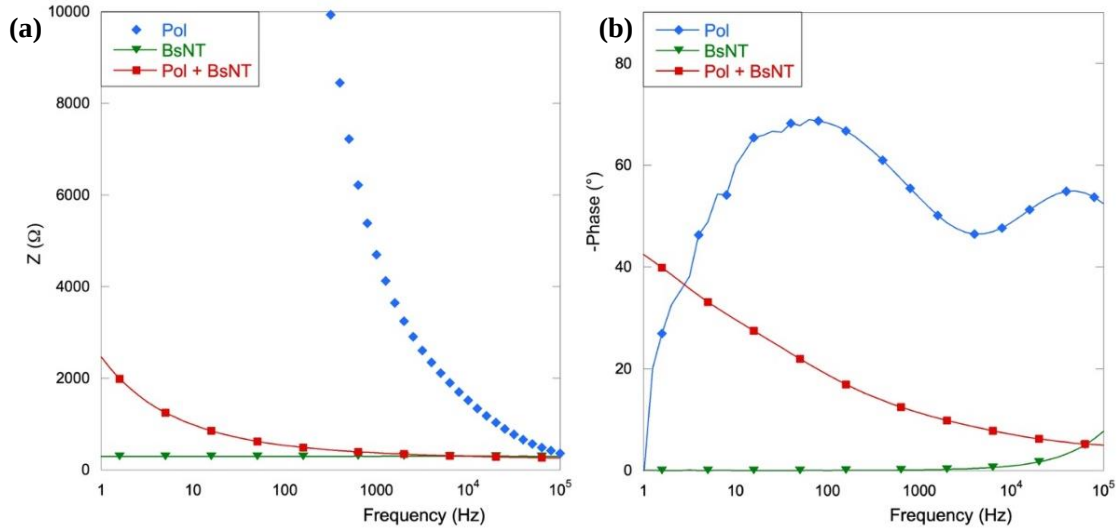

Figure 4.8 Evolutions of a) impedance and b) phase with the frequency.

Afterwards, electrochemical impedance spectroscopy (EIS) was carried out, as it provides valuable insights into the processes occurring at the electrode. It is especially useful for characterizing rapid charge transfer reactions, low-frequency relaxation processes associated with diffusion, and the relaxation of surface concentration.

Figure 4.8a illustrates that as the frequency decreases, the mobility of charge carriers within the materials varies significantly. In the case of the polymer, this mobility is particularly slow, with the curve steeply rising, indicating high resistivity. In contrast, the CNT-modified basalt fabric behaves almost like a metallic conductor, maintaining impedance consistently close to zero across the entire investigated frequency range.

In the assembled system, the impedance is very low at high-frequency values. However, below 100 Hz, an increase in impedance can be observed, suggesting a potential evolution toward capacitive behaviour. This is further confirmed by the phase behaviour depicted in Figure 4.8b.

Finally, cyclic voltammetry was conducted on the samples. From this test, crucial information can be deduced about the occurrence of reduction and oxidation reactions, as well as the mechanisms and kinetics of these reactions, along with capacitive and faradaic behaviour. In particular, the latter relies on the observation of several key aspects of the current-potential (I-V) curves. The curve shape that indicates capacitive behaviour is characterized by a rapid increase in current with potential, often exhibiting a linear or rectangular pattern in certain regions. On the other hand, faradaic behaviour displays distinct peaks (oxidation and reduction), indicating electrochemical reactions with non-linear current variations.

The system was studied over a potential range of -1 to +1 V to avoid breakdown phenomena in the polymer itself. As shown in Figure 4.9a, within the investigated range, the polymer alone behaves as an insulating material, with the measured current remaining negligible, especially at the scan rates used. The basalt, on the other hand, exhibits a typical conductor behaviour, which is better illustrated in Figure 4.9b, where the current varies between 100 and -100 mA. The cycle resembles a straight line, with its slope corresponding to the material's resistance, calculable using Ohm's law.

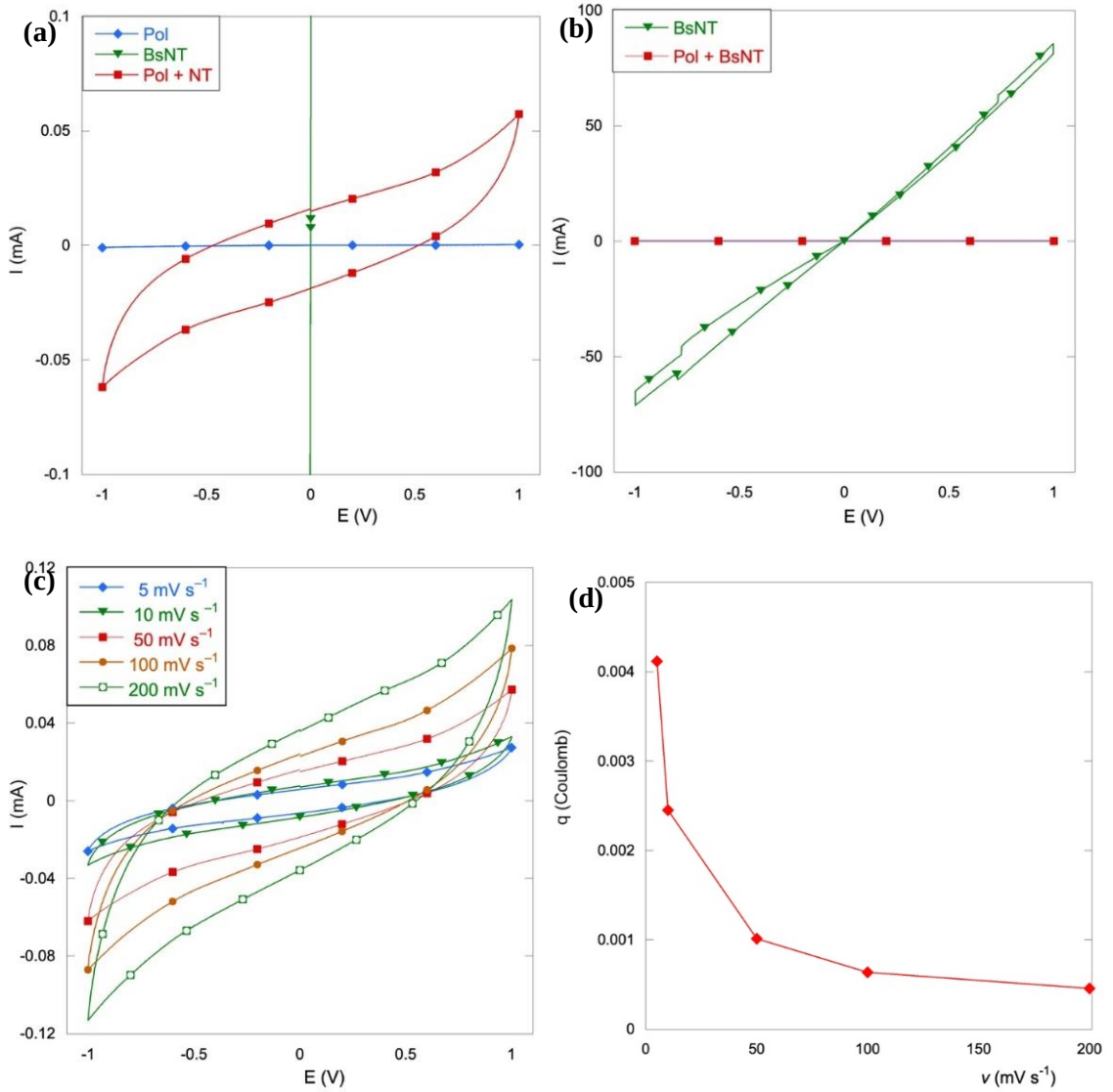

Figure 4.9 Results of cyclic voltammetry tests: a) current (I)-potential (E) curves in the range of -1 to +1 V and -0.1 to 0.1 mA; b) current (I)-potential (E) curves in the range of -1 to +1 V and -100 to 100 mA; c) a) Current (I)-potential (E) curves at varying potential scan rates; d) evolution of the voltametric charge with the scan rate.

The assembled system, within the -1 to +1 V range, shows a cycle devoid of peaks, indicating the absence of faradaic processes. This lack of peaks may suggest that the system behaves capacitively, with the current related to charge accumulation on the electrode surface rather than redox reactions.

Figure 4.9c shows that as the scan rates of the potential increase, the area enclosed within the cycle increases as well, while Figure 4.9d demonstrates that the voltammetric charge decreases, confirming that the system behaves like a capacitor.

In conclusion, the results obtained from the electrochemical tests confirm the potential application of CNT-decorated basalt fabrics in the field of electrochemical devices, particularly those for energy harvesting and storage, paving the way for future investigations of these materials within hierarchical composites for the use as structural electrochemical devices.

PART IV – CONCLUSIONS AND FUTURE PERSPECTIVES

In this research work, the issue of the thermal degradation of the mechanical properties of fibre substrates was addressed as a major current limitation of the direct growth of carbon nanotubes (CNTs) on reinforcing fibres for the development of both high-performance and multifunctional structural composite materials. Particularly, two strategies, namely a plasma-enhanced chemical vapour deposition (PE-CVD) technique and the use of innovative catalyst systems, were proposed for achieving the synthesis of CNTs at low temperatures (≤550 °C) on quartz and basalt fibres.

The effects of exposure to typical CVD temperatures (600 – 800 °C) on the mechanical properties of quartz fibres, lacking a comprehensive evaluation and understanding in the literature, were thoroughly investigated in the first part of the work. Single fibre tensile tests evidenced a severe loss of the fibre tensile strength with increasing temperature, up to 86% of the original value after heat treatment at 800 °C. On the other hand, the fibre bulk properties, including Young's modulus, density, and hardness appeared to be relatively stable up to 800 °C, with only a limited increase in the fracture toughness — equal to a 9% variation from the untreated to the 800 °C sample— which cannot compensate for the drastic strength decay. Furthermore, the fibre structure was found to remain totally amorphous up to 800 °C, with no evidence of either bulk or localized crystallization phenomena nor radial property gradients being observed. These findings revealed the capability of quartz fibres to retain their bulk properties to a greater extent than general-purpose glass fibres and basalt fibres [29], [111], [217], thus showing a better suitability as substrates for direct CVD growth. However, the issue of tensile strength degradation persisted, strengthening the need for strategies allowing a low temperature growth. Surface-controlled damage mechanisms, including sizing removal, mechanical handling damage, relaxation of structural anisotropy and water attacking, all of them causing the development and growth of surface flaws, are proposed as possible causes of strength degradation, requiring future investigations to be verified.

In the second part of this work, the use of a PE-CVD technique was investigated and compared to conventional thermal CVD for the Fe-catalysed growth on quartz fibre substrates at different temperatures. The results confirmed the effectiveness of this strategy for the low temperature synthesis of CNTs, as it allowed a reduction in the processing temperatures of around 100 °C that was not possible through the thermal path. SEM, TEM and Raman characterizations of CNT-modified fibres revealed that, although leading to the growth of shorter CNTs (up to 3 μm compared to the long VA-CNT forests – up to 80 μm – achieved through high temperature thermal CVD, i.e., T-CVD 620/640 °C), PE-CVD 520/540 °C produced radially-aligned MWCNTs with smaller diameters (~12 nm) and lower tortuosity than T-CVD 620/640 °C. The latter was ascribed to the combination of plasma assistance, causing the alignment of the growing CNTs along the electric field lines, and a good dispersion of catalyst nanoparticles seeding the growth, as assessed by TEM investigation at the fibre/CNT interface. This catalyst distribution is believed to be mainly achieved during the plasma assisted synthesis step, rather than during annealing, thanks to the energy supplied through plasma and heating which allowed to both complete nanoparticle formation and trigger CNT growth at low temperatures.

In the third part of the work, innovative catalyst systems were studied both individually and in combination with PE-CVD as alternative strategies for the low temperature synthesis of CNTs. The native iron content of basalt fibres was exploited as catalyst for the growth of CNTs at low temperatures by combining a recently developed *in-situ* catalyst generation approach [36] and plasma assistance. The results revealed, also in this case, the benefits of the use of a PE-CVD technique, allowing for a considerable reduction of the processing temperatures (optimized at 460 °C for the annealing step and 510 °C for the growth step) compared to the thermal synthesis (above 700 °C) reported in the reference study [36]. A morphology completely comparable to the reference one [36], consisting of an abundant coverage of long (~30 μm) dense VA-CNT forests, was achieved on basalt fabrics through PE-CVD 460/510 °C. Furthermore, MWCNTs with a superior structural quality were produced, as highlighted by the 48% decrease in the ratio between D and G bands (I_D /I_G) in the Raman spectrum. Interestingly, the investigation of the morphology of CNT-modified basalt fibres at different annealing temperatures

revealed that the native iron of basalt can be effectively activated as catalyst through thermal annealing at temperatures as low as 460 °C. However, lower annealing temperatures (420 °C) led to an inhomogeneous CNT coverage which was ascribed to incomplete catalyst activation, thus revealing a lower temperature limit inherent in the *in-situ* catalyst generation approach.

The use of an innovative copper-based catalyst allowed the synthesis of CNTs on quartz fibres at temperatures as low as 510 °C and 420 °C through thermal CVD at the expense of an increase in the total process duration from the ~15-minute duration of the previously optimized Fe-catalysed growth to ~1 hour. Although the growth of relatively short (~1-2 µm for T-CVD 510 °C and ~0.2 µm for T-CVD 420 °C) CNTs with a bamboo-type morphology was obtained, these findings demonstrated the catalytic activity of copper at temperatures much lower than more common Fe-based catalysts, providing a viable alternative to the use of PE-CVD. Additionally, the possibility of combining the use of a Cu catalyst with PE-CVD was assessed through a preliminary investigation, requiring further tuning of the process parameters specific to the glow discharge to achieve an optimal growth.

In the last part of the work, the properties of the fibres subjected to the different growth processes were characterized with a twofold focus: (i) their use as reinforcements in structural composite materials, (ii) their additional electrochemical functions provided by the presence of CNTs. As demonstrated through single fibre tensile tests, the reduction of processing temperatures operated through all the strategies proposed in this work effectively mitigated the strength loss of the fibre substrates, i.e., quartz and basalt fibres, compared to high temperature thermal CVD. As regards quartz fibres, the best results were obtained in the case of Fe-catalysed PE-CVD 520/540 °C, leading to only a negligible 5% strength loss as opposed to the 74% strength loss of the thermal counterpart (T-CVD 620/640 °C). This was ascribed to the shorter exposure time (~15 minutes) compared to Cu-catalysed thermal processes at 510 °C and 420 °C (~1 hour) which led to strength losses of ~42% and ~37%, respectively. As regards basalt fibres, a strength loss of ~35% was measured following PE-CVD 460/510 °C which, in accordance with previous studies reporting consistent strength degradation of basalt fibres in the range

400–500 °C [29], suggests the need for further research to lower the process temperatures below 400 °C. The evaluation of the wetting properties of CNT-decorated quartz fibres revealed a significant reduction in the polar component of the surface energy – with a corresponding increase in the contact angle with water – and a slight increase in the dispersive component compared to commercially sized quartz fibres. This suggested a higher affinity for liquids with a mainly dispersive character as confirmed by the increase in Young-Dupré (Y-D) work of adhesion with epoxy for l-CNT-QFs and by the slight increase in the values of W_A for s-CNT-QFs calculated according to Owens, Wendt, Rabel e Kaelble (WORK) and Wu approaches. Finally, the investigation of the electrochemical properties of CNT-decorated quartz fibres showcased potential applications of these materials as cathodes in the field of environmental remediation for the electrochemical generation of hydrogen peroxide, with current efficiencies comparable to that of typical carbon-based electrodes [310], while electrochemical characterizations on CNT-modified basalt fabric samples revealed an electrochemical behaviour typical of capacitive processes which opens possibilities for applications in the field of electrochemical devices for energy harvesting and storage, such as supercapacitors.

In conclusion, this work proved the potential of different strategies for the low temperature synthesis of CNTs, providing viable routes for direct CVD growth which may find application not only in the field of hierarchical fibres, where they can effectively mitigate the undesired strength deterioration effect of the fibre substrate, but also in many other fields involving temperature-sensitive substrates, such as flexible electronic devices and sensors [159], [160]. Furthermore, the outcomes of the mechanical characterization of quartz fibres following medium-high temperature exposure (600 – 800 °C) can be used to design solutions that prevent the thermal strength loss of quartz fibres, including high-temperature resistant coatings [222], [229], [317] which might reduce the susceptibility of quartz fibres to surface degradation and consequent strength reduction, thus enlarging the in-service temperature range of these fibres often used as reinforcements for heat insulation and shielding materials in aerospace and military applications.

Among all the proposed strategies, fast (~15 minutes) Fe-catalysed PE-CVD on quartz fibres gave the best results in terms of preserved tensile properties of the substrate, while

the combination of PE-CVD with *in-situ* catalyst generation led to the best quality of synthesized CNTs both in terms of crystallinity degree, as evidenced by the I_D /I_G ratio in the Raman spectrum, and spatial arrangement, with the growth of dense forests of long and well-aligned CNTs. Furthermore, the copper catalyst proved to have the highest catalytic efficiency at low temperatures, being able to catalyse the synthesis of CNTs at temperatures as low as 420 °C without plasma assistance. The investigation at various synthesis temperatures pointed out the role of low temperature formation and activation of suitable-sized and evenly distributed catalyst nanoparticles as an essential requirement for achieving a low temperature growth. In sight of this, the introduction of plasma during the annealing step might overcome the observed lower temperature limits of each strategy, often dictated by the non-complete catalyst activation after thermal annealing. This perspective, requiring future investigations and a careful tuning of the process parameters specific to the annealing stage, might allow the growth at even lower temperatures, being attractive especially for basalt fibre substrates.

Once reached the process optimization at the laboratory scale, a future perspective will be the possibility of transferring this technology to industrial-scale production with the main challenge consisting in the development of a suitable continuous manufacturing process for CNT-modified fibre/fabric preforms. Although some studies already proposed laboratory-scale continuous CVD processes on reinforcing fibres [16], [18], [19], the research is still in its infancy. The progressively increasing global demand of multifunctional structural materials, combining high-performance mechanical properties and light weight with additional functionalities, might drive the technological developments required for achieving the industrial-scale production of hierarchical composite materials. In this context, the preliminary electrochemical investigations carried out in this work provided an interesting contribution, revealing the potential use of CNT-modified fibres in highly demanding sectors such as environmental remediation – through the electrochemical generation of a widely-used green oxidant such as H_2O_2 – and transportation, where energy storage and harvesting functionalities are highly attractive for the development of structural supercapacitors to be used in electric vehicles or aircrafts, allowing weight reduction and consequent lower fuel consumption and CO_2 emissions. Consequently, future research might be devoted to comprehensively study the

H_2O_2 production and energy harvesting/storage functions of these materials both at the single fibre level and at the composite level. To transfer lab-scale research to industrial-scale mass production of CNT-based hierarchical materials, therefore, an interdisciplinary approach will be required, involving different fields of materials science and engineering to develop advanced composite components with combined structural and multifunctional performances.

References

[1] Straits Research, “Fiber-Reinforced Composites Market Size, Share & Trends Analysis Report By Fiber Type (Carbon Fibers, Glass Fibers, Aramid Fibers, Others), By Resin Type (Thermoset Composites, Thermoplastic Composites), By End-Use Industry (Building & Construction, Autom,” 2022. https://straitsresearch.com/report/fiber-reinforced-composites-market.

[2] R. E. Swain, K. L. Reifsnider, K. Jayaraman, and M. el-Zein, “Interface/Interphase Concepts in Composite Material Systems,” *J. Thermoplast. Compos. Mater.*, vol. 3, no. 1, pp. 13–23, 1990, doi: 10.1177/089270579000300102.

[3] R. Fragoudakis, *Failure Concepts in Fiber Reinforced Plastics*. 2017.

[4] D. Nepal *et al.*, “Hierarchically structured bioinspired nanocomposites,” *Nat. Mater.*, vol. 22, no. 1, pp. 18–35, 2023, doi: 10.1038/s41563-022-01384-1.

[5] J. Zhang, R. Zhuang, J. Liu, E. Mäder, G. Heinrich, and S. Gao, “Functional interphases with multi-walled carbon nanotubes in glass fibre/epoxy composites,” *Carbon N. Y.*, vol. 48, no. 8, pp. 2273–2281, 2010, doi: 10.1016/j.carbon.2010.03.001.

[6] H. Qian, E. S. Greenhalgh, M. S. P. Shaffer, and A. Bismarck, “Carbon nanotube-based hierarchical composites: A review,” *J. Mater. Chem.*, vol. 20, no. 23, pp. 4751–4762, 2010, doi: 10.1039/c000041h.

[7] I. Kang *et al.*, “Introduction to carbon nanotube and nanofiber smart materials,” *Compos. Part B Eng.*, vol. 37, no. 6, pp. 382–394, 2006, doi: 10.1016/j.compositesb.2006.02.011.

[8] J. Li, Z. Zhang, J. Fu, Z. Liang, and K. R. Ramakrishnan, “Mechanical properties and structural health monitoring performance of carbon nanotube-modified FRP composites: A review,” *Nanotechnol. Rev.*, vol. 10, no. 1, pp. 1438–1468, 2021, doi: 10.1515/ntrev-2021-0104.

[9] Y. Wang, C. Pan, W. Chu, A. K. Vipin, and L. Sun, “Environmental remediation applications of carbon nanotubes and graphene oxide: Adsorption and catalysis,” *Nanomaterials*, vol. 9, no. 3, 2019, doi: 10.3390/nano9030439.

[10] M. H. Islam, S. Afroj, M. A. Uddin, D. V. Andreeva, K. S. Novoselov, and N. Karim, “Graphene and CNT-Based Smart Fiber-Reinforced Composites: A Review,” *Adv. Funct. Mater.*, vol. 32, no. 40, 2022, doi: 10.1002/adfm.202205723.

[11] G. Wu *et al.*, “Interfacially reinforced methylphenylsilicone resin composites by chemically grafting multiwall carbon nanotubes onto carbon fibers,” *Compos. Part B Eng.*, vol. 82, pp. 50–58, 2015, doi: 10.1016/j.compositesb.2015.08.012.

[12] I. Pillin, M. Castro, S. N. Chowdhury, and J. F. Feller, “Robustness of carbon nanotube-based sensor to probe composites’ interfacial damage in situ,” *J. Compos. Mater.*, vol. 50, no. 1, pp. 109–113, 2016, doi: 10.1177/0021998315571029.

[13] S. Tamrakar, Q. An, E. T. Thostenson, A. N. Rider, B. Z. Haque, and J. W. Gillespie, “Tailoring Interfacial Properties by Controlling Carbon Nanotube Coating Thickness on Glass Fibers Using Electrophoretic Deposition,” *ACS Appl. Mater. Interfaces*, vol. 8, no. 2, pp. 1501–1510, 2016, doi: 10.1021/acsami.5b10903.

[14] M. Zhao *et al.*, “Layer-by-layer grafting CNTs onto carbon fibers surface for enhancing the interfacial properties of epoxy resin composites,” *Compos. Sci. Technol.*, vol. 154, pp. 28–36, 2018, doi: 10.1016/j.compscitech.2017.11.002.

[15] T. Förster, B. Hao, E. Mäder, F. Simon, E. Wölfel, and P. C. Ma, “CVD-Grown CNTs on basalt fiber surfaces for multifunctional composite interphases,” *Fibers*, vol. 4, no. 4, 2016, doi: 10.3390/fib4040028.

[16] R. Guzmán De Villoria, A. J. Hart, and B. L. Wardle, “Continuous high-yield production of vertically aligned carbon nanotubes on 2D and 3D substrates,” *ACS Nano*, vol. 5, no. 6, pp. 4850–4857, 2011, doi: 10.1021/nn2008645.

[17] H. C. Malecki and M. Zupan, “Scalable continuous growth of carbon nanotubes on moving fiber substrates,” *Compos. Part A Appl. Sci. Manuf.*, vol. 43, no. 11, pp. 1914–1920, 2012, doi: 10.1016/j.compositesa.2012.06.019.

[18] R. Guzman De Villoria, S. A. Steiner, A. J. Hart, and B. L. Wardle, “Continuous growth of vertically aligned carbon nanotubes,” *ICCM Int. Conf. Compos. Mater.*, pp. 3–5, 2011.

[19] H. G. De Luca, D. B. Anthony, E. S. Greenhalgh, A. Bismarck, and M. S. P. Shaffer, “Piezoresistive structural composites reinforced by carbon nanotube-grafted quartz fibres,” *Compos. Sci. Technol.*, vol. 198, p. 108275, 2020, doi: 10.1016/j.compscitech.2020.108275.

[20] S. A. Steiner, R. Li, and B. L. Wardle, “Circumventing the mechanochemical origins of strength loss in the synthesis of hierarchical carbon fibers,” *ACS Appl. Mater. Interfaces*, vol. 5, no. 11, pp. 4892–4903, 2013, doi: 10.1021/am4006385.

[21] S. Feih, E. Boiocchi, G. Mathys, Z. Mathys, A. G. Gibson, and A. P. Mouritz, “Mechanical properties of thermally-treated and recycled glass fibres,” *Compos. Part B Eng.*, vol. 42, no. 3, pp. 350–358, 2011, doi: 10.1016/j.compositesb.2010.12.020.

[22] F. T. Wallenberger, J. C. Watson, and H. Li, “Glass Fibers,” in *ASM Handbook*, vol. 21 Composi, 2001, pp. 27–34.

[23] M. H. Lapena, G. Marinucci, and O. De Carvalho, “Mechanical Characterization of Unidirectional Basalt Fiber Epoxy Composite Tube,” *Mater. Res.*, vol. 21, no. 1, pp. 1–7, 2018, [Online]. Available: http://www.scielo.br/scielo.php?script=sci_arttext&pid=S1516-14392018000100110&nrm=iso.

[24] L. C. Hao and W. D. Yu, “Evaluation of thermal protective performance of basalt fiber nonwoven fabrics,” *J. Therm. Anal. Calorim.*, vol. 100, no. 2, pp. 551–555, 2010, doi: 10.1007/s10973-009-0179-0.

[25] A. E. Al Ghali, N. E. El Ezz, B. Hamad, J. Assaad, and A. Yehya, “Comparative study on shear strength and life cycle assessment of reinforced concrete beams containing different types of fibers,” *Case Stud. Constr. Mater.*, vol. 19, no. September, p. e02497, 2023, doi: 10.1016/j.cscm.2023.e02497.

[26] H. Jamshaid and R. Mishra, “A green material from rock: basalt fiber – a review,” *J. Text. Inst.*, vol. 107, no. 7, pp. 923–937, 2016, doi: 10.1080/00405000.2015.1071940.

[27] L. Yan *et al.*, “Review of research on basalt fibers and basalt fiber-reinforced composites in China (I): Physicochemical and mechanical properties,” *Polym. Polym. Compos.*, vol. 29, no. 9, pp. 1612–1624, 2021, doi: 10.1177/0967391120977396.

[28] M. Lilli *et al.*, “Basalt fibre surface modification via plasma polymerization of tetravinylsilane/oxygen mixtures for improved interfacial adhesion with unsaturated polyester matrix,” *Mater. Chem. Phys.*, vol. 274, no. April, pp. 1–7, 2021, doi: 10.1016/j.matchemphys.2021.125106.

[29] M. Lilli *et al.*, “Quantitative multi-scale characterization of single basalt fibres: Insights into strength loss mechanisms after thermal conditioning,” *Mater. Sci. Eng. A*, vol. 797, no. June, 2020, doi: 10.1016/j.msea.2020.139963.

[30] Y. Zheng and S. Wang, “Effect of moderately high temperature heat treatment on surface morphology and structure of quartz fibers,” *Appl. Surf. Sci.*, vol. 258, no. 10, pp. 4698–4701, 2012, doi: 10.1016/j.apsusc.2012.01.062.

[31] Y. Xiao, Z. Ahmed, Z. Ma, C. Zhou, L. Zhang, and M. Chan, “Low temperature synthesis of high-density carbon nanotubes on insulating substrate,” *Nanomaterials*, vol. 9, no. 3, pp. 1–9, 2019, doi: 10.3390/nano9030473.

[32] C. Bower, W. Zhu, S. Jin, and O. Zhou, “Plasma-induced alignment of carbon nanotubes,” *Appl. Phys. Lett.*, vol. 77, no. 17, pp. 830–832, 2000, doi: 10.1063/1.1306658.

[33] N. Halonen *et al.*, “Low-temperature growth of multi-walled carbon nanotubes by thermal CVD,” *Phys. Status Solidi Basic Res.*, vol. 248, no. 11, pp. 2500–2503,

2011, doi: 10.1002/pssb.201100137.

[34] R. Li *et al.*, "Low-Temperature Growth of Carbon Nanotubes Catalyzed by Sodium-Based Ingredients," *Angew. Chemie - Int. Ed.*, vol. 58, no. 27, pp. 9204–9209, 2019, doi: 10.1002/anie.201902516.

[35] L. H. Acauan, A. L. Kaiser, and B. L. Wardle, "Direct synthesis of carbon nanomaterials via surface activation of bulk copper," *Carbon N. Y.*, vol. 177, pp. 1–10, 2021, doi: 10.1016/j.carbon.2021.02.045.

[36] F. Sarasini *et al.*, "Highly aligned growth of carbon nanotube forests with in-situ catalyst generation: A route to multifunctional basalt fibres," *Compos. Part B Eng.*, vol. 243, p. 110136, 2022, doi: 10.1016/j.compositesb.2022.110136.

[37] P. G. Jenkins, S. Riopedre-Méndez, E. Sáez-Rodríguez, L. Yang, and J. L. Thomason, "Investigation of the strength of thermally conditioned basalt and E-glass fibres," *ICCM Int. Conf. Compos. Mater.*, vol. 2015-July, no. July, pp. 19–24, 2015.

[38] D. K. Rajak, D. D. Pagar, P. L. Menezes, and E. Linul, "Fiber-reinforced polymer composites: Manufacturing, properties, and applications," *Polymers (Basel).*, vol. 11, no. 10, 2019, doi: 10.3390/polym11101667.

[39] M. Akhtarul Islam, "Natural Fiber as a substitute to Synthetic Fiber in Polymer Composites: A Review," *Res. J. Eng. Sci.*, vol. 2, no. 3, pp. 46–53, 2013, [Online]. Available: https://www.researchgate.net/publication/284223539.

[40] A. Saleem, L. Medina, M. Skrifvars, and L. Berglin, "Hybrid Polymer Composites of Bio-Based Bast Fibers with Glass, Carbon and Basalt Fibers for Automotive Applications—A Review," *Molecules*, vol. 25, no. 21, p. 4933, 2020, doi: 10.3390/molecules25214933.

[41] M. Mohammed *et al.*, "Comprehensive insights on mechanical attributes of natural-synthetic fibres in polymer composites," *J. Mater. Res. Technol.*, vol. 25, pp. 4960–4988, 2023, doi: 10.1016/j.jmrt.2023.06.148.

[42] D. K. Rajak, P. H. Wagh, and E. Linul, "A Review on Synthetic Fibers for Polymer Matrix Composites: Performance, Failure Modes and Applications," *Materials (Basel).*, vol. 15, no. 14, 2022, doi: 10.3390/ma15144790.

[43] B. A. Newcomb, "Processing, structure, and properties of carbon fibers," *Compos. Part A Appl. Sci. Manuf.*, vol. 91, pp. 262–282, 2016, doi: 10.1016/j.compositesa.2016.10.018.

[44] E. Frank, F. Hermanutz, and M. R. Buchmeiser, "Carbon fibers: Precursors, manufacturing, and properties," *Macromol. Mater. Eng.*, vol. 297, no. 6, pp. 493–501, 2012, doi: 10.1002/mame.201100406.

[45] M. Etcheverry and S. E. Barbosa, “Glass fiber reinforced polypropylene mechanical properties enhancement by adhesion improvement,” *Materials (Basel).*, vol. 5, no. 6, pp. 1084–1113, 2012, doi: 10.3390/ma5061084.

[46] N. Wiegand and E. Mäder, “Commingled yarn spinning for thermoplastic/glass fiber composites,” *Fibers*, vol. 5, no. 3, 2017, doi: 10.3390/fib5030026.

[47] P. Zinck, E. Mäder, and J. F. Gerard, “Role of silane coupling agent and polymeric film former for tailoring glass fiber sizings from tensile strength measurements,” *J. Mater. Sci.*, vol. 36, no. 21, pp. 5245–5252, 2001, doi: 10.1023/A:1012410315601.

[48] P. Zinck, M. F. Pay, R. Rezakhanlou, and J. F. Gerard, “Mechanical characterisation of glass fibres as an indirect analysis of the effect of surface treatment,” *J. Mater. Sci.*, vol. 34, no. 9, pp. 2121–2133, 1999, doi: 10.1023/A:1004572112470.

[49] A. R. Bunsell and J. Renard, *Fundamentals of Fibre Reinforced Composite Materials*. 2005.

[50] G. Yang, M. Park, and S. J. Park, “Recent progresses of fabrication and characterization of fibers-reinforced composites: A review,” *Compos. Commun.*, vol. 14, no. May, pp. 34–42, 2019, doi: 10.1016/j.coco.2019.05.004.

[51] MarketsandMarkets, “GFRP Composite Market by End-Use Industry (Transportation, Electrical & Electronics), Resin Type (Epoxy, Polyester, Vinyl Ester), Manufacturing Process (Compression & Injection Molding, RTM/VARTM, Layup), and Region - Global Forecast to 2022,” 2018. https://www.marketsandmarkets.com/Market-Reports/glass-fiber-reinforced-plastic-composites-market-142751329.html.

[52] S. Sathees Kumar, B. Sridhar Babu, C. N. Chankravarthy, and N. Prabhakar, “Review on natural fiber polymer composites,” *Mater. Today Proc.*, vol. 46, no. 2, pp. 777–782, 2021, doi: 10.1016/j.matpr.2020.12.599.

[53] H. Abdollahiparsa, A. Shahmirzaloo, P. Teuffel, and R. Blok, “A review of recent developments in structural applications of natural fiber-Reinforced composites (NFRCs),” *Compos. Adv. Mater.*, vol. 32, p. 263498332211475, 2023, doi: 10.1177/26349833221147540.

[54] European Parliament and Council of the European Union, “Council of the European Union.” 2000.

[55] E. Chioatto and P. Sospiro, “Transition from waste management to circular economy: the European Union roadmap,” *Env. Dev Sustain*, vol. 25, pp. 249–276, 2023, doi: https://doi.org/10.1007/s10668-021-02050-3.

[56] Precedence Research, “Natural Fiber Composites Market Size | Share and Trends

2024 to 2034," 2024, [Online]. Available: https://www.precedenceresearch.com/natural-fiber-composites-market#:~:text=The global natural fiber composites,sustainable and eco-friendly materials.

[57] S. V. Joshi, L. T. Drzal, A. K. Mohanty, and S. Arora, "Are natural fiber composites environmentally superior to glass fiber reinforced composites?," *Compos. Part A Appl. Sci. Manuf.*, vol. 35, no. 3, pp. 371–376, 2004, doi: 10.1016/j.compositesa.2003.09.016.

[58] C. I. Madueke, O. M. Mbah, and R. Umunakwe, "A review on the limitations of natural fibres and natural fibre composites with emphasis on tensile strength using coir as a case study," *Polym. Bull.*, vol. 80, no. 4, pp. 3489–3506, 2023, doi: 10.1007/s00289-022-04241-y.

[59] S. Maiti, M. R. Islam, M. A. Uddin, S. Afroj, S. J. Eichhorn, and N. Karim, "Sustainable Fiber-Reinforced Composites: A Review," *Adv. Sustain. Syst.*, vol. 6, no. 11, 2022, doi: 10.1002/adsu.202200258.

[60] L. Kerni, S. Singh, A. Patnaik, and N. Kumar, "A review on natural fiber reinforced composites," *Mater. Today Proc.*, vol. 28, pp. 1616–1621, 2020, doi: 10.1016/j.matpr.2020.04.851.

[61] Z. N. Azwa, B. F. Yousif, A. C. Manalo, and W. Karunasena, "A review on the degradability of polymeric composites based on natural fibres," *Mater. Des.*, vol. 47, pp. 424–442, 2013, doi: 10.1016/j.matdes.2012.11.025.

[62] S. Begum, S. Fawzia, and M. S. J. Hashmi, "Polymer matrix composite with natural and synthetic fibres," *Adv. Mater. Process. Technol.*, vol. 6, no. 3, pp. 547–564, 2020, doi: 10.1080/2374068X.2020.1728645.

[63] S. O. Amiandamhen, M. Meincken, and L. Tyhoda, "Natural Fibre Modification and Its Influence on Fibre-matrix Interfacial Properties in Biocomposite Materials," *Fibers Polym.*, vol. 21, no. 4, pp. 677–689, 2020, doi: 10.1007/s12221-020-9362-5.

[64] X. Li, L. G. Tabil, and S. Panigrahi, "Chemical treatments of natural fiber for use in natural fiber-reinforced composites: A review," *J. Polym. Environ.*, vol. 15, no. 1, pp. 25–33, 2007, doi: 10.1007/s10924-006-0042-3.

[65] O. Faruk, A. K. Bledzki, H. P. Fink, and M. Sain, "Progress report on natural fiber reinforced composites," *Macromol. Mater. Eng.*, vol. 299, no. 1, pp. 9–26, 2014, doi: 10.1002/mame.201300008.

[66] V. Fiore, T. Scalici, G. Di Bella, and A. Valenza, "A review on basalt fibre and its composites," *Compos. Part B Eng.*, vol. 74, pp. 74–94, 2015, doi: 10.1016/j.compositesb.2014.12.034.

[67] F. Sarasini, J. Tirillò, and M. C. Seghini, “Influence of thermal conditioning on tensile behaviour of single basalt fibres,” *Compos. Part B Eng.*, vol. 132, pp. 77–86, 2018, doi: 10.1016/j.compositesb.2017.08.014.

[68] J. Liu, M. Chen, J. Yang, and Z. Wu, “Study on Mechanical Properties of Basalt Fibers Superior to E-glass Fibers,” *J. Nat. Fibers*, vol. 19, no. 3, pp. 882–894, 2022, doi: 10.1080/15440478.2020.1764438.

[69] J. Militký, V. Kovačič, and J. Rubnerová, “Influence of thermal treatment on tensile failure of basalt fibers,” *Eng. Fract. Mech.*, vol. 69, no. 9, pp. 1025–1033, 2002, doi: 10.1016/S0013-7944(01)00119-9.

[70] T. Deák and T. Czigány, “Chemical Composition and Mechanical Properties of Basalt and Glass Fibers: A Comparison,” *Text. Res. J.*, vol. 79, no. 7, pp. 645–651, 2009, doi: 10.1177/0040517508095597.

[71] N. Kaitwade, “Basalt Fibre Market Outlook for 2024 to 2034,” *Future Market Insights Inc.*, 2024. https://www.futuremarketinsights.com/reports/basalt-fibre-market.

[72] S. J. Park and J. S. Jin, “Effect of silane coupling agent on interphase and performance of glass fibers/unsaturated polyester composites,” *J. Colloid Interface Sci.*, vol. 242, no. 1, pp. 174–179, 2001, doi: 10.1006/jcis.2001.7788.

[73] S. Zhandarov and E. Mäder, “Characterization of fiber/matrix interface strength: Applicability of different tests, approaches and parameters,” *Compos. Sci. Technol.*, vol. 65, no. 1, pp. 149–160, 2005, doi: 10.1016/j.compscitech.2004.07.003.

[74] J. Karger-Kocsis, H. Mahmood, and A. Pegoretti, “Recent advances in fiber/matrix interphase engineering for polymer composites,” *Prog. Mater. Sci.*, vol. 73, pp. 1–43, 2015, doi: 10.1016/j.pmatsci.2015.02.003.

[75] J.-K. Kim and Y.-W. Mai, *Engineered Interfaces in Fiber Reinforced Composites*. 1988.

[76] L. T. Drzal and M. Madhukar, “Fibre-matrix adhesion and its relationship to composite mechanical properties,” *J. Mater. Sci.*, vol. 28, no. 3, pp. 569–610, 1993, doi: 10.1007/BF01151234.

[77] S. Huang, Q. Fu, L. Yan, and B. Kasal, “Characterization of interfacial properties between fibre and polymer matrix in composite materials – A critical review,” *J. Mater. Res. Technol.*, vol. 13, pp. 1441–1484, 2021, doi: 10.1016/j.jmrt.2021.05.076.

[78] P. J. Liotier *et al.*, “Role of interface formation versus fibres properties in the mechanical behaviour of bio-based composites manufactured by Liquid Composite Molding processes,” *Compos. Part B Eng.*, vol. 163, no. October 2018,

pp. 86–95, 2019, doi: 10.1016/j.compositesb.2018.10.103.

[79] D. A. Hays, “Role of Electrostatics in Adhesion,” *Fundam. Adhes.*, pp. 249–278, 1991, doi: 10.1007/978-1-4899-2073-7_8.

[80] E. M. Petrie, *8 - Adhesive bonding of textiles: principles, types of adhesive and methods of use*. Woodhead Publishing Series in Textiles, Joining Textiles, Woodhead Publishing, 2013.

[81] S. Shokoohi, A. Arefazar, and R. Khosrokhavar, “Silane coupling agents in polymer-based reinforced composites: A review,” *J. Reinf. Plast. Compos.*, vol. 27, no. 5, pp. 473–485, 2008, doi: 10.1177/0731684407081391.

[82] M. D. H. Beg and K. L. Pickering, “Mechanical performance of Kraft fibre reinforced polypropylene composites: Influence of fibre length, fibre beating and hygrothermal ageing,” *Compos. Part A Appl. Sci. Manuf.*, vol. 39, no. 11, pp. 1748–1755, 2008, doi: 10.1016/j.compositesa.2008.08.003.

[83] M. Guigon and E. Klinklin, “The interface and interphase in carbon fibre-reinforced composites,” *Composites*, vol. 25, no. 7, pp. 534–539, 1994, doi: https://doi.org/10.1016/0010-4361(94)90181-3.

[84] C. Scarponi and C. S. Pizzinelli, “Interface and mechanical properties of Natural Fibres reinforced composites: a review,” *Int. J. Mater. Prod. Technol.*, vol. 36, pp. 278–303, 2009, doi: https://doi.org/10.1504/IJMPT.2009.027837.

[85] F. Sbardella *et al.*, “Interface tailoring between flax yarns and epoxy matrix by ZnO nanorods,” *Compos. Part A Appl. Sci. Manuf.*, vol. 140, no. October 2020, 2021, doi: 10.1016/j.compositesa.2020.106156.

[86] L. Li, W. Liu, F. Yang, W. Jiao, L. Hao, and R. Wang, “Interfacial reinforcement of hybrid composite by electrophoretic deposition for vertically aligned carbon nanotubes on carbon fiber,” *Compos. Sci. Technol.*, vol. 187, no. November 2019, p. 107946, 2020, doi: 10.1016/j.compscitech.2019.107946.

[87] M. Shivashankar and B. K. Mandal, “A review on interpenetrating polymer network,” *Int. J. Pharm. Pharm. Sci.*, vol. 4, no. SUPPL. 5, pp. 1–7, 2012.

[88] A. Y. Matveeva, S. V. Lomov, and L. Gorbatikh, “Debonding at the fiber/matrix interface in carbon nanotube reinforced composites: Modelling investigation,” *Comput. Mater. Sci.*, vol. 159, pp. 412–419, 2019, doi: 10.1016/j.commatsci.2018.10.031.

[89] E. T. Thostenson and T. W. Chou, “Carbon nanotube networks: Sensing of distributed strain and damage for life prediction and self healing,” *Adv. Mater.*, vol. 18, no. 21, pp. 2837–2841, 2006, doi: 10.1002/adma.200600977.

[90] C. Peng, S. Zhang, D. Jewell, and G. Z. Chen, “Carbon nanotube and conducting

polymer composites for supercapacitors," *Prog. Nat. Sci.*, vol. 18, no. 7, pp. 777–788, 2008, doi: 10.1016/j.pnsc.2008.03.002.

[91] F. H. Gojny, M. H. G. Wichmann, B. Fiedler, W. Bauhofer, and K. Schulte, "Influence of nano-modification on the mechanical and electrical properties of conventional fibre-reinforced composites," *Compos. Part A Appl. Sci. Manuf.*, vol. 36, no. 11, pp. 1525–1535, 2005, doi: 10.1016/j.compositesa.2005.02.007.

[92] M. H. Islam, S. Afroj, M. A. Uddin, D. V. Andreeva, K. S. Novoselov, and N. Karim, "Graphene and CNT-Based Smart Fiber-Reinforced Composites A Review." Advanced Functional Materials, p. 2205723, 2022, doi: 10.1002/adfm.202205723.

[93] V. S. Romanov, S. V. Lomov, I. Verpoest, and L. Gorbatikh, "Stress magnification due to carbon nanotube agglomeration in composites," *Compos. Struct.*, vol. 133, pp. 246–256, 2015, doi: 10.1016/j.compstruct.2015.07.069.

[94] I. El Sawi, P. A. Olivier, P. Demont, and H. Bougherara, "Processing and electrical characterization of a unidirectional CFRP composite filled with double walled carbon nanotubes," *Compos. Sci. Technol.*, vol. 73, no. 1, pp. 19–26, 2012, doi: 10.1016/j.compscitech.2012.08.016.

[95] Z. Zhao *et al.*, "Mechanical, thermal and interfacial performances of carbon fiber reinforced composites flavored by carbon nanotube in matrix/interface," *Compos. Struct.*, vol. 159, pp. 761–772, 2017, doi: 10.1016/j.compstruct.2016.10.022.

[96] E. Y. Choi, M. H. Kim, and C. K. Kim, "Fabrication of carbon fiber grafted with acyl chloride functionalized multi-walled carbon nanotubes for mechanical reinforcement of nylon 6,6," *Compos. Sci. Technol.*, vol. 178, no. May, pp. 33–40, 2019, doi: 10.1016/j.compscitech.2019.05.012.

[97] K. H. Hung, W. S. Kuo, T. H. Ko, S. S. Tzeng, and C. F. Yan, "Processing and tensile characterization of composites composed of carbon nanotube-grown carbon fibers," *Compos. Part A Appl. Sci. Manuf.*, vol. 40, no. 8, pp. 1299–1304, 2009, doi: 10.1016/j.compositesa.2009.06.002.

[98] H. Qian, A. Bismarck, E. S. Greenhalgh, and M. S. P. Shaffer, "Carbon nanotube grafted silica fibres: Characterising the interface at the single fibre level," *Compos. Sci. Technol.*, vol. 70, no. 2, pp. 393–399, 2010, doi: 10.1016/j.compscitech.2009.11.014.

[99] S. Zeng, P. Duan, M. Shen, X. Lu, Y. Xue, and L. Yang, "Interlaminar fracture toughness, adhesion and mechanical properties of MWCNT–glass fiber fabric composites: Effect of MWCNT aspect ratios," *Polym. Compos.*, vol. 40, no. S2, pp. E1329–E1337, 2019, doi: 10.1002/pc.24990.

[100] F. H. Zhang, R. G. Wang, X. D. He, C. Wang, and L. N. Ren, "Interfacial shearing

strength and reinforcing mechanisms of an epoxy composite reinforced using a carbon nanotube/carbon fiber hybrid," *J. Mater. Sci.*, vol. 44, pp. 3574–3577, 2009, doi: 10.1007/s10853-009-3484-x.

[101] H. Zhang, Y. Liu, M. Kuwata, E. Bilotti, and T. Peijs, "Improved fracture toughness and integrated damage sensing capability by spray coated CNTs on carbon fibre prepreg," *Compos. Part A Appl. Sci. Manuf.*, vol. 70, pp. 102–110, 2015, doi: https://doi.org/10.1016/j.compositesa.2014.11.029.

[102] L. Tzounis *et al.*, "CNT-grafted glass fibers as a smart tool for epoxy cure monitoring, UV-sensing and thermal energy harvesting in model composites," *RSC Adv.*, vol. 6, no. 60, pp. 55514–55525, 2016, doi: 10.1039/c6ra09800b.

[103] S. Xiong, Y. Zhao, Y. Wang, J. Song, X. Zhao, and S. Li, "Enhanced interfacial properties of carbon fiber/epoxy composites by coating carbon nanotubes onto carbon fiber surface by one-step dipping method," *Appl. Surf. Sci.*, vol. 546, p. 149135, 2021, doi: 10.1016/j.apsusc.2021.149135.

[104] Q. Chen *et al.*, "Grafting carbon nanotubes densely on carbon fibers by poly(propylene imine) for interfacial enhancement of carbon fiber composites," *Carbon N. Y.*, vol. 158, pp. 704–710, 2020, doi: 10.1016/j.carbon.2019.11.043.

[105] A. Haghbin, G. Liaghat, H. Hadavinia, A. M. Arabi, and M. H. Pol, "Enhancement of the electrical conductivity and interlaminar shear strength of CNT/GFRP hierarchical composite using an electrophoretic deposition technique," *Materials (Basel).*, vol. 10, no. 10, 2017, doi: 10.3390/ma10101120.

[106] Z. Wu *et al.*, "Enhancing the Mechanical Performance of Fiber-Reinforced Polymer Composites Using Carbon Nanotubes as an Effective Nano-Phase Reinforcement," *Adv. Mater. Interfaces*, vol. 10, no. 3, 2023, doi: 10.1002/admi.202201935.

[107] A. Gaurav and K. K. Singh, "Effect of pristine MWCNTs on the fatigue life of GFRP laminates-an experimental and statistical evaluation," *Compos. Part B Eng.*, vol. 172, pp. 83–96, 2019, doi: 10.1016/j.compositesb.2019.05.069.

[108] M. Sánchez, M. Campo, A. Jiménez-Suárez, and A. Ureña, "Effect of the carbon nanotube functionalization on flexural properties of multiscale carbon fiber/epoxy composites manufactured by VARIM," *Compos. Part B Eng.*, vol. 45, no. 1, pp. 1613–1619, 2013, doi: 10.1016/j.compositesb.2012.09.063.

[109] H. Rong, K. H. Dahmen, H. Garmestani, M. Yu, and K. I. Jacob, "Comparison of chemical vapor deposition and chemical grafting for improving the mechanical properties of carbon fiber/epoxy composites with multi-wall carbon nanotubes," *J. Mater. Sci.*, vol. 48, no. 14, pp. 4834–4842, 2013, doi: 10.1007/s10853-012-7119-2.

[110] K. Yildiz, İ. Gürkan, F. Turgut, F. Cebeci, and H. Cebeci, “Fracture toughness enhancement of fuzzy CNT-glass fiber reinforced composites with a combined reinforcing strategy,” *Compos. Commun.*, vol. 21, no. December 2019, 2020, doi: 10.1016/j.coco.2020.100423.

[111] P. G. Jenkins, L. Yang, J. J. Liggat, and J. L. Thomason, “Investigation of the strength loss of glass fibre after thermal conditioning,” *J. Mater. Sci.*, vol. 50, no. 3, pp. 1050–1057, 2015, doi: 10.1007/s10853-014-8661-x.

[112] M. D. Lund and Y. Yue, “Impact of drawing stress on the tensile strength of oxide glass fibers,” *J. Am. Ceram. Soc.*, vol. 93, no. 10, pp. 3236–3243, 2010, doi: 10.1111/j.1551-2916.2010.03879.x.

[113] L. Yang and J. L. Thomason, “The thermal behaviour of glass fibre investigated by thermomechanical analysis,” *J. Mater. Sci.*, vol. 48, no. 17, pp. 5768–5775, 2013, doi: 10.1007/s10853-013-7369-7.

[114] W. H. OTTO, “Compaction Effects in Glass Fibers,” *J. Am. Ceram. Soc.*, vol. 44, no. 2, pp. 68–72, 1961, doi: https://doi.org/10.1111/j.1151-2916.1961.tb15352.x.

[115] J. L. Thomason, L. Yang, and R. Meier, “The properties of glass fibres after conditioning at composite recycling temperatures,” *Compos. Part A Appl. Sci. Manuf.*, vol. 61, pp. 201–208, 2014, doi: 10.1016/j.compositesa.2014.03.001.

[116] M. Zhao *et al.*, “Multiscale modeling of stress transfer in continuous microscale fiber reinforced composites with nano-engineered interphase,” *Compos. Sci. Technol.*, vol. 114, no. 9, pp. 2273–2281, 2010, doi: 10.1016/j.compscitech.2010.04.010.

[117] M. Ahmadi, O. Zabihi, M. Masoomi, and M. Naebe, “Synergistic effect of MWCNTs functionalization on interfacial and mechanical properties of multi-scale UHMWPE fibre reinforced epoxy composites,” *Compos. Sci. Technol.*, vol. 134, pp. 1–11, 2016, doi: 10.1016/j.compscitech.2016.07.026.

[118] W. Zhang, X. Deng, G. Sui, and X. Yang, “Improving interfacial and mechanical properties of carbon nanotube-sized carbon fiber/epoxy composites,” *Carbon N. Y.*, vol. 145, pp. 629–639, 2019, doi: 10.1016/j.carbon.2019.01.063.

[119] G. Cho, S. Azzouzi, G. Zucchi, and B. Lebental, “Electrical and electrochemical sensors based on carbon nanotubes for the monitoring of chemicals in water—a review,” *Sensors*, vol. 22, no. 1, 2022, doi: 10.3390/s22010218.

[120] D. K. Kim, W. Han, K. W. Kim, and B. J. Kim, “Electromagnetic Interference Shielding Effectiveness of Direct-Grown-Carbon Nanotubes/Carbon and Glass Fiber-Reinforced Epoxy Matrix Composites,” *Materials (Basel).*, vol. 16, no. 7, 2023, doi: 10.3390/ma16072604.

[121] D. He *et al.*, “Design of electrically conductive structural composites by

modulating aligned CVD-grown carbon nanotube length on glass fibers," *ACS Appl. Mater. Interfaces*, vol. 9, no. 3, pp. 2948–2958, 2017, doi: 10.1021/acsami.6b13397.

[122] E. Kandare *et al.*, "Improving the through-thickness thermal and electrical conductivity of carbon fibre/epoxy laminates by exploiting synergy between graphene and silver nano-inclusions," *Compos. Part A Appl. Sci. Manuf.*, vol. 69, pp. 72–82, 2015, doi: 10.1016/j.compositesa.2014.10.024.

[123] M. Gagné and D. Therriault, "Lightning strike protection of composites," *Prog. Aerosp. Sci.*, vol. 64, pp. 1–16, 2014, doi: 10.1016/j.paerosci.2013.07.002.

[124] R. Baby, B. Saifullah, and M. Z. Hussein, "Carbon Nanomaterials for the Treatment of Heavy Metal-Contaminated Water and Environmental Remediation," *Nanoscale Res. Lett.*, vol. 14, no. 1, 2019, doi: 10.1186/s11671-019-3167-8.

[125] G. Vilardi, T. Mpouras, D. Dermatas, N. Verdone, A. Polydera, and L. Di Palma, "Nanomaterials application for heavy metals recovery from polluted water: The combination of nano zero-valent iron and carbon nanotubes. Competitive adsorption non-linear modeling," *Chemosphere*, vol. 201, pp. 716–729, 2018, doi: 10.1016/j.chemosphere.2018.03.032.

[126] S. S. Fiyadh *et al.*, "Review on heavy metal adsorption processes by carbon nanotubes," *J. Clean. Prod.*, vol. 230, pp. 783–793, 2019, doi: 10.1016/j.jclepro.2019.05.154.

[127] X. Ren, C. Chen, M. Nagatsu, and X. Wang, "Carbon nanotubes as adsorbents in environmental pollution management: A review," *Chem. Eng. J.*, vol. 170, no. 2–3, pp. 395–410, 2011, doi: 10.1016/j.cej.2010.08.045.

[128] G. Ghasemzadeh, M. Momenpour, F. Omidi, M. R. Hosseini, M. Ahani, and A. Barzegari, "Applications of nanomaterials in water treatment and environmental remediation," *Front. Environ. Sci. Eng.*, vol. 8, no. 4, pp. 471–482, 2014, doi: 10.1007/s11783-014-0654-0.

[129] M. Yellappa, J. S. Sravan, O. Sarkar, Y. V. R. Reddy, and S. V. Mohan, "Modified conductive polyaniline-carbon nanotube composite electrodes for bioelectricity generation and waste remediation," *Bioresour. Technol.*, vol. 284, no. January, pp. 148–154, 2019, doi: 10.1016/j.biortech.2019.03.085.

[130] N. E. Eltayeb and A. Khan, "Design and Preparation of a New and Novel Nanocomposite with CNTs and Its Sensor Applications," *J. Mater. Res. Technol.*, vol. 8, no. 2, pp. 2238–2246, 2019, doi: 10.1016/j.jmrt.2019.03.002.

[131] N. Muralidharan *et al.*, "Carbon Nanotube Reinforced Structural Composite Supercapacitor," *Sci. Rep.*, vol. 8, no. 1, pp. 1–9, 2018, doi: 10.1038/s41598-018-

34963-x.

[132] H. Zhou *et al.*, “Structural composite energy storage devices — a review,” *Mater. Today Energy*, vol. 24, p. 100924, 2022, doi: 10.1016/j.mtener.2021.100924.

[133] Y. Zhong, X. Xia, W. Mai, J. Tu, and H. J. Fan, “Integration of Energy Harvesting and Electrochemical Storage Devices,” *Adv. Mater. Technol.*, vol. 2, no. 12, pp. 1–14, 2017, doi: 10.1002/admt.201700182.

[134] S. Wang, K. Cao, L. Xu, and Y. Tong, “Improving electrochemical properties of carbon nanotubes/reduced graphene oxide composite fibers by chemical modification,” *Appl. Phys. A Mater. Sci. Process.*, vol. 129, no. 1, pp. 1–11, 2023, doi: 10.1007/s00339-022-06340-z.

[135] L. Wen, F. Li, and H. M. Cheng, “Carbon Nanotubes and Graphene for Flexible Electrochemical Energy Storage: from Materials to Devices,” *Adv. Mater.*, vol. 28, no. 22, pp. 4306–4337, 2016, doi: 10.1002/adma.201504225.

[136] N. Shirshova *et al.*, “Multifunctional Structural Energy Storage Composite Supercapacitors,” *J. Mater. Chem. C*, vol. 172, 2014, doi: 10.1039/C4FD00055B.

[137] Y. M. Manawi, Ihsanullah, A. Samara, T. Al-Ansari, and M. A. Atieh, “A review of carbon nanomaterials’ synthesis via the chemical vapor deposition (CVD) method,” *Materials (Basel).*, vol. 11, no. 5, 2018, doi: 10.3390/ma11050822.

[138] M. M. A. Rafique and J. Iqbal, “Production of Carbon Nanotubes by Different Routes-A Review,” *J. Encapsulation Adsorpt. Sci.*, vol. 01, no. 02, pp. 29–34, 2011, doi: 10.4236/jeas.2011.12004.

[139] M. F. L. De Volder, S. H. Tawfick, R. H. Baughman, and A. J. Hart, “Carbon nanotubes: Present and future commercial applications,” *Science (80-.).*, vol. 339, no. 6119, pp. 535–539, 2013, doi: 10.1126/science.1222453.

[140] K. S. Munir and C. Wen, “Deterioration of the Strong sp2 Carbon Network in Carbon Nanotubes during the Mechanical Dispersion Processing—A Review,” *Crit. Rev. Solid State Mater. Sci.*, vol. 41, no. 5, pp. 347–366, 2016, doi: 10.1080/10408436.2015.1127205.

[141] H. Dai, “Carbon nanotubes: Opportunities and challenges,” *Surf. Sci.*, vol. 500, no. 1–3, pp. 218–241, 2002.

[142] M. L. Terranova, V. Sessa, and M. Rossi, “The world of carbon nanotubes: An overview of CVD growth methodologies,” *Chem. Vap. Depos.*, vol. 12, no. 6, pp. 315–325, 2006, doi: 10.1002/cvde.200600030.

[143] A. Takakura *et al.*, “Strength of carbon nanotubes depends on their chemical structures,” *Nat. Commun.*, vol. 10, no. 1, pp. 1–7, 2019, doi: 10.1038/s41467-019-10959-7.

[144] J. P. Salvetat *et al.*, “Mechanical properties of carbon nanotubes,” *Appl. Phys. A Mater. Sci. Process.*, vol. 69, no. 3, pp. 255–260, 1999, doi: 10.1007/s003390050999.

[145] B. Q. Wei, R. Vajtai, and P. M. Ajayan, “Reliability and current carrying capacity of carbon nanotubes,” *Appl. Phys. Lett.*, vol. 79, no. 8, pp. 1172–1174, 2001, doi: 10.1063/1.1396632.

[146] P. Kim, L. Shi, A. Majumdar, and P. L. McEuen, “Thermal transport measurements of individual multiwalled nanotubes,” *Phys. Rev. Lett.*, vol. 87, no. 21, pp. 215502-1-215502–4, 2001, doi: 10.1103/PhysRevLett.87.215502.

[147] M. Ahmad and S. R. P. Silva, “Low temperature growth of carbon nanotubes – A review,” *Carbon N. Y.*, vol. 158, pp. 24–44, 2020, doi: 10.1016/j.carbon.2019.11.061.

[148] V. Jourdain and C. Bichara, “Current understanding of the growth of carbon nanotubes in catalytic chemical vapour deposition,” *Carbon N. Y.*, vol. 58, pp. 2–39, 2013, doi: 10.1016/j.carbon.2013.02.046.

[149] L. S. Ulloa *et al.*, “Carbon nanotubes substrates alleviate pro-calcific evolution in porcine valve interstitial cells,” *Nanomaterials*, vol. 11, no. 10, p. 2724, 2021, doi: 10.3390/nano11102724.

[150] H. Wang and Z. F. Ren, “The evolution of carbon nanotubes during their growth by plasma enhanced chemical vapor deposition,” *Nanotechnology*, vol. 22, no. 40, 2011, doi: 10.1088/0957-4484/22/40/405601.

[151] R. Alexandrescu *et al.*, “Synthesis of carbon nanotubes by CO2-laser-assisted chemical vapour deposition,” *Infrared Phys. Technol.*, vol. 44, no. 1, pp. 43–50, 2003, doi: 10.1016/S1350-4495(02)00158-5.

[152] A. C. Dupuis, “The catalyst in the CCVD of carbon nanotubes-a review,” *Prog. Mater. Sci.*, vol. 50, no. 8, pp. 929–961, 2005, doi: 10.1016/j.pmatsci.2005.04.003.

[153] M. Kumar and Y. Ando, “Chemical vapor deposition of carbon nanotubes: A review on growth mechanism and mass production,” *J. Nanosci. Nanotechnol.*, vol. 10, no. 6, pp. 3739–3758, 2010, doi: 10.1166/jnn.2010.2939.

[154] J. P. Tessonnier and D. S. Su, “Recent progress on the growth mechanism of carbon nanotubes: A review,” *ChemSusChem*, vol. 4, no. 7, pp. 824–847, 2011, doi: 10.1002/cssc.201100175.

[155] Y. Li *et al.*, “How catalysts affect the growth of single-walled carbon nanotubes on substrates,” *Adv. Mater.*, vol. 22, no. 13, pp. 1508–1515, 2010, doi: 10.1002/adma.200904366.

[156] L. Jodin, A. C. Dupuis, E. Rouvière, and P. Reiss, “Influence of the catalyst type

on the growth of carbon nanotubes via methane chemical vapor deposition," *J. Phys. Chem. B*, vol. 110, no. 14, pp. 7328–7333, 2006, doi: 10.1021/jp056793z.

[157] D. Takagi, Y. Homma, H. Hibino, S. Suzuki, and Y. Kobayashi, "Single-walled carbon nanotube growth from highly activated metal nanoparticles," *Nano Lett.*, vol. 6, no. 12, pp. 2642–2645, 2006, doi: 10.1021/nl061797g.

[158] I. Rago *et al.*, "Carbon Nanotubes, Directly Grown on Supporting Surfaces, Improve Neuronal Activity in Hippocampal Neuronal Networks," *Adv. Biosyst.*, vol. 3, no. 5, p. 1800286, 2019, doi: 10.1002/adbi.201800286.

[159] S. Ahmad, D. Copic, C. George, and M. De Volder, "Hierarchical Assemblies of Carbon Nanotubes for Ultraflexible Li-Ion Batteries," *Adv. Mater.*, vol. 28, no. 31, pp. 6705–6710, 2016, doi: 10.1002/adma.201600914.

[160] K. Chen *et al.*, "Printed Carbon Nanotube Electronics and Sensor Systems," *Adv. Mater.*, vol. 28, no. 22, pp. 4397–4414, 2016, doi: 10.1002/adma.201504958.

[161] C. A. Hewitt, A. B. Kaiser, S. Roth, M. Craps, R. Czerw, and D. L. Carroll, "Multilayered carbon nanotube/polymer composite based thermoelectric fabrics," *Nano Lett.*, vol. 12, no. 3, pp. 1307–1310, 2012, doi: 10.1021/nl203806q.

[162] V. Jelicic *et al.*, "Towards Internet of Things for event-driven low-power gas sensing using carbon nanotubes," *Proc. - 2015 6th IEEE Int. Work. Adv. Sensors Interfaces, IWASI 2015*, pp. 271–276, 2015, doi: 10.1109/IWASI.2015.7184980.

[163] Z. Yao, A. Xia, D. Wang, and C. Wang, "Low temperature multi-catalytic growth and growth mechanism of carbon nanotubes on carbon fiber surfaces," *Nanotechnology*, vol. 35, no. 1, 2024, doi: 10.1088/1361-6528/acfef7.

[164] G. D. Nessim *et al.*, "Low temperature synthesis of vertically aligned carbon nanotubes with electrical contact to metallic substrates enabled by thermal decomposition of the carbon feedstock," *Nano Lett.*, vol. 9, no. 10, pp. 3398–3405, 2009, doi: 10.1021/nl900675d.

[165] A. Magrez *et al.*, "Low-temperature, highly efficient growth of carbon nanotubes on functional materials by an oxidative dehydrogenation reaction," *ACS Nano*, vol. 4, no. 7, pp. 3702–3708, 2010, doi: 10.1021/nn100279j.

[166] Q. Wang, Y. Zheng, C. Zhou, M. Chan, and C. Y. Yang, "Low-temperature grown vertically aligned carbon nanotube array for an optimal infrared bolometer," *Nanotechnology*, vol. 32, no. 50, 2021, doi: 10.1088/1361-6528/ac28dc.

[167] R. Cartwright *et al.*, "Low temperature growth of carbon nanotubes on tetrahedral amorphous carbon using Fe-Cu catalyst," *Carbon N. Y.*, vol. 81, no. 1, pp. 639–649, 2015, doi: 10.1016/j.carbon.2014.10.001.

[168] W. Fan, Y. Wang, C. Wang, J. Chen, and Y. Yuan, "Communication—Catalyst

Study on the Large-Scale Preparation of Carbon Nanotube-Grafted Carbon Fibers with High Tensile Strength," *ECS J. Solid State Sci. Technol.*, vol. 5, no. 6, pp. M35–M37, 2016, doi: 10.1149/2.0131606jss.

[169] S. Su *et al.*, "Continuous method for grafting CNTs on the surface of carbon fibers based on cobalt catalyst assisted by thiourea," *J. Mater. Sci.*, vol. 54, no. 19, pp. 12498–12508, 2019, doi: 10.1007/s10853-019-03827-8.

[170] Q. Zhang, L. Yu, and Z. Cui, "Effects of the size of nano-copper catalysts and reaction temperature on the morphology of carbon fibers," *Mater. Res. Bull.*, vol. 43, no. 3, pp. 735–742, 2008, doi: 10.1016/j.materresbull.2007.03.022.

[171] C. H. Hsiao and J. H. Lin, "Growth of a superhydrophobic multi-walled carbon nanotube forest on quartz using flow-vapor-deposited copper catalysts," *Carbon N. Y.*, vol. 124, pp. 637–641, 2017, doi: 10.1016/j.carbon.2017.09.023.

[172] B. Cui *et al.*, "Ultra-Low-Temperature Growth of Carbon Nanofilament on Continuous Carbon Fiber for Simultaneous Tensile and Interfacial Enhancement," *ACS Appl. Nano Mater.*, vol. 6, no. 9, pp. 7234–7244, 2023, doi: 10.1021/acsanm.3c00330.

[173] E. C. Neyts, "PECVD growth of carbon nanotubes: From experiment to simulation," *J. Vac. Sci. Technol. B, Nanotechnol. Microelectron. Mater. Process. Meas. Phenom.*, vol. 30, no. 3, 2012, doi: 10.1116/1.3702806.

[174] C. Ducati, I. Alexandrou, M. Chhowalla, J. Robertson, and G. A. J. Amaratunga, "The role of the catalytic particle in the growth of carbon nanotubes by plasma enhanced chemical vapor deposition," *J. Appl. Phys.*, vol. 95, no. 11 I, pp. 6387–6391, 2004, doi: 10.1063/1.1728293.

[175] M. Katagiri *et al.*, "Carbon nanotube vias fabricated by remote plasma-enhanced chemical vapor deposition," *Jpn. J. Appl. Phys.*, vol. 47, no. 4 PART 1, pp. 2024–2027, 2008, doi: 10.1143/JJAP.47.2024.

[176] M. Katagiri *et al.*, "Low-temperature growth of multiwalled carbon nanotubes by surface-wave plasma-enhanced chemical vapor deposition using catalyst nanoparticles," *Jpn. J. Appl. Phys.*, vol. 48, no. 9 Part 1, pp. 0902051–0902053, 2009, doi: 10.1143/JJAP.48.090205.

[177] Y. Yamazaki *et al.*, "Synthesis of a closely packed carbon nanotube forest by a multi-step growth method using plasma-based chemical vapor deposition," *Appl. Phys. Express*, vol. 3, no. 5, 2010, doi: 10.1143/APEX.3.055002.

[178] S. Li, C. Zhou, S. Raju, and M. Chan, "Catalyst design for high-density and low-temperature CNT synthesis on conductive Ti silicide substrate," *Diam. Relat. Mater.*, vol. 75, pp. 39–43, 2017, doi: 10.1016/j.diamond.2017.01.003.

[179] M. Baro, D. Gogoi, A. R. Pal, N. C. Adhikary, H. Bailung, and J. Chutia, "Pulsed

PECVD for low-temperature growth of vertically aligned carbon nanotubes," *Chem. Vap. Depos.*, vol. 20, no. 4–6, pp. 161–169, 2014, doi: 10.1002/cvde.201307093.

[180] M. Chen, C. M. Chen, and C. F. Chen, "Preparation of high yield multi-walled carbon nanotubes by microwave plasma chemical vapor deposition at low temperature," *J. Mater. Sci.*, vol. 37, no. 17, pp. 3561–3567, 2002, doi: 10.1023/A:1016544001173.

[181] B. O. Boskovic, V. Stolojan, R. U. A. Khan, S. Haq, and S. R. P. Silva, "Large-area synthesis of carbon nanofibres at room temperature," *Nat. Mater.*, vol. 1, no. 3, pp. 165–168, 2002, doi: 10.1038/nmat755.

[182] K. B. K. Teo *et al.*, "The significance of plasma heating in carbon nanotube and nanofiber growth," *Nano Lett.*, vol. 4, no. 5, pp. 921–926, 2004, doi: 10.1021/nl049629g.

[183] M. Meyyappan, "A review of plasma enhanced chemical vapour deposition of carbon nanotubes," *J. Phys. D. Appl. Phys.*, vol. 42, no. 21, 2009, doi: 10.1088/0022-3727/42/21/213001.

[184] S. Hofmann, C. Ducati, J. Robertson, and B. Kleinsorge, "Low-temperature growth of carbon nanotubes by plasma-enhanced chemical vapor deposition," *Appl. Phys. Lett.*, vol. 83, no. 1, pp. 135–137, 2003, doi: 10.1063/1.1589187.

[185] V. Cech, R. Prikryl, R. Balkova, A. Grycova, and J. Vanek, "Plasma surface treatment and modification of glass fibers," *Compos. Part A Appl. Sci. Manuf.*, vol. 33, no. 10, pp. 1367–1372, 2002, doi: 10.1016/S1359-835X(02)00149-5.

[186] Z. Sha *et al.*, "Low-temperature plasma assisted growth of vertical graphene for enhancing carbon fibre/epoxy interfacial strength," *Compos. Sci. Technol.*, vol. 184, p. 107867, 2019, doi: 10.1016/j.compscitech.2019.107867.

[187] C. Zhang *et al.*, "Improvement for interface adhesion of epoxy/carbon fibers endowed with carbon nanotubes via microwave plasma-enhanced chemical vapor deposition," *Polym. Compos.*, vol. 39, pp. E1262–E1268, 2018, doi: 10.1002/pc.24843.

[188] Z. Luo *et al.*, "Effect of ion bombardment on the synthesis of vertically aligned single-walled carbon nanotubes by plasma-enhanced chemical vapor deposition," *Nanotechnology*, vol. 19, no. 25, 2008, doi: 10.1088/0957-4484/19/25/255607.

[189] Y. Li *et al.*, "Preferential Growth of Semiconducting Single-Walled Carbon Nanotubes by a Plasma Enhanced CVD Method," *Nano Lett.*, vol. 4, no. 2, pp. 317–321, 2004, doi: 10.1021/nl035097c.

[190] G. Zhang *et al.*, "Selective etching of metallic carbon nanotubes by gas-phase reaction," *Science (80-.).*, vol. 314, no. 5801, pp. 974–977, 2006, doi:

10.1126/science.1133781.

[191] T. Nozaki, S. Yoshida, T. Karatsu, and K. Okazaki, “Atmospheric-pressure plasma synthesis of carbon nanotubes,” *J. Phys. D. Appl. Phys.*, vol. 44, no. 17, 2011, doi: 10.1088/0022-3727/44/17/174007.

[192] M. F. Pucci, P. J. Liotier, and S. Drapier, “Tensiometric method to reliably assess wetting properties of single fibers with resins: Validation on cellulosic reinforcements for composites,” *Colloids Surfaces A Physicochem. Eng. Asp.*, vol. 512, pp. 26–33, 2017, doi: 10.1016/j.colsurfa.2016.09.047.

[193] R. P. Yadav *et al.*, “Evaluation of vertical alignment in carbon nanotubes: A quantitative approach,” *Nucl. Instruments Methods Phys. Res. Sect. A Accel. Spectrometers, Detect. Assoc. Equip.*, vol. 1060, no. January, p. 169081, 2024, doi: 10.1016/j.nima.2024.169081.

[194] E. Schifano *et al.*, “Plasma-Etched Vertically Aligned CNTs with Enhanced Antibacterial Power,” *Nanomaterials*, vol. 13, no. 6, p. 1800286, 2023, doi: 10.3390/nano13061081.

[195] S. Tayyab *et al.*, “Spectromicroscopy Study of Induced Defects in Ion-Bombarded Highly Aligned Carbon Nanotubes,” *Nanomaterials*, vol. 14, no. 77, 2024, doi: 10.3390/nano14010077.

[196] N. Jiménez-Arévalo *et al.*, “Potassium doping of vertically aligned multi-walled carbon nanotubes,” *J. Chem. Phys.*, vol. 160, no. 21, p. 214707, 2024.

[197] ASTM, “C1557 : Standard Test Method for Tensile Strength and Young ’ s Modulus of Fibers,” *Annu. B. ASTM Stand.*, vol. 03, no. Reapproved 2013, pp. 1–10, 2014.

[198] R. Danzer, “A general strength distribution function for brittle materials,” *J. Eur. Ceram. Soc.*, vol. 10, no. 6, pp. 461–472, 1992, doi: 10.1016/0955-2219(92)90021-5.

[199] J. D. Sullivan and P. H. Lauzon, “Experimental probability estimators for Weibull plots,” *J. Mater. Sci. Lett.*, vol. 5, no. 12, pp. 1245–1247, 1986, doi: 10.1007/BF01729379.

[200] W. C. Oliver and G. M. Pharr, “An improved technique for determining hardness and elastic modulus (Young’s modulus),” *J. Mater. Res.*, 1992.

[201] M. Sebastiani, R. Moscatelli, F. Ridi, P. Baglioni, and F. Carassiti, “High-resolution high-speed nanoindentation mapping of cement pastes: Unravelling the effect of microstructure on the mechanical properties of hydrated phases,” *Mater. Des.*, vol. 97, pp. 372–380, 2016, doi: 10.1016/j.matdes.2016.02.087.

[202] E. P. Koumoulos *et al.*, “Metrology and nano-mechanical tests for nano-

manufacturing and nano-bio interface: Challenges & future perspectives," *Mater. Des.*, vol. 137, pp. 446–462, 2018, doi: 10.1016/j.matdes.2017.10.035.

[203] B. Vignesh, W. C. Oliver, G. S. Kumar, and P. S. Phani, "Critical assessment of high speed nanoindentation mapping technique and data deconvolution on thermal barrier coatings," *Mater. Des.*, vol. 181, p. 108084, 2019, doi: 10.1016/j.matdes.2019.108084.

[204] P. Sudharshan Phani and W. C. Oliver, "A critical assessment of the effect of indentation spacing on the measurement of hardness and modulus using instrumented indentation testing," *Mater. Des.*, vol. 164, p. 107563, 2019, doi: 10.1016/j.matdes.2018.107563.

[205] G. Constantinides, K. S. Ravi Chandran, F. J. Ulm, and K. J. Van Vliet, "Grid indentation analysis of composite microstructure and mechanics: Principles and validation," *Mater. Sci. Eng. A*, vol. 430, no. 1–2, pp. 189–202, 2006, doi: 10.1016/j.msea.2006.05.125.

[206] F. J. Ulm, M. Vandamme, C. Bobko, J. Alberto Ortega, K. Tai, and C. Ortiz, "Statistical indentation techniques for hydrated nanocomposites: Concrete, bone, and shale," *J. Am. Ceram. Soc.*, vol. 90, no. 9, pp. 2677–2692, 2007, doi: 10.1111/j.1551-2916.2007.02012.x.

[207] M. Sebastiani, K. E. Johanns, E. G. Herbert, F. Carassiti, and G. M. Pharr, "A novel pillar indentation splitting test for measuring fracture toughness of thin ceramic coatings," *Philos. Mag.*, vol. 95, no. 16–18, pp. 1928–1944, Jun. 2015, doi: 10.1080/14786435.2014.913110.

[208] M. Sebastiani, K. E. Johanns, E. G. Herbert, and G. M. Pharr, "Measurement of fracture toughness by nanoindentation methods: Recent advances and future challenges," *Curr. Opin. Solid State Mater. Sci.*, vol. 19, no. 6, pp. 324–333, Dec. 2015, doi: 10.1016/j.cossms.2015.04.003.

[209] G. Bolelli *et al.*, "Damage progression in thermal barrier coating systems during thermal cycling: A nano-mechanical assessment," *Mater. Des.*, vol. 166, p. 107615, Mar. 2019, doi: 10.1016/j.matdes.2019.107615.

[210] T. Beirau, E. Rossi, M. Sebastiani, W. C. Oliver, H. Pöllmann, and R. C. Ewing, "Fracture toughness of radiation-damaged zircon studied by nanoindentation pillar-splitting," *Appl. Phys. Lett.*, vol. 119, no. 23, p. 231903, Dec. 2021, doi: 10.1063/5.0070597.

[211] M. Ghidelli, M. Sebastiani, K. E. Johanns, and G. M. Pharr, "Effects of indenter angle on micro-scale fracture toughness measurement by pillar splitting," *J. Am. Ceram. Soc.*, vol. 100, no. 12, pp. 5731–5738, Dec. 2017, doi: 10.1111/jace.15093.

[212] A. M. Korsunsky, M. Sebastiani, and E. Bemporad, "Focused ion beam ring

drilling for residual stress evaluation," *Mater. Lett.*, vol. 63, no. 22, pp. 1961–1963, Sep. 2009, doi: 10.1016/j.matlet.2009.06.020.

[213] A. C. Ferrari and J. Robertson, "Interpretation of Raman Spectra of disordered and amorphous carbon," *Phys. Rev. B*, vol. 61, no. 20, pp. 14095–14107, 2000, doi: 10.1103/PhysRevB.61.14095.

[214] D. K. Owens and R. C. Wendt, "Estimation of the surface free energy of polymers," *J. Appl. Polym. Sci.*, vol. 13, no. 8, pp. 1741–1747, 1969, doi: 10.1002/app.1969.070130815.

[215] W. Zhou, X. Meng, J. Gao, and A. N. Alshawabkeh, "Hydrogen peroxide generation from O2 electroreduction for environmental remediation: A state-of-the-art review," *Chemosphere*, vol. 225, no. 617, pp. 588–607, 2019, doi: 10.1016/j.chemosphere.2019.03.042.

[216] S. Feih, K. Manatpon, Z. Mathys, A. G. Gibson, and A. P. Mouritz, "Strength degradation of glass fibers at high temperatures," *J. Mater. Sci.*, vol. 44, no. 2, pp. 392–400, 2009, doi: 10.1007/s10853-008-3140-x.

[217] S. Feih, A. P. Mouritz, and S. W. Case, "Determining the mechanism controlling glass fibre strength loss during thermal recycling of waste composites," *Compos. Part A Appl. Sci. Manuf.*, vol. 76, pp. 255–261, 2015, doi: https://doi.org/10.1016/j.compositesa.2015.06.006.

[218] L. Yang and J. L. Thomason, "Effect of silane coupling agent on mechanical performance of glass fibre," *J. Mater. Sci.*, vol. 48, no. 5, pp. 1947–1954, 2013, doi: 10.1007/s10853-012-6960-7.

[219] M. H. Berger and D. Jeulin, "Statistical analysis of the failure stresses of ceramic fibres: Dependence of the Weibull parameters on the gauge length, diameter variation and fluctuation of defect density," *J. Mater. Sci.*, vol. 38, no. 13, pp. 2913–2923, 2003, doi: 10.1023/A:1024405123420.

[220] Q. Wei *et al.*, "Disposing of silica fiber' surface," *Key Eng. Mater.*, vol. 512–515, pp. 559–562, 2012, doi: 10.4028/www.scientific.net/KEM.512-515.559.

[221] Q. Wei *et al.*, "Effects of different heat treatment temperatures on the properties of quartz fibers," *Adv. Mater. Res.*, vol. 105–106, no. 1, pp. 115–118, 2010, doi: 10.4028/www.scientific.net/AMR.105-106.115.

[222] L. Wang, Y. D. Huang, L. Liu, and J. B. Zhang, "The influence of PBO coating on room temperature mechanic properties of heat-treated quartz fiber-reinforced methyl silicon resin composites. I. Flexural properties," *Mater. Sci. Eng. A*, vol. 465, no. 1–2, pp. 22–28, 2007, doi: 10.1016/j.msea.2007.04.036.

[223] H. G. De Luca, D. B. Anthony, E. S. Greenhalgh, A. Bismarck, and M. S. P. Shaffer, "Piezoresistive structural composites reinforced by carbon nanotube-

grafted quartz fibres," *Compos. Sci. Technol.*, vol. 198, p. 108275, 2020, doi: 10.1016/j.compscitech.2020.108275.

[224] S. Feih, A. Thraner, and H. Lilholt, "Tensile strength and fracture surface characterisation of sized and unsized glass fibers," *J. Mater. Sci.*, vol. 40, no. 7, pp. 1615–1623, 2005, doi: 10.1007/s10853-005-0661-4.

[225] P. G. Jenkins, L. Yang, J. L. Thomason, X. Chen, J. F. Watts, and S. J. Hinder, "Investigation of chemical and physical surface changes of thermally conditioned glass fibres," *Fibers*, vol. 7, no. 1, p. 7, 2019, doi: 10.3390/fib7010007.

[226] M. D. Lund and Y. Yue, "Fractography and tensile strength of glass wool fibres," *J. Ceram. Soc. Japan*, vol. 116, no. 1356, pp. 841–845, 2008, doi: 10.2109/jcersj2.116.841.

[227] F. Islam, S. Joannès, and L. Laiarinandrasana, "Evaluation of critical parameters in tensile strength measurement of single fibres," *J. Compos. Sci.*, vol. 3, no. 3, p. 69, 2019, doi: 10.3390/jcs3030069.

[228] J. L. Thomason, U. Nagel, L. Yang, and D. Bryce, "A study of the thermal degradation of glass fibre sizings at composite processing temperatures," *Compos. Part A Appl. Sci. Manuf.*, vol. 121, no. December 2018, pp. 56–63, 2019, doi: 10.1016/j.compositesa.2019.03.013.

[229] H. R. Lu and C. A. Wang, "Fabrication and characterization of ceramic coatings with alumina-silica sol-incorporated α-alumina powder coated on woven quartz fiber fabrics," *Ceram. Int.*, vol. 39, no. 6, pp. 6041–6050, 2013, doi: 10.1016/j.ceramint.2013.01.020.

[230] J. Murach and R. Briickner, "Preparation and structure-sensitive investigations on silica glass fibers," vol. 211, pp. 250–261, 1997.

[231] A. A. Griffith, "The phenomena of rupture and flow in solids," 1997.

[232] P. Sharma, V. Pavelyev, S. Kumar, P. Mishra, S. S. Islam, and N. Tripathi, *Analysis on the synthesis of vertically aligned carbon nanotubes: growth mechanism and techniques*, vol. 31. Springer US, 2020.

[233] Y. Yao, Z. Li, and C. P. Wong, "Quality control of vertically aligned carbon nanotubes grown by chemical vapor deposition," *IEEE Trans. Components, Packag. Manuf. Technol.*, vol. 3, no. 11, pp. 1804–1810, 2013, doi: 10.1109/TCPMT.2013.2278174.

[234] M. Lilli *et al.*, "Low temperature direct growth of carbon nanostructures on basalt fibers," *Compos. Part B Eng.*, vol. 262, no. April, 2023, doi: 10.1016/j.compositesb.2023.110826.

[235] N. Yamamoto *et al.*, "High-yield growth and morphology control of aligned carbon

nanotubes on ceramic fibers for multifunctional enhancement of structural composites," *Carbon N. Y.*, vol. 47, no. 3, pp. 551–560, 2009, doi: 10.1016/j.carbon.2008.10.030.

[236] M. Bedewy, B. Viswanath, E. R. Meshot, D. N. Zakharov, E. A. Stach, and A. J. Hart, "Measurement of the Dewetting, Nucleation, and Deactivation Kinetics of Carbon Nanotube Population Growth by Environmental Transmission Electron Microscopy," *Chem. Mater.*, vol. 28, no. 11, pp. 3804–3813, 2016, doi: 10.1021/acs.chemmater.6b00798.

[237] N. P. Pampaloni *et al.*, "Transparent carbon nanotubes promote the outgrowth of enthorino-dentate projections in lesioned organ slice cultures," *Dev. Neurobiol.*, vol. 80, no. 9–10, pp. 316–331, 2020, doi: 10.1002/dneu.22711.

[238] L. Jin, L. Zhang, D. Su, and C. Li, "Direct growth of aligned carbon nanotubes on quartz fibers for structural epoxy composites," *Ind. Eng. Chem. Res.*, vol. 51, no. 13, pp. 4927–4933, 2012, doi: 10.1021/ie202306v.

[239] A. V. Melechko *et al.*, "Vertically aligned carbon nanofibers and related structures: Controlled synthesis and directed assembly," *J. Appl. Phys.*, vol. 97, no. 4, 2005, doi: 10.1063/1.1857591.

[240] A. Gohier, T. M. Minea, M. A. Djouadi, and A. Granier, "Impact of the etching gas on vertically oriented single wall and few walled carbon nanotubes by plasma enhanced chemical vapor deposition," *J. Appl. Phys.*, vol. 101, no. 5, 2007, doi: 10.1063/1.2654647.

[241] A. Gohier, C. P. Ewels, T. M. Minea, and M. A. Djouadi, "Carbon nanotube growth mechanism switches from tip- to base-growth with decreasing catalyst particle size," *Carbon N. Y.*, vol. 46, no. 10, pp. 1331–1338, 2008, doi: 10.1016/j.carbon.2008.05.016.

[242] I. K. Song, Y. S. Cho, G. S. Choi, J. B. Park, and D. J. Kim, "The growth mode change in carbon nanotube synthesis in plasma-enhanced chemical vapor deposition," *Diam. Relat. Mater.*, vol. 13, no. 4–8, pp. 1210–1213, 2004, doi: 10.1016/j.diamond.2004.01.006.

[243] J. H. Lehman, M. Terrones, E. Mansfield, K. E. Hurst, and V. Meunier, "Evaluating the characteristics of multiwall carbon nanotubes," *Carbon N. Y.*, vol. 49, no. 8, pp. 2581–2602, 2011, doi: 10.1016/j.carbon.2011.03.028.

[244] K. A. Wepasnick, B. A. Smith, J. L. Bitter, and D. Howard Fairbrother, "Chemical and structural characterization of carbon nanotube surfaces," *Anal. Bioanal. Chem.*, vol. 396, no. 3, pp. 1003–1014, 2010, doi: 10.1007/s00216-009-3332-5.

[245] A. Jorio and R. Saito, "Raman spectroscopy for carbon nanotube applications," *J. Appl. Phys.*, vol. 129, no. 2, 2021, doi: 10.1063/5.0030809.

[246] P. B. Amama *et al.*, "Role of water in super growth of single-walled carbon nanotube carpets," *Nano Lett.*, vol. 9, no. 1, pp. 44–49, 2009, doi: 10.1021/nl801876h.

[247] O. T. Gul, "Decoupling the catalyst reduction and annealing for suppressing Ostwald ripening in carbon nanotube growth," *Appl. Phys. A Mater. Sci. Process.*, vol. 127, no. 10, pp. 1–11, 2021, doi: 10.1007/s00339-021-04916-9.

[248] B. Ingham, T. H. Lim, C. J. Dotzler, A. Henning, M. F. Toney, and R. D. Tilley, "How nanoparticles coalesce: An in situ study of Au nanoparticle aggregation and grain growth," *Chem. Mater.*, vol. 23, no. 14, pp. 3312–3317, 2011, doi: 10.1021/cm200354d.

[249] M. Bedewy, E. R. Meshot, H. Guo, E. A. Verploegen, W. Lu, and A. J. Hart, "Collective mechanism for the evolution and self-termination of vertically aligned carbon nanotube growth," *J. Phys. Chem. C*, vol. 113, no. 48, pp. 20576–20582, 2009, doi: 10.1021/jp904152v.

[250] J. Lee, M. Abdulhafez, and M. Bedewy, "Decoupling catalyst dewetting, gas decomposition, and surface reactions in carbon nanotube forest growth reveals dependence of density on nucleation temperature," *J. Phys. Chem. C*, vol. 123, no. 47, pp. 28726–28738, 2019, doi: 10.1021/acs.jpcc.9b07894.

[251] U. Sharma and S. C. Sharma, "A parametric study to unravel the alignment mechanism of carbon nanotubes during its plasma-assisted growth," *Phys. Plasmas*, vol. 25, no. 10, 2018, doi: 10.1063/1.5049866.

[252] M. Bedewy, E. R. Meshot, M. J. Reinker, and A. J. Hart, "Population growth dynamics of carbon nanotubes," *ACS Nano*, vol. 5, no. 11, pp. 8974–8989, 2011, doi: 10.1021/nn203144f.

[253] V. Balakrishnan *et al.*, "Real-Time Imaging of Self-Organization and Mechanical Competition in Carbon Nanotube Forest Growth," *ACS Nano*, vol. 10, no. 12, pp. 11496–11504, 2016, doi: 10.1021/acsnano.6b07251.

[254] D. N. Futaba *et al.*, "84% Catalyst activity of water-assisted growth of single walled carbon nanotube forest characterization by a statistical and macroscopic approach," *J. Phys. Chem. B*, vol. 110, no. 15, pp. 8035–8038, 2006, doi: 10.1021/jp060080e.

[255] X. Tang and X. Yan, "Dip-coating for fibrous materials: mechanism, methods and applications," *J. Sol-Gel Sci. Technol.*, vol. 81, no. 2, pp. 378–404, 2017, doi: 10.1007/s10971-016-4197-7.

[256] C. Scheffler, T. Förster, E. Mäder, G. Heinrich, S. Hempel, and V. Mechtcherine, "Aging of alkali-resistant glass and basalt fibers in alkaline solutions: Evaluation of the failure stress by Weibull distribution function," *J. Non. Cryst. Solids*, vol.

355, no. 52–54, pp. 2588–2595, 2009, doi: 10.1016/j.jnoncrysol.2009.09.018.

[257] C. Tang, H. Jiang, X. Zhang, G. Li, and J. Cui, “Corrosion behavior and mechanism of basalt fibers in sodium hydroxide solution,” *Materials (Basel).*, vol. 11, no. 8, pp. 1–16, 2018, doi: 10.3390/ma11081381.

[258] Z. Li, T. Xiao, Q. Pan, J. Cheng, and S. Zhao, “Corrosion behaviour and mechanism of basalt fibres in acidic and alkaline environments,” *Corros. Sci.*, vol. 110, pp. 15–22, 2016, doi: 10.1016/j.corsci.2016.04.019.

[259] S. I. Gutnikov, M. S. Manylov, Y. V. Lipatov, B. I. Lazoryak, and K. V. Pokholok, “Effect of the reduction treatment on the basalt continuous fiber crystallization properties,” *J. Non. Cryst. Solids*, vol. 368, no. 1, pp. 45–50, 2013, doi: 10.1016/j.jnoncrysol.2013.03.007.

[260] M. Halasová, I. Kuběna, P. Roupcová, M. Černý, A. Strachota, and Z. Chlup, “Iron precipitation in basalt fibres embedded in partially pyrolysed methylsiloxane matrix,” *Compos. Part A Appl. Sci. Manuf.*, vol. 123, no. May, pp. 286–292, 2019, doi: 10.1016/j.compositesa.2019.05.026.

[261] Y. Yue, M. Korsgaard, L. F. Kirkegaard, and G. Heide, “Formation of a nanocrystalline layer on the surface of stone wool fibers,” *J. Am. Ceram. Soc.*, vol. 92, no. 1, pp. 62–67, 2009, doi: 10.1111/j.1551-2916.2008.02801.x.

[262] D. Xing *et al.*, “Morphologies and mechanical properties of basalt fibre processed at elevated temperature,” *J. Non. Cryst. Solids*, vol. 582, no. January, p. 121439, 2022, doi: 10.1016/j.jnoncrysol.2022.121439.

[263] L. Hornbøll, N. Lönnroth, and Y. Yue, “Energy release in isothermally stretched silicate glass fibers,” *J. Am. Ceram. Soc.*, vol. 89, no. 1, pp. 70–74, 2006, doi: 10.1111/j.1551-2916.2005.00736.x.

[264] Y. Yue, “Anomalous enthalpy relaxation in vitreous silica,” *Front. Mater.*, vol. 2, no. August, pp. 1–11, 2015, doi: 10.3389/fmats.2015.00054.

[265] M. Ya, J. Deubener, and Y. Yue, “Enthalpy and anisotropy relaxation of glass fibers,” *J. Am. Ceram. Soc.*, vol. 91, no. 3, pp. 745–752, 2008, doi: 10.1111/j.1551-2916.2007.02100.x.

[266] C. Chang, X. Yue, B. Hao, D. Xing, and P. C. Ma, “Direct growth of carbon nanotubes on basalt fiber for the application of electromagnetic interference shielding,” *Carbon N. Y.*, vol. 167, pp. 31–39, 2020, doi: 10.1016/j.carbon.2020.05.074.

[267] K. Reinhold-López, A. Schmitt, A. Braeuer, N. Popovska, and A. Leipertz, “In situ monitoring of the flow field, acetylene decomposition and gas temperature under reaction conditions for the chemical vapor deposition of carbon nanotubes,” *AIChE Annu. Meet. Conf. Proc.*, vol. 18, no. 17, pp. 18223–18228, 2010.

[268] J. Zieliński, I. Zglinicka, L. Znak, and Z. Kaszkur, “Reduction of Fe2O3 with hydrogen,” *Appl. Catal. A Gen.*, vol. 381, no. 1–2, pp. 191–196, 2010, doi: 10.1016/j.apcata.2010.04.003.

[269] W. K. Jóźwiak, E. Kaczmarek, and W. Ignaczak, “Determination of reduction mechanism by TPR data for FeO-H2 system,” *Ann. Univ. Mariae Curie-Skłodowska*, vol. 62, no. 5, pp. 49–58, 2007.

[270] H. Y. Lin, Y. W. Chen, and C. Li, “The mechanism of reduction of iron oxide by hydrogen,” *Thermochim. Acta*, vol. 400, no. 1–2, pp. 61–67, 2003, doi: 10.1016/S0040-6031(02)00478-1.

[271] A. Pineau, N. Kanari, and I. Gaballah, “Kinetics of reduction of iron oxides by H2. Part I: Low temperature reduction of hematite,” *Thermochim. Acta*, vol. 447, no. 1, pp. 89–100, 2006, doi: 10.1016/j.tca.2005.10.004.

[272] A. Pineau, N. Kanari, and I. Gaballah, “Kinetics of reduction of iron oxides by H2. Part II. Low temperature reduction of magnetite,” *Thermochim. Acta*, vol. 456, no. 2, pp. 75–88, 2007, doi: 10.1016/j.tca.2007.01.014.

[273] X. Guo, J. C. Mauro, M. Potuzak, and Y. Yue, “Structural relaxation in annealed hyperquenched basaltic glasses: Insights from calorimetry,” *J. Non. Cryst. Solids*, vol. 358, no. 11, pp. 1356–1361, 2012, doi: 10.1016/j.jnoncrysol.2012.03.009.

[274] R. F. Cooper, J. B. Fanselow, and D. B. Poker, “The mechanism of oxidation of a basaltic glass: Chemical diffusion of network-modifying cations,” *Geochim. Cosmochim. Acta*, vol. 60, no. 17, pp. 3253–3265, 1996, doi: 10.1016/0016-7037(96)00160-3.

[275] E. Raymundo-Piñero, P. Azaïs, T. Cacciaguerra, D. Cazorla-Amorós, A. Linares-Solano, and F. Béguin, “KOH and NaOH activation mechanisms of multiwalled carbon nanotubes with different structural organisation,” *Carbon N. Y.*, vol. 43, no. 4, pp. 786–795, 2005, doi: 10.1016/j.carbon.2004.11.005.

[276] T. Kinoshita, M. Karita, T. Nakano, and Y. Inoue, “Two step floating catalyst chemical vapor deposition including in situ fabrication of catalyst nanoparticles and carbon nanotube forest growth with low impurity level,” *Carbon N. Y.*, vol. 144, pp. 152–160, 2019, doi: 10.1016/j.carbon.2018.12.019.

[277] R. Prasad and P. Singh, “A novel route of single step reactive calcination of copper salts far below their decomposition temperatures for synthesis of highly active catalysts,” *Catal. Sci. Technol.*, vol. 3, no. 12, pp. 3326–3334, 2013, doi: 10.1039/c3cy00626c.

[278] J. Y. Kim, J. A. Rodriguez, J. C. Hanson, A. I. Frenkel, and P. L. Lee, “Reduction of CuO and Cu2O with H2: H embedding and kinetic effects in the formation of suboxides,” *J. Am. Chem. Soc.*, vol. 125, no. 35, pp. 10684–10692, 2003, doi:

10.1021/ja0301673.

[279] H. Zhang, H. R. Tan, S. Jaenicke, and G. K. Chuah, “Highly efficient and robust Cu catalyst for non-oxidative dehydrogenation of ethanol to acetaldehyde and hydrogen,” *J. Catal.*, vol. 389, pp. 19–28, 2020, doi: 10.1016/j.jcat.2020.05.018.

[280] J. Tian *et al.*, “Surface structure deduced differences of copper foil and film for graphene CVD growth,” *Appl. Surf. Sci.*, vol. 300, pp. 73–79, 2014, doi: 10.1016/j.apsusc.2014.02.004.

[281] N. Tajima, T. Kaneko, J. Nara, and T. Ohno, “A first principles study on the CVD graphene growth on copper surfaces: A carbon atom incorporation to graphene edges,” *Surf. Sci.*, vol. 653, pp. 123–129, 2016, doi: 10.1016/j.susc.2016.06.012.

[282] B. Cui *et al.*, “In-situ growth of bamboo-like carbon nanotubes from Cu catalyst on continuous carbon fibre for interfacial enhancement,” *Compos. Sci. Technol.*, vol. 234, no. January, p. 109933, 2023, doi: 10.1016/j.compscitech.2023.109933.

[283] Z. Lin, D. Han, and S. Li, “Study on thermal decomposition of copper(II) acetate monohydrate in air,” *J. Therm. Anal. Calorim.*, vol. 107, no. 2, pp. 471–475, 2012, doi: 10.1007/s10973-011-1454-4.

[284] S. I. Fujita, S. Moribe, Y. Kanamori, and N. Takezawa, “Effects of the calcination and reduction conditions on a Cu/ZnO methanol synthesis catalyst,” *Reaction Kinetics and Catalysis Letters*, vol. 70, no. 1. pp. 11–16, 2000, doi: 10.1023/A:1010390010841.

[285] W. Zhou *et al.*, “Copper Catalyzing Growth of Single-Walled Carbon Nanotubes on Substrates,” *Nano Lett.*, vol. 16, no. 12, 2006, doi: 10.1021/ja809635s.

[286] S. H. Kwon, D. H. Han, H. J. Choe, and J. J. Lee, “Synthesis of copper nanoparticles by solid-state plasma-induced dewetting,” *Nanotechnology*, vol. 22, no. 24, 2011, doi: 10.1088/0957-4484/22/24/245608.

[287] R. Saxena, M. J. Frederick, G. Ramanath, W. N. Gill, and J. L. Plawsky, “Kinetics of voiding and agglomeration of copper nanolayers on silica,” *Phys. Rev. B - Condens. Matter Mater. Phys.*, vol. 72, no. 11, pp. 1–7, 2005, doi: 10.1103/PhysRevB.72.115425.

[288] Y. M. Shyu and F. Chau-Nan Hong, “The effects of pre-treatment and catalyst composition on growth of carbon nanofibers at low temperature,” *Diam. Relat. Mater.*, vol. 10, no. 3–7, pp. 1241–1245, 2001, doi: 10.1016/S0925-9635(00)00550-1.

[289] C. J. Lee, T. J. Lee, and J. Park, “Carbon nanofibers grown on sodalime glass at 500°C using thermal chemical vapor deposition,” *Chem. Phys. Lett.*, vol. 340, no. 5–6, pp. 413–418, 2001, doi: 10.1016/S0009-2614(01)00363-3.

[290] S. H. Yoon *et al.*, “A conceptual model for the structure of catalytically grown carbon nano-fibers,” *Carbon N. Y.*, vol. 43, no. 9, pp. 1828–1838, 2005, doi: 10.1016/j.carbon.2005.02.031.

[291] C. W. Huang, H. C. Wu, W. H. Lin, and Y. Y. Li, “Temperature effect on the formation of catalysts for growth of carbon nanofibers,” *Carbon N. Y.*, vol. 47, no. 3, pp. 795–803, 2009, doi: 10.1016/j.carbon.2008.11.033.

[292] P. Puech *et al.*, “Analyzing the Raman Spectra of Graphenic Carbon Materials from Kerogens to Nanotubes: What Type of Information Can Be Extracted from Defect Bands?,” *C*, vol. 5, no. 4, p. 69, 2019, doi: 10.3390/c5040069.

[293] M. A. Pimenta, G. Dresselhaus, M. S. Dresselhaus, L. G. Cançado, A. Jorio, and R. Saito, “Studying disorder in graphite-based systems by Raman spectroscopy,” *Phys. Chem. Chem. Phys.*, vol. 9, no. 11, pp. 1276–1291, 2007, doi: 10.1039/b613962k.

[294] J. Schwan, S. Ulrich, V. Batori, H. Ehrhardt, and S. R. P. Silva, “Raman spectroscopy on amorphous carbon films,” *J. Appl. Phys.*, vol. 80, no. 1, pp. 440–447, 1996, doi: 10.1063/1.362745.

[295] A. Ferrari and J. Robertson, “Interpretation of Raman spectra of disordered and amorphous carbon,” *Phys. Rev. B - Condens. Matter Mater. Phys.*, vol. 61, no. 20, pp. 14095–14107, 2000, doi: 10.1103/PhysRevB.61.14095.

[296] P. Lv, Y. Y. Feng, P. Zhang, H. M. Chen, N. Zhao, and W. Feng, “Increasing the interfacial strength in carbon fiber/epoxy composites by controlling the orientation and length of carbon nanotubes grown on the fibers,” *Carbon N. Y.*, vol. 49, no. 14, pp. 4665–4673, 2011, doi: 10.1016/j.carbon.2011.06.064.

[297] H. S. Bedi, S. Kumar, and P. K. Agnihotri, “Wettability of thermoplastic and thermoset polymers with carbon nanotube grafted carbon fiber,” *Mater. Today Proc.*, vol. 41, pp. 838–842, 2020, doi: 10.1016/j.matpr.2020.09.162.

[298] J. Wang *et al.*, “Wettability of carbon nanotube-grafted carbon fibers and their interfacial properties in polypropylene thermoplastic composite,” *Compos. Part A Appl. Sci. Manuf.*, vol. 159, no. May, p. 106993, 2022, doi: 10.1016/j.compositesa.2022.106993.

[299] A. H. Barber, S. R. Cohen, and H. Daniel Wagner, “Static and dynamic wetting measurements of single carbon nanotubes,” *Phys. Rev. Lett.*, vol. 92, no. 18, pp. 5–8, 2004, doi: 10.1103/PhysRevLett.92.186103.

[300] S. C. Ramos, G. Vasconcelos, E. F. Antunes, A. O. Lobo, V. J. Trava-Airoldi, and E. J. Corat, “Wettability control on vertically-aligned multi-walled carbon nanotube surfaces with oxygen pulsed DC plasma and CO2 laser treatments,” *Diam. Relat. Mater.*, vol. 19, no. 7–9, pp. 752–755, 2010, doi:

10.1016/j.diamond.2010.01.044.

[301] D. Mattia and Y. Gogotsi, “Review: Static and dynamic behavior of liquids inside carbon nanotubes,” *Microfluid. Nanofluidics*, vol. 5, no. 3, pp. 289–305, 2008, doi: 10.1007/s10404-008-0293-5.

[302] S. Li, H. Li, X. Wang, Y. Song, Y. Liu, and L. Jiang, “Super-Hydrophobicity of Large-Area Honeycomb-Like Aligned Carbon Nanotubes,” pp. 9274–9276, 2002.

[303] H. Qian, A. Bismarck, E. S. Greenhalgh, G. Kalinka, and M. S. P. Shaffer, “Hierarchical composites reinforced with carbon nanotube grafted fibers: The potential assessed at the single fiber level,” *Chem. Mater.*, vol. 20, no. 5, pp. 1862–1869, 2008, doi: 10.1021/cm702782j.

[304] S. Shalel-Levanon and A. Marmur, “Validity and accuracy in evaluating surface tension of solids by additive approaches,” *J. Colloid Interface Sci.*, vol. 262, no. 2, pp. 489–499, 2003, doi: 10.1016/S0021-9797(02)00231-X.

[305] S. Nuriel, L. Liu, A. H. Barber, and H. D. Wagner, “Direct measurement of multiwall nanotube surface tension,” *Chem. Phys. Lett.*, vol. 404, no. 4–6, pp. 263–266, 2005, doi: 10.1016/j.cplett.2005.01.072.

[306] L. Zhang *et al.*, “Wettability of carbon nanotube fibers,” *Carbon N. Y.*, vol. 122, pp. 128–140, 2017, doi: 10.1016/j.carbon.2017.06.027.

[307] E. Dujardin, T. W. Ebbesen, H. Hiura, and K. Tanigaki, “Capillarity and Wetting of Carbon Nanotubes,” *Science (80-.).*, vol. 265, no. 5180, pp. 1850–1852, 1994, doi: 10.1126/science.265.5180.1850.

[308] F. An, C. Lu, J. Guo, S. He, H. Lu, and Y. Yang, “Preparation of vertically aligned carbon nanotube arrays grown onto carbon fiber fabric and evaluating its wettability on effect of composite,” *Appl. Surf. Sci.*, vol. 258, no. 3, pp. 1069–1076, 2011, doi: 10.1016/j.apsusc.2011.09.003.

[309] G. Xia, Y. Lu, and H. Xu, “Electrogeneration of hydrogen peroxide for electro-Fenton via oxygen reduction using polyacrylonitrile-based carbon fiber brush cathode,” *Electrochim. Acta*, vol. 158, pp. 390–396, 2015, doi: 10.1016/j.electacta.2015.01.102.

[310] E. Petrucci, A. Da Pozzo, and L. Di Palma, “On the ability to electrogenerate hydrogen peroxide and to regenerate ferrous ions of three selected carbon-based cathodes for electro-Fenton processes,” *Chem. Eng. J.*, vol. 283, pp. 750–758, 2016, doi: 10.1016/j.cej.2015.08.030.

[311] F. Yu, Y. Chen, and H. Ma, “Ultrahigh yield of hydrogen peroxide and effective diclofenac degradation on a graphite felt cathode loaded with CNTs and carbon black: An electro-generation mechanism and a degradation pathway,” *New J. Chem.*, vol. 42, no. 6, pp. 4485–4494, 2018, doi: 10.1039/c7nj04925k.

[312] D. Carlstedt and L. E. Asp, “Performance analysis framework for structural battery composites in electric vehicles,” *Compos. Part B Eng.*, vol. 186, no. December 2019, p. 107822, 2020, doi: 10.1016/j.compositesb.2020.107822.

[313] J. Tian, N. Cui, P. Chen, K. Guo, and X. Chen, “High-performance wearable supercapacitors based on PANI/N-CNT@CNT fiber with a designed hierarchical core-sheath structure,” *J. Mater. Chem. A*, vol. 9, no. 36, pp. 20635–20644, 2021, doi: 10.1039/d1ta03663g.

[314] Y. Xia, H. Shang, Q. Zhang, Y. Zhou, and X. Hu, “Electrogeneration of hydrogen peroxide using phosphorus-doped carbon nanotubes gas diffusion electrodes and its application in electro-Fenton,” *J. Electroanal. Chem.*, vol. 840, no. November 2018, pp. 400–408, 2019, doi: 10.1016/j.jelechem.2019.04.009.

[315] W. Wang *et al.*, “Enhancement of hydrogen peroxide production by electrochemical reduction of oxygen on carbon nanotubes modified with fluorine,” *Chemosphere*, vol. 259, p. 127423, 2020, doi: 10.1016/j.chemosphere.2020.127423.

[316] Z. Qiang, J. H. Chang, and C. P. Huang, “Electrochemical generation of hydrogen peroxide from dissolved oxygen in acidic solutions,” *Water Res.*, vol. 36, no. 1, pp. 85–94, 2002, doi: 10.1016/S0043-1354(01)00235-4.

[317] Y. Zheng and S. Wang, “The effect of SiO 2 -doped boron nitride multiple coatings on mechanical properties of quartz fibers,” *Appl. Surf. Sci.*, vol. 258, no. 7, pp. 2901–2905, 2012, doi: 10.1016/j.apsusc.2011.11.004.